UNIVERSITÀ
degli STUDI
di CATANIA

Dipartimento
di Fisica
e Astronomia
"Ettore Majorana"

PhD programme in physics

Eugenia Naselli

Experimental study of Electron Cyclotron Resonance plasmas by a multi-diagnostics system in stationary vs. turbulent regimes: perspectives to in-plasma β-decay investigations of nuclear and astrophysical interest

PhD thesis

Supervisors:
Chiar.mo Prof. F. Leone
Dr. D. Mascali

---

academic year 2019/2020

Contents

Introduction

This thesis presents an interdisciplinary study concerning a new way of measuring nuclear decays as a function of thermodynamical conditions of the environment, namely a magnetized plasma obtained via Electron Cyclotron Resonance and trapped in strong magnetic fields. Plasmas physics applies to many multidisciplinary contexts having implications both in fundamental sciences as well as technology. Laboratory plasmas are for example widely used both in the context of controlled nuclear fusion or for feeding particle accelerators, i.e. as ion sources - such as the Electron Cyclotron Resonance (ECR) Ion Source (ECRIS) - producing high intensity beams of highly charged ions. In this work, magnetized ECR plasmas in compact traps are investigated as *experimental environments* for the study of nuclear β-decays of nuclear and nuclear astrophysical interest. In particular, theoretical predictions and former experiments have shown that the ionization state of the in-plasma isotopes can dramatically modify, even of several orders of magnitudes, the isotopes lifetimes [1, 2], due to mechanisms such as the bound state β-decay [3]. Studies related to fundamental physics of nuclear decays in astrophysics environments are expected to have a major impact in the study of nuclear-astrophysics processes and cosmology (Big Bang nucleosynthesis, s-processing, CosmoChronometers, Early Solar System formation) and only few experimental evidences have been collected, up to now, but using radically different (and complementary) setups, i.e. storage rings [3, 4, 5].

This thesis has been thus carried out in the frame of the PANDORA_Gr3 (Plasma for Astrophysics, Nuclear Decay Observation and Radiation for

Archaeometry) project [6, 7], supported by the National Scientific Committee 3 (CSN3) of INFN, which proposes a new and complementary experimental approach to those attempted in the past. It aims to build a compact and flexible magnetic plasma trap for measuring, for the first time, in-plasma nuclear β-decay rate as a function of the plasma temperature, impacting on the charge state distribution of the in-plasma ions. In the PANDORA_Gr3 setup, a dense and hot plasma - made of multicharged ions immersed in a dense cloud of energetic electrons - is confined by multi-Tesla magnetic fields and resonantly heated by some kWs of microwave power in the $18 - 21$ GHz frequency range. The plasmas can reach $n_e \sim 10^{11} - 10^{13}$ cm^{-3}, $T_e \sim 0.1 - 100$ keV of electron density and temperature, respectively and thus mimic some stellar-like environments as it concerns, mainly, the charge state distribution (CSD) conditions. Thus, the radionuclides can be trapped in a dynamic-equilibrium, in a Magneto Hydro Dynamically (MHD) stable plasma, maintaining an on-average locally stable density, temperature and CSD for several days of even weeks. First calculation at ECRIS densities and temperatures confirm that even in non-LTE conditions (due to the low density) the abundances of charge states are - for many of the physics cases of interest - very similar to the ones occurring in astrophysical conditions, where densities are ten order of magnitude higher. This makes the experiments running in an ECRIS more directly scalable to astrophysical systems.

The PhD's scientific activities described in this work, carried out at National Institute for Nuclear Physics – Laboratori Nazionali del Sud (INFN-LNS) and in collaboration with the ATOMKI Laboratories (Debrecen, Hungary), deal particularly with the study, development and use of an innovative multi-diagnostics system with advanced analytical techniques aiming at characterizing the thermodynamical properties of the ECR plasma; when the PANDORA setup will be ready (expected by the end of 2023) the system will allow simultaneous characterization of plasma properties and β-decay rates (in combination with a gamma-multidetectors array, also studied in this thesis), to be correlated each other, and also to monitor plasma stability and mitigate kinetic turbulences naturally occurring in these plasmas. Results reported in the thesis have been collected on downsized testbenches very well emulating the main features of PANDORA, even if at lower energy contents (both

lower densities and temperatures), operating at INFN and ATOMKI-labs in Hungary.
The direct correlation of the plasma environment and the decay itself can be done only by simultaneously identifying and discriminating - through the above-mentioned multi-diagnostic detection system - the photons emitted by the plasma (from microwave to hard X-ray) and γ-rays emitted after the isotope's β-decay. Due to the non homogenous-non isotropic nature of ECR magnetoplasma, the characterization of plasma proprieties has to be done also using space and time-resolved techniques. Setup and tools, typically at the service of particle accelerators physics and applications, have been redesigned and improved for performing multidisciplinary and fundamental physics studies. The obtained results that will be shown and commented in the coming pages are not relevant in the perspectives of in-plasma β-decay investigations only, but they resulted to be really important for the physics and technology ion sources as well. Innovative methods to master plasma turbulent regimes have been investigated and a new plasma heating method able to damp the plasma instabilities, improving the ECRIS stability performances, has been found. Several obtained results have been already published in peer reviewed papers and personally presented in international conferences.

The most relevant personal contributions to the activities described in this work rely, in particular, to the development and use of the aforementioned multi-diagnostics setup and associated analysis techniques: I took part to both the experimental campaigns that permitted to collect the data hereby reported, playing a major role in setup-preparation, data taking and following analysis. The first campaign was carried out at the INFN-LNS - in the period December 2017 / January 2018 - aimed at characterizing the Cyclotron Maser Instability processes in a multi-diagnostic approach; the second one was carried out at the ATOMKI-Debrecen laboratories (Hungary), subdivided into two parts, one during March 2018 while the second during July 2018; both these experiments aimed at characterizing plasma stable and turbulent regimes by heating the plasma in single and double frequency mode. By virtue of the results collected by this multi-diagnostics setup during these two experimental campaigns I was selected as an invited speaker at the 3^{rd} European Conference on Plasma Diagnostics (held in Lisboa, on May 2019) and published in

[8, 9, 10].

Using the ECR-ATOMKI testbench, we investigated the so-called Two Close Frequency Heating Effect. In particular, I dealt with the time- and space-resolved X-ray measurements and analysis, implementing a dedicated Matlab codes-suite. Plasma kinetic turbulence regimes were studied for the first time in a quantitative way. It has been also possible to demonstrate that TCFH was a powerful method to damp the instabilities, significantly improving the performance of the source (optimizing the distribution of high ion charge states and the intensity of the extracted beam, resulting to be much more stable). These results were discussed in an oral talk given at the 23^{rd} International Workshop on ECR ion sources (Catania, Italy, September 2018) and then published in [11, 12].

A specific analysis was focused on the development and implementation of an algorithm for analyzing Single Photon-Counting images and thus performing high resolution spectrally-resolved X-ray imaging. It allowed detailed studies of plasma confinement dynamics vs plasma internal structure modifications. These outcomes were presented during the 24^{rd} International Workshop on ECR ion sources (organized in online mode by the Michigan State University, USA, on September 2020) and during the 106^{th} National Congress Italian Physical Society (on September 2020) and are now under publication (papers submitted [13, 14, 15, 16]).

Finally, further studies were performed in order to figure out the final setup of PANDORA that will run, as said above, by correlating plasma properties to gamma-rays (as by-products of beta-decays) detection. This was done by carrying out Monte Carlo simulations supporting the design of the array of γ detectors. In particular, I was involved in the implementation of GEANT4 simulation code, in order to evaluate the total detection efficiency. Once determined acceptance and overall efficiencies of this setup, also the sensitivity of the PANDORA setup was specifically checked, in particular I explored the measurability of isotopes lifetimes a kind of "*virtual experiment*". This permitted to estimate the experimental run durations for getting enough statistical significance in terms of σ-levels. Results were presented in the 1^{st} workshop on PANDORA_Gr3 (that was held in Perugia, on October 2019) and in the 10^{th} European Summer School on Experimental Nuclear Astrophysics (that was held in

Catania, on July 2019), then published in [17, 6].

In summary, this thesis is organized on six chapters.
First chapter discusses the general features of ECR plasmas. Basics on the magnetic mirror trapping, models of ECR heating and radiation processes in the plasma are here described.
The *second chapter* is focused on the idea of β-decay measurements in ECR plasmas, discussing the state of the art and highlighting the main aspects of the PANDORA_Gr3 experimental approach. Selection of isotopes for the PANDORA phase-1 studies is here commented, along with their expected lifetimes and needed plasma properties also in terms of dynamical equilibrium to be achieved.
The original contribution is mainly reported from the third chapter on.
In fact, the *third chapter* describes the multi-diagnostic setup, with details about the developed tools: the high resolution spectrally-resolved imaging tool (i.e. the X-ray pin-hole CCD camera setup) and the time-resolved spectroscopy device (plasma-immersed two-pins RF probe connected with a Spectrum Analyzer). Comparative descriptions of the three types of ECR ion sources used as testbenches is also given (PANDORA_Gr3, Flexible Plasma Trap, and ATOMKI-ECR).
In the *fourth chapter*, the on-purpose developed analytical methods are described. A suite of MatLab codes has been developed from the ground, supporting the analysis of the X-ray pin-hole camera images (allowing photon energy analysis, photon energy filtering, CCD image post-processing techniques, noise reduction, etc.) and of the signals collected by the two-pins RF probe (used to determine the plasma turbulence levels).
The whole set of the experimental results about spatial and temporal analysis of ECR plasmas are described in the *chapter five*, highlighting the original impact of these results on the plasma physics research. In particular, the effect of the TCFH on the suppression of the plasma turbulences in B-minimum magnetic configurations, and on the confinement of the plasma warm electrons is discussed.
Finally, the *chapter six* reports on the GEANT4 simulations implemented for supporting the design of the γ-ray detectors array in PANDORA_Gr3.

Chapter 1

Fundamental of ECRIS plasma physics

Plasma physics is a fundamental branch of modern science and has a large number of applications in different fields of research, from astrophysics and nuclear astrophysics, for studying the stars and the universe, to the problems related to the production of energy through the nuclear fusion.
Plasma is commonly known as the fourth state of matter, composed of electrons, ion and neutral particles. Although plasma is viewed as a rare form of matter aggregation, since it is so rare on Earth (mainly the ionosphere layer of the Earth's atmosphere), about the 98% of the matter of the entire Universe is plasma: stars, nebulae, interstellar space.
Plasma is defined as a quasi-neutral gas that exhibits collective behaviors, i.e. the motion of particles in a given region of the plasma is affected by the overall state of the system and not only by local conditions.
In every gas at non-zero temperature there is an amount of ionized atoms. The law that describes the state of ionization of a gas is given by Saha's formula [18]:

$$\frac{n_e n_i}{n_n} = \frac{2(2\pi m_e T)^{\frac{3}{2}}}{h^3} e^{\frac{-E_i}{T}} \tag{1.1}$$

where n_e, n_i and n_n are, respectively, the electron density, the ion density and the neutral atoms density. T is the plasma temperature and m_e, E_i, h

are, respectively, the mass of the electron, the ionization energy and the Plank's constant. As highlighted by the relation 1.1, for an ordinary gas ionized atoms are in extremely low quantities compared to neutral atoms; instead, the contrary occurs for plasma where the majority of atoms are ionized.
Known plasmas cover a very wide range of densities n and temperatures T, spanning of 25 order of magnitude for the first and of 7 for the second. Several example are shown in the table 1.1.

Table 1.1: Several known plasmas with range of densities n and temperature T.

	n [m^{-3}]	**T [keV]**
thermonuclear fusion plasmas (magnetic confinement)	$\sim 10^{20}$	~ 10
thermonuclear fusion plasmas (inertial confinement)	$\sim 10^{31}$	~ 10
solar wind	$\sim 5 \cdot 10^{6}$	~ 0.2
earth ionosphere	$\sim 5 \cdot 10^{12}$	~ 0.0001
ECR ion sources plasmas	$\sim 10^{17} \div 10^{19}$	$\sim 0.1 \div 100$

Of particular interest, for the present thesis, are the plasmas generated in compact magnetic traps, such as Electron Cyclotron Resonance Ion Sources (ECRIS). In the following pages only some aspects directly related to the properties of Electron Cyclotron Resonance (ECR) plasmas will be treated with some details, especially regarding the confinement of ECR plasma in compact traps, the radiative X-ray plasma emission and methods for plasma heating by the microwave, in single frequency and in double frequencies heating mode. These are the main aspects that will then be recalled during the thesis, in the original and experimental chapters.

1.1 Plasma parameters

The main fundamental parameters characterize the plasma generated in an ECRIS are:

- the electron density n_e (measured in cm^{-3} or m^{-3});
- the temperature T of each species (usually measured in eV in units of KT, being K the Boltzmann constant, where 1 $eV = 11605°K$);
- the steady state magnetic field B (measured in Tesla);
- the confinement time τ_c.

A host of subsidiary parameters (e.g., Debye length, Larmor radius, plasma frequency, cyclotron frequency, thermal velocity) can be derived from these three fundamental parameters. For partially-ionized plasmas, the fractional ionization and cross-sections of neutrals are also important.

1.2 The plasma confinement: Simple mirror and $B_{minimum}$ configuration

The confinement of the plasma, has a primary importance in case of ECRIS, and in general of all the ion sources and plasma traps. The ions must live inside the plasma for time long enough allowing high number of collisions, and the most effective way to confine charged particles is by means of a magnetic field. The most simple device for plasma confinement is named *Simple Mirror (SM)*. In this magnetic configuration the field is provided by two solenoids with coinciding axes, located to definite distances each other. Figure 1.1 features the shape of the field lines of one half of the SM structure (symmetric with reference to the midplane). Some condition must be fulfilled for trapping a charged particle in a given magnetic field structure [19]:

- the magnetic field has to have a gradient $\vec{\nabla}_{\parallel} B$ parallel to the magnetic field axis;
- even in the simple cases like Simple Mirror configurations, the field maybe axisymmetric but it must have a radial component;
- the velocity vector of the charged particle must form a particular angle with the field lines. A boundary exists for this angle, and for smaller angles the particle is not confined anymore.

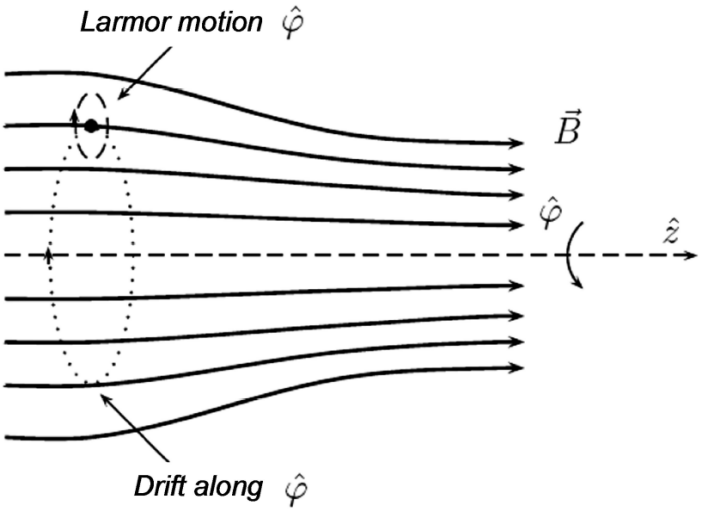

Figure 1.1: Magnetic field lines produced in a simple mirror configuration. The density of the field lines increases going to right, and this generates the gradient which allows the confinement of the charged particles [19].

In figure 1.1 only one of the two mirrors is displayed. It can be seen that the field strongly depends on the z coordinate; the density of the field lines increases going to the right side, and this generates the gradient which allows the confinement of the charged particles [19]. In addition, we can neglect the dependence on φ, i.e. $B_\varphi = 0$.
All the field components must satisfy the Maxwell equation: $\vec{\nabla} \cdot \vec{B} = 0$.
The simplest profile to trap charged particles satisfying this condition is [20]:

$$B_z = B_0 + B_1 z^2 \tag{1.2}$$

$$B_r = -rzB_1 \tag{1.3}$$

with constant B_0 and B_1.
The particle motion evolves by keeping the guiding center of the spiral-like trajectory along to a fixed field line; slow drifts also affect the motion, the most important one around the system axis. In a single particle scenario, transversally, i.e. along the perpendicular direction with respect to the mirror axis, the particles are automatically confined because they

gyrate around the magnetic field lines. From the Lorentz force comes that the component along the z axis can be written as [19]:

$$F_z = \frac{1}{2} q v_\varphi r \left(\frac{\partial B_z}{\partial z} \right) \tag{1.4}$$

replacing B_r with the expression 1.3:

$$F_z = q v_\varphi r z B_1 \tag{1.5}$$

then, along z a force arises and it is able to confine the particles if some conditions are satisfied.
By averaging F_z on a gyro-period, considering a particle moving along the mirror axis we obtain [19]:

$$\bar{F}_z = -\frac{m v_\perp^2}{B} B_1 z \tag{1.6}$$

then the force is directed in the opposite direction with respect to the particle motion.
We can also define the so-called magnetic moment of the charged particle as [19]:

$$\mu = \frac{1}{2} \frac{m v_\perp^2}{B} \tag{1.7}$$

Then the force along z becomes:

$$\bar{F}_z = -\mu \left(\frac{\partial B}{\partial z} \right) \tag{1.8}$$

generalizing for a whatever gradient along the particle motion:

$$\vec{F}_\parallel = -\mu \frac{\partial B}{\partial s} = -\mu \vec{\nabla}_\parallel B \tag{1.9}$$

where $d\vec{s}$ is a line element along $\vec{B}$ direction.
The most important characteristic of μ is its invariance with respect to the time (it is known as *adiabatic invariant*). μ is an adiabatic invariant under two hypothesis:

- The variation of the B_z component with respect to z, namely, $\frac{\partial B_z}{\partial z}$ has to be constant with r;

- The B_z component must vary smoothly with the z coordinate in the time that the particle does a gyro-period. This condition can be written in the following manner:

$$\frac{r_L}{L} \ll 1 \tag{1.10}$$

  i.e. the Larmor radius r_L must be much smaller than L, the characteristic length for the B variation.

The mirror effect in terms of the μ invariance can be explained as it follows: consider a proof particle moving from the center to the periphery of the magnetic bottle; it sees a growing magnetic field; as μ must be kept constant the perpendicular component of the velocity $v_\perp$ must increase because of the B increase. As the magnetic field does not make any work on the system, then the kinetic energy remains constant. Hence, as $v_\perp$ increases, the $v_\parallel$ decreases. If B is sufficiently high at the periphery, there will be a mirror point where $v_\parallel = 0$ and the particle is reflected.
The ability to confine the particles by means of a magnetic bottle depends on the so called *loss cone aperture* [21]. In fact it can be easily understood from the above discussion that particles with $v_\perp = 0$ do not feel any mirror force, as they have $\mu = 0$; anyway $v_\perp \neq 0$ does not mean that the particle is confined, because particles with $\frac{v_\perp}{v_\parallel}$ very small on the midplane escape from the trapping if B_m at the system boundary is not sufficiently high to make $v_\parallel$ null. A minimum angle exists at the midplane (see figure 1.2), formed by the velocity vector and the magnetic lines, below which particles are lost because the maximum field cannot guarantee the mirroring. A smaller θ requires a stronger B in order to have the mirroring effect. A mathematical relation can be found to link this angle and the *mirror ratio*, i.e. the ratio between the maximum and the minimum field in the system:

$$sin^2\theta_{min} = \frac{B_0}{B_m} = \frac{1}{R_m} \tag{1.11}$$

where R_m is the mirror ratio $\frac{B_m}{B_0}$. The equation 1.11 allows to determine the so called ***loss cone***, i.e. that region in the velocity space ($\theta < \theta_{min}$) where particles that cannot be mirrored lie. The figure 1.3 shows a loss-cone shape in the velocity space.

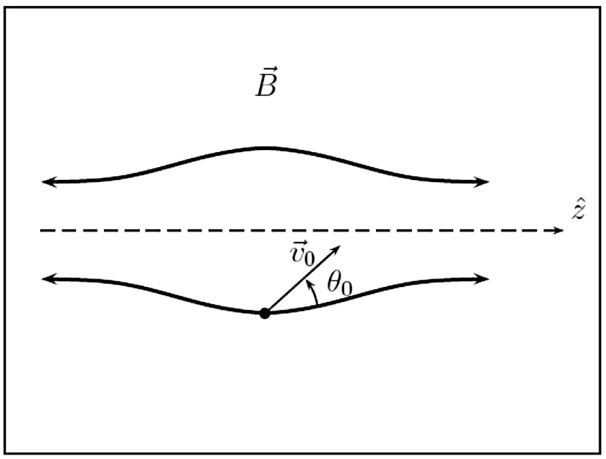

Figure 1.2: Schematic representation of the geometrical meaning of the θ_0 angle.

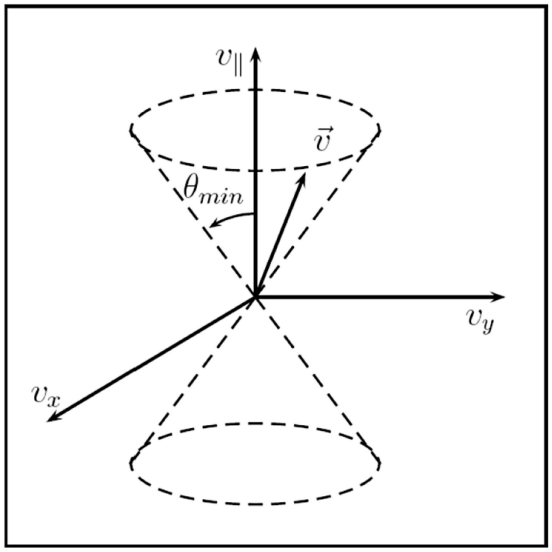

Figure 1.3: Schematic representation of the loss cone in the velocity space; θ_{min} indicates the cone aperture.

1.2.1 The MHD stability of magnetically confined plasmas

The simple mirror configuration allows to confine those particles obeying to the adiabatic invariance of the magnetic moment. In [22] it has been proved experimentally that single charged particles remained trapped in a magnetic mirror according to the prediction of the adiabatic theory.
Single particles are satisfactorily trapped in a magnetic mirror field but however this does not mean that the plasma reaches a stable equilibrium. Not only the losses induced by the collisions, which can change the velocity vector direction putting it inside the loss cone, but also other fluid instabilities may arise increasing the particles losses. Because of the magnetic confinement, the simple mirror plasmas have a non isotropic energy distribution function $f(\epsilon)$. This leads to some instabilities in the velocity space, the so-called loss cone instability. However, some hydrodynamical instabilities may be more dangerous. The most important instability involving simple mirror plasmas is the so called flute instability.

For magnetically confined plasmas it is equivalent to the well known Rayleigh-Taylor instability (arising when an accelerating force acts on an inverted density gradient), which arises in neutral fluids and also in plasmas subjected to the gravitational force. In this case, the magnetic field lines curvature triggers the instability. In figure 1.4 a schematic representation of the mechanism at the basis of the flute instability is reported.
It can be seen that by perturbing the plasma boundary flutes arise which change the energy balance of the plasma-field system. In particular the magnetic field energy remains unchanged (only some distortion of the field lines may change the magnetic energy), whereas the plasma energy increases. If the magnetic field lines have the curvature shown in figure, the perturbation will self develop with time, producing a flux of plasma in the perpendicular direction with respect to the mirror axis.

Figure 1.5 clearly shows that if the magnetic field lines curve into the plasma, the confinement will be stable. This result gives us some practical information on how to realize optimal plasma traps that are also hydromagnetically stable. The figure 1.6 shows the cusp field configuration: in this case the magnetic field lines curve into the plasma everywhere, and this ensures a stable confinement by the point of view of the flute instability. However the magnetic field lines are shaped in such a way that

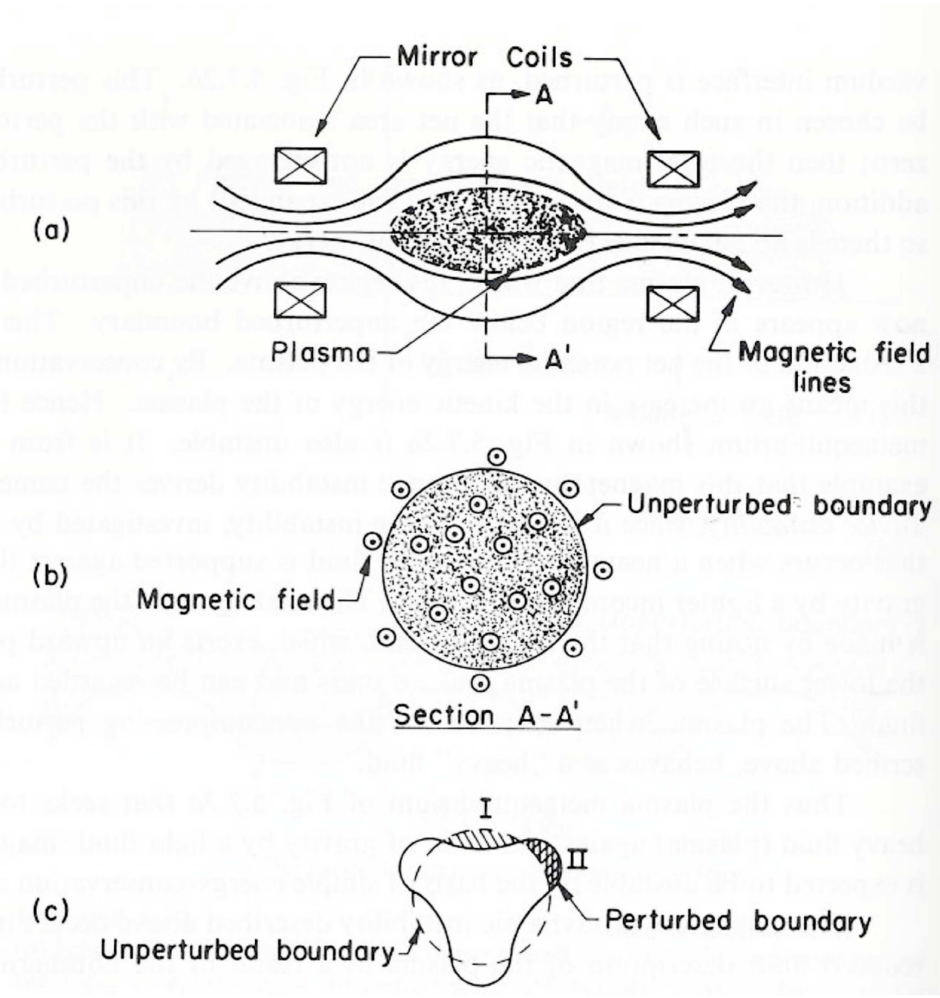

Figure 1.4: Description of the possible instability arising in a plasma confined by a magnetic field. (a) The plasma confined in the simple mirror configuration. (b) The midsection view of the plasma before the pertubation. (c) The same view of (b), but here plasma has been perturbed and the figure shown the first development of the "*flutes*" [23].

two large loss cones appear in the midplane, thus reducing the plasma lifetime (the plasma is lost because of particle scattering into four loss cones).

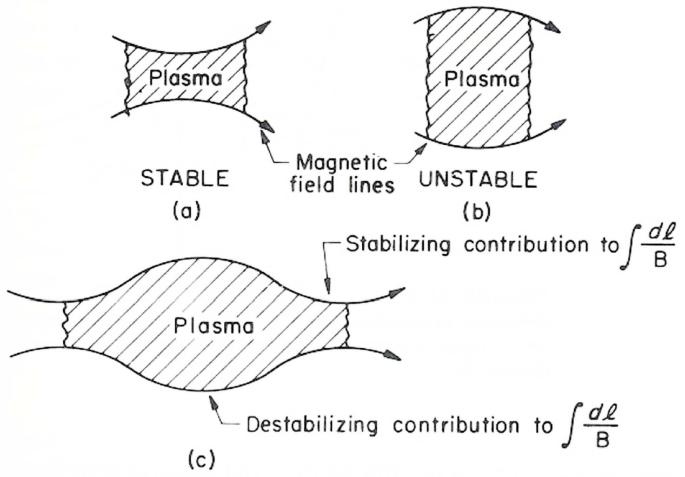

Figure 1.5: Schematic representation of the stable and unstable field line shapes in magnetically confined plasmas [23].

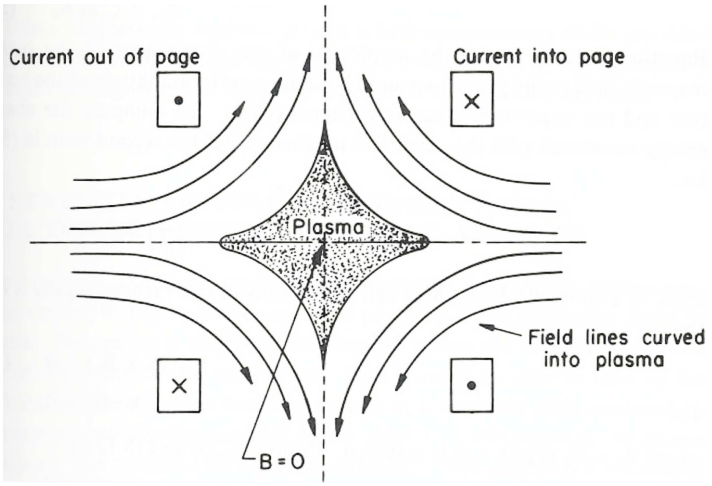

Figure 1.6: Cusp magnetic field configuration: the magnetic lines are curved into the plasma everywhere [23].

1.2.2 B_{min} magnetic configuration

In 1962 Ioffe [24] first reported about plasma-confinement experiments in a magnetic field configuration that had the desiderable feature of a magnetic field increasing in every direction away from the plasma boundary, and that did not have the undesirable feature of a region where the magnetic field went to zero inside the plasma (as in the case of cusp configurations). Such a configuration, called $B_{minimum}$, can be obtained as a superposition of two different magnetic fields:

- one created by two solenoids (*simple mirror*);
- and the other created by six conductors surrounding the plasma chamber (an *hexapole*).

In this way the magnetic field increases in every direction going from the plasma center to the periphery. In fact the field produced by the hexapole increases along the plasma radius, and it is constant along the plasma axis. This stabilizes radially, being the simple mirror able to confine the plasma axially.
This configuration can also be thought as a multi-mirror device: then the particle is reflected in many points travelling along the field lines. Thus, the the hydromagnetic instability suppression with a $B_{minimum}$ configuration was demonstrated.

The figure 1.7 schematically shows the structure of such a field. Note that the geometrical locus where B is constant are *egg-shaped surfaces*. As there are no axial symmetries, the adiabatic invariance cannot be invoked to study the particles confinement. Another adiabatic invariant can be used [21], [19]:

$$J = \oint v_{\parallel} dl \tag{1.12}$$

J essentially determines the field lines length between two reflection points. The J invariance implies that even after the reflection the particle will move along the same field line, or at least along a field line with the same J value.
Field lines with the same J value define a surface over which particles with fixed values of $\frac{W}{\mu}$ will move, being W the electron energy.

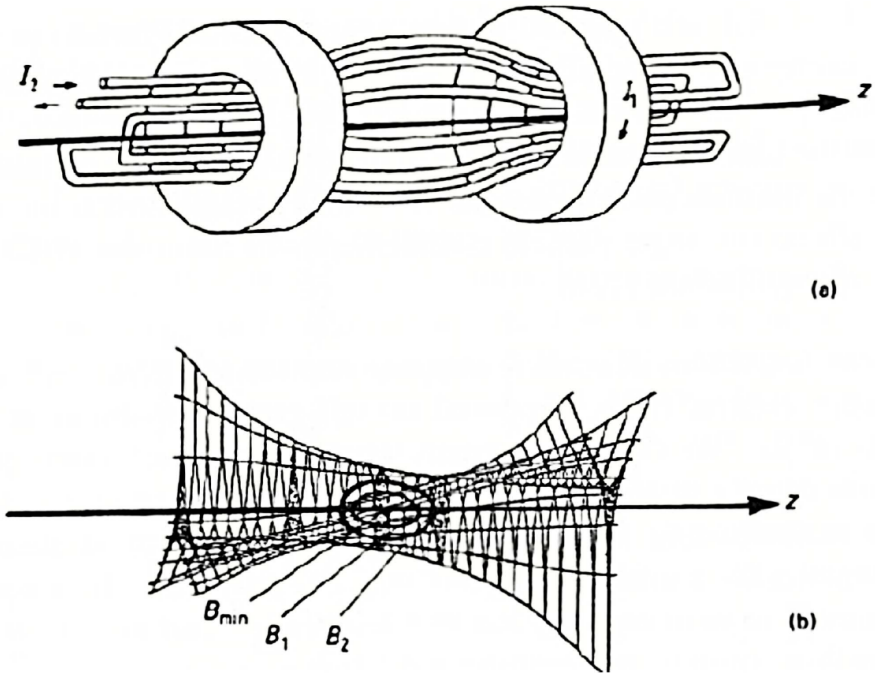

Figure 1.7: Magnetic system (a) and magnetic field structure obtained by the superposition of the field produced by two solenoids and an hexapole ($B_{minimum}$ field) (b) [21]. Field lines and iso-magnetic surfaces are shown, featuring a three-cusp shape twisting along the magnetic axis.

Then the plasma trap obeys to the condition that the constant J surfaces do not intercept the plasma chamber walls.
In figure 1.8 a sketch of the $B_{minimum}$ confinement system with the confined plasma is shown.

In the ECR plasma traps it is possible to maintain a Magneto Hydro Dynamically (MHD) plasma, living for several hours or days with on-average constant local density and temperature (the plasmas reach $n_e \sim 10^{11} \div 10^{13} cm^{-3}, T_e \sim 0.1 \div 100 keV$ of electron density and temperature, respectively). Typically, the plasma is confined by multi-Tesla magnetic fields and resonantly heated by some kWs of microwave power in the 2.45 - 28 GHz frequency range.

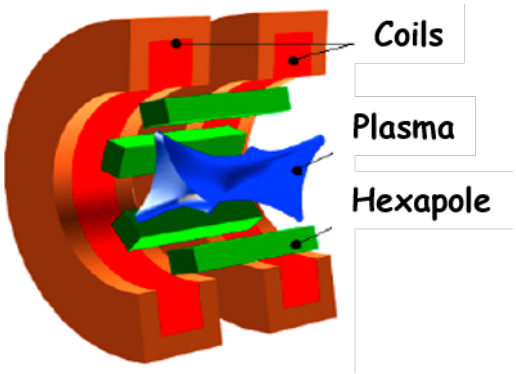

Figure 1.8: Sketch of the ECR confinement system and the confined plasma.

1.3 Plasma heated by microwaves

Lieberman et al. [25] proposed a single particle model based on momentum randomization via stochastic effects in order to explain the collisionless electron heating in ECRIS plasmas. The model assumes that the bouncing motion of the electrons provides the randomization of the wave-particle relative phase. In a parabolic-like B field: $B = B_{min}(1 + z^2/L^2)$, where $L = \left(\frac{\nabla B}{B}\right)^{-1}$ is the B characteristic scale-length of B, the z coordinate of an electron bouncing in the trap is:

$$z = z_0 cos(\omega_b t + \psi_0) \tag{1.13}$$

where ω_b is the bouncing frequency. Each resonance crossing gives a perpendicular energy kick, depending on a random phase term ϕ:

$$\epsilon = \epsilon_i + \Delta\epsilon + 2cos(\phi)\sqrt{\epsilon_i \cdot \Delta\epsilon} \tag{1.14}$$

Taking a general equation for the wave's E field, including eq.1.13, we obtain:

$$E(r, \theta, z, t) = E_0 cos[\omega_{RF} t + \theta - k z_0 cos(\omega_b t + \psi_0)] \tag{1.15}$$

The above formula accounts for an effective multi-resonance interaction of the electrons at the ECR. This model goes also under the name of "*non-linear pendulum model*": in the phase space the separatrices of each virtual

wave are overlapped on a broad range of velocity, that means chaotic diffusion and effective heating. The heating stops when the separatrices split (adiabatic invariants activate when this condition holds. In the phase space some "*islands*" appears in the chaotic sea, thus limiting a further heating of electrons), i.e. $\omega_b \cong \omega_c \approx \omega_{RF}$, being W_S the energy for which this condition holds; the absolute stochastic barrier (ASB) will be:

$$W_b \approx 5W_S = \left[m_e L \left(1 + \frac{l^2}{L^2} \right) \right]^{\frac{1}{4}} l \omega^{\frac{1}{2}} (eE)^{\frac{3}{4}} \tag{1.16}$$

where l is the distance of the resonance from B_{min}; eq. 1.16 predicts a power law scaling of W_b with the main operational parameters: P_{RF}, ω_{RF} and L.

A more general description of electron heating can be given assuming a diffusion-like mechanism in velocity space. Employing spherical polar coordinates (v, μ, θ), where v is the speed, *arcos* μ the pitch angle and θ the angle about the axial magnetic field, the diffusion tensor is formed by the diagonal elements [26]:

$$D_{vv} = \frac{\Delta v^2}{2\Delta t} = \pi \left(\frac{eE}{2m_e} \right)^2 \frac{L}{d\omega} \quad and: \quad D_{\mu\mu} = \frac{\Delta \mu^2}{2\Delta t} = D_{\mu\mu} \left(\frac{v}{v_\phi} \right)^2 \tag{1.17}$$

where d is the plasma length and v_ϕ the wave's phase velocity (the other parameters assume here the usual meaning). The general form of the distribution function kinetic equation will be:

$$\frac{\partial f_e}{\partial t} = \left(\frac{\partial f_e}{\partial t} \right)_{coll} + \left(\frac{\partial f_e}{\partial t} \right)_{RF} + S_{i,e} \;\; with: \;\; \left(\frac{\partial f_e}{\partial t} \right)_{RF} = \frac{\partial}{\partial v_i} \left(D_{i,j} \frac{\partial f_e}{\partial v_i} \right) \tag{1.18}$$

where the terms $S_{i,e}$ are sources of ions and electrons due to ionization and secondary wall emission.

The RF term has been written in terms of the diffusion coefficients. The diffusion is anisotropic due to the pitch angle scattering provided by the RF field, which acts along μ. One conclusion coming from this model is that the heating rapidity would grow linearly with L (while the single particle model gives a proportionality to $L^{1/2}$). The impact of the pitch angle scattering on the plasma density depends on v_ϕ; close to the reso-

nance, the cold plasma refraction index can be replaced by:

$$\frac{k^2c^2}{\omega^2} \approx -\frac{\omega_p^2}{\omega k v_t} \tag{1.19}$$

where v_t is the thermal velocity and ω_p the plasma frequency. Hence v_ϕ will be:

$$v_\phi^3 \approx \frac{\omega^2}{\omega_p^2} v_t c^2 = \frac{n_c}{n_e} v_t c^2 \tag{1.20}$$

According to eq. 1.17, $D_{\mu\mu}$ grows for decreasing v_ϕ, i.e., through eq. 1.20, for increasing n_e. When v_t approaches v_ϕ, the RF scattering efficiently injects electrons into the loss cone, and this limits n_e. To further increase n_e, n_c must be increased as well, hence: $n_e \propto \omega_{RF}^2$; ω_{RF} also fixes the characteristic electron energy: $E_{char} \approx 1/2 m_e v_\phi^2$. This approach correctly explains the "*omega squared*" law derived by Geller (see [21]) and the increase of the average energy of the electrons for increasing ω_{RF}, as experimentally observed when passing, for example, from 18 to 28 GHz (see figure 1.9). The single particle approach predicts the increase of the ASB with $\omega_{RF}^{1/2}$.

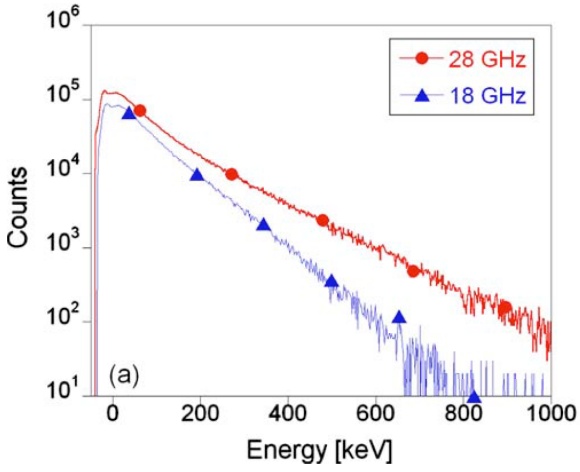

Figure 1.9: X-ray spectra at different frequency [27]

Issue of plasma stability

Strongly anisotropic distribution of the electrons in the velocity space can cause the kinetic instabilities [28], triggered when the transverse velocity of the electrons respect to the magnetic field starts to dominate over the longitudinal one. A characteristic feature of the cyclotron instability is the emission of microwaves, the energy of fast electrons may be released as coherent (maser) electromagnetic radiation due to development of electron cyclotron instabilities. The emission frequency depends on the electron cyclotron frequency, i.e. on local magnetic field B. The occurrence of the instabilities events are followed by sudden radio and X-ray emission of the plasma and plasma chamber complex [29, 30]. Thus, since plasma kinetic instabilities are characterized by fast RF and X-ray bursts, the plasma self radio-emission, in GHz ranges, can be considered as a signature of the plasma instability regime, as described in [31, 29].
Even if along the years many studies have been performed, the exact mechanism of turbulent regimes of plasmas is still unknown. A deeper investigation is so necessary in order to improve the plasma stability, also by means of new plasma heating methods.

1.3.1 Two Frequency Heating

In the context of ECR ion sources, to obtain intense highly charged ion a dense and energetic ECR plasma, having anisotropic distribution of the electrons in the velocity space, is required.
General approach of the way for the improvement is pointed by the scaling laws [21]. Accordingly, higher plasma density is needed to produce higher charge state ions, which requires higher microwave heating power. However in order to still remain below the critical density (to avoid the cut-off of the microwaves), which is scaling with the frequency square the heating frequency and the corresponding magnetic field should be increased, as well.
Milestones in this way are symbolized by different generations of ECRISs. However, the steps between two generations are money- and time-consuming, requiring many investments from cryogenic and radiofrequency engineering sides. Therefore, at a given generation level (where the magnetic

field and frequency configuration is determined) tricks were worked out to significantly improve the beam parameters without drastically changing the ECRIS configuration. They are widely applied in the ECRIS committee e.g. gas mixing [32], biased disc [33], fine frequency tuning [34], and two frequency heating [35].
Since the first half of the '90 multiple frequency heating has been tested and used as a technique which provides remarkable improvement of the ion source performance by improving the stability of the plasma and by shifting the ion charge state distribution toward the higher charge ones [36]. It consists in injecting lower frequency (and usually lower power) microwaves in addition to the primary microwave radiation into the ECRIS plasma. The first experiments providing promising results were performed applying two far frequencies (e.g. 10 GHz + 14 GHz, 14 GHz + 18 GHz) obtaining two well separated ECR heating zones (Two Far Frequency Heating (TFFH)). The effects were explained by the increase of the ECR heating volumes [37], which enhances the ionization efficiency and improves the electron confinement [38]. TFFH of ECRIS plasma enhances the extracted ion beam current of high charge states intensities (up to 30%) and improves the extracted beam and plasma stability [39, 40, 37, 41, 42]. However, in 2008 Gammino at al. [43] pointed out a possible "*extra*" interplay between the two resonant zones having the two frequencies close to each other (Two Close Frequency Heating (TCFH)). TCFH mode is possible through the use of two frequencies with a difference of the order of some hundreds of MHz (instead of > 1 GHz as typically done in TFFH). Particularly, some kind of "*electron surfing*" is expected; the electrons that leave the first resonant zone may be further accelerated by the second one (two close frequency is needed because the phase randomization of the electrons should not be occurred). The idea was confirmed by numerical simulations showing remarkable variation in electron energy as function of the relative phase difference between the two close frequencies.
Independently of the magnitude of the relative frequency difference (TCFH or TFFH) the importance of the fine tuning at least one of the two microwave frequencies was stated, since strong fluctuation of highly charged ions were obtained by slight tuning of the relative frequency difference [44, 45]. In the case of TCFH mode the optimal effect was obtained when

the distance between the two resonant layers were close to the Larmor radius of the warm electrons [46].
It was highlighted that the plasma stability and therefore the ion beam stability can be improved by adding an extra frequency [47, 41]. Higher net microwave power can be injected to the plasma chamber still maintaining stable plasma conditions at TFH mode therefore, higher current of highly charged ions are reachable.
It was also shown that the instabilities limiting the performance of the ion source occur at certain conditions [48] only i.e. at suitably high microwave power and at $\frac{B_{min}}{B_{ECR}}$ ratios higher than 0.75.
The role of the TCFH to mitigate kinetic instabilities occurring in magnetoplasma has been experimentally investigated (see [11]) and detailed experimental results will be discussed in the chapter 5. The origin of the stabilizing effect of the second frequency, currently under investigation, could be connected with the suppression of electron cyclotron instability due to the interaction between the secondary microwave radiation and the hot electron component of ECR [41, 11, 49, 50, 43, 48]. It is possible summarizing that the two frequency heating can help the ionization efficiency of ECR plasma and can suppress the ion beam oscillation caused by the kinetic instabilities in two far and two close frequency operations, as well.

1.3.2 Two Close Frequency Heating vs. Two Frequency Heating

Normally, the frequency of the two waves differs of more than 1 GHz, typically 3 or 4 GHz. The role of the TFH has been explored also in terms of its impact on the instability dynamics, as described in [41, 51]. In this paper, authors demonstrate that other than increase the beam current and the average charge state, the method is able to provide a stabilizing effect by suppressing the kinetic instabilities. Some qualitative explanations are attempted, inferring in summary that probably the interplay between the two waves re-distribute the plasma in real and phase space, reducing the amount of hot electrons that are deemed to support the instability growth.

It is very interesting to investigate the role of double frequency heating of the plasma when the two frequencies gap is consistent with the estimation given by [52], under which the two resonance zones are overlapped. Hereinafter this condition (i.e. the overlapping of the two resonance zones) will uniquely define the TCFH, thus distinguishing it from the classical TFH.
From a mathematical point of view, the $\delta\omega/\omega$ (omega is the heating frequency) condition fulfilling TCFH is given by the following formula:

$$\frac{\delta\omega}{\omega} \leq \frac{Y}{M^{\frac{5}{12}}} \tag{1.21}$$

where M, in a parabolic mirror, is given by:

$$M = \frac{\pi R_1^{\frac{1}{2}} \omega_1 L \rho}{2\left(Ai(0)\frac{4\pi e}{m}\right)^{\frac{3}{5}} \left(\mathcal{E}_1^2 + \mathcal{E}_2^2 \frac{B_1}{B_2}\right)^{\frac{3}{10}} \left(\frac{2B_1}{(dB/dz)_1 \omega_1^{\frac{1}{2}}}\right)^{\frac{2}{5}}} \tag{1.22}$$

and Y depends on the resonant and minimum B fields.
Part of the work will be presented in this thesis has been finalized to investigate the role of the TCFH under this condition, i.e. when the two resonance zones are partially overlapped. The characterization has been carried out for the first time in TCFH mode, through the use of two frequencies with a difference of the order of some hundreds of MHz, as will be described in the chapter 5.
In the paper of Lieberman, Lichtember and co-workers [52], quasi-linear theory of two frequency heating was used to give a robust explanation of TCFH consequences on the heating and confinement dynamics. Basically, authors claim the TCFH can turn the diffusion in velocity space into a four-dimensional process which enhances the diffusion rate also along $v_{\|}$, of more than a factor 2 even if the total power is just shared among the two frequencies.
The instability dynamically grows or damps according to the competitive balance between the growth and damping rate:

$$\frac{dE_\mu}{dt} \approx (\Gamma - \Delta) E_\mu \tag{1.23}$$

and the growth rate Γ is:

$$\Gamma \propto \frac{Ne_{hot}}{Ne_{cold}} \tag{1.24}$$

i.e. it depends basically on the ratio between the number of hot over cold electrons in the plasma, and in particular on the anisotropy of the Electron Energy Distribution Function. In fact, a more complete relation between the growth rate and the EEDF states the instability grows for enhanced $\frac{\partial f}{\partial v_\perp}$.
In TCFH, the higher diffusion along $v_\parallel$ should reduce the growth rate, thus limiting the energy that the plasma can self-couple to the electromagnetic modes supporting the instability.
Entering more into the details of the mechanism underlying the expected instability damping by TCFH, in summary, the consequences of TCFH on the electron dynamics are:

- The phase space describing the diffusion in velocity space becomes four-dimensional, instead of two-dimensional as with a single frequency;
- As a consequence of that, the adiabatic barrier limiting electron heating from below is deemed to increase, causing higher diffusion in $E_\perp$, i.e. in the perpendicular energy, but also in $E_\parallel$, i.e. the parallel energy component;
- As a consequence of higher diffusion in the parallel direction of particles' energy, particles scattering into the loss cone is hugely enhanced and it becomes more than competitive with collisions (diffusion due to TCFH is more than a factor two larger than collisions).

Therefore, it comes out that the TCFH plays a relevant role in making less anisotropic the EEDF.
This assumption can be more in details investigated by looking at the theory of TCFH and comparing it to the instability onset conditions.
The amount of electrons that are considered to be prone for developing an instability is considered to be dependent from $\frac{T_\parallel}{T_\perp}$ ratio. In most cases, other authors have found this amounts to around 1% up to 40% of the

global plasma electrons [31]. Estimation of the total amount of electrons that shows a distribution function that is globally prone to develop kinetic instabilities is normally done as considering the relation $\frac{B}{B_{ECR}} < 1 - \frac{T_\parallel}{T_\perp}$. This relation states that for increasing $\frac{T_\parallel}{T_\perp}$ ratio the region of the plasma where the $\frac{\partial f(v_\perp)}{\partial v_\perp} > 0$ condition is fulfilled (what in [31] is called 'butterfly' distribution) reduces more and more. Normally, in single frequency heating mode, interparticles collisions represent the main mechanism of electrons scattering in the $v_\parallel$ direction. But TCFH acts right in the mechanism of re-balancing the $\frac{T_\parallel}{T_\perp}$ ratio since the diffusion coefficient $D_\parallel$ due to quasi-linear diffusion is greatly enhanced, scaling as:

$$D_{\parallel Q} = \frac{\Delta E_\parallel^2}{2\tau_b} \propto \frac{\mathcal{E}_1}{\mathcal{E}_2} \Delta v^4 \left(\frac{\delta\omega}{\omega}\right)^2 \tag{1.25}$$

where $\mathcal{E}_1$ and $\mathcal{E}_2$ are the electric field amplitudes of the first and second wave (the label 1 identifies the lower frequency) while Δv is the velocity jump at the resonance, being $\Delta v \propto \mathcal{E}^{12/5}$.
From the above relation it follows that the quasi-linear diffusion applies for TCFH only parallel. It depends on the ratio between the two electric field amplitudes, meaning that for an unbalance of power on the first frequency (i.e., the inner resonance) the parallel diffusion is enhanced. Strong enhancement is also expected for increasing the power on the lower frequency, due to the term $\frac{\mathcal{E}_2}{\mathcal{E}_1}$, but the predominant effect is anyway related to the different coupling of the global RF power, which directly affects the velocity jump δ_v: it now causes the δ_v scaling more than linearly with the RF power itself (i.e., as $\propto \mathcal{E}^{12/5}$).
These basic assumptions on the quasi-linear diffusion are in qualitative agreement with the experimental observations, as it will be shown in the chapter 5; the TCFH seems to be able to reduce the regions of velocity space where $\frac{\partial f(v_\perp)}{\partial v_\perp} > 0$ due to the much more efficient balancing of $\frac{T_\parallel}{T_\perp}$ ratio.
Other details will be presented in sections where the experimental results

and the consideration about the TCFH damping effect on plasma kinetic instabilities will be presented.
Relevant part of the experimental study described in this thesis has been, in fact, aimed to investigate plasma turbulent regimens and the role of the TCFH on plasma stability and confinement improvement. The results will be presented in details in the chapter 5. The characterization has been carried out for the first time in TCFH mode, through the use of two frequencies with a difference of the order of some hundreds of MHz. Besides the above mentioned ECRIS improvement for the applied context, for $PANDORA_{Gr3}$ these studies are fundamental too. There is, in fact, the necessity to maintain ECR plasma in the same condition for weeks (as will be demonstrated in the chapter 6).
Consequently, finding innovative plasma heating methods able to maintain the plasma as much as possible stable, minimizing the turbulences trigger, is crucial.

1.4 The ECR plasma X-ray radiative properties

Plasma emits electromagnetic radiation in the X-ray domain essentially through three main mechanisms [53]:

- the **Bremsstrahlung**;
- the **recombination**;
- the **emission of characteristic lines**;

The analysis of the emission of this radiation is very important from the experimental point of view for plasma diagnostics as it gives information on the plasma internal structure.
The first mechanism consists in a loss of the electron's kinetic energy through an irradiation caused by the acceleration undergone by the electron in the field of the nucleus; it is a *free-free* transition since the electron passes from one state to another of free electron and therefore involves an emission characterized by a continuous spectrum. Also the recombination involves a continuous spectrum since the emission, in this case, is due to transitions from a free electron state to a bound electron state

(transition *free-bound*). Finally, the transitions between two *bound-bound* states produce line emissions, characteristics of the element from which the plasma was produced. In the figure 1.10 the three upcoming emission mechanisms are represented schematically, they will be discussed in detail in the following sections.

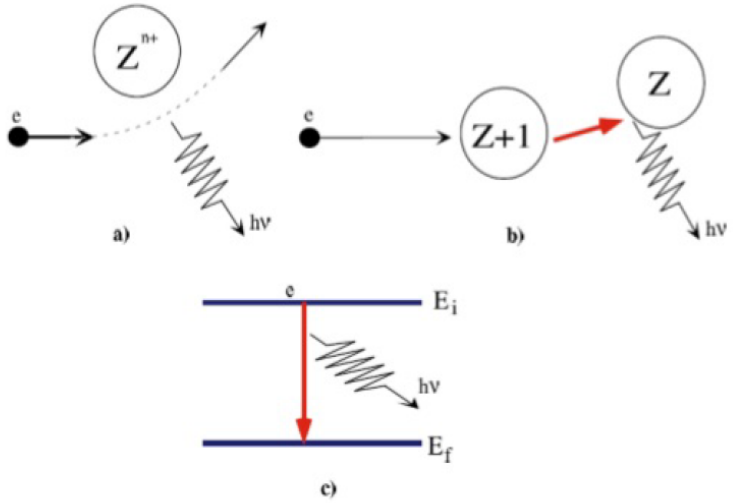

Figure 1.10: Schematic representation of the emission mechanisms: a) Bremsstrahlung; b) Recombination; c) Line emission.

1.4.1 The Bremsstrahlung radiation

As already mentioned, the Bremsstrahlung (or braking) radiation emission is consequent to the loss of kinetic energy from a free electron in the Coulomb field created by the ions in the plasma. For electrons of energy of a few hundred of eV, the radiation is emitted in the X-ray domain and is characterized by a continuous spectrum.
Full process analysis requires quantum mechanics, but we will limit to a classic treatment.
In each elementary collision, the acceleration of an electron (of mass m_e) is given by $a = \frac{F}{m_e}$, where the interaction force F varies along the trajectory.

In particular, as we are interested in collisions with small angle of deflection, from the analysis of the collision of an electron with an ion with charge Ze, the maximum interaction force is of the order of $F = Ze^2/b^2$, where b is the impact parameter. Then, the maximum acceleration undergone by the electron is given from [53]:

$$a = \frac{Ze^2}{m_e b^2} \tag{1.26}$$

and this maximum acceleration value occurs only for the time necessary to travel, at velocity v, a length about $2b$ in the region of minimum distance between the particles, so we can put:

$$\tau = \frac{2b}{v} \tag{1.27}$$

Thus, it is possible to estimate the energy ΔE radiated by the electron in the single impact.

$$\Delta E \simeq \frac{2e^2 a^2 \tau}{3c^3} = \frac{4Z^2 e^6}{3c^3 m_e^2 b^3 v} \tag{1.28}$$

To obtain the total energy radiated by an electron per unit of time we must integrate the eq.1.28 considering all possible collisions. The ion density of the plasma is called n_i, the collisions number per unit of time with collision parameter between b and $b + db$ is $2\pi n_i v b db$. Hence the radiated power for electron w will be a given by the energy contribution of the single electron evaluated for all collisions:

$$w = \int_{b_{min}}^{b_{max}} \Delta E 2\pi n_i v b db \simeq \frac{8\pi Z^2 e^6 n_i}{3c^3 m_e^2} \int_{b_{min}}^{b_{max}} \frac{db}{b^2} \tag{1.29}$$

where the integration extremes are respectively: $b_{max} = \Lambda_D$ as, due the shielding effect existing in the plasma, the action radius of the Coulomb force is limited to the Debye distance Λ_D; while the value of b_{min} will be given by the De Broglie wavelength associated with the electron ($b_{min} = \frac{h}{2\pi m_e v}$).
Carrying out the integral calculation we obtain:

$$w = \frac{16\pi^2}{3} \frac{Z^2 e^6 n_i}{c^3 m_e h} v \tag{1.30}$$

This is the expression of the power emitted by an electron of velocity v; to obtain the total contribution to the braking radiation, we must add the eq. 1.30 on all electrons, i.e. we must integrate it on the electron distribution function, therefore, since the problem is spherical symmetry, we have:

$$W = \frac{8\pi}{3}\frac{Z^2e^6n_i}{c^3m_eh}\int_0^\infty vf_e(v)dv \tag{1.31}$$

where $f_e(v)$ is the velocity distribution of the electrons. Assuming that $f(v)$ is a Maxwellian, it results:

$$\int_0^\infty vf_e(v)dv = n_e\left(\frac{m_e}{2\pi k_BT_e}\right)^{\frac{3}{2}}\int_0^\infty v\left(4\pi v^2e^{-\frac{m_ev^2}{2k_BT_e}}\right)dv = 2n_e\left(\frac{2k_BT_e}{\pi m_e}\right)^{\frac{1}{2}} \tag{1.32}$$

where $f_e(v)$ is the velocity distribution of the electrons.
Assuming that $f(v)$ is a Maxwellian, it results:

$$W = \frac{16\pi}{3}\frac{Z^2e^6n_in_e}{c^3m_eh}\left(\frac{2k_BT_e}{\pi m_e}\right)^{\frac{1}{2}} \tag{1.33}$$

The exact result differs from 1.33 by a factor $\sqrt{3/8}$ and, expressing T_e in eV and n_i and n_e in cm^{-3}, it is given by:

$$W = 1.6x10^{-27}Z^2n_in_eT_e^{\frac{1}{2}}\ erg\ sec^{-1}\ cm^{-3} \tag{1.34}$$

Equation 1.34 clearly shows the dependence on electron density and electron temperature. In particular, the power depends quadratically on the density being $n_e \simeq n_i$.
To estimate the spectral emission distribution for Bremsstrahlung we consider again the equation 1.29; considering again the relationship between the frequency and the impact parameter $\nu \simeq \frac{1}{2\pi\tau} = \frac{v}{4\pi b}$, we make a change of variable and assuming that $v_{max} >> v_{min}$ and that $v_{min} \simeq 0$ we obtain an equation analogous to 1.30 for the radiated power for electron:

$$w(\nu) = \Delta E\frac{\pi n_iv^3}{2\nu^3}d\nu = \frac{4}{3}\frac{Z^2e^6n_iv^3}{c^3m_e^2v\nu^3}\left(\frac{2\nu}{v}\right)^3\frac{\pi d\nu}{2} = \frac{16\pi}{3}\frac{Z^2e^6n_i}{c^3m_e^2v}d\nu \tag{1.35}$$

To have the overall emission we have to integrate 1.35 on the electrons distribution function. Therefore, adding over the electrons and remembering that the part of spectrum around a given frequency can only contribute electrons with velocity v satisfied condition $\frac{1}{2}m_e v^2 \geq h\nu$ (i.e. electrons that have sufficient energy for emitting ν frequency radiation) the contribution of all electrons is considered with Maxwellian distribution. Finally, the spectral intensity is:

$$W(\nu) = \frac{32\pi}{3}\frac{Z^2 e^6 n_i n_e}{c^3 m_e^2}\left(\frac{m_e}{2\pi k_B T_e}\right)^{\frac{1}{2}} e^{-\frac{h\nu}{k_B T_e}} \tag{1.36}$$

specifying the numerical value of the constants, it becomes [54]:

$$W(\nu) = 6.8x10^{-38}\frac{Z^2 n_i n_e}{T_e^{\frac{1}{2}}} e^{-\frac{h\nu}{k_B T_e}}\ erg\ sec^{-1}\ cm^{-3}\ Hz^{-1} \tag{1.37}$$

Moreover, by expressing equation 1.37 as spectral intensity per unit of wavelength:

$$W(\lambda) = 2x10^{-27}\frac{Z^2 n_i n_e}{T_e^{\frac{1}{2}}} e^{-\frac{hc}{\lambda k_B T_e}}\ erg\ sec^{-1}\ cm^{-4} \tag{1.38}$$

As shown in figure 1.11, the maximum spectral emission is for $\lambda_{max}(A) = \frac{6200}{T_e(eV)}$. The "*bell*" shape of the distribution is similar to the emission one of a black-body which has the same energy density and the same temperature. The difference is that in case of the black-body radiation the maximum of the spectral emission occurs at the wavelength $\lambda_{max}(A) = \frac{2500}{T_e(eV)}$; furthermore, the scale law for the black-body depends on the temperature like T^4, while for the Bremsstrahlung emission as function of $T^{\frac{1}{2}}$.
In plasmas characterized by high temperatures the emission of X rays due to Bremsstrahlung represents a process of considerable importance in terms of radiative dissipation of electron energy. It also represents a powerful method of quantitative investigation of the hot electron component. In fact, the eq.1.38 highlights how the spectral intensity $W(\lambda)$ decays at high energies (i.e. small λ) as $e^{-\frac{hc}{\lambda k_B T_e}}$, the electron temperature

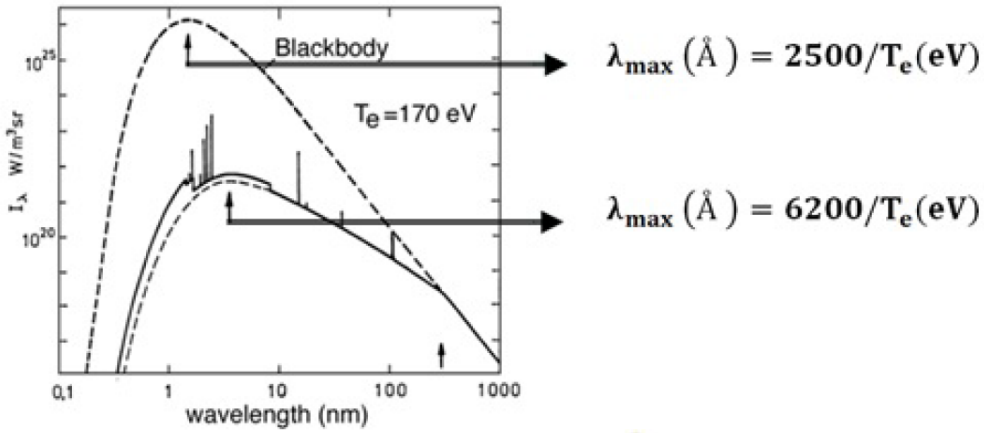

Figure 1.11: Spectral emission for black body radiation and for Bremsstrahlung radiation.

can be obtained from a linear fit of the spectrum $logW(\lambda)$ vs. ϵ, with ϵ X photons energy (i.e. $\frac{hc}{\lambda}$). The slope with which $logW(\lambda)$ decays, in fact, is inversely proportional to the temperature.

1.4.2 Recombination emission

Recombination radiation is emitted following transitions from free to bound states, and therefore the spectrum is a continuum (free states are a continuum of levels). This emissive mechanism occurs whenever a free electron is captured by a ionized atom (Z + 1), reducing it to an ionized atom Z. Energetically the equation that regulates the mechanism is expressed as [54]:

$$h\nu = \frac{1}{2}mv^2 + E_Z^n \tag{1.39}$$

in which the first term is the initial kinetic energy of the electron, while the second is the energy of the atomic state at end process, with Z number of ionization and n principal quantum number.
Since the minimum required condition is that $h\nu \geq E_Z^n$, the continuous

spectrum will also be a characterized by "*shoulders*" corresponding to different states of recombination, each having different principal quantum number. The spectral density of the radiation can be expressed in function of Bremsstrahlung one as follows:

$$W_R(\nu) = W(\nu)\ 2.2\ x\ 10^{-32} \frac{Z^3 n_e^2}{T^{\frac{3}{2}}} \sum_{n=1}^{\infty} \frac{1}{n^3} exp\left(\frac{Z^2 E_H}{n_e^2 k_B T_e} - \frac{h\nu}{k_B T_e}\right) ergsec^{-1} cm^{-3} Hz^{-1} \tag{1.40}$$

where $E_H = 13,6\ eV$ is the ionization energy of the hydrogen atom.
It can be observed that the argument of the exponential term is always negative. Furthermore, for low Z values and/or high plasma temperatures, the emission for Bremsstrahlung is dominant with respect to the recombination mechanism.

1.4.3 Bound-bound transition: line emission

Last important contribution to the spectrum of the X radiation emitted by a plasma and that linked to electronic transitions in ionized atoms, with consequent emission of characteristic X lines. Such transitions are due to the fact that the plasma atoms become continuously ionized by free electrons; consequence of such interactions and creation gaps in the innermost electronic levels that are filled by electronic transitions from higher levels (or shells). The specific power per unit of volume, solid angle and frequency range of the emission X corresponding to the transition from an initial state i to a final state f and expressed as follows [54]:

$$\epsilon_\nu = \left(\frac{h\nu}{4\pi}\right) A_{i,f} n_i L(\nu - \nu_{i,f})\ erg\ sec^{-1} cm^{-3} Hz^{-1} sr^{-1} \tag{1.41}$$

where $n_i$is the ion density of the initial state and $L(\nu - \nu_{i,f})$ is the function of the line form centered on the frequency $\nu_{i,f}$. This function satisfies the normalization condition:

$$\int_0^\infty L(\nu - \nu_{i,f}) = 1 \tag{1.42}$$

and ν_i is the characteristic frequency of the transition between two states expressed as:

$$h\nu_{i,f} = E_i - E_f \tag{1.43}$$

with E_i and E_f the characteristic energies of the two states. $A_{i,f}$ is the Einstein coefficient of spontaneous emission:

$$A_{i,f} = \frac{8\pi h\nu^3}{c^3} B_{i,f} = \frac{64\pi^4}{c^3 h} \nu^3 P_{i,f}^2 sec^{-1} \tag{1.44}$$

$A_{i,f}$ and $B_{i,f}$ represent, respectively, the probability per unit of time of spontaneous and induced emission, while $P_{i,f}^2$ expresses the square modulus of the matrix element of electric dipole moment evaluated between the initial state and the final state.
The quantities E_i, E_f and $A_{i,f}$ are related to intrinsic characteristics of the ions or atoms and the relative values are tabulated in [55]. The populations of the levels and the lines shape depend, instead, of the equilibrium conditions of the ions inside the plasma. In particular, the populations of the levels are determined by the dynamic equilibrium between the various collisional and radiative processes that happen within the plasma, while for determining the line shape it is necessary to take into account four main processes:

1. Mean lifetime of transitions (natural broadening);
2. Thermal motion of radiant systems (Doppler effect);
3. Interaction of the radiant systems with the rest of the plasma (collisional or pressure broadening);
4. Stark broadening.

The Natural broadening (item 1) is determined by all the spontaneous processes between the two states involved and in this case the line shape will be a Lorentzian:

$$L(\nu - \nu_{i,f}) = \frac{L_0}{1 + \left[\frac{2(\nu - \nu_{i,f})}{\Delta\nu_N}\right]^2} \tag{1.45}$$

Since starting from the energy-time uncertainty principle, it is possible to obtain the uncertainty as a function of the frequency:

$$\Delta\nu = \frac{1}{2\pi\tau} \tag{1.46}$$

where τ is the mean lifetime of the electron in the level, concerning the involved states it is possible to write:

$$\Delta\nu_N = \frac{1}{2\pi\tau_i} + \frac{1}{2\pi\tau_f} \tag{1.47}$$

In the case of the Doppler effect (item 2) let's consider a source that emits at frequency $\bar{\nu}$ and moving at v_x velocity towards the detector. It is found that the frequency detected is:

$$\nu = \bar{\nu}\left(1 + \frac{v_x}{c}\right) \tag{1.48}$$

Therefore, in the non-relativistic limit the Doppler shift is given by:

$$\Delta\nu = (\nu - \bar{\nu}) = \bar{\nu}\left(1 + \frac{v_x}{c}\right) \tag{1.49}$$

assuming the ionic velocity distribution is Maxwellian, the line shape assumes the behavior of a Gaussian:

$$L(\nu - \nu_{i,f}) = L_0\, exp\left[-\frac{2\sqrt{ln2}(\nu - \nu_{i,f})}{\Delta\nu_D}\right]^2 \tag{1.50}$$

and since $n(v_x) \propto exp - \frac{mv^2}{2k_B T_e}$, the FWHM depends on the ion temperature T_i (eV) and from the atomic mass number A:

$$\Delta\nu_D = \frac{2\nu_{i,f}}{c}\sqrt{\frac{2ln2k_B T_i}{M}} \approx 6.65 \cdot 10^{-9}\sqrt{\frac{T_i(eV)}{A}} \tag{1.51}$$

The collisional broadening (item 3) is the result of the reduction of the mean lifetime of the electron in its excited state as a consequence of the collision suffered by the ionized atom to which it belongs. The characterizing parameter of this phenomenon is ν_{coll}, i.e. the frequency of collisions between the various atoms. If we consider the impact duration negligible with respect to the mean lifetime of the atomic levels involved

in the transition and σ the cross section, then the line shape is essentially a Lorentzian and the FWHM is given by [54]:

$$\Delta\nu_{coll} = \frac{1}{2\pi\tau_{coll}} \approx \frac{\sigma v_{rel} \nu_p}{2\pi} \tag{1.52}$$

where n_p is the density of the perturbators and v_{rel} is the relative velocity between the interacting atomic systems.
Finally, the broadening process produced by the Stark effect (item 4) is the most important collisional (or pressure) broadening mechanism and is due to the interaction of the systems with the microscopic electric field generated by the particles that surround. Stark broadening becomes dominant only for plasmas with high densities ($n_e > 10^{23}\ cm^{-3}$) and with strongly ionized atomic species.
The amplitude for natural broadening is negligible compared to the amplitude due to Doppler and Stark effects; but, for our plasmas the X emission is linked to hottest electronic population whose density is $10^{10} <$ n $< 10^{12}\ cm^{-3}$ and temperatures are some keV, therefore, although the line broadening is due to intra-plasma collisions, there is not a relevant contribution of the Stark effect.
Another essential contribution should come from Doppler effect related to ion thermal agitation. However, the latter effect should produce $\Delta\nu$ correspondending to photon energies of the order of $1 - 100\ eV$. At the present time these energies, on the basis of the used detector systems, cannot be distinguished and therefore detailed studies about related broadening have not been carried out. The latter could instead represent in the future a very interesting field of investigation as it would allow the ion temperature measurement.

Chapter 2

Measuring β decays in ECR plasmas

Magnetized ECR plasmas in compact traps may become experimental environments for the investigation of nuclear $\beta-$decays of astrophysical and nuclear astrophysical interest.
In the last decades, there was a growing interest in Nuclear Astrophysics involving low-energy heavy-ion reactions and radioactive-decays in astrophysical environment. Terrestrial measurements involve, up to now, neutral species, while both nuclear reactions and decays involved in nuclear astrophysics should be investigated in peculiar plasma environments. Indeed, plasma is a quite common state of matter in our universe, having properties unlike those of the other states. There is great interest in Nuclear Astrophysics for any attempt at providing improved knowledge of weak interactions in physical conditions similar to those of nucleosynthesis environments (stars, the Big Bang and cosmic rays).
Since the ionization state of the in-plasma isotopes can modify, even of several orders of magnitudes, the expected isotope lifetimes [1, 2], the **PANDORA$_{\mathbf{Gr3}}$** (**P**lasmas for **A**strophysics, **N**uclear **D**ecays **O**bservation and **R**adiation for **A**rchaeometry) project [6, 7] aims to measure, for the first time, the influence of the plasma charge state distribution and the other parameters (such as plasma density and temperature) on the nuclear lifetime.
An innovative design of a new high-performance ECR (Electron Cyclotron

Resonance) plasma trap, in combination with a new multi-diagnostics setup consisting of a set of non invasive tools, has been developed for this purpose.
In this chapter, we will outline the experimental method for using laboratory plasmas for $\beta-$decays measurement, and the most relevant scientific cases, then emphasizing a few of them for which the $PANDORA_{Gr3}$ experiment will provide significant new insight.

2.1 State of Art about β-decay measurement in the matter

Nucleosynthesis proceeds by nuclear fusion in massive stars until iron, where it stops because the fusion of heavier nuclei needs energy instead of providing it. Heavier nuclei are created by a subtle interplay between neutron capture and $\beta-$decay which represent the driving mechanisms allowing the increase of nuclear mass and charge up to the limits imposed by the nuclear stability. This interplay determines the pathways of stellar nucleosynthesis and, thus, the abundances of atomic nuclei observed in the Universe. One of the major tasks of nuclear astrophysics consists in revealing these pathways investigating the reactions leading to the production of unstable nuclei and precisely elucidating their main features such as cross sections and $\beta-$decay probabilities. However a major difference exists between terrestrial and stellar conditions: stellar nucleosynthesis proceeds in a hot and dense environment which affects the degree of ionization of the atoms involved in the stellar nucleosynthesis. This raises the question whether or not the high degree of ionization could induce any significant differences of the beta-decay properties with respect to neutral atoms.
An even more general reason for investigating the decay properties of highly ionized ions is connected to the long standing question of how constant are the nuclear decay constant.
Several studies have been performed in the past decades:

- Early attempts to investigate the stability of the decay constant of

natural radioactive elements were performed significantly varying for example the temperature up to more 1000 K, applying pressure up to about 2000 atm or the magnetic field up to about 80000 $Gauss$. Results of these early investigations firmly established the constancy of the nuclear life time the variations observed being lower than about 0.05% [56].

- A revival of interest in the field took place in the '70s with the discovery of a chemically induced change of about 3.5% in half-life of ^{7}Be [56]. Since this evidence much experimental and theoretical works have shown that the orbital electron capture, the ^{7}Be decay mechanism leading to ^{7}Li, is influenced by the surrounding environment depending on both lattice structure and electron affinity of the host atoms.

- Further evidences of a half-life variation of were found in ^{99m}Tc compressed at a pressure of 100 $kbar$ [57]. The observed fractional variation was however very small, its value being of the order of 10^{-4} [57].

An important breakthrough in the field was achieved with the use of Storage Rings because they can allow high atomic charge states to be preserved for extended periods of time (up to several hours) to allow the ions to decay. Experimental results using highly ionized atoms showed strong variations of their half-life:

- Bare $^{187}Re^{75+}$ ions decay, due to the bound-state beta decay, by 9 orders of magnitude faster than neutral ^{187}Re atoms with a half-life of 42 Gyr [3].

- Bare $^{163}Dy^{66+}$ nuclei, being stable as neutral atoms, become radioactive, thus allowing the s process, with a half-life of 33 days [4].

- The measured electron-capture decay constant of hydrogenlike $^{140}Pr^{58+}$ ions is about 50% larger than that of heliumlike $^{140}Pr^{57+}$ ions while ^{140}Pr ions with one bound electron decay faster than neutral $^{140}Pr^{0+}$ atoms with 59 electrons [5].

2.2 The use of ECR plasmas for β-decays measurements

The $PANDORA_{Gr3}$ project proposes to develop a totally new and complementary approach aiming at measuring the variation of the half-life of β-decaying nuclei, due to a high degree of ionization of the atomic species investigated, in the magnetically confined ECR plasma. The main decay mechanism investigated in this approach is the bound-state β decay where the electrons emitted in the decay process remain bound in the atomic orbitals and the neutron decay energy is essentially carried off by the neutrino.
In the plasma traps like the one $PANDORA_{Gr3}$ project plans to build, the radionuclides can be trapped in a dynamic-equilibrium, in a Magneto Hydro Dynamically (MHD) plasma, living for several hours or days with on-average constant local density and temperature (the plasmas reach $n_e \sim 10^{11} \div 10^{13} cm^{-3}$, $T_e \sim 0.1 \div 100 keV$ of electron density and temperature, respectively). The plasma is confined by multi-Tesla magnetic fields and resonantly heated by some kWs of microwave power in the 2.45 - 28 GHz frequency range. The Charge State Distribution (CSD) can be modulated according to the pumping RF power, the magnetic field and the background pressure. The decay rates can be then characterized with respect to the CSD variation, and versus the plasma density and temperature, in a stellar-like condition (as concerns, mainly, the CSD conditions). The ECRIS plasmas displays charge distributions very closely resembling the ones of stellar environments. First calculation at ECRIS densities and temperatures confirm that even in non-LTE (non-Local Thermodynamic Equilibrium) conditions (due to the low density) the abundances of charge states are - for many of the selected physics cases of astrophysics interest - very similar to the ones occurring in astrophysical conditions, where densities are ten order of magnitude higher [58]. In particular, some considerations starting from evaluating the CSD in a "*stellar-like*" scenario, then going down to the range of densities feasible in PANDORA, in order to understand how the thermodynamical domain (from LTE to non-LTE regimes) can influence the CSD, and then the accountability and significance of the laboratory measurements vs. the astrophysical

scenario, has been done. Results show a significant variation of the CSD, in a temperature range of interest at T >= 10 keV, only beyond density values of n $\sim 10^{20}\ cm^{-3}$, whereas at lower densities achievable in the laboratory context the CSD does not present strong differences [59]. This makes the experiments running in an ECRIS directly scalable to astrophysical systems, which is a remarkable aspect for the accountability of envisaged measurements for all the considered nuclei.
The experimental method is based on the possibility to find a dynamical equilibrium between the injected amount of atoms into the trap and the losses due to the intrinsically imperfect magnetic confinement, in order to keep stable density and temperature (thus, the concentration of decaying nuclei in the trap) for a long period of time, extending to months.
MHD stability will be an important condition to investigate nuclear decays, since a stationary plasma state is needed in order to correlate nuclear phenomena with plasma observables, especially average charge state, temperature and density.
The experimental procedure includes the following steps:

- A "*buffer plasma*" is created by He, O or Ar up to densities of $10^{13}\ cm^{-3}$;
- The isotope is then directly fluxed (if gaseuous) or vaporized by appropriate ovens and then fluxed inside the chamber to be turned into plasma-state;
- Relative abundances of buffer versus isotope densities range from 100 : 1 (if the isotope is in metal state) to 3 : 1 (in case of gaseous elements);
- The plasma is maintained in dynamical equilibrium by equalizing input fluxes of particles to losses from the magnetic confinement;
- While the isotopes decay, the daughter nuclei still confined in the plasma emit $\gamma - rays$ in the range of hundreds of keV;
- $\gamma - rays$ will be detected through an appropriate γ-detectors array surrounding the magnetic trap;

- The in-plasma measured radioactivity can be directly correlated to the plasma density and temperature, monitored by a multi-diagnostics setup as the one shown in the sketch of fig. 3.13.

The plasma is maintained in dynamical equilibrium by equalizing input fluxes of particles to losses from the magnetic confinement. In particular, the number of decays per unit of times can be written as:

$$\frac{dN}{dt} = \lambda n_i V \tag{2.1}$$

where $\frac{dN}{dt}$ is the number of decays per unit of time, λ is the isotope's activity, n_i is the plasma ions density and V is the plasma volume. If the plasma is in dynamical equilibrium (i.e. fluxes of ionized particles is equal to the ones of ion losses from the trap), then the term, $\lambda\ n_i V$ is constant in time, and the equation 2.1 can be easily integrated. Therefore, the total amount of decays, detectable via $\gamma-$rays tagging, can be determined according to the following formula:

$$\int_0^{t_{meas.}} \frac{dN(t)}{dt} dt = \int_0^{t_{meas.}} \lambda n_i V dt \tag{2.2}$$

$$N(T_{meas}) = \lambda n_i V T_{meas} \tag{2.3}$$

where $t_{meas.}$ is the overall measurement time over which the γ-rays produced by the excited states of the decays products are counted by the detector array.
It implies that the number of expected decays linearly increases vs. the measurement time T_{meas}, being the proportionality due to λ only provided that the plasma parameters remains constant. Any physical condition (combination of density and temperature) in non-LTE determines a certain CSD of the in-plasma ions, similarly to what happens in the stars interiors (where, however, the plasma in under LTE equilibrium). Equation 2.3 implies also that the plasma density and volume must be known and on-line monitored all along the measurement in order to deconvolve λ (it worth to be noticed that, as will shown in the chapter 5, $n \equiv n(x, y, z)$ whose spatial dependence can be determined by spectrally-resolved X-ray Imaging).

The measured lifetime, therefore, has to be correlated with a charge state distribution to deduce information on the evolution of the β-decay lifetime as a function of plasma parameters.

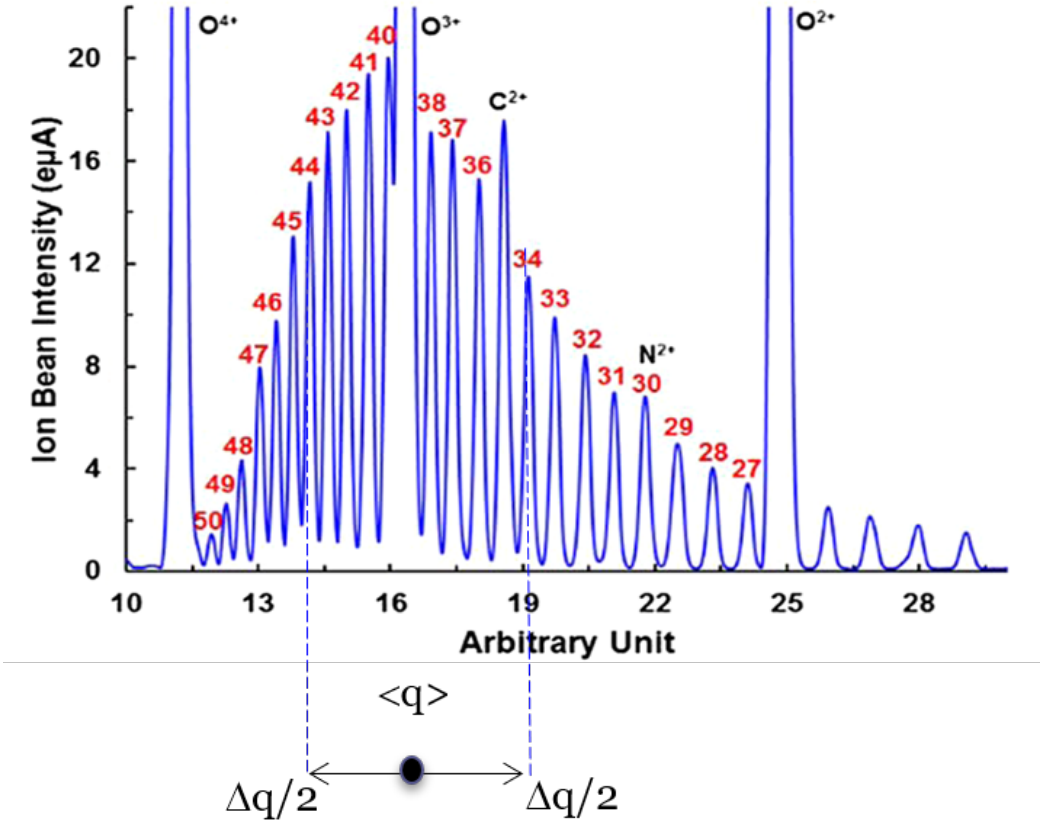

Figure 2.1: Experimental charge state distribution measured in the SECRAL source at Lanzhou, China, in a Bi plasma.

A typical experimentally obtained CSD is shown in figure 2.1. It has been measured on the SECRAL ECR ion source [60] operating at Lanzhou, China, using a Bi plasma.
A "*bell-like*" distribution of the several charge states is reached during dynamical equilibrium operations of the plasma. The peak, the value of the average charge state <q> and the width of the spectrum depend on the thermodynamical conditions of the plasma (especially, density and tem-

perature).
The $PANDORA_{Gr3}$ collaboration is now designing the plasma trap able to reach the needed plasma densities, temperatures and CSD. The $PANDORA_{Gr3}$ trap design has been addressed to maximize as much as possible the ionization state (higher ionization states are associated to the stronger effects of lifetimes variation). The details about the $PANDORA_{Gr3}$ trap design will be presented in the next chapter 3.
Moreover, advanced and innovative multi-diagnostic system is necessary for an accurate on-line monitoring of all plasma parameters aiming to characterize in detail the plasma environment. It has been developed and it will be described in the chapter 3. Finally, since as above mentioned several physics cases involve emission of γ-rays, the total amount of decays become, in these cases, detectable via γ-rays tagging by means of an array of several HyperPure Germanium (HPGe) detectors. The design of the detection system has been based on GEANT4 simulations and details will be discussed in the chapter 6.
The construction of the $PANDORA_{Gr3}$ trap is expected for the years 2021-2022, first measurements in 2023.

2.3 Radioactive nuclei relevant for slow neutron capture

Among the different processes of nucleosynthesis occurring in stars, we here focus our attention on the s-process. The relative abundances of elements and isotopes produced depends on the interplay between neutron abundances (neutron fluxes coming from reactions producing neutrons and their evolution over time are critical parameters), nuclear cross sections and decay rates; the latter, have been not deeply investigated up to now and their relevance will be discussed in details in the following. Slow neutron capture in the s-process is a crucial mechanism for the production of about 50% of the nuclei heavier than iron [61, 62, 63, 64, 65, 66, 67, 2, 68]. The impact of an experiment like PANDORA on these studies would be significant, even if limited to a range of temperatures that in its first phase would be between 1 and 30 KeV.
Modern stellar evolution and nucleosynthesis codes include thousands of

nuclear processes. A significant fraction are neutron capture reactions on more than 120 unstable nuclei close to the valley of beta stability. Examples include: ^{32}Si, ^{35}S, ^{36}Cl, $^{37,39}Ar$, $^{41,45}Ca$, $^{32,33}P$, $^{46,47}Sc$, $^{55,59}Fe$, ^{60}Co, $^{59,63}Ni$, ^{64}Cu, $^{65,67}Zn$, $^{72,73}Ga$, $^{71,75}Ge$, $^{76,77,79}As$, ^{79}Se, $^{80,82}Br$, $^{81,85}Kr$, ^{86}Rb, $^{89,90}Sr$, ^{90}Y, $^{93,95}Zr$, $^{94,95,96}Nb$, $^{97,98,99}Tc$, $^{93,99}Mo$, ^{103}Ru, ^{104}Rh, $^{107,109}Pd$, ^{108}Ar, $^{109,115}Cd$, ^{114}In, $^{120,121,123}Sn$, $^{122,124,125}Sb$, ^{127}Te, $^{128,129,130}I$, ^{133}Xe, $^{134,135,136,137}Cs$, ^{139}Ba, ^{140}La, ^{141}Ce, $^{142,143}Pr$, $^{147,149}Nd$, $^{145,146,147,148,149}Pm$, $^{151,153,155}Sm$, $^{152,154,155,156}Eu$, $^{153,159}Gd$, $^{160,161}Tb$, $^{163,165}Dy$, $^{163,164,166}Ho$, $^{165,169,171}Er$, $^{170,171,172}Tm$, ^{175}Yb, $^{176,177}Lu$, $^{181,182}Hf$, $^{179,180,182}Ta$, $^{181,185}W$, $^{186,188}Re$, ^{191}Os, $^{192,194}Ir$, $^{193,197}Pt$, ^{198}Au, ^{203}Hg, $^{204,205}Tl$, ^{205}Pb (see e.g. [61, 62, 63, 64, 65, 66, 67]). In some cases (e.g. ^{163}Dy, or ^{205}Tl) the nuclides are stable in terrestrial laboratories, but become unstable when they are ionized. The high-temperature stellar plasma, in fact, introduces enormous uncertainties on the lifetimes of many radioactive isotopes, which are exposed to neutron captures over a wide range of time durations: from less than 20 years in the thermal instabilities of shell He-burning in low mass stars, up to several thousand times longer intervals in core He-burning conditions.
For several nuclei in the list above, the ionization conditions open the bound-state (or two-body) decay channel, in which the produced electron is not emitted, but captured in a stable (free) atomic energy state [1]. The lack of this information, in addition, has so far hampered the possibility of using long-lived chronometers as cosmological tools, since uncertainties in their lifetime do not allow to be confident in estimating the age of a given astrophysical object by just looking at the relative abundances of certain isotopes (i.e., measuring the "father-son" abundances ratio).

Many interesting physical cases could be investigated using such a new approach. We plan to start our experimental investigation from isotopes for which:

i) samples can be found rather easily;

ii) $\gamma-$rays are emitted by the daughter nuclei in a suitable energy interval;

iii) lifetimes variations are in a range such that the sensitivity of the setup will allow to detect the predicted half-life variations.

Table 2.1: Preliminary list of potential physics cases of astrophysical interest.

Isotope	**Lab $\tau_{\frac{1}{2}}$ [yr]**	**J_π**	**Z**	**E_γ [keV]**	**Decay**
^{63}Ni	100.1	$1/2^-$	28	No	β^-
^{79}Se	1.13x10^6	$7/2^+$	34	No	β^-
(^{79m}Se	3.9m	$1/2^-$	34	95.7	IT, β^-)
^{81}Kr	2.29x10^5	$7/2^+$	36	276	ϵ
(^{81m}Kr	13.1s	$1/2^-$	36	190.62	IT, ϵ)
^{85}Kr	10.756	$9/2^+$	36	130-514	β^-
(^{85m}Kr	4.48 h	$1/2^+$	36	129-731	It, β^-)
^{93}Zr	1.5x10^6	$5/2^+$	40	30.7	β^-
^{95}Zr	64d	$5/2^+$	40	235-756	β^-
^{99}Tc	2.1x10^5	$9/2^+$	43	98.6	β^-
^{134}Cs	2.065	4^+	55	>600	β^-, ϵ
(^{134m}Cs	2.903h	8^-	55	138.74	IT
^{135}Cs	2.3x10^6	$7/2^+$	55	786,846	β^-
^{137}Cs	30.07	$7/2^+$	55	238-661	β^-
^{147}Pm	2.6	$7/2^+$	61	76-197	β^-
^{151}Sm	90	$5/2^-$	62	No	β^-
^{155}Eu	4.7	$5/2^+$	63	10-146	β^-
^{171}Tm	1.92d	$1/2^+$	69	66.7	β^-
^{176}Lu	3.78x10^{10}	7^-	71	88-400	β^-
(^{176m}Lu	3.635h	1^-	71	82-1237	β^-, ϵ)
^{204}Tl	5.45	2^+	81	511ϵ^+e^-	$\beta^-\epsilon^+\beta^+$
^{94}Nb	2.03x10^4	6^-	41	702-871	β^-
^{93}Mo	4x10^3	$5/2^+$	43	30.7	ϵ
^{129}I	1.57x10^7	$7/2^+$	53	40	β^-
^{205}Tl	stable	$1/2^+$	81	No	if ion. β^-
^{163}Dy	stable	$5/2^-$	66	77.5(Ho)	if ion. β^-

Table 2.1 shows a list of cases relevant for the s-process, for which experimental data would be strongly desirable. In the next section 2.3.1 a very limited set of case studies will be presented in details, as they offer a good combination of astrophysical relevance and experimental feasibility.

2.3.1 Selection of the first three cases for $PANDORA_{Gr3}$

Due to the large number of different situations and nuclear paths near the valley of β-stability, only a limited subset of cases have been chosen for starting the study. We adopted a selection procedure for sorting out – from the list of tens of radioisotopes reported in table 2.1 – three cases for the first run of measurements. The selection procedure took into account a combination of four "*ratings*", concerning:

i) Scientific relevance: relevance as benchmarks for comparison to nuclear theory and models, role played in stellar nucleosynthesis, etc.);

ii) Expected effects on the lifetime due to charge states or ion temperature;

iii) Trap size: The trap design has been addressed to maximize as much as possible the ionization state (higher ionization states are associated to the stronger effects of lifetimes variation). Trap dimensions in terms of B field maximum-to-maximum length (the so called, mirror length) are crucial issues if one wants to reach long confinement times;

iv) Type of element (gas, metal, rare isotope, commercial or not, etc.).

Being the identification of the decay products based on the $\gamma-$ray detection (as will be described in the chapter 6), isotopes whose daughter nuclei don't emit $\gamma-$rays have to be discarded as well as the those emitting $\gamma-$rays at energies lower than 300 keV, since they would be overwhelmed by high intensity background emitted from the plasma. The selection procedure has finally given as output three isotopes, reported in the table 2.2): ^{176}Lu (is it a cosmo-thermometer or a cosmo-chronometer?), ^{134}Cs (relevant for the production of the s-only isotopes ^{134}Ba and ^{136}Ba) and ^{94}Nb (relevant for the abundance of ^{94}Mo in single or binary systems of stars).
The relevance in nuclear physics and astrophysics of the three cases selected for the first phase of the experimental program is discussed below.

Table 2.2: $PANDORA_{Gr3}$ physical cases.

Isotope	$\mathbf{T}_{\frac{1}{2}}$ **[yr]**	$\mathbf{E}_{\gamma}$ **[keV]**
^{176}Lu	$3.78 \cdot 10^{10}$	202.88 & 306.78
^{134}Cs	2.06	795.86
^{94}Nb	$2.03 \cdot 10^{4}$	702.65

The physical cases of ^{176}Lu

The ^{176}Lu nucleus is very long-lived in laboratory conditions and in principle might act as a cosmo-chronometer (a long-lifetime radionuclide used to determine the age of astrophysical objects and/or the Universe itself), if not for its complex behaviour in hot stellar plasmas. Here, the s-process branching point at ^{176}Lu is among the most important ones for a precise understanding of slow neutron captures in the AGB phases of low and intermediate mass stars. It determines the abundance of ^{176}Hf, an "s-only" nucleus, since it cannot be produced by the r-process because the ^{176}Lu has no viable decay channels in its ground state (if it remains long lived) and/or by ^{176}Yb (see the figure 2.2).

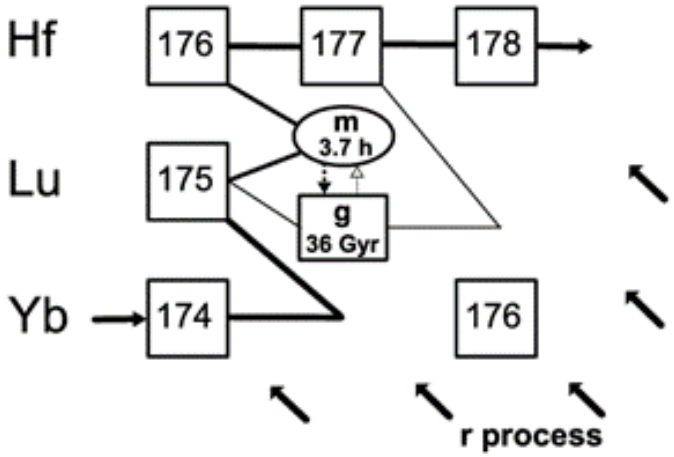

Figure 2.2: Reactions network for the Lu isotopes.

A discussion of the temperature and density dependence of ^{176}Lu decay was presented theoretically in [2, 69], assuming a Local Thermody-

namic Equilibrium (LTE) and with a somewhat simplified approach. A direct measurement would be therefore extremely interesting for stellar nucleosynthesis and appears to be feasible by $PANDORA_{Gr3}$. It would also clarify whether ^{176}Lu can be still considered as a chronometer, or has instead to be regarded as a thermometer of the s-processing site (this last being the current interpretation prevailing today).

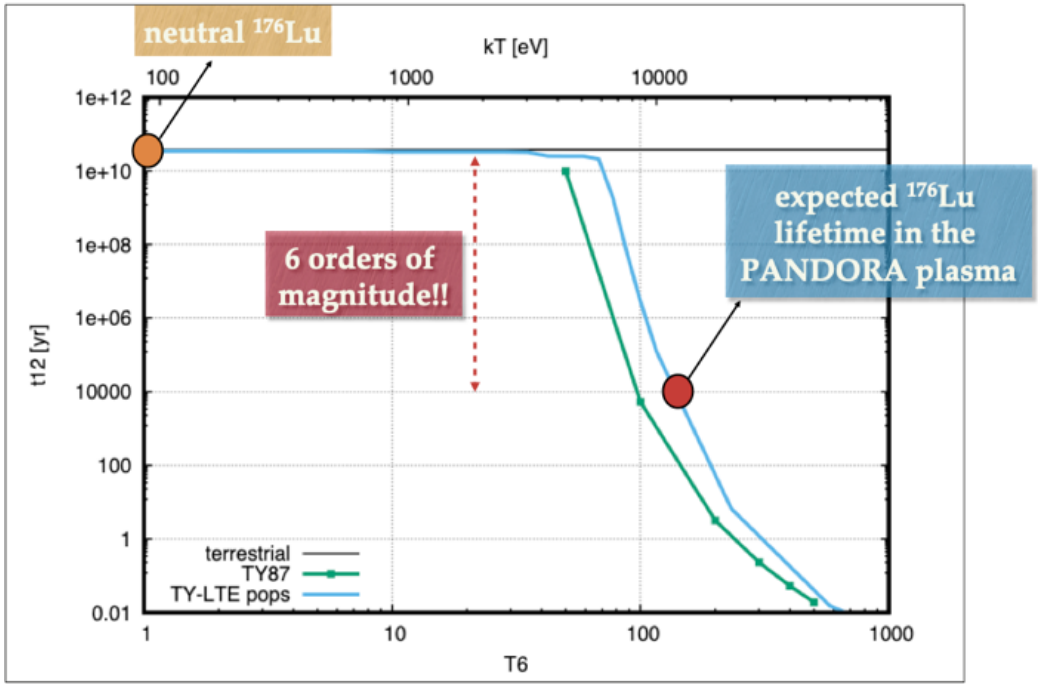

Figure 2.3: Expected lifetime versus plasma temperature trend at densities of $PANDORA_{Gr3}$'s plasmas, for the ^{176}Lu isotope. The maximum expected temperature in $PANDORA_{Gr3}$ is highlighted.

Ionization of ^{176}Lu might induce important differences in the half-life which could reach even 6 order of magnitude reduction around 10 keV (see fig. 2.3). Figure 2.3 reports about expectations of ^{176}Lu lifetime variation as a function of the plasma temperature (namely, of its charge state distribution). Under terrestrial conditions, the lifetime was measured to be of order 10^{10} years. In [2] the authors determined a collapse of several order of magnitude from theoretical calculations, at temperatures above

2-3 keV. Calculations have been now repeated by applying the FLYCHK code considering LTE (local thermal equilibrium) approximation for the plasma electrons, being in reasonable agreement with the previous ones. Despite this assumption is questionable, in low density plasmas, calculations performed by the FLYCHK code say that for most of the selected cases the LTE and non-LTE scenarios do not differ hugely from each other.

The physical cases of ^{134}Cs

A scheme of the reaction branching occurring at ^{134}Cs in s-process situations is shown in figure 2.4 [62]. Here, for simplicity, a possible further branching point at ^{135}Cs is omitted.

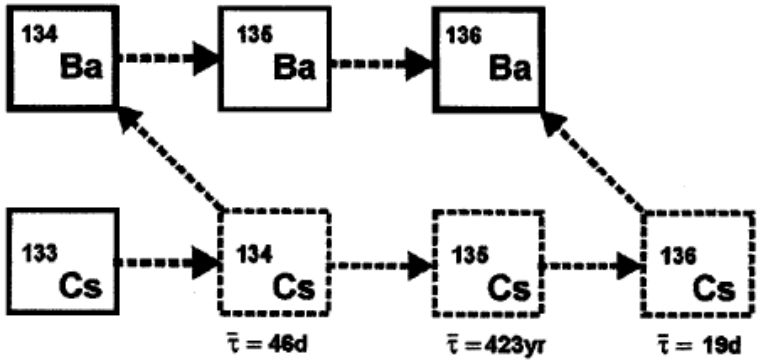

Figure 2.4: Reaction network for the formation of Cs isotopes.

In laboratory conditions the lifetime of ^{134}Cs is 2.9 y (half-life 2 y). According to theoretical predictions [69] ^{134}Cs lifetime is reduced to 48 days at $T = 3x10^8$ K (i.e. around 30 keV, representing typical conditions in thermal pulses of low mass Asymptotic Giant Branch (AGB) stars [62, 61]). This datum seems at the moment unsatisfactory, as it inhibits the proper reproduction of the two s-only isotopes ^{134}Ba, ^{136}Ba in suitable proportions. This impossibility is known to have a nuclear origin, as it holds in astrophysical situations in which the other details about abundances coming from s-process distribution are accurately accounted for. Hence, a measurement in plasma could shed light on the role played by the ionization state affecting the $\beta-$decay.

Modern nucleosynthesis models predict that the neutron flux proceeds more effectively to ^{135}Cs and ^{136}Cs, thus better feeding ^{136}Ba. This can occur either through a longer half-life of ^{134}Cs in stellar conditions, or through a more efficient neutron-capture process (larger cross section) on ^{134}Cs itself. However, a cross-section measurement for this radioactive nucleus is for the moment unfeasible, so that measuring its half-life in ionized conditions appears as the best way to solve the dilemma. As for ^{176}Lu, we performed calculations of ^{134}Cs lifetime variation in plasmas. At $kT_e > 10\ keV$, a reduction of the lifetime of more than one order magnitude is expected.

The physical cases of ^{94}Nb

The ^{94}Nb nucleus provides the main production channel of ^{94}Mo, an isotope that cannot be populated through the r-process and must therefore derive either from the s-process or from the p-process. The situation met by reaction network calculations in this area is rather peculiar, and its uniqueness motivates the requirements of a better knowledge of the ^{94}Nb β decay. In particular, here s-processing strongly depends on ^{93}Zr, a rather long-lived species ($t_{\frac{1}{2}} = 1.5 \cdot 10^6\ y$). During the TP-AGB phase of evolution, when most slow neutron captures above Sr occur, ^{93}Zr behaves as a stable nucleus, as the whole duration of this phase is around 1 Myr. In such a condition, production of ^{93}Nb is inhibited and AGB stars end their life with essentially zero ^{93}Nb in their atmosphere. Any contribution to the ISM (Inter-Stellar Medium), especially in dust form, will have no Nb (which has a unique stable isotope) and the lighter isotopes of Mo would be sharply under abundant. However more than 50% of stars are in binary or multiple systems: mass transfer to a secondary component often allows the s-process distribution produced by neutron captures in a TP-AGB star to be deposited into the atmosphere of a companion. In this case, ^{93}Zr has time to decay and ^{93}Nb is produced, thus providing its present cosmic abundance. Even so, neutron captures on ^{93}Nb produce ^{94}Nb, whose relatively long half life induces a branching between further n-captures and decay. The exact contribution of s-processing to ^{94}Mo can, at present, be only determined with large uncertainties. It is known that in pre-solar SiC grains of AGB origin this nucleus is under abundant with

respect to the (uncertain) predictions, an indication that disentangling its p- and s-components still requires revisions in this complex scheme of processes, probably mainly in the lifetime of 94Nb itself. A measurement of its lifetime using $PANDORA_{Gr3}$ could give complementary information to solve the puzzle.

Chapter 3

Experimental Setups

At INFN-LNS, along with the partner laboratories such as the ATOMKI Laboratories (Debrecen), efforts have been paid to the study, development and use of an innovative multi-diagnostic setup aiming to characterize in details the ECR magnetized plasmas confined in compact traps and to investigate turbulent versus stable plasma regimes of nuclear and nuclear astrophysics interest in laboratory plasmas. Setup and tools typically at the service of particle accelerators physics and applications have been redesigned on purpose, by means of innovative upgrade and improvements, for realizing new experimental system for fundamental and multidisciplinary studies.
The diagnostic system allows to reach unprecedented plasma proprieties investigation and, in the framework of the $PANDORA_{Gr3}$ project [6, 7], it will equip the innovative compact and flexible magnetic plasma trap for measuring, for the first time, nuclear $\beta - decay$ rates in stellar-like conditions (as concerns, mainly, the CSD).
In order to maintain the radionuclides in a dynamical equilibrium for several days or even weeks, with a locally stable density, temperature and CSD inside a compact ECR plasma trap, it is mandatory to have:

- high plasma density ($n_e > 10^{12} cm^{-3}$);
- stable and reproducible plasma conditions;

- an accurate on-line monitoring of the plasma proprieties and plasma parameters;
- a method to tag the $\beta - decaying$ isotopes of interest.

Such requirements can be fulfilled by the innovative design of the new high-performance $PANDORA_{Gr3}$ ECR plasma trap in combination with the new plasma diagnostics, which plays a relevant role in order to relate the *plasma environment* properties to the eventually measured lifetimes variation.
In summary, the development of the diagnostic setup and advanced analysis methods are mandatory. Plasma diagnostics work synergically with detection system (i.e. the array of HPGe detectors) for two main reasons for the future $PANDORA_{Gr3}$ experiment:

- **1)** Accurate on-line monitoring of all plasma parameters aiming to characterize in detail the plasma environment; on this purpose, the developed multi-diagnostic setup will be able to investigate the plasma properties in all energetic domains, also performing high-resolution spatial and time resolved analysis. The multi-diagnostic setup allows unprecedented investigations of magnetoplasmas properties in terms of density, temperature, CSD and inner plasma EM wave emission, consisting in a number of non invasive tools that can be simultaneously used in compact plasma traps.
- **2)** Estimate the lifetime of the isotopes to find an efficient detection method for decays tagging. Since several physics cases involve emission of γ-rays, the total amount of decays become detectable via γ-rays tagging by means of an array of several HyperPure Germanium (HPGe) detectors. In order to estimate the efficiency of decay products tagging, simulations by GEANT4 have been carried out, and details will be discussed in the chapter 6.

In a nutshell, the overall structure of $PANDORA_{Gr3}$ project (a sketch is shown in the figure 3.1 and 3.2) can be structured on three main pillars:

- *The Magnetic Trap*: a set of superconducting coils able to confine the plasma. The design will allow access to the plasma core for the diagnostics system and γ-ray detectors;

- *The Array of HPGe detectors* for γ-ray spectroscopy: the array will be used to tag the in-plasma nuclear decays via the γ-rays emitted from the excited states of the daughter nuclei;
- *The plasma diagnostics system*: for the non-intrusive inspection of the plasma environment proprieties and the measurement of plasma parameters to be correlated with the nuclear decays;

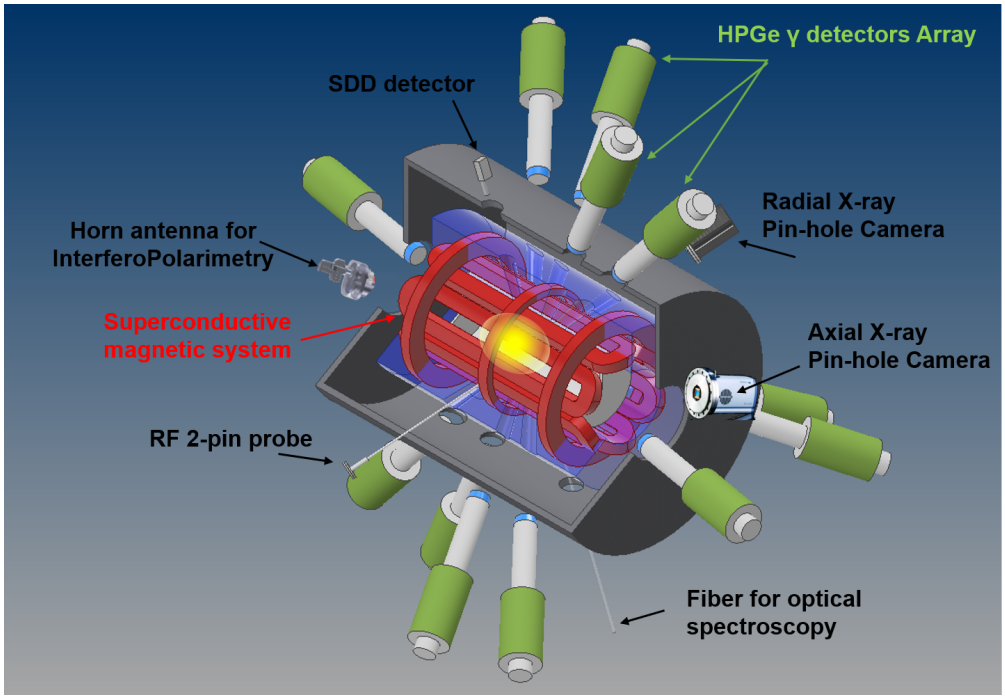

Figure 3.1: Rendering of the $PANDORA_{Gr3}$ trap with the experimental setup to be used for the measurement of the in plasma activity (14 HPGe detectors array) and on-line monitoring of plasma density and temperature (i.e., two X-ray CCD cameras, optical spectrometer, horn antennas for microwave Interfero-Polarimetry, two-pin RF probe and SDD).

The same setup is also suitable for other studies of astrophysical interest, such as turbulent plasma regimes dominated by the so-called *Cyclotron Maser Instability*, which is a typical kinetic turbulence occurring in astrophysical objects like magnetized stars, brown dwarfs, etc. [70, 71, 72].

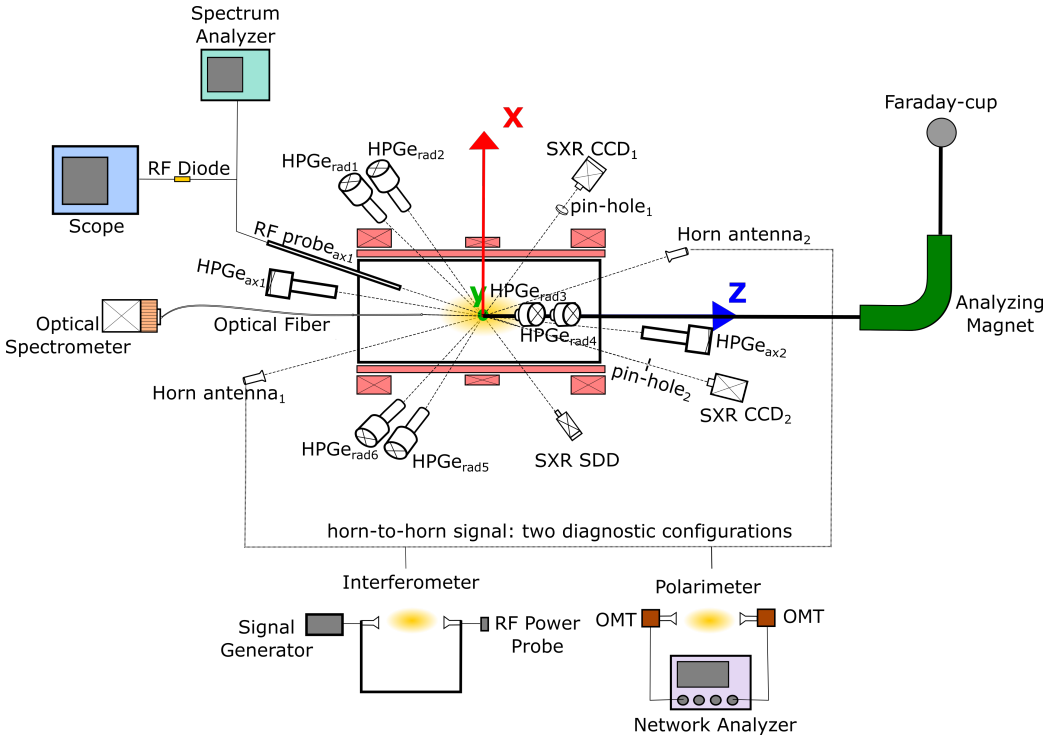

Figure 3.2: Sketch of the PANDORA_Gr3 trap with the experimental setup to be used for the measurement of the in-plasma activity (14 HPGe detectors array) and on-line monitoring of plasma density and temperature (multi-diagnostics system).

Since the design of the advanced $PANDORA_{Gr3}$ plasma trap is on going, all **the experimental measurements described in this thesis have been carried out in the two down-sized compact traps used as $PANDORA_{Gr3}$ test-benches, the compact *F*lexible *P*lasma *T*rap (*FPT*), installed at INFN-LNS, and the 2^{nd} generation ECRIS at the ATOMKI laboratories**. They will be described in the section 3.1.2, whilst the design of the $PANDORA_{Gr3}$ trap will be presented in the section 3.1.1.
The overall developed multi-diagnostic system, highlighting the most relevant characteristics of the two innovative and original tools used for performing the analysis presented in this work - a pin-hole CCD system for X-ray imaging and a two-pin RF plasma-immersed probe for probing plasma-self emitted radiation in the GHz range - will be presented in the

section 3.2. Finally, chapter 6 will be dedicate of to the illustrationg of the MonteCarlo simulations performed by means of GEANT4, and aiming at designing and dimensioning the $PANDORA_{Gr3}$ array of γ-rays detectors.

3.1 Electron Cyclotron Resonance Plasma Traps

The Electron Cyclotron Resonance plasmas are commonly confined in compact trap typically used as ion sources, i.e. the first stage of an acceleration apparatus. Among the several methods to generate plasmas in laboratories - with significantly different electron temperature, electron density and plasma lifetime - frequently used in modern accelerator facilities are the ion sources based on the ECR method, i.e. the ECRISs, which produce plasmas by means of electromagnetic waves interacting with gases or vapours in presence of a well shaped magnetic field. These ion sources generate charge states and extracted currents much higher than other devices, supporting the growing interest of intense beams of multicharged ions in the areas of both fundamental science (nuclear and particle Physics especially) and applied research.
In ECRIS the ion beam is extracted from a plasma that can be created by microwaves with frequency between 2.45 GHz and 28 GHz with quite different magnetic field amplitude and structure, so that the plasma properties, as well as the ion beam properties, will be completely different. Differences in ion beam parameters strongly depend on the plasma electron temperature T_e, on the ion lifetime τ_i, and on the electron density n_e; the operation of ECRIS can be described in terms of such parameters, which determine the production of highly charged ion beams whose intensity may reach hundreds of $e\mu A$ of Ar^{12+} and up to some tens of $e\mu A$ of Xe^{34+}, Ar^{14+} and higher charge states [60, 73, 27, 74, 70]; mA of current is produced for ion beams a low state of charge.
In ECRIS, the ion confinement time is a crucial parameter to determine the maximum achievable charge state. In addition, the number of available electrons is important, because it is clearly related to the number of electrons able to ionize the atoms down to inner shells. Hence we have:

$$< q > \propto n_e \tau_i \tag{3.1}$$

where $n_e\tau_i$ is usually defined as Q and it is, typically, the most important quality parameter characterizing ion sources. The electron-atom collisions and quite long confinement times ($\sim 10^{-3} \div 10^{-2}$ s) generate multiply-charged ions and very high charge states.
A novel approach, based on the study of decay rates in these ECR plasmas, whose conditions mimick hot stellar environments, has been conceived in $PANDORA_{Gr3}$: in this framework, ECR magnetized plasmas in compact traps may become experimental environments for fundamental physics studies.
Inside a machine like an ECR ion source a dense and hot plasma - made of multicharged ions immersed in a dense cloud of energetic electrons - is confined by multi-Tesla magnetic fields and resonantly heated by some kWs of microwave power in the 2.45 - 28 GHz frequency range. The plasmas reach $n_e \sim 10^{11} - 10^{13} cm^{-3}$, $T_e \sim 0.1 - 100$ keV of electron density and temperature, respectively and the CSD can be modulated according to the RF power level sustaining the plasma, the magnetic field strength, the background pressure, etc. This will allow to characterize decay rates with respect to the CSD variation, and versus the plasma density and temperature, in a stellar-like condition at least as concerns the CSD conditions, and the decay probability will be measured as a function of charge-state distribution in a long-term stationary dynamic-equilibrium: ECR plasmas are in fact Magneto Hydro Dynamically (MHD) stable, living several hours or days with on average constant local density and temperature.
Despite the complexity of the diagnostics system, the lower complexity of the overall setup and the necessity of running for weeks or months make ECRIS preferable with respect other types of ion sources (such as the Electron Beam Ion Trap (EBIT)). But even more important are the physical conditions of the ECRIS plasmas, that produce CSD very closely resembling the ones of stellar environments. First calculation at ECRIS densities and temperatures confirm that even in non-LTE conditions (due to the low density) the abundances of charge states are - for many of the selected physics cases - very similar to the ones occurring in astrophysical conditions, where densities are ten order of magnitude higher. This makes the experiments running in an ECRIS more directly scalable to astrophysical systems.

In the next sections the design of the $PANDORA_{Gr3}$ trap and the multi-diagnostic setup will be illustrated.

3.1.1 The PANDORA$_{Gr3}$ Trap Design

The ECR ion sources, as well as the ECR plasma traps, are based on a complex technology, such as superconducting magnets and of high frequency microwave generators. Typically the main systems are:

- The magnetic confinement system;
- The microwave injection system;
- The plasma trap;
- Additional devices, like oven for metallic beam production;

the main characteristics of each of them are here presented.

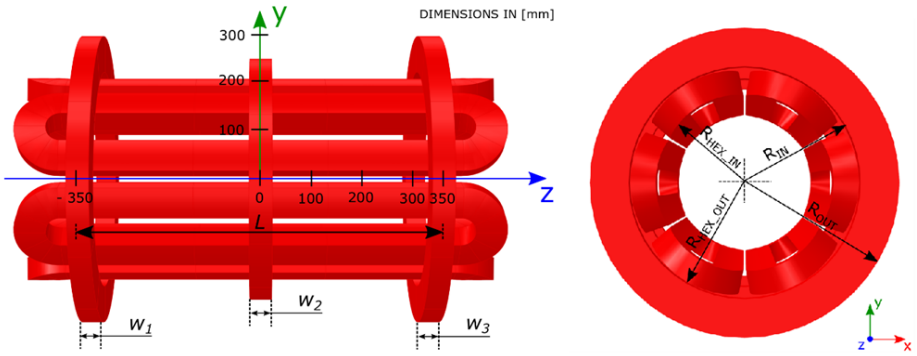

Figure 3.3: Side and front views of the magnetic system. The three axial coils are placed at -350, 0 and 350 mm along the longitudinal z-axis of the structure. R_{IN} and R_{OUT} are the axial coils inner and outer radii. The hexapole inner and outer radii are equal to $RHEX_{IN} = 165\ mm$, $RHEX_{OUT} = 212\ mm$.

The $PANDORA_{Gr3}$ magnetic confinement system will be fully superconductive and composed by *three* superconducting coils for axial confinement and by *six* superconducting hexapole coils for radial confinement, which are coaxial with respect to the axial coils. It is the largest

magnetic trap ever designed in a B_{min} scheme, supporting a cylindrical plasma chamber of 700 mm length and 150 mm external radius (internal radius of 140 mm). A sketch of the $PANDORA_{Gr3}$ magnetic system is shown in Figures 3.3 and 3.4.
The maximum fields of 2.7 T and 3 T along the chamber axis and 1.5 T along the chamber inner surface will allow stable plasma generation through an RF field at the frequencies of 18 and 21 GHz via Electron Cyclotron Resonance.

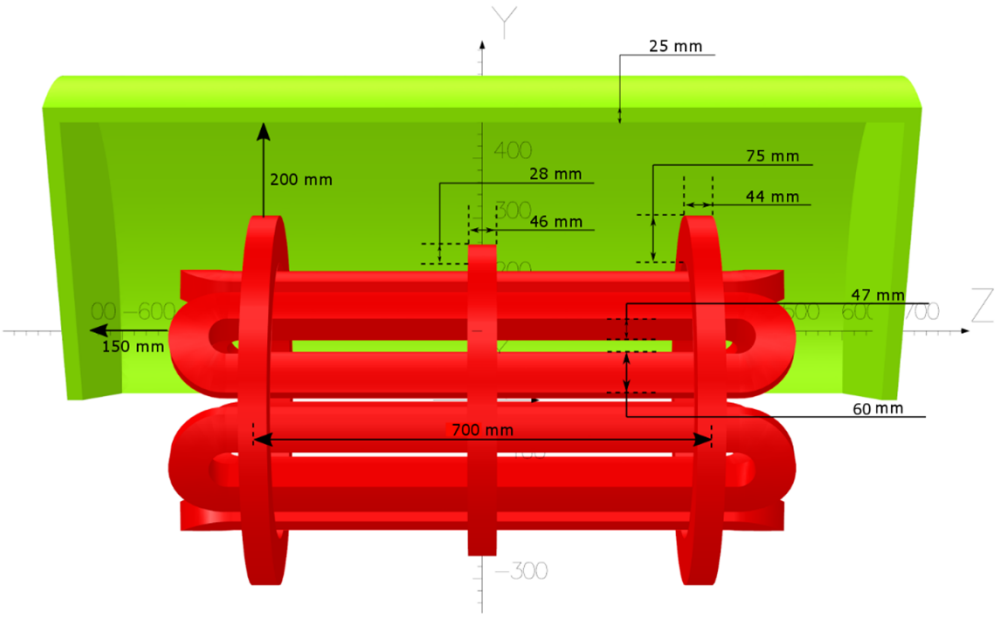

Figure 3.4: Perspective view of the 3D model of the magnetic system: it is composed by three superconducting coils and a superconducting hexapole composed of six separate conductors. A single cryostat, surrounded by an iron yoke (green object) shall be used for both the axial and the radial superconductors.

High charge state ions are primarily produced by sequential impact ionization, which means that the ions must remain in the plasma long enough (tens of ms) to reach high charge states. So, as above mentioned, the main quality parameter for an ECR ion source is the product of the plasma density and ion confinement time: (n_e x τ_i), as described by the eq.

3.1. The $PANDORA_{Gr3}$ trap design has been addressed to maximize the ionization state (higher ionization states are associated to the stronger effects of lifetimes variation). Trap dimensions in terms of distance between field maxima (the so called, *mirror length*) are crucial issues to reach long confinement times, which is an important parameter to determine the maximum achievable charge state (see eq. 3.1).
Moreover, from the Geller scaling laws [21], it is known that the plasma density scales with the square of the frequency as $n_e \propto \omega_{RF}^2$, thus in order to increase the plasma density, high operating frequencies must be chosen. Also, double (or triple) frequency heating improves plasma stability and source performances.
From the above considerations the $PANDORA_{Gr3}$'s trap has been designed to operate at $18 + 21$ GHz frequencies in MHD-stable configuration.
The needed magnetic field values (following the scaling laws [21]) are resumed in Table 3.1. Note that in our configuration $B_{inj} = B_{ext}$: this is because the $PANDORA_{Gr3}$ magnetic system will operate only in a plasma confining configuration and the extraction system will not be present.

A solution employing a single cryostat that contains the three coils plus the hexapole magnets will be adopted. The magnetic trap will be surrounded by an ARMCO iron yoke, that in the actual design is distant 150 mm from the hexapole ends (along the axis), 200 mm from the INJ, EXT axial coils outer radius and having thickness of 25 mm. The iron yoke is visible in Figure 3.4 (1/3 symmetry).

Moreover, in order to have direct views of the plasma inside the trap for using $\gamma - rays$ detectors and the other diagnostic tools, both the cryostat bulk body, the external iron yoke and the plasma chamber need to be radially drilled with 18 holes of proper shapes and diameters. The holes need to be extended along the entire radius of the cryostat bulk body and along the external iron yoke in order to obtain vacuum channels acting as collimators for the detectors. Consequently, the cryostat plays the role of multi-collimator for the HPGe array and suppresses as much as possible the sources of background arising from photons coming from the walls and not directly from the plasma core, so improving the signal-to-noise ratio.

Table 3.1: PANDORA magnetic system field requirements.

MAGNETIC SYSTEM FIELD REQUIREMENTS	
B_{inj} max @ z = -350 mm	3 T
B_{inj} operative range	2.7 T – 3 T
B_{ext} max @ z = 350 mm	3 T
B_{ext} operative range	1.7 T – 3 T
B_{min} @ $B_{inj,\,ext} \simeq$ 2.7 T (18 GHz)	< 0.4 T
B_{min} @ $B_{inj,\,ext} \simeq$ 3 T (21 GHz)	≤ 0.5 T
B_{hex} @ R_{CH_IN} = 140 mm	1.5 T
LHe	Free
Warm Bore radius	150 mm

The side view of the magnetic system including the cryostat and iron yoke geometries, plus the detector holes with their inclination angles with respect to the z axis, are shown in Figure 3.5.
These "*hole-collimators*" have been dimensioned, in terms of shape, number, position, dimension, etc., by means of MonteCarlo simulations performed in GEANT4. The detailed description is reported in the chapter 6.
In summary, the position of the azimuthal holes have been chosen along the inter-space axis of each hexapole conductor (see Figure 3.5). There are three holes for each conductor inter-space (labelled 1,2,3 for the first conductor and 4,5,6 for the second one, relatively to the xz cut plane shown in figure 3.5), two holes placed in pair (labelled 1,2 and 4,5 respectively) and one hole as single (labelled 3 and 6 respectively).
As concerns the $PANDORA_{Gr3}$ trap microwave injection system, it will include three different microwaves injections lines based on standard rectangular waveguides in order to excite (separately or even simultaneously) the plasma.

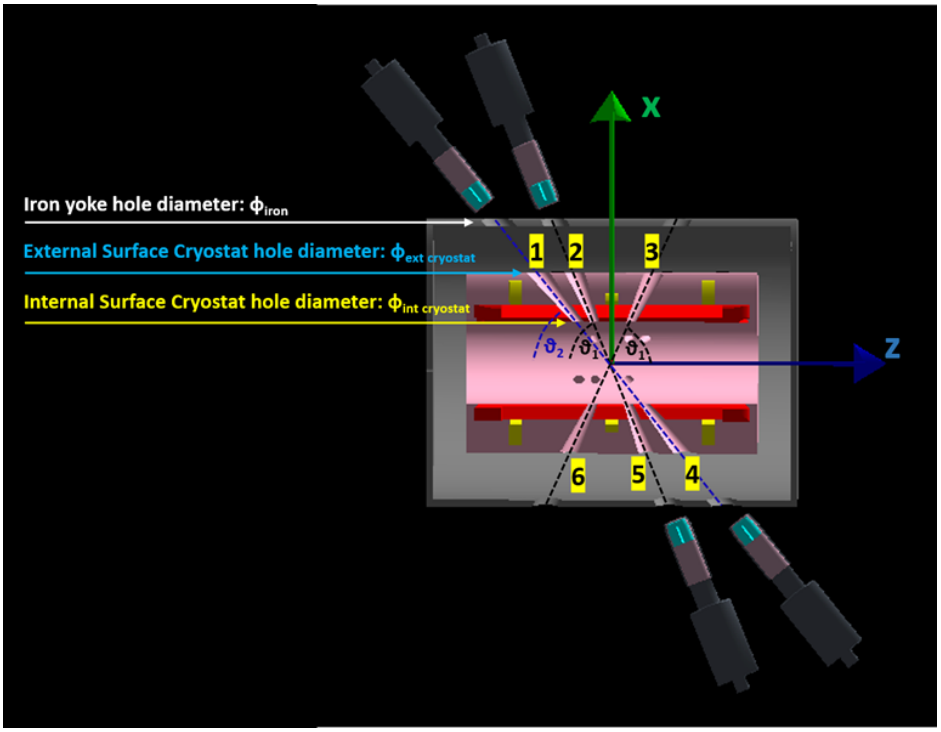

Figure 3.5: Whole magnetic system with cryostat (pink transparent object) and iron yoke (gray object) inserted. Six of the 18 conical azimuthal for the HPGe detector displacement are shown

Therefore, the plasma chamber shall have three waveguide ports for:

- a primary microwave injection provided by a DBS-Band Klystron amplifier operating in the frequency range from 17.3 to 18 GHz at 2.4 kW (in Continuous Wave – CW mode) of minimum power. The microwave power is delivered through WR62 standard waveguides.

- a secondary microwave injection provided by a 2 kW CW (min. output power) K-band Klystron amplifier operating in the frequency range $21 - 22$ GHz. The microwave power is delivered through WR51 standard waveguides.

- a tertiary microwave injection from a 500W CW (min. output power) Ku-band Traveling Wave Tube Amplifier (TWTA) at $15 - 17GHz$.

The microwave power is delivered through WR62 waveguides.

Three separate frequency generators will be used to provide different drive signals for the two Klystrons and the TWTA.
This microwave heating setup allows to excite the plasma both in TFFH and in TCFH scheme. We have already discussed in the section 1.3.1 and 1.3.2 about the advantages of the double frequency heating scheme. Thus, in PANDORA_Gr3, it will be possible to operate according to different microwave injection schemes:

- *Single Frequency Heating (SFH)* mode: only one amplifier (typically the Klystron) is used.
- *Two Far Frequency Heating* and *Two Close Frequency Heating* scheme mode, also with the possibility to vary the power ratio between two microwave amplifiers: usually the lower frequency of the tunable TWTA at lower power is varied and the Klystron main heating power is kept at a fixed frequency.
- *Three Frequency Heating* mode from the two Klystrons and the TWT amplifier.
- a *Four frequency heating* mode, since TWT can be driven simultaneously with two frequencies, if a low power-combiner is added, permitting further improvement especially in the case of the highest charge states.

Finally, the $PANDORA_{Gr3}$ plasma chamber will make of stainless steel, having 300 *mm* outer diameter, 700 *mm* length and 10 *mm* thickness. Such a strong structure gives the system the mechanical strength and rigidity necessary to connect many ancillary devices. The end-caps, through several flanges and feedthroughs, allow to connect the vacuum pipe, the RF injection waveguide, the gas inlet, the oven (to vaporize solids), the beam extractor and some diagnostic devices. Moreover, the cylinder wall hosts 18 *holes* (diameter 40 *mm*) that will be "*sealed*" with 12 $\gamma - ray$ detectors and 6 other diagnostic tools, pointing to the center of the plasma chamber. The holes position and dimension will be in detail described in the chapter 6. Another hole (diameter 40 *mm*) is placed

on each end-cap, still pointing to the chamber's center. The chamber includes a cooling coil for the circulation of demineralized water, integrated on the external wall of the cylinder. A sketch is shown in the fig.3.6.

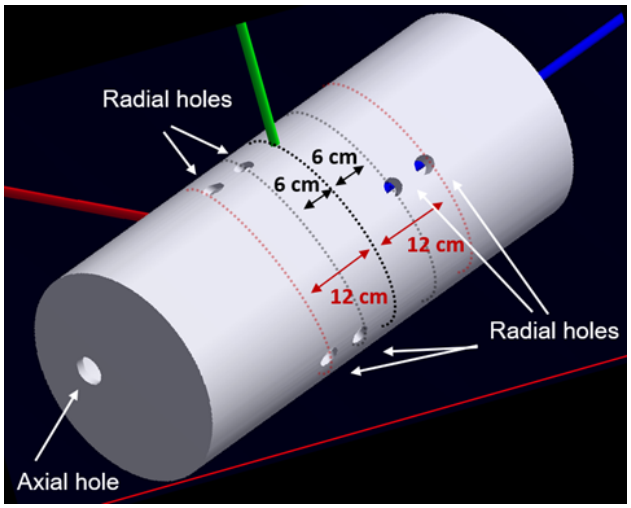

Figure 3.6: Stainless steel plasma chamber drilled with 20 holes of diameter 40 *mm*.

3.1.2 PANDORA$_{Gr3}$ test-benches: the ECRIS at ATOMKI and the Flexible Plasma Trap at LNS

Since the design of the advanced $PANDORA_{Gr3}$ plasma trap is on going, all experimental measurements described in this thesis have been carried out in the two down-sized compact traps used as $PANDORA_{Gr3}$ test-benches. The main experiments, which results will be discussed in the chapter 5, were carried out at the ECR Laboratory of Atomki, in Debrecen (Hungary), in the 2^{nd} generation ECRIS, based on a $B_{minimum}$ magnetic configuration. Other experimental measurements have been carried out in the compact, simple mirror ECR plasma trap installed at INFN-LNS, in Catania (Italy), called *Flexible Plasma Trap* (*FPT*).

The FPT (see fig.3.7, up) is made of three solenoids allowing simple mirror, magnetic beach and flat magnetic field configuration (see fig. 3.7, down), with a maximum magnetic field about 0.5 T; it has three mi-

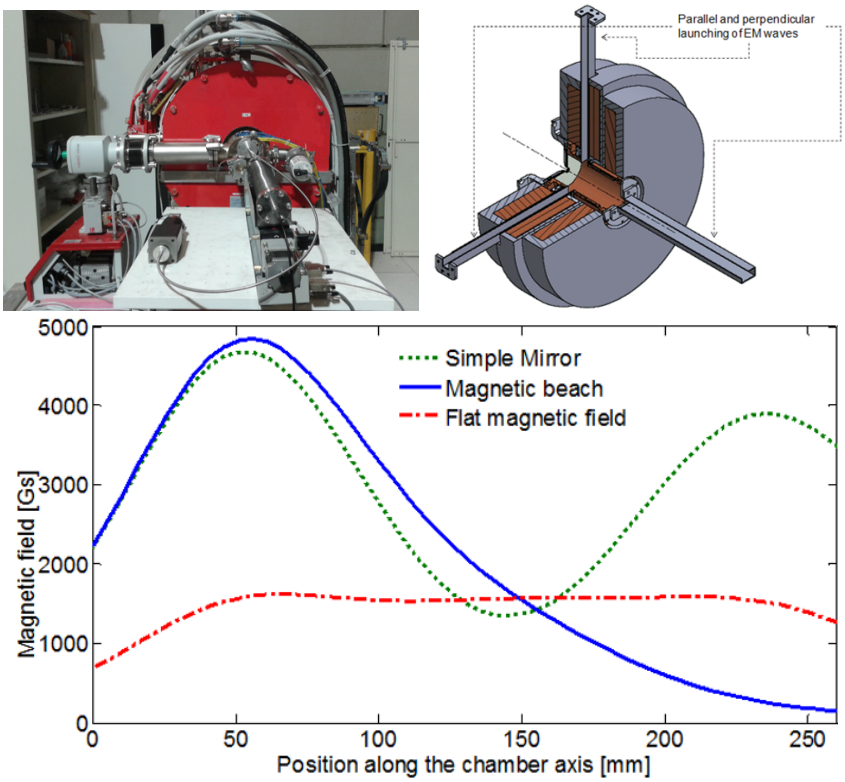

Figure 3.7: Up - The Flexible Plasma Trap (FPT) installed at LNS-INFN. Down - The axial magnetic field distribution for three different configuration of the FPT.

crowaves inputs, one axial and two radials, and operates in the microwave frequency range $4 \div 7\ GHz$. The pumping frequencies are amplified by a Travelling Wave Tube (TWT).
The Atomki-ECRIS (see fig.3.8, left) is a 2^{nd} generation ion source and the basic operation frequency is typically 14.25 GHz, produced by a Klystron. It is also possible to generate a second tuneable frequency, provided by a TWT amplifier (TWTA), with an operating range from 13.60 GHz to 14.60 GHz, by applying the power combiner technique described in [10]. The axial magnetic field is 1.26 T at injection side, 0.39 T (B_{min}) and 0.95 T at the extraction, whilst the radial magnetic field produced by the hexapole and at the plasma chamber wall ($R = 29\ mm$) is about 1.2 T

(the $B_{minimum}$ magnetic field profile is sketched in fig.3.8, right). The ion source is not connected to any accelerator, thus it is suitable and available for plasma physics investigations. Further technical and application details are in the paper [75].

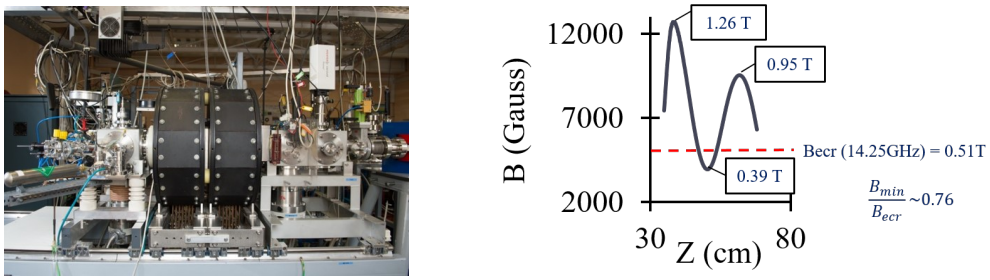

Figure 3.8: Left -The ATOMKI-ECR ion source. Right - The axial magnetic field distribution of the Atomki-ECRIS in the $B_{minimum}$ magnetic field configuration.

Both the Klystron amplifier (14.25 GHz fixed frequency, power max 1000 W) and the TWTA (13.60 - 14.60 GHz variable frequency, power max 500 W) are fed by sweep oscillators. A special combiner unifies the two amplified signal and forwards them toward the plasma chamber. A broadband frequency circulator was applied to save the amplifiers from damages caused by reflected powers. A cross-guide was mounted as close to the plasma chamber as possible to the simultaneous measurement of the forwarded and reflected RF-powers. This solution made us possible to fix the net power (which is the difference of the two ones mentioned) at a constant value. Then the waveguide system was connected to the plasma chamber through high voltage and vacuum windows (figure 3.9). During the measurements the ECRIS was operated at maximum coils' power resulting in an axial magnetic field distribution as it is in figure 3.8-right.
When we use only the Klystron fixed frequency (14.25 GHz) the ratio of $\frac{B_{min}}{B_{ECR}}$ is 0.76; this value is very close to the *critical* 0.75 value (or ranges of values typically around $0.75 \div 0.80$) for the instability onset [48, 76]. Operating the source in TCFH mode, the second frequency amplified by the TWT can be varied between 13.60 GHz and 14.60 GHz resulting in

a $\frac{B_{min}}{B_{ECR}}$ value ranging from 0.80 to 0.75. So, it is possible to study what happens when we approach or pass the critical value without changing the axial magnetic field configuration.

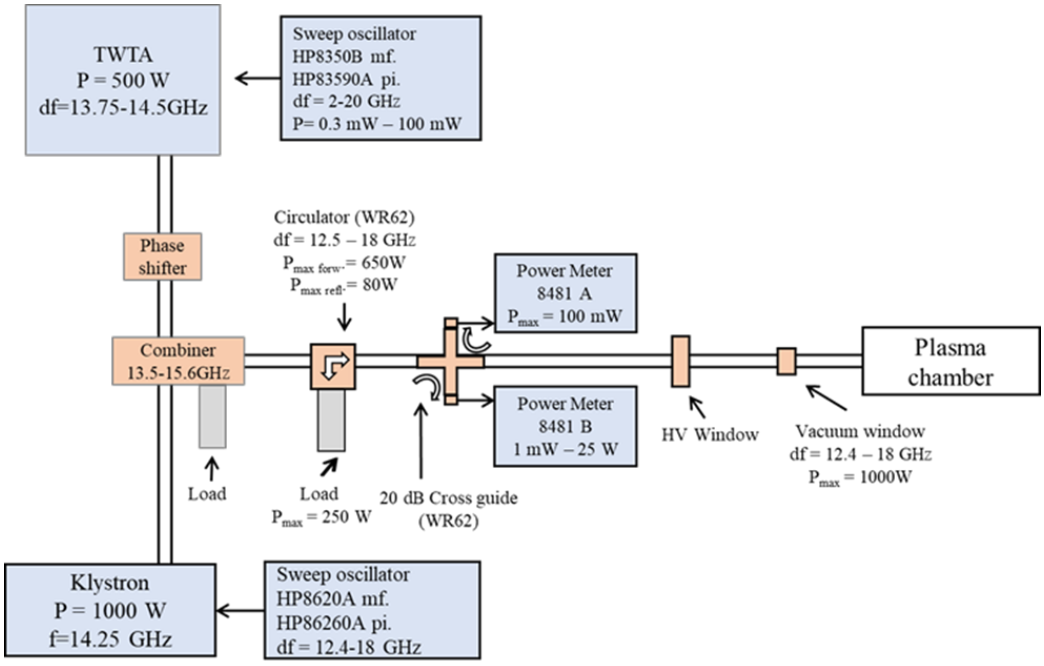

Figure 3.9: The microwave coupling system to study the two-close-frequency operation mode in ECR ion sources.

The ion source was optimized for middle charged Argon ion production while the gas pressure measured at the injection box of the ion source was $2 \cdot 10^{-6}$ $mbar$. Ion beam was extracted from the plasma by 10 kV extraction voltage.
Finally, an innovative design of the plasma chamber, made of different metals for each its main parts (injection plate, plasma electrode and lateral walls) has been used. After a careful material selection, the plasma chamber wall has been covered with a Tantalum liner (diameter: 58 mm, length: 210 mm, thikness: 50μm) shown in fig. 3.10.c), while the injection plate was made of Aluminium (fig. 3.10.a)) and the plasma extraction electrode was covered by a 1 mm thick Titanium, shown in fig. 3.10.b).

About 2/3*rd* part of the injection plate was made of Al mesh providing closed resonant cavity and transparency for X-ray imaging at same time. The remained 1/3*rd* surface ensured the injection of the microwave and the working gas. The mesh structure of the Al plate, sketched in fig. 3.10.a, has a wire diameter of $400\mu m$, guaranteeing more than 60% of optical X-ray transmission. Figure 3.10 and Table 3.2 show the details.

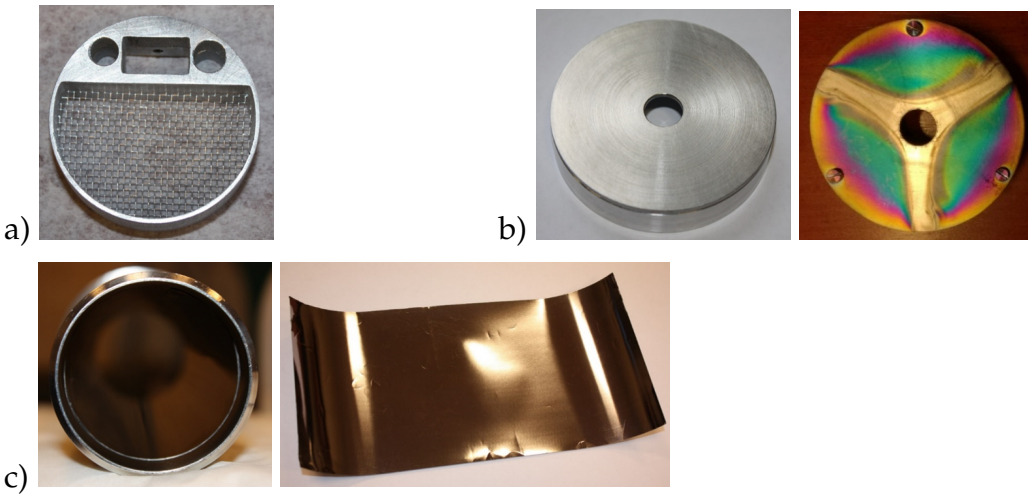

Figure 3.10: New materials in the plasma chamber. a) Injection plate, Aluminum, mesh transparency is 60%. b) Plasma electrode covered with Titanium (left and right, before and after the experiment, respectively). c) Lateral wall is Tantalum (right, Ti liner only).

Table 3.2: The most probable K and L shell related characteristic X-ray energies from the different metals used to cover the inner chamber walls.

Part of chamber	**Material**	$K\alpha$ **[keV]**	$K\beta$ **[keV]**	$L\alpha$ **[keV]**
Injection plate	Al	**1.49**	**1.56**	-
Lateral wall	Ta	57	65	**8.14**
Plasma electrode	Ti	**4.51**	**4.93**	0.45
Plasma	Ar	**2.93**	**3.19**	-

From the table 3.2 it is obvious that by using these materials when an Argon plasma is present, all the characteristic peaks can be well separated

by our soft X-ray detectors between 1.49 *keV* and 8.14 *keV* energies. This solution also makes possible a post-processing energy filtering of the X-ray photos taken by the pinhole camera. If so, the origin of the different X-ray photons and also the role of the different part of the plasma chamber can be revealed (as will be illustrated in details in the chapter 5).

3.2 The multidiagnostics setup

The multi-diagnostic setup, based on non-invasive tools and on advanced techniques of analysis, allows detailed investigations of magnetoplasmas properties in terms of density, temperature, CSD and inner plasma EM wave emission and is able to perform high-resolution spatial and time resolved analysis too.
In ECR plasmas confined in $B_{minimum}$ structures the energy of the electrons ranges from a *few eV* to hundreds of *keV* or even 1 *MeV* and, since ECRIS plasmas are in non-LTE (non-Local Thermodynamic Equilibrium) condition, the typical Electron Energy Distribution Function (EEDF) consists of three different electron populations that can be distinguished in a typical spectra (see the sketch in fig. 3.11): the *hot population*, which presents typical temperatures around 100 *keV* or more; a *warm population* with temperatures in the range 100 $eV \div$ up to tens of *keV*; the *cold population*, with temperatures in the range of 1 $eV \div 100$ *eV*.

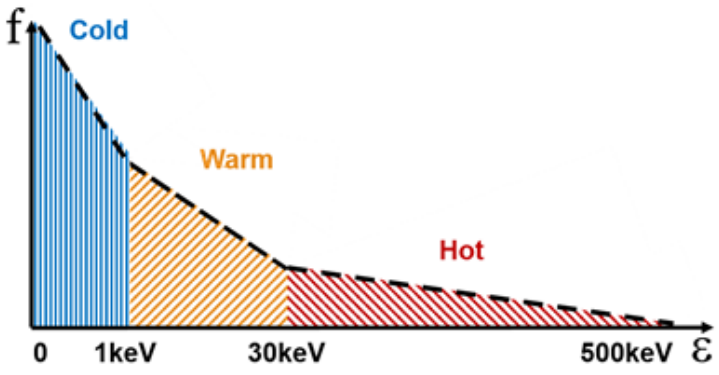

Figure 3.11: Sketch of the typical EEDF in ECR plasmas with the three different electron populations

Only the warm component of the electron energy distribution function has the right energy to ionize the atoms up to high charge states, since the cold electrons have insufficient energy to remove electrons from the inner shells of atoms (although they are highly involved in the confinement dynamics) and in the hot electron domain the ionization cross section inversely proportional to the electron energy.
For a complete characterization of ECR plasmas - measuring the plasma parameters in all three different energy regimes and performing plasma density and temperature evaluation - a multiplicity of different tools and analysis methods become necessary.
A render view of the several diagnostics tools needed (and already partially available at LNS) for characterizing microwave generated plasmas are shown in the figure see fig.3.12.

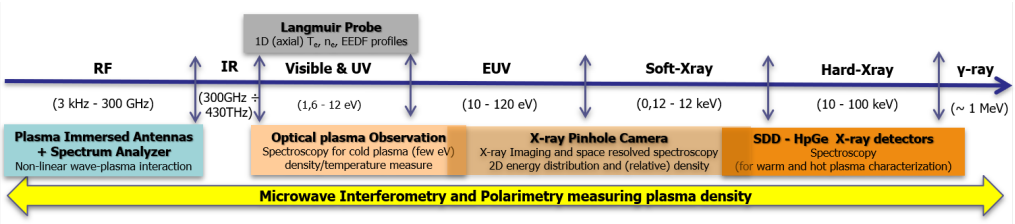

Figure 3.12: Render view of the several diagnostics tools needed (and already partially available at LNS) for characterizing microwave generated plasmas.

The several tools developed along the years can be now implemented simultaneously for probing the entire Electron Energy Distribution Function. The developed multi-diagnostic setup [10, 8] (see Fig.3.13) consists of:

a) A **Silicon Drift Detector (SDD)** for plasma density and temperature measurement in soft X-ray domain (quantum efficiency (Q.E.) $\sim$ 1.0 - 30 keV).

b) A **High-purity Germanium (HPGe) detector** for spectral temperature measurement of hard X-ray domain (Q.E. $\sim$ 30 - 2000 keV and 0.2% of resolution at 1 MeV), including time resolved spectroscopy.

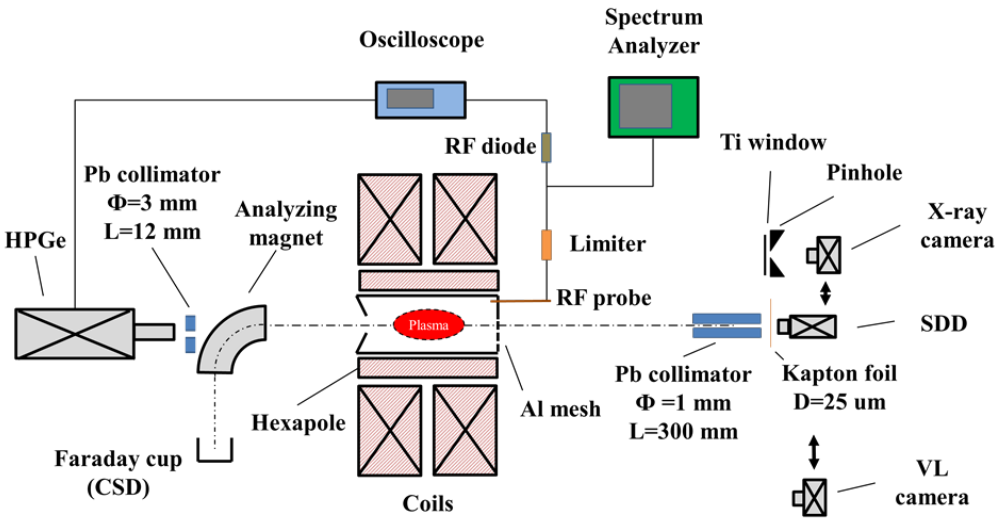

Figure 3.13: Sketch of the multi-diagnostic setup consisting in a collection of non invasive tools (see [10, 8] for more details).

c) A **Visible light (VL) camera** for the plasma-emitted visible light characterization with a resolution of $R = 13500\ nm$ ($\Delta\lambda$= 0.04 nm).

d) A **two-pins RF probe** installed inside the plasma chamber in the injection plate, **connected to a Spectrum Analyzer (SA)** in order to detect the plasma emitted EM wave in GHz ranges.

e) An **X-ray pin-hole camera** for 2D space resolved spectroscopy (Q.E. $\sim$ 2 - 20 keV), used alternatively to the SDD. This tool is a powerful method to study the plasma structure and, more recently, with the aid of an improved setup of the plasma chamber, it has also permitted to investigate the intensity of the electron losses.

f) A **microwave Interferometer** and a **microwave Polarimeter** for line integrated total density measurement.

g) All diagnostics tools can operate simultaneously with the **Faraday cup** in order to measure the CSD. It has been possible to correlate all the detected plasma parameters with the characteristics of the beam extracted on-line.

h) Alternatively, **the RF probe can be connected with a diode and an oscilloscope** in order to obtain the time-resolved but totally integrated power emitted from the plasma, using this value as trigger signal for instability signature and to perform time resolved X-ray analysis too. The time-resolved setup, sketched in figure 3.14 consists in fact in two multi-pins probe (one for the axial line and the other for the radial one inspection) connected with a diode and an 80 Gs/s scope, studying very fast phenomena (with time scales below ns).

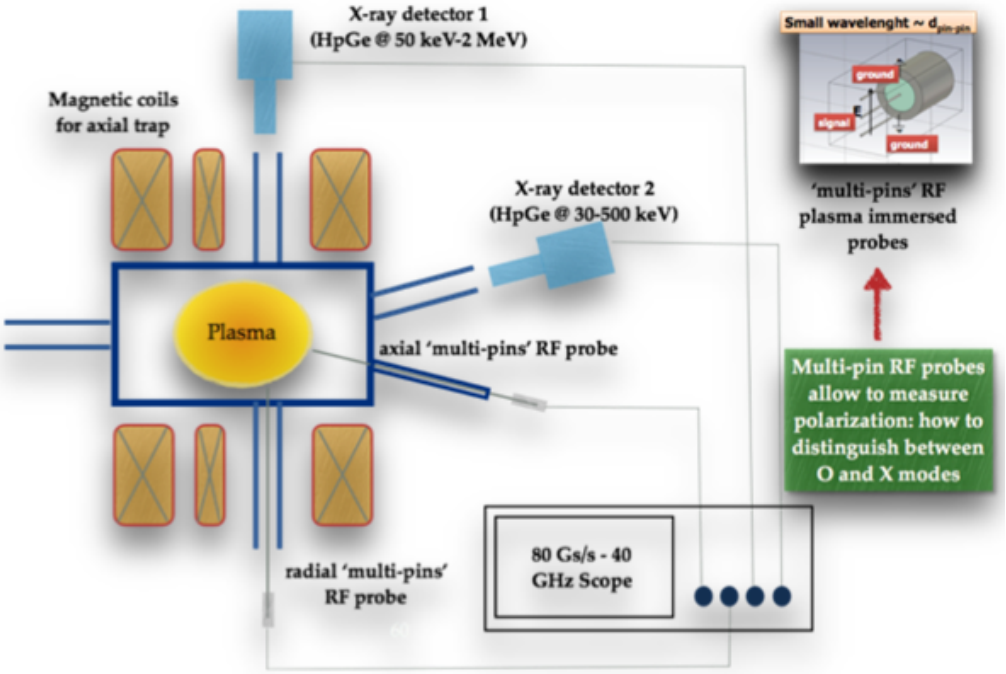

Figure 3.14: Experimental setup including the multidiagnostics system for time-resolved characterization of the plasma in stable and turbulent regimes.

In the table 3.3 the most relevant characteristics of the developed tools are summarized (see [10, 8] for more details). The simultaneous use of all setups plays a crucial role for the detailed and complete characterization. The numbers in the table state that the plasma temperature and density

can be measured - eventually in space and resolved way - with an uncertainty that is less than 7% for the temperature, and around 25% for the total density. Partial densities of warm and hot electrons are measured via X-ray spectroscopy with about 10% uncertainty, while use of OES in the next future will reduce density measurements uncertainties of at least a factor 2.

Table 3.3: Lists of the non invasive diagnostic tools, with their most relevant characteristics, being part of the multi-diagnostic setup.

Diagnostic Tool	**Sensitive Range**	**Measurement**	**Resolution & Meas. Error**
SDD	1.0-30 keV	Soft X-ray Spectr.: warm T_e and n_e	Res. $\sim$ 120 eV $\epsilon_{n_e} \sim 7\%$, $\epsilon_{T_e} \sim 5\%$
HpGe	30-2000 keV	Hard X-ray Spectr.: hot T_e and n_e	$FWHM_{@1332.5keV} < 2.4$ keV $\epsilon_{n_e} \sim 7\%$, $\epsilon_{T_e} \sim 5\%$
Visible Light Camera	1.0-12 eV	Optical Spectr.: cold T_e and n_e	$\Delta\lambda$ = 0.04nm R=12500
Microwave Interferometer	K-band 18-26.5GHz	Interferometry: line integrated n_e	$\epsilon_{n_e} \sim 50\%$
Microwave Polarimeter	K-band 18-26.5 GHz	Polarimetry: line integrated n_e	$\epsilon_{n_e} \sim 25\%$
X-ray pin-hole Camera	2-15 keV	2D Space-resolved soft X-ray Spectr.	Energy Res.$\sim$0.32 keV Spatial Res.$\sim$0.56 mm
RF probe + SA	10-26.5 GHz *(probe)*	Frequency-resolved Spectr.	Resolution bandwidth: RBW = 3 MHz
RF probe + Scope + HpGe	10-26.5 GHz *(probe)*	Time-resolved X-ray Spectroscopy	80 Gs/s *(scope)* time scales $\sim$ ns

Among the illustrated diagnostic tools, two of them, i.e. the pin-hole CCD camera and the two-pin RF probe, are those that have been developed and used specifically to obtain the experimental results described in this work. The stable and unstable plasma regimes have been characterized through this pair of non invasive tools, allowing investigations of magnetoplasmas properties in terms of inner plasma EM wave emission both in X-ray and RF energy ranges. Thus, in the next sections the description of their characteristics will be discussed in detail.
The diagnostic system used for characterizing kinetic instabilities and

performing simultaneously spatial high-resolution X-ray imaging is shown in figure 3.15.

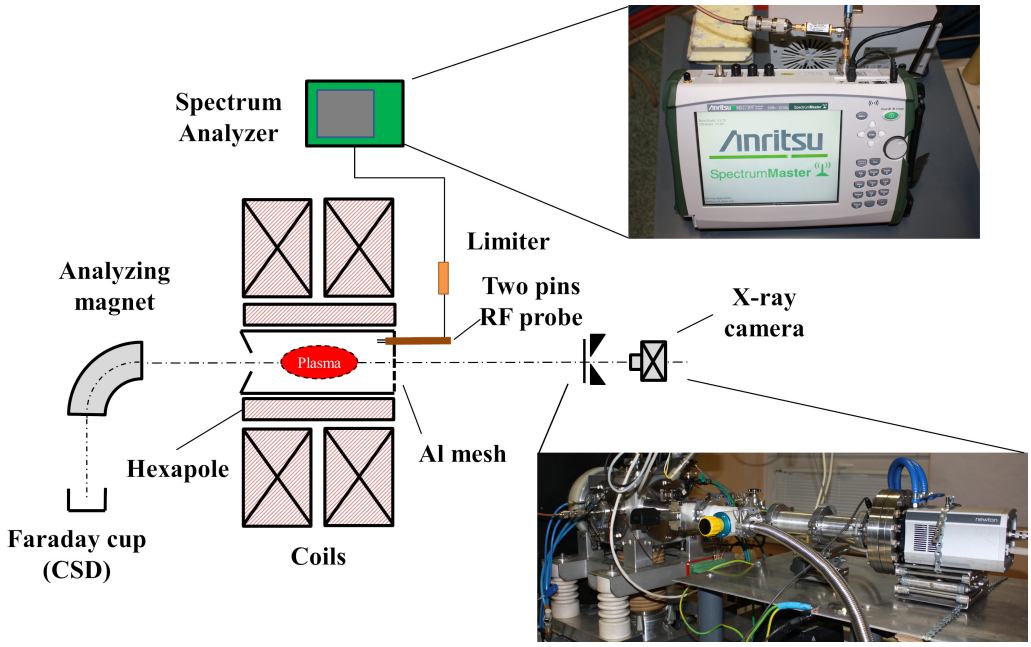

Figure 3.15: Sketch of the diagnostic setup and images taken of the diagnostic tools.

3.2.1 The two-pins RF probe and Spectrum Analyzer

The two-pins RF probe, installed inside the plasma chamber in the injection plate and protruded through one of the gas input holes (see fig.3.16), has been designed on purpose to detect the EM wave emission directly inside the plasma chamber. A blocks diagram of the system is sketch in the figure 3.16.
The two-pins RF probe was flexible with an outer diameter of 4 mm, a pin length of 3.5 mm and a pin distance of 2 mm.
The Spectrum Analyzer operated with a frequency span in the range 13-15 GHz with a resolution bandwidth (RBW) of 3 MHz, and a sweep time of 400 ms. By these operative parameters, the ratio between the frequency span and the RBW fixes the number of points in the frequency spectrum.

From this latter, it is possible to estimate the temporal baseline the analyzer took in order to perform the FFT with the given RBW, resulting by the ratio between the sweep time and the number of frequency points per spectrum. This number is around 0.7 ms; the sampling in the time domain is instead in the range of tens of ps (it is comparable to the inverse of the bandwidth and, since the bandwidth is 40 GHz, sampling occurs at $1/40$ GHz).

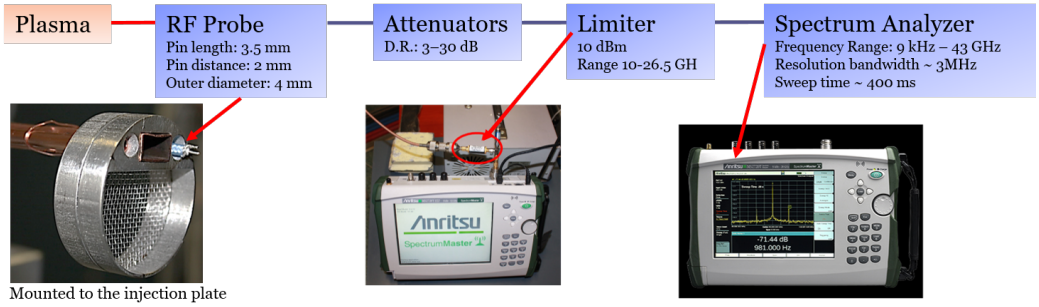

Figure 3.16: Blocks diagram of the system with the multi-pin RF probe, connected to the Spectrum Analyzer, to detect the electromagnetic wave emission inside the plasma chamber.

The probe acquisition setup consists also of a RF power limiter, 10 dBm limiting and operating in the range $10 \div 26.5$ GHz, and a set of variable attenuators in the dynamical range $3 \div 30$ dB.
A typical experimental spectrum of the detected power versus the position of the probe along the axis is shown in figure 3.17, on the left. By means of a movable bellow tube, the probe has moved inside the plasma chamber at steps of 40 μm, connecting the two-pin probe to a RF power probe. More details about probe properties can be found in [77].
Whilst, connecting the two-pins RF probe to the Spectrum Analyzer (as sketched in figure 3.15), it has been possible to characterize the EM emission in GHz ranges inside the plasma chamber performing "*frequency-resolved*" spectra, as shown in figure 3.17, on the right. In the example shown in the figure the measurement has been performed in the ATOMKI-ECRIS using a pumping frequency of 14.05 GHz, provided by the TWTA. It is worth to be highlighted that this setup is able to detect both the main pumping frequency, and self-plasma emitted radiations in-

side the plasma chamber, consisting in several sub-harmonics (as shown in figure 3.17-right).

a)

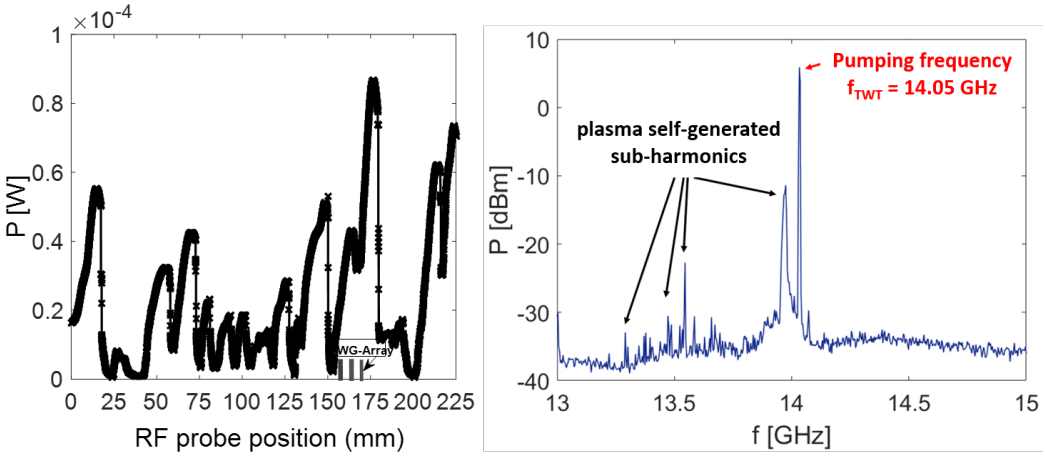

Figure 3.17: Trend of the detected power vs. the position of the two-pins probe along the axis (on the left), and frequency-resolved spectrum of the detected power (on the right).

Since the RF plasma self-emission sub-harmonics can represent signatures of plasma kinetic instabilities (characterized by fast RF and X-ray bursts [31, 29]), this tool can be used to detect and characterize turbulent plasma regimes, in order to: a) find a way to damp them and, consequently, improve the ECR plasma stability and ECRIS performances [11, 12]; b) reproduce and study these interesting phenomena of astrophysics interest (such as the so-called Cyclotron Maser Instability, which is a typical kinetic turbulence occurring in astrophysical objects) in laboratory plasmas. These characterizations and studies will be discussed in details in chapter 5.
The RF antenna was calibrated in the standard way, i.e. by measuring the reflection coefficient S_{11} in free space. The S_{11} trend is shown in fig. 3.18. In the experimental frequency range $13 \div 15\ GHz$ the $S_{11} < -9.25\ dB$ condition is satisfied almost everywhere. This condition implies the antenna matching was good. Only for about $f < 13.2\ GHz$ the S_{11} parameter becomes $> -9.25\ dB$. Anyway, experimental date renormalized by this

factor did not differ considerably.

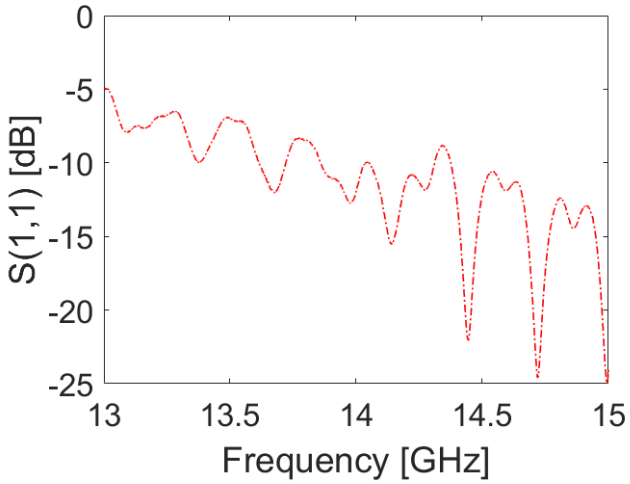

Figure 3.18: The $|S_{11}|$ trend of the RF probe measured in free space.

We calibrated also all the cables connecting the antenna to the SA. The measured attenuation trend is shown in fig. 3.19, and all experimental data have been renormalized by these factors.

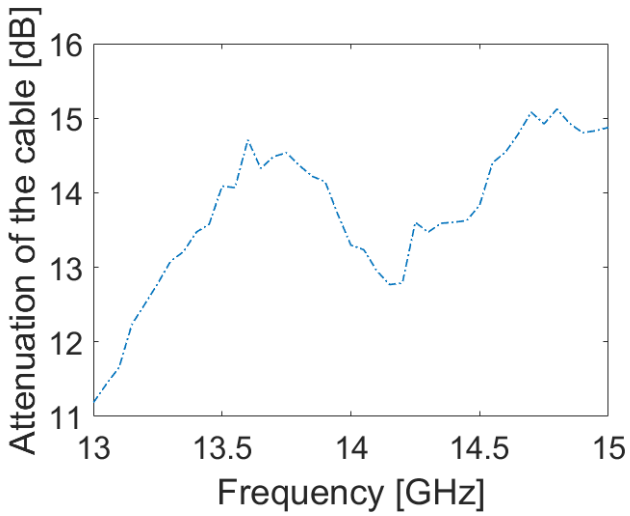

Figure 3.19: The measured attenuation trend of the cables.

3.2.2 The X-ray pin-hole camera

The X-ray pin-hole camera system for 2D space resolved spectroscopy is here described. The CCD X-ray camera (model Andor, iKon-M SO series) is made of 1024 x 1024 pixels and with an optimal quantum efficiency in the range 500 eV - 20 keV. It was coupled to a Pb pin-hole (thickness 2 mm, diameter Φ = 400 μm) and placed along the axis, facing the chamber from the injection flange. A Titanium window with 9.5 μm thickness was used to screen the CCD from the visible and UV light coming out from the plasma. A multi-disks lead collimator (described in details later, in the subsection 3.2.3) as extra shielding - disks with different thickness and hole diameter – developed to acquire X-ray picture in relatively high RF-power operation mode, up to 200 W total incident power. The tool is a very powerful method to study the plasma structure and the intensities of the electron losses.
The pin-hole setup is sketched in fig. 3.20. The magnification M of the pin-hole system (developed by the position of the pin-hole with respect to the plasma and to the CCD chip) was optimized to be: $M = 0.244$ (distance pinhole-CCD = 232 mm, distance pinhole-plasma centre = 952 mm).

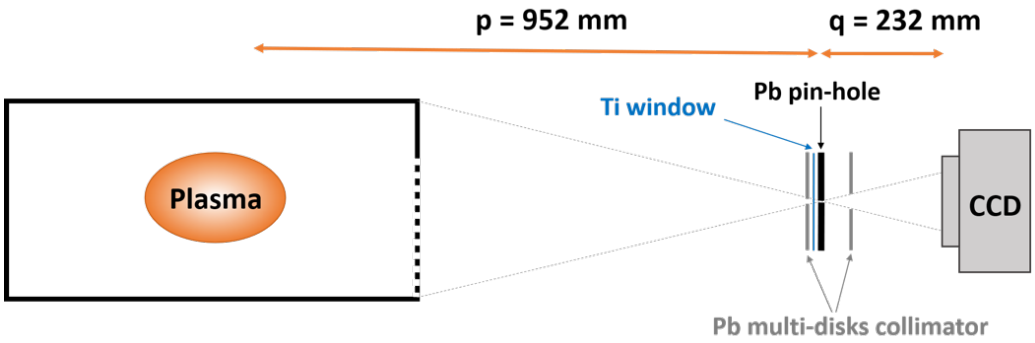

Figure 3.20: Sketch of the X-ray pin-hole camera setup.

As above mentioned, the ATOMKI plasma chamber walls has been covered with a Tantalum liner, while the injection plate was made of Aluminium and the plasma extraction electrode by Titanium.
The sketch of the ATOMKI plasma chamber is illustrated in the fig. 3.21,

whilst the perspective front-view of the plasma chamber is sketched in fig.3.22. The mesh structure of the Al plate, sketched in fig. 3.22.a), has a wire diameter of 400 μm, guaranteeing more than 60% of optical X-ray transmission. In figure 3.22.b) a typical X-ray plasma image is shown. This image was collected with an exposure time of 50 *seconds*, at 1 MHz of readout rate and using the full-frame (1024 x 1024 pixels) acquisition mode. It is possible to recognize the lateral wall of plasma chamber, the extraction hole and both the mesh structure and the bulk Al of the injection plate.

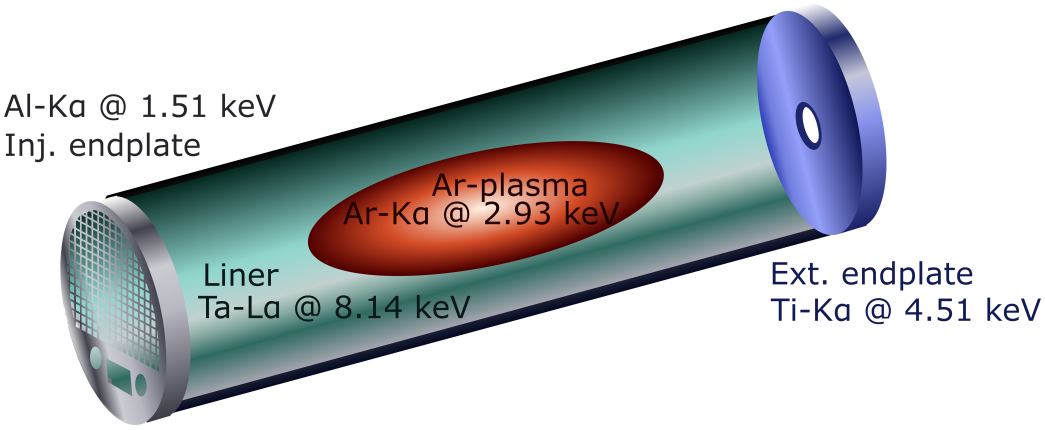

Figure 3.21: Simplified sketch of the plasma chamber composed of different materials.

Since, we are interested to study plasma kinetic instabilities, we needed to work in high powerful configurations like never before for X-ray spectroscopy in the field of ECR Ion Sources and ECR compact traps. The pin-hole CCD technique has been upgraded in order to allow measurements at much higher RF power and the pin-hole structure has been redesigned in order to reduce the huge X-ray scattering affecting the image quality: in 2014 the use of this technique was limited to 30 W, whilst now 200 W operations are possible [78, 79]. Therefore, we developed and manufactured on purpose an innovative multi-disks lead collimator as extra shielding. The multi-disks collimator consists of two lead disks with same thickness (1 mm) and different diameter Φ (2 mm, 1 mm). In the centre between the two lead collimator, the lead pin-hole has been placed, and in front of it

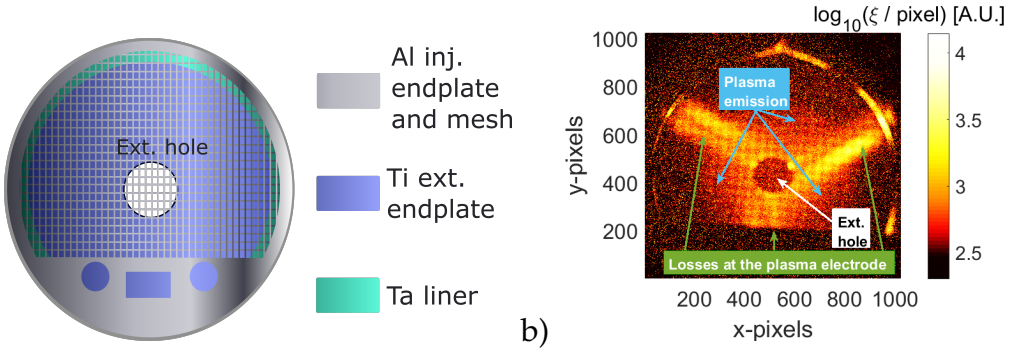

Figure 3.22: (a) Sketch of the perspective front-view of the plasma chamber. (b) Typical X-ray image obtained by pin-hole camera setup; it is possible to recognize the lateral wall of plasma chamber, the extraction hole and both the mesh structure and the bulk Al of the injection plate. Emission coming from plasma and losses at the plasma electrode are highlighted.

two Titanium windows (with a total of 9.5 μm thickness). The two lead disks are located at distances of $l_1 = 40\ mm$ far from the pin-hole at the CCD side, and $l_2 = 6\ mm$ far from the pin-hole at the plasma side.

By means of the collimation system it was possible to acquire X-ray picture with acceptable noise level and in relatively high RF-power operation mode, up to 200 W total incident power. The sketch of the multi-collimator system is shown in the figure 3.23.a) and the picture of it is shown in the figure 3.23.b).

3.2.3 Multi-disks collimator and noise reduction

By installing the multi-disk collimation system, we could remarkably increase the signal noise ratio and the spatial resolution at energetic plasma (strong confinement and high microwave power) cases. The improvement reached by the usage of the collimator is shown by the two images in fig. 3.24 - acquired in the same operative configurations using TWT only at a fixed frequency of 13.80 GHz and a RF power of 200 $Watt$. The image

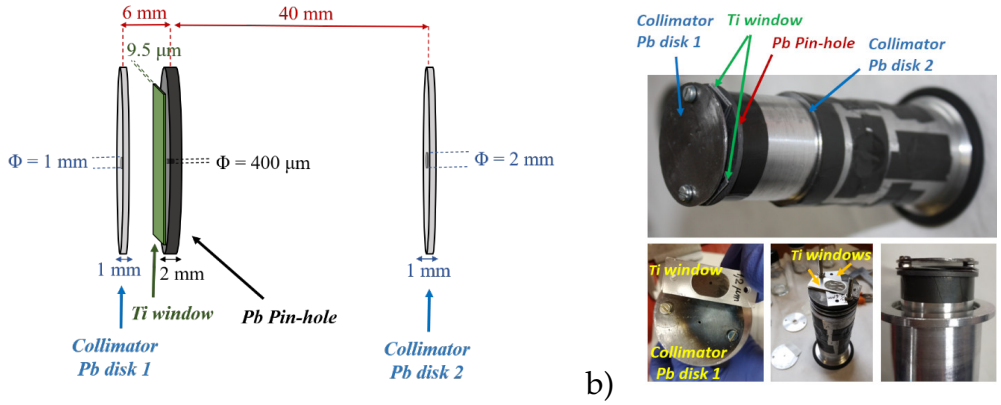

Figure 3.23: Sketch (a) and picture (b) of the multi-disks collimator and Ti windows.

a) has been acquired without using the *multi-disks* collimator, whilst the image b) has been acquired using the *multi-disks* collimator.

It is possible to note the periodic grid-like modulation caused by the mesh in the fig. 3.24.b) only, for which the spatial resolution increases significantly; moreover, also the scattering effects have been drastically suppressed. The effect is quantitatively compared. X-ray counts in three different ROIs were selected. Spatial positions of the ROIs are marked in figure 3.24, as well: the first (squared in green) dominated from X-ray scattering noise in the region outside the plasma chamber $N_{bkg_{out}}$; the second (squared in cyan) dominated from X-ray scattering noise in the region inside the plasma chamber $N_{bkg_{in}}$; the third (squared in white) dominated from X-ray coming from Argon plasma only N_{hole}. In the table 3.4 the mean values of each ROIs with their corresponding error have been reported both for the case with collimator and without. For each value, also the discrepancy expressed in percentage at the case with using collimator and without has been estimated.

Considering the ratio *signal over noise* both inside and outside the plasma chamber it is possible to observe that using the *multi-disks* collimator they drastically increase: by 70% in the first case (outside the plasma chamber) and by 39% in the second case (inside the plasma chamber).
Finally, for a more quantitative estimation of the spatial resolution improvement, we performed the distribution along two (horizontal and ver-

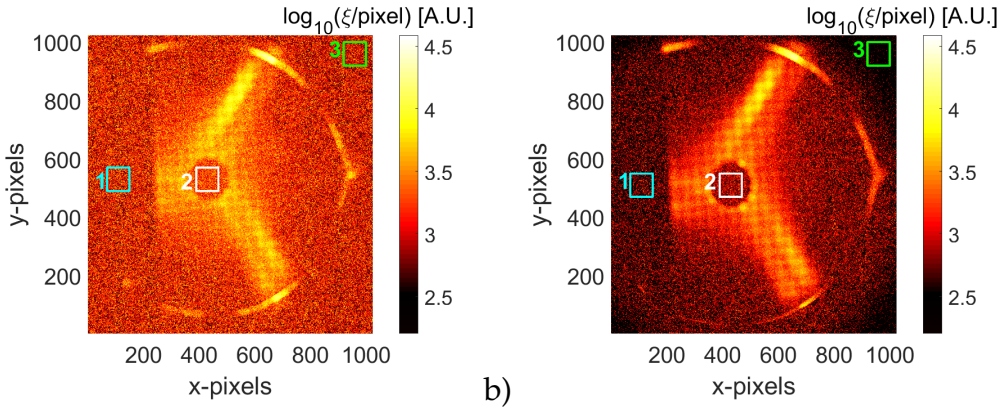

Figure 3.24: Pseudo-colour representation of X-ray flux (in logarithmic scale), putting in evidence the ROI (region of interest) where the radiation coming from Ar plasma only (squared in white), and the ROIs where radiation is due to scattering effects (squared in cyan and in green). a) without the *multi-disks* collimator. b) in the pin-hole setup the *multi-disks* collimator has been used.

Table 3.4: Mean values of X-ray flux for three ROIs with their corresponding errors, both for the image acquired using the collimator and without it. In the table the ratio signal over noise both inside and outside the plasma chamber has been also reported. For each value, also the discrepancy expressed in percentage at the case with using collimator and without has been estimated.

	With Collimator	**Without Collimator**	**Difference [%]**
$\mathbf{N_{hole}}$	2889 ± 54	4441 ± 67	- 54 %
$\mathbf{N_{bkg_{out}}}$	332 ± 18	1677 ± 41	- 405 %
$\mathbf{N_{bkg_{in}}}$	847 ± 29	2136 ± 46	- 152 %
$\frac{\mathbf{N_{hole}}}{\mathbf{N_{bkg_{out}}}}$	8.70 ± 0.50	2.65 ± 0.08	+ 70 %
$\frac{\mathbf{N_{hole}}}{\mathbf{N_{bkg_{in}}}}$	3.41 ± 0.13	2.08 ± 0.05	+ 39 %

tical) ROIs: we selected a row - choosing a ROI of [1024x40] pixels (shown squared in white in the figure 3.25.a)), considering the mean values of the 40 pixels along the y axis - and a column - choosing a ROI of [40x1024] pixels (shown squared in cyan in the figure 3.25.a)), considering the mean values of the 40 pixels along the x axis. The distributions are shown in the figures 3.25.b) and 3.25.c), on the top using the multi-disks collimator, on the bottom without using it. Also in this case it is possible to note the resolution improve very much using the *multi-disks* collimator. In fig. 3.25 on the top show the characteristic periodic trend very well compared to the bottom distribution.

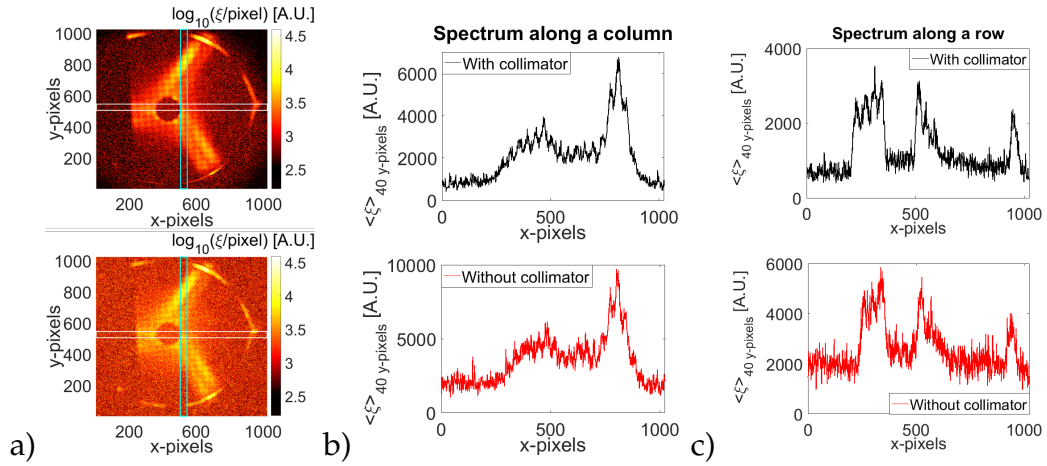

Figure 3.25: a) Pseudo-colour representation of X-ray flux (in logarithmic scale), putting in evidence two ROIs corresponding to a row and to a column. b) The distribution along the column. c) The distribution along the row. Top - in the pin-hole setup the *multi-disks* collimator has been used. Bottom - without the *multi-disks* collimator.

We evaluated the spatial resolution analysing a ROI (region of interest) in the X-ray image, bordered by a blue rectangle in fig.3.26 on the left, and performing the intensity profile.

The intensity profile, displayed in fig.3.26 on the right, shows a characteristic periodic trend where the length of the valley represents the wire diameter (in fact the intensity reaches the minimum value), and we measured an experimental value of 0.565 *mm*; whilst, the distance peak-to-

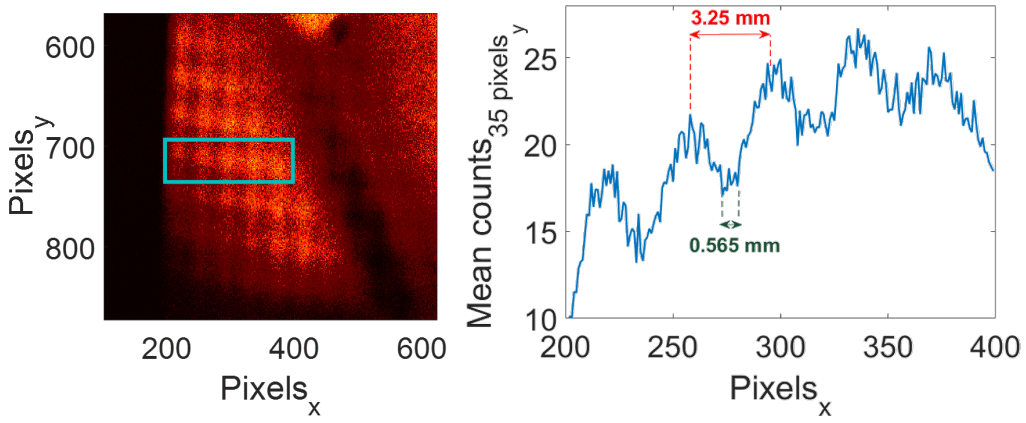

Figure 3.26: Zoom of a ROI of the X-ray image (on the left), and correspondent intensity profile (on the right).

peak is the spacing from each wires (equal to 3.25 *mm*).
Finally, an energy resolution of 0.326 *keV* at 8.1 *keV*, corresponding to the Ta-Lα line has been estimated (details are discussed in the chapter 4).
All the images shown in the next sections (except the ones versus the magnetic field) have been acquired using the *multi-disks* collimator.

3.3 The other diagnostic devices

In order to complete the diagnostic tools overview, also the other devices that will be used, in perspective, in the $PANDORA_{Gr3}$ experiment simultaneously with the RF probe and the pin-hole CCD camera, are summarized.

- A microwave interferometer and a microwave polarimeter, operating in the K-band 18.0 - 26.5 *GHz*, for the total plasma density measurement is available. The mentioned Interfero-Polarimetric setup — named VESPRI (VEry Sensitive evaluation of Plasma density by micRowave Interferometry) — represented one of the first non-intrusive microwave diagnostics methods in compact traps for the evaluation of the integrated electron density. The polarimetric system is based on evaluating Faraday rotation of the probing wave's

polarization plane crossing the magnetoplasma; whilst, in the interferometry, the density determination is based on the phase-shift induced by the plasma refractive index. Two analysis methods have been developed in order to perform the line-integrated total density measurement, for the first time in a compact trap. The results and the details about the polarimetric setup are published in [9], whilst the one concerning the interferometer are reported in [80]. Since the VESPRI setup is able for the moment to measure only the line-integrated plasma density, we are developing a dedicated microwave inverse profilometry (MIP) technique, based on inverse scattering, in order to retrieve the 1D-plasma density profile along the horn-to-horn path; simulations are already available [81] and the measurements are expected in the near future.

- Volume-integrated X-ray diagnostics in the soft-X domain (2 - 30 keV), since the only measurements available to that time were solely from scintillators or HPGe detectors sensitive above 100 keV. Soft X-ray spectroscopy was developed to probe the "*warm*" plasma population, since it plays a crucial role in ionization and charge distribution build-up. Similarly to hard X-rays, also in the case of soft X-ray spectroscopy the main drawback comes from walls-emitted radiation, due to deconfined electrons. Therefore, we developed a series of collimators of various shapes and lengths in order to suppress as much as possible photons flux coming from the walls and not directly from the plasma core. As concern the X-ray volumetric spectroscopy, several experimental campaigns were carried out at INFN-LNS, at the GSI-Darmstadt and at ATOMKI-Debrecen [82, 79]. The warm electrons temperature was estimated by applying an emissivity model developed in [83], which allows to directly fit experimental data in order to get the temperature and density estimations at the same time.

Chapter 4

Analytical Methods: X-rays and RF probes

In this chapter two innovative analytical methods developed for performing time-, frequency- and space-resolved high resolution spectroscopy, will be presented. The X-ray analytical methods represent an original contribution to the overall study developed in this document, allowing to improve the knowledge of the ECR plasma parameters and of the plasma physics processes in general in compact plasma traps.
The first algorithm (described in the section 4.1) has been finalized to analyze the raw data acquired using the X-ray pin-hole camera tool in order to obtain high resolution spatially-resolved X-ray spectroscopy. It represents a powerful method for plasma structure evaluation and for locally determining plasma density and temperature. In particular, the algorithm is able to analyse the *Single Photon-Counting* images for energy-resolved investigation pixel-by-pixel.
The second algorithm (described in the section 4.2) has been finalized to characterize and study the plasma kinetic turbulences, for the first time in a quantitative way. The method provided a new parameter that defines the strength of instabilities in stable and unstable regimes. Studies about the TCFH effect have been carried out in this way.
Both the analytical methods have been developed using MatLab. By simultaneously using and combining the two methods, results will be discussed in details in the dedicated chapter 5.

4.1 X-ray spectrally-resolved imaging algorithm

Each photon impinging in the CCD camera releases its energy in the silicon generating a characteristic number of photo electrons that is proportional to its own energy. The Analogue Digital Unit (ADU), corresponding to the information read by the CCD in each pixel, is therefore proportional to the product of the incident photons by their energies. Typically, there are two main operative modes to acquire the images: the *Spectrally Integrated* (*SpI*) mode and the *Single Photon Counting* (*SPhC*) mode.
During a long exposure time - for example images collected with several tens of seconds - multi events are cumulated by the camera, and the spectral information of the incoming X-rays is lost. Therefore, and hereinafter, images obtained with long exposure times will be called ***Sp**ectrally **I**ntegrated* (**SpI**) images. Even if in this case energy discrimination of the events is not possible, ADUs are anyway able to reveal the energy content of the plasma and plasma chamber complex. The advantage, in this case, is that these acquisitions are relatively fast (tens of seconds) and thus it is possible to master, likely *"on line"*, any change of plasma structures or to monitor losses on the plasma chamber walls.
The more powerful investigations, able to perform local energy determination, is provided by **S**ingle ***Ph**oton **C**ounting* (**SPhC**) mode. By this approach it is possible to decouple the photon number versus their energy. This technique enables space-resolved spectroscopy (thus evidencing the local displacement of electrons at different energies, as well as of plasma ions highlighted by fluorescence lines emission) versus the main tuning parameters, such as the pumping wave frequency or the strength of the confining magnetic field. It is therefore very useful in order to study how the operative parameters (RF pumping frequency and power, magnetic field and also phenomena such as plasma turbulence) affect the plasma confinement, stability and turbulence onset and to investigate dynamics of plasma versus plasma losses.
In this case, the development of proper acquisition protocol and post-processing procedures was required.
The SPhC mode is obtained by fixing a very short exposure-time for each of the acquired image-frame (typically in the range of several tens of milliseconds). Multi-images are recorded in SPhC (of the order of thousands

image frames). The SPhC mode allows minimizing the probability that two (or more) photons hit the same pixel or its nearest neighbours during the exposure of a single image-frame; in case it would happen, in fact there could be a loss of information about their energies.
SPhC mode is empirically set-up, tryning to adjust the single-frame exposure time in suach a way that only a few number of pixels are illuminated on the full CCD matrix; when it happens, each one can be associated with a single photon event and, consequently, the information (in terms of deposited charge) can be correlated to the energy of the incident photon. A sequential acquisition of thousands of SPhC frames allows to reach the statistics necessary for obtaining high quality X-ray fluorescence spectra and images.
The developed analytical method for SPhC imaging and spectroscopy consists of five different steps:

- the ***Gr**ouping **p**rocess* (**Gr-p**);
- the ***E**nergy **Cal**ibration and **E**vent **C**ounting **Norm**alization* (**E-Cal** and **EC-Norm**);
- the ***E**nergy **F**iltering **p**rocess* (**EF-p**);
- the ***H**igh **D**ynamical **R**ange (HDR) **imag**ing and **spect**roscopy (**HDR-img** and **HDR-spect**)*;
- the ***R**ead**O**ut **N**oise (RON) **r**emoval* (**RON-r**).

The details of each step are described, respectively, in the next five subsections.

4.1.1 The grouping process

Even working in SPhC mode, some pixel-clusters are often in each of the image-frame acquired: they could be associated with a single photon that interacts with more than one pixel or with two (or more) photons that hit neighboring pixels. On this purpose, a proper algorithm has been elaborated for recognizing and poperly reprocessing the X clusters. This procedure is called ***Gr**ouping **p**rocess* (**Gr-p**).

In order to be sure about the direct proportionality ADU vs. single-photon energy, we need to assign the charge of a given cluster of pixels to a single photon-detection event. Thus, overlapped clusters are considered as spurious events and discarded.
On this purpose, we introduced a parameter - called *S parameter* - that represents the maximum cluster *size* (defined as the number of neighbours pixels in a cluster) that can be considered as single-photon events. Consequently, clusters having size larger than S are filtered out. Moreover, noise contribution has been removed setting a threshold, by introducing the parameters:

- $\boldsymbol{L} \rightarrow$ count **L**imit, i.e. a threshold to select only those pixels above the noise level;
- $\boldsymbol{S} \rightarrow$ cluster **S**ize, i.e. the maximum number of pixels in a not-overlapped cluster;

In more detail, the algorithm works in the following way:

STEP-1: considering a given image-frame J, "*turning off*" all pixels having ADU $< L$, putting to zero all their values, later, pixel by pixel scan for each of the image-frames is done and when an illuminated pixel of coordinates $(X, Y)_J$ is identified, in a generic frame J, its neighbouring pixels are checked. If no charge is present into the surrounding pixels, the event is considered to be generated by a single photon and it is associated with a 3-coordinates point $(X, Y, E)_J$. The coordinate E is the energy associated with the photon (and it is determined by means of the energy response function of the detector, see section 4.1.2).

STEP-2: when a group of neighbouring pixels (forming a *cluster*) is identified during the scan of an image-frame, the algorithm processes this multipixel event in order to reconstruct its nature (i.e., single or multiple-event):

- (a) in the group associated with a single photon-event (typically characterized by the presence of a pixel with a clear maximum

of intensity) the code integrates the total charge **(STEP-3)**, thus giving the energy of the photon; the hitting coordinate $(X, Y)_J$ is then fixed as the one of the pixel of the maximal intensity;

- (b) groups associated with multiple-hit events (typically characterized by the presence of different relative maxima in a large size of the group of pixels) are filtered out. The algorithm assigns these events to overlapping photons, labelling them as spurious events (charges of all those pixels are set to zero).

STEP-3: the third step integrates the charge of all pixels composing a given non-spurious cluster (i.e. the one of STEP-2 (a)).

The algorithm sequentially analyzes the pixels in the positions (X_i,Y_i), with the above procedure that is repeated pixel by pixel in all the frames. Let us consider, for example, a ROI (Region of Interest) of 20X30 pixels of a given image-frame. In figure 4.1 it is possible to observe how Gr-p processes the images: we considered *S=5* and *L=10* as input parameters.

(a) Fig.4.1.a) relies to STEP-1 (pixels having charge $< L = 0$). In this step, the algorithm evaluates clusters size (in red squared the clusters having size larger than S, in green squared the other ones). Red-squared clusters typically show two or more local maxima.

(b) The STEP-2 filters out $> S$ clusters (ADU values are shown in fig. 4.1.b)).

(c) Finally, the STEP-3 integrates the charge of green-clusters, thus obtaining the image shown in fig. 4.1.c).

The corresponding images considering a larger ROI of 200X200 pixels are shown in fig.4.2.
After that the Gr-p has been performed for all the image-frames composing a measurement, it is assigned a variable N to each coordinate (X,Y) of the CCD matrix; N is the number of photons with energy E in the position (X, Y). N is incremented by a unit during the scanning of all the frames when a photon of energy E is detected in the same position (X, Y) in another frame K. At the end of the scanning of all the image-frames a

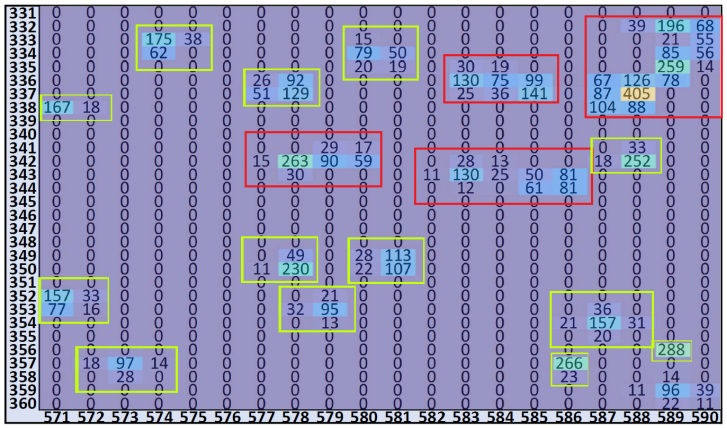

a)

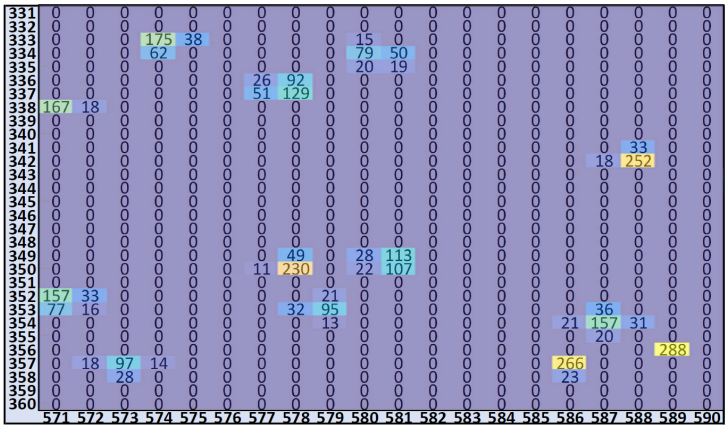

b)

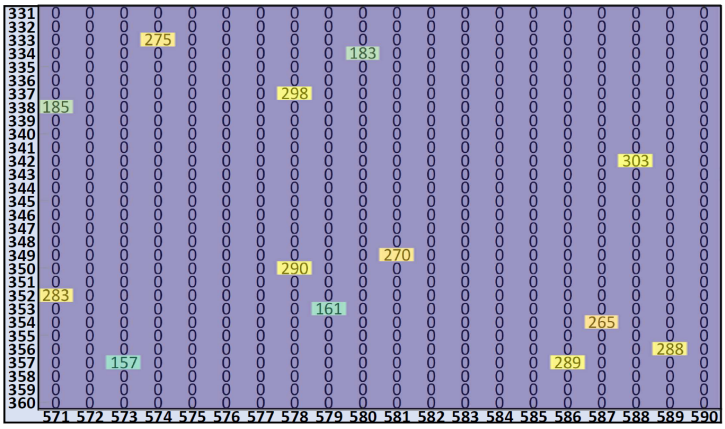

c)

Figure 4.1: ROI of 20X30 pixels analyzed implementing the three different steps (described in the text) of the Gr-p: a) after the STEP-1; b) after the STEP-2; c) after the STEP-3.

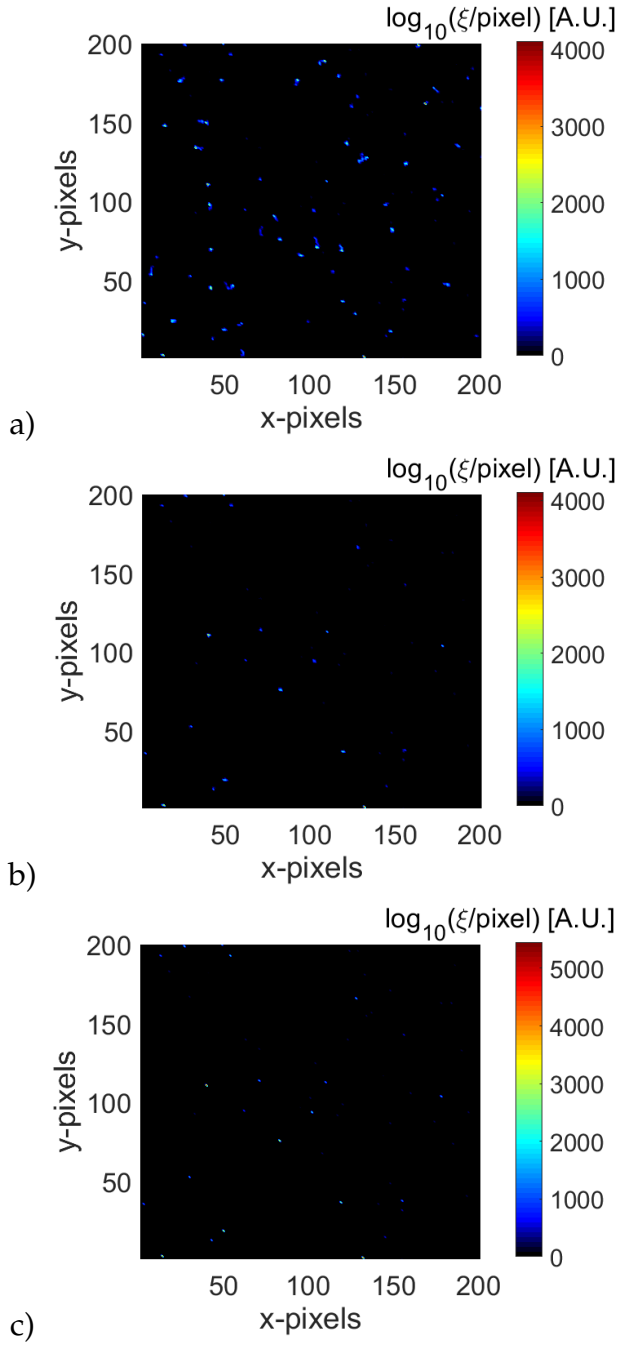

Figure 4.2: ROI of 200X200 pixels analyzed implementing the three different steps of the Gr-p: a) after the STEP-1; b) after the STEP-2; c) after the STEP-3.

set of points with coordinates (X, Y, E, N_{tot}) is obtained. The plot of the total counts N_{tot} versus the energy E provides the full X-ray spectrum. The impact of the Gr-p data processing is shown in figure 4.3. The figure shows the full field X-ray spectrum collected from a plasma obtained at 200 Watt of RF power and 13.9 GHz of RF frequency.

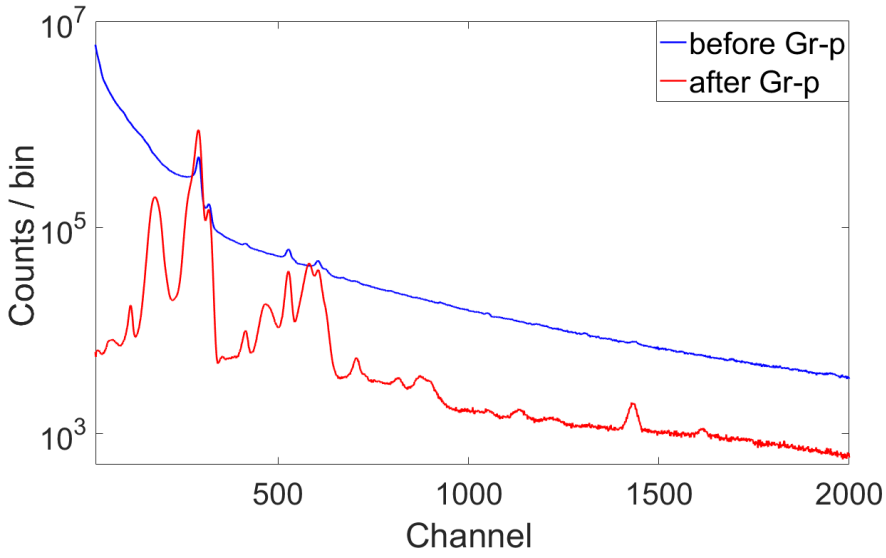

Figure 4.3: Full field X-ray spectrum (experimental configuration: RF power of 200 *Watt*, frequency 13.9 *GHz*). In blue, the spectrum evaluated before implementing the Gr-p, where it is not possible to distinguish any fluorescence peak. In red, the spectrum evaluated after implement the Gr-p, where all characteristic fluorescence peaks become well distinguished (L=10 and S=5 were used as processing parameters).

In the figure, the raw overall spectrum (over the entire CCD chip) is compared with the Gr-p post-processed one. In the raw spectrum it is not possible to distinguish any of the fluorescence characteristic peaks due to the main elements composing the plasma chamber walls (Aluminium, Titanium, Tantalum) and the plasma itself (Argon). This comparison demonstrates that raw data are almost useless due to the really poor energy resolution, because the image is not in photon counted mode. After the application of the grouping algorithm all characteristic fluorescence peaks become well distinguishable in the red, post-processed spectrum.

4.1.2 Energy calibration and counting normalization

In order to perform the energy calibration, four characteristic peaks corresponding to the Ti_{K_α}, Ti_{K_β}, Ta_{L_α} and Ta_{L_γ} fluorescence peaks have been considered. The energy and channel values of each peak have been plotted, with the linear fit, in fig. 4.4, where the linear correlation coefficient results *R=1*. The values are summarized in the table 4.1.2.

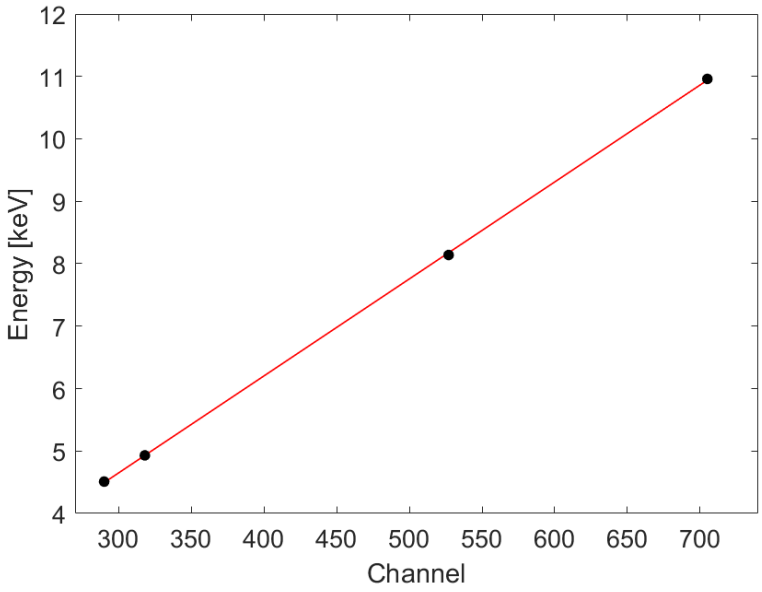

Figure 4.4: Linear fit (red line) with the four experimental data points (black dots) used to perform the energy-channel calibration.

	$\mathbf{Ti_{K_a}}$	$\mathbf{Ti_{K_b}}$	$\mathbf{Ta_{L_a}}$	$\mathbf{Ta_{L_g}}$
Channel	290	318	527	705
Energy	4.51	4.93	8.14	10.96

Table 4.1: Energy and channel values of the four characteristic fluorescence peaks chosen to perform the energy calibration.

The spectra, expressed in logarithmic scale, before and after the calibration have been shown, respectively, in fig.4.5.a) and in fig.4.5.b).

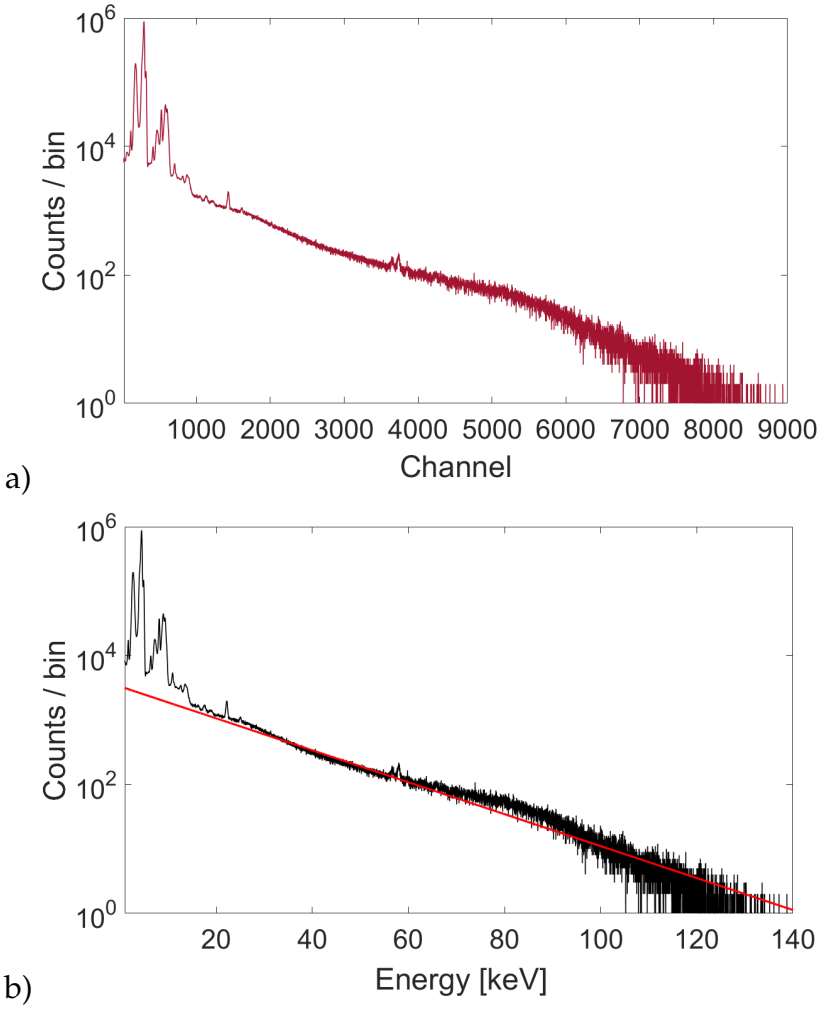

Figure 4.5: Typical X-ray spectrum expressed in logarithmic scale. a) Before energy calibration; b) After energy calibration. The red line shown in b) is the exponential fit performed in the 30 - 100 keV range.

A zoom of the calibrated spectrum in the energy range 1-15 keV, with the labels of all characteristics peaks, is shown in fig.4.6.
It is possible to distinguish the characteristic fluorescence peaks of the materials composing the plasma chamber (the K_α and K_β of Titanium, the L_α, L_β, L_γ and M_α of Tantalum) and of the plasma (K_α and K_β of Argon). Moreover, the *dimer peaks* and the *escape peaks* (generating from the

Si CCD detector) are visible in the spectrum, too. Typically, in energy dispersive detectors, the incoming X-ray photon having energy higher than $Si_{K\alpha} = 1.74\ keV$ may generate Si fluorescence. This generated photon can be absorbed by the Si matrix itself or there is a probability that the generated $Si_{K\alpha}$ X-rays escape from the detector volume and do not contribute to the charge collected for the original photon that is detected. The resulting energy detected for the original photon is reduced by $\sim$ 1.74 keV (the energy of $Si_{K\alpha}$ X-ray), showing a new peak. Dimer and escape peaks deteriorate the quantitative and qualitative spectroscopic analysis: in the next sections, methods to minimize these contributes will be also discussed.

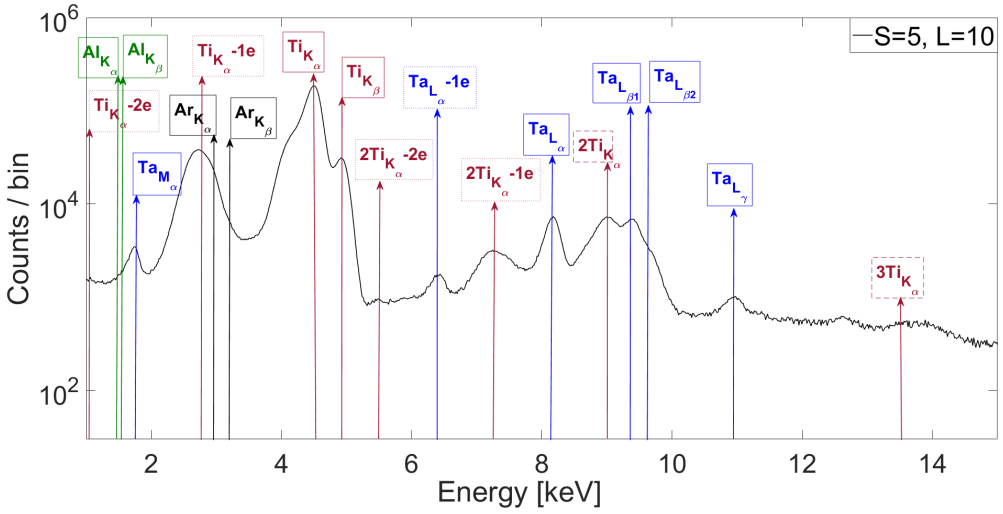

Figure 4.6: Typical calibrated X-ray spectrum with the labels of each characteristic peak.

From the spectrum of figure 4.6, the estimated energy resolution is 0.326 keV at 8.1 keV [8] (corresponding to the Ta_{L_α} line). A zoom of the spectrum in the range 6 - 10 keV showing the Gaussian fit to estimate the energy resolution FWHM (full width at half maximum) is shown in figure 4.7.

Moreover, aiming to remove the Bremsstrahlung continuum radiation, generated by the deceleration of the energetic electrons colliding with heavy ions in the plasma and with the atoms of the plasma chamber walls, an exponential fit has been performed. The fit in the range 30 -

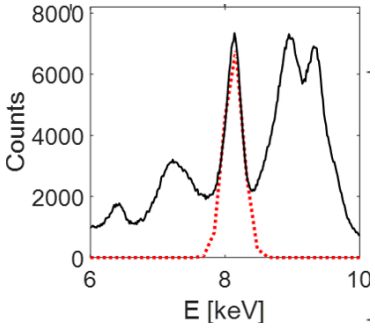

Figure 4.7: Zoom of a typical X-ray plasma spectrum in the range 6-10keV, with the Gaussian fit (in red) to estimate the energy resolution, as FWHM.

100 keV (it corresponds to the red line in fig.4.5.b)) was done to remove Bremsstrahlung contribution to the overall spectrum coming from the hot electron population. The spectrum obtained removing the Bremsstrahlung contribution is shown in fig.4.8.

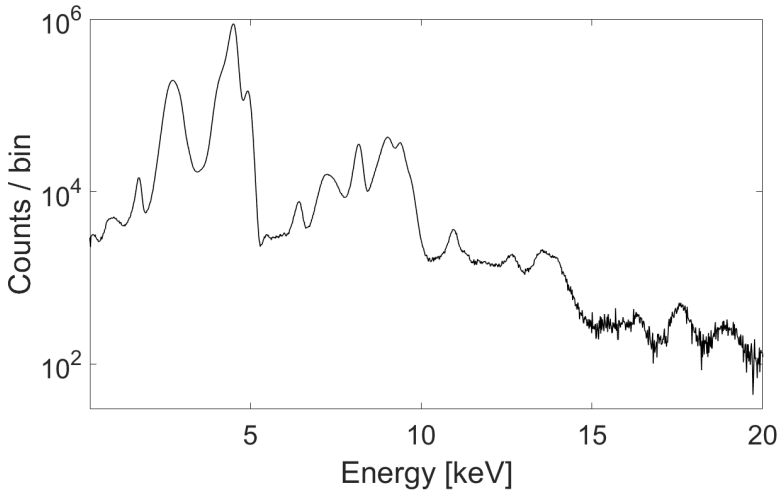

Figure 4.8: Energy calibrated spectrum where the Bremsstrahlung contribution coming from the hot electron population has been removed.

Finally, spectra need to be renormalized including both the Quantum Efficiency (Q.E.) of the CCD camera (absorption efficiency in 15 μm of Si) and the transmission efficiency through the Titanium windows (9.5 μm

of Ti thickness): this has been done by means the NIST database [84]. The total detection efficiency, called *F(E)*, has been obtained multiplying the Quantum and the Transmission efficiencies. The three curves are shown in fig.4.9.a). All event counts have been normalized, dividing them for *F(E)*. An example of event count normalized spectrum is shown in fig.4.9.b).

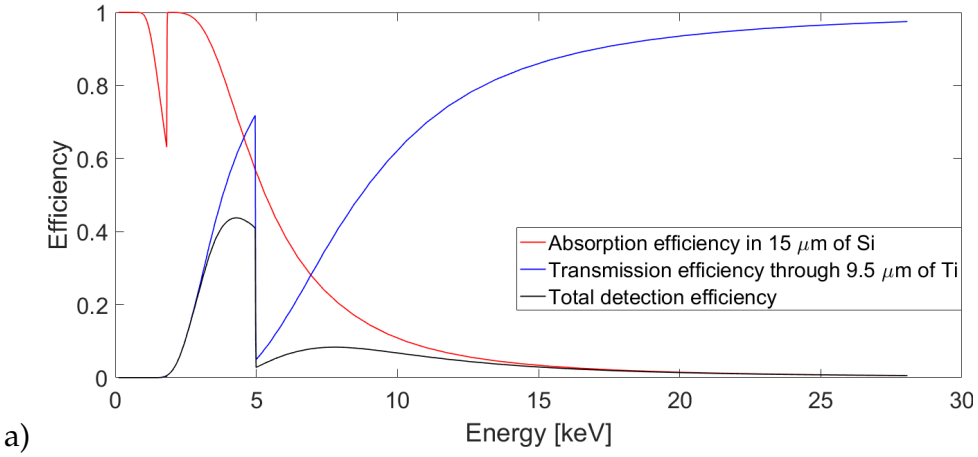

a)

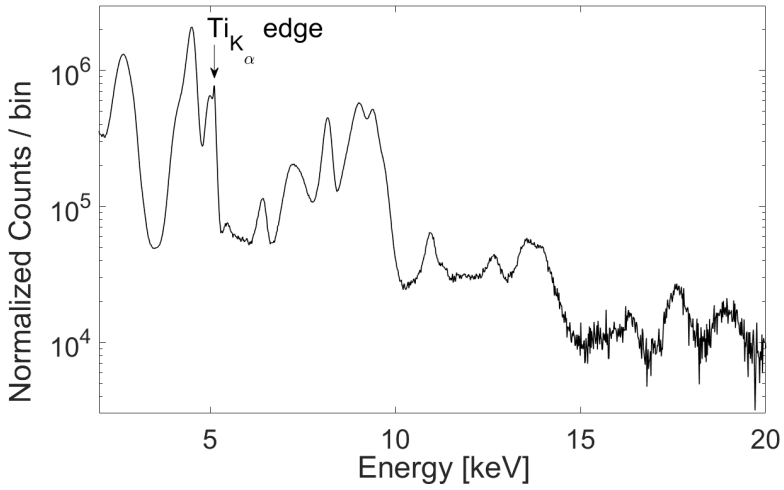

b)

Figure 4.9: a) Q.E. of the CCD camera (red), transmission efficiency through the Titanium windows (blue), total detection efficiency (black), curves. b) Typical *event count normalized* and *energy calibrated* spectrum.

Optimization of the algorithm

Spectrum shape and intensity change as a function of *L* and *S* values have been then optimized trying to reach a trade-off between spectral resolution and high enough statistics.
In the figure 4.10 five different spectra evaluated setting different *S* values (from *1* up to *5*), fixing *L=10*, are shown (in the energy range 1-15 keV). The spectra in the whole energy range are instead shown in figure 4.11.

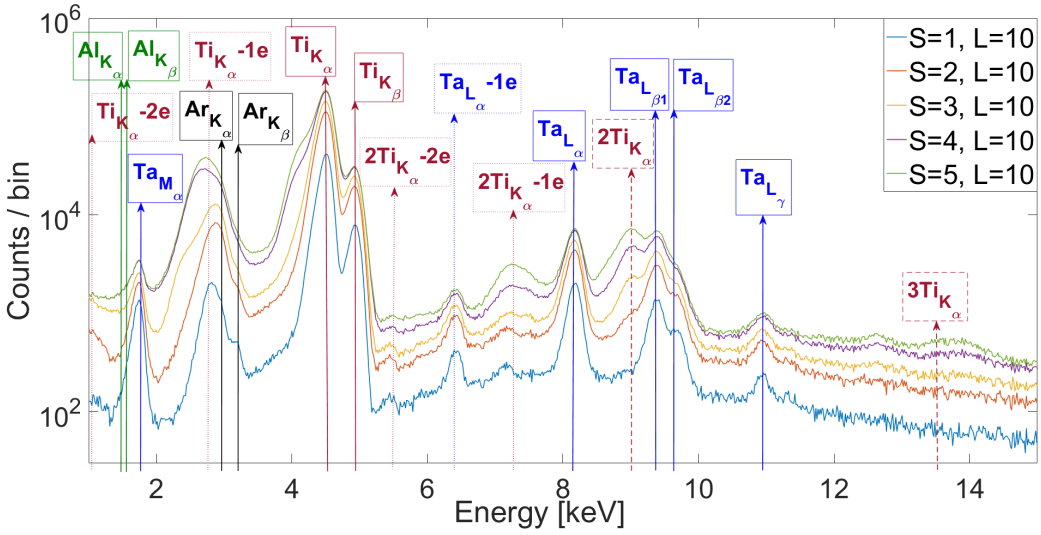

Figure 4.10: X-ray spectra evaluated setting five different *S* values (from *1* up to *5*) and fixing *L=10* in the energy range 1-15 keV.

Using *S=1* (the blue spectrum shown in fig. 4.10 and 4.11, i.e. events where only one photon impacts in each pixel, releasing its total energy in a single pixel) the spectrum shows the higher resolution but the lowest intensity; in this case, in fact, the SPhC condition is always verified but, on the other hand, several good events (i.e. eben small clusters due to single photons) anyway filtered out. When increasing the *S* value, the resolution decreases but the intensity increases.

Moreover, comparing the slope of the spectra in the higher energy domain ($\sim$ 30 - 80 keV) the maximum energy (consequently, the electron temperature that is inversely proportional to the spectrum slope) decreases as a function of *S*, as shown in the fig.4.11.

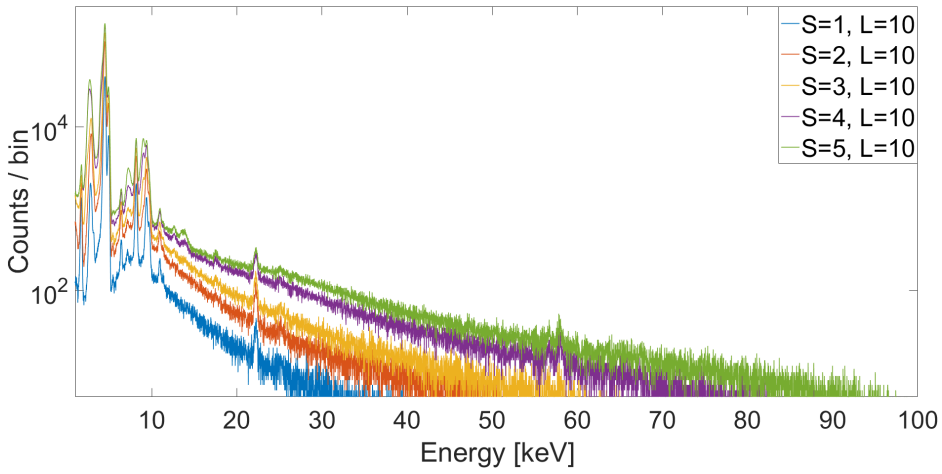

Figure 4.11: X-ray spectra evaluated setting five S values (*1-5*) and fixing *L=10*.

This fact comes from the definition of the S parameter: i.e., the higher is the energy of the impacting photon, the higher are - on average - the cluster sizes; therefore, the probability to filter out photons at higher energy increases at lower S values.
Finally, since dimer and escape peaks can deteriorate the quantitative and qualitative spectroscopic analysis, the implemented algorithm is able to:

a) optimize the input S and L parameters for improving as much as possible the $\frac{I_{MP}}{I_{EP}}$ and $\frac{I_{MP}}{I_{DP}}$ ratios;

b) post processing filter out the residual escape peak contribution (for more details, see the section 4.1.3).

where I_{MP}, I_{EP} and I_{DP} are, respectively, the main peak intensity, the escape peak intensity and the dimer peak intensity.
To get the optimal parameters, the grouping code has been run for twenty different combinations of L and S values: we set three L (5, 10, 15) values, for L=5 and L=15 the code run for five S values (1-5), whilst for the case L=10 ten S parameters (from 1 to 10) have been investigated. The plots of figure 4.12 report the whole set of obtained spectra.
Optimization was searched by a trade-off between overall statistics and minimization of spurious peaks (escape, dimer, triplet, etc.).

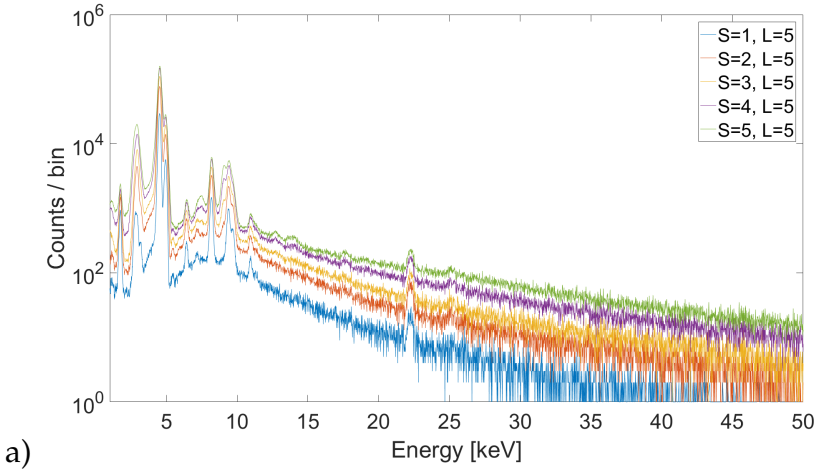

a)

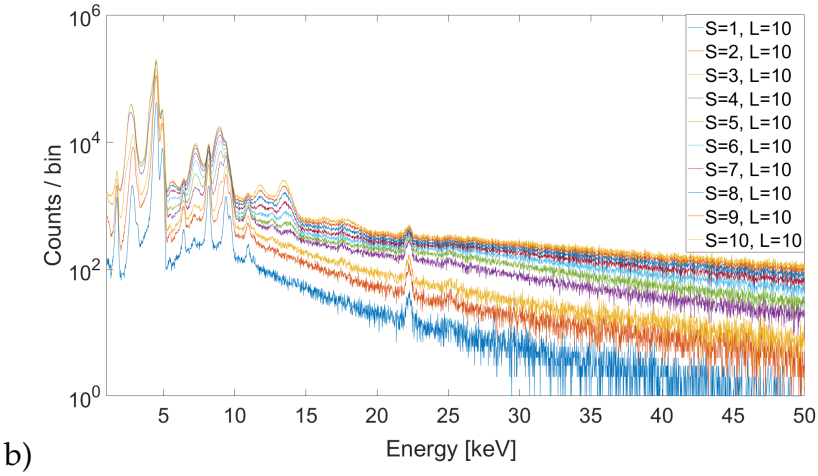

b)

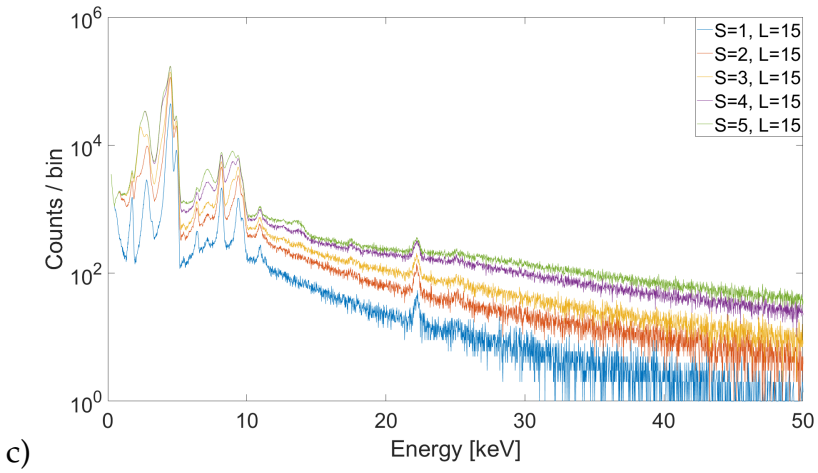

c)

Figure 4.12: X-ray spectra evaluated setting different S values and fixing L. a) S=1-5, L=5; b) S=1-10, L=10; c) S=1-5, L=15.

For each configuration the following three values have been estimated:

a) the $\frac{I_{MP}}{I_{EP}}$ ratio for Ta_{L_α};

b) the $\frac{I_{MP}}{I_{DP}}$ ratio for Ti_{K_α};

c) the total I_{MP} for Ti_{K_α};

From the analysis results that:

a) **the escape peak intensity** respect to the main peak **is almost independent of L and S**;

b) **the dimer peak intensity is dramatically increasing** respect to the main peak **by increasing the size of the clusters**;

c) **the intensity of the spectral components** (e.g. $I_{Ti_{K\alpha}}$) **is increasing with the cluster size**.

Ratios

I[Ta-La]/I[Ta-La-1e (Escape)]

L\S	1	2	3	4	5
5	4,736334	4,580599	4,533404	4,542265	4,396688
10	4,858173	4,623958	4,589154	4,350866	4,140361
15	4,746102	4,503441	4,371654	3,949664	3,673314

I[Ti-Ka]/I[2Ti-Ka (Dimer)]

L\S	1	2	3	4	5
5	167,7273	135,0175	82,93413	51,69521	35,09235
10	154,0959	113,2457	62,82837	37,55751	25,38293
15	135,076	90,45662	48,18942	29,99821	21,13982

I[Ti-Ka]

L\S	1	2	3	4	5
5	29520	77230	110800	147900	159600
10	41760	112000	143500	179600	185600
15	44440	114699	138400	167900	171000

Normalized To the maximum

I[Ta-La]/I[Ta-La-1e (Escape)]

L\S	1	2	3	4	5
5	0,974921	0,942865	0,93315	0,934974	0,905009
10	1	0,95179	0,944625	0,895577	0,852246
15	0,976932	0,926983	0,899855	0,812994	0,75611

I[Ti-Ka]/I[2Ti-Ka (Dimer)]

L\S	1	2	3	4	5
5	1	0,804982	0,494458	0,30821	0,209223
10	0,918729	0,675178	0,374586	0,22392	0,151335
15	0,805331	0,539308	0,287308	0,178851	0,126037

I[Ti-Ka]

L\S	1	2	3	4	5
5	0,159052	0,41611	0,596983	0,796875	0,859914
10	0,225	0,603448	0,773168	0,967672	1
15	0,23944	0,61799	0,74569	0,904634	0,921336

Product of the three matrix

L\S	1	2	3	4	5
5	0,155063	0,315823	0,27545	0,229634	0,162823
10	0,206714	0,387792	0,273581	0,194055	0,128974
15	0,18838	0,308951	0,192787	0,131538	0,087801

Optimum parameters:
L=10 , S=2

Figure 4.13: From top to bottom: I_{MP}/I_{EP} ratio for the Ta L_α peak; I_{MP}/I_{DP} ratio for the Ti K_α peak; total I_{MP} for the Ti K_α peak; product of the three contribution, vs. 15 set of L and S parameters.

The results are shown in fig.4.13. By adding the same relative weight of the three optimization procedures (low escape, low dimer, high intensity), the best selection results to be *L=10* and *S=2*. Whilst, for all the experimental measurements where statistic is low, the *L=10* and *S=5* is the best choice (corresponding to the maximum intensity) in order to be able to perform quantitative spectroscopic analysis and, as described before, avoid to filter out the higher energy population. In summary, the whole process described in the previous sections (i.e. from raw data to calibrated and optimized spectra) is summarized in the sketch 4.14.

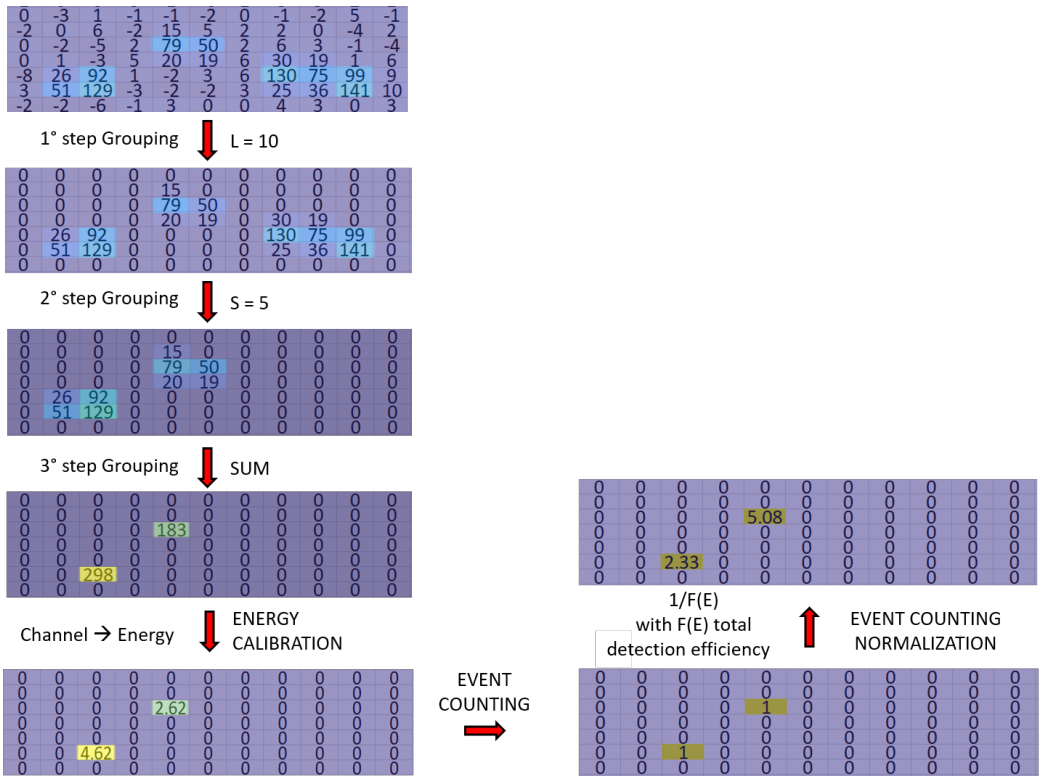

Figure 4.14: Summary of the implemented procedure of post-process image analysis, considering a sub-matrix of [7X11] pixels. *Left, from top to bottom* - Raw image; post-processed image after the 1° GR-p step; post-processed image after the 2° GR-p step; post-processed image after the 3° GR-p step; energy calibrated image. *Right, from bottom to top* - Event counted image; event counted and normalized image.

4.1.3 Energy filtered images and space-resolved spectroscopy

When applying the procedure described in the previous sections and summarized in the fig. 4.14 it is possible to evaluate the single photon counted image and the corresponding spectrum. An example of an image is shown in figure 4.15. The image is the result of the analysis of 4200 image-frames acquired with an exposure time of 500 milliseconds, at 1 MHz of readout rate and full-frame (1024x1024 pixels) acquisition mode. The spectrum of the full size image is the one shown in the figure 4.10 (for *S=5* and *L=10*).

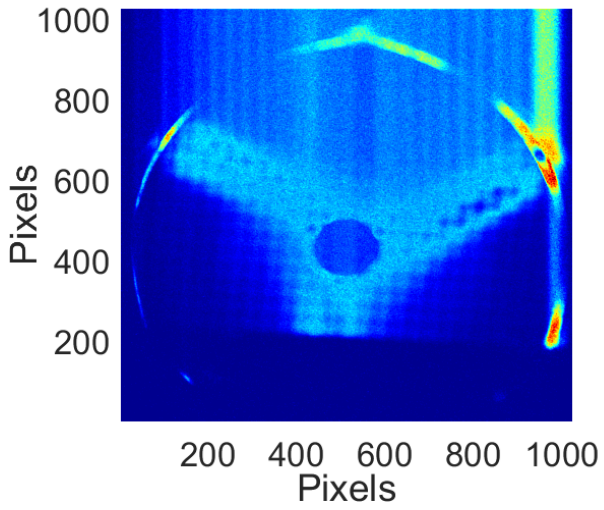

Figure 4.15: Single photon counted image collected by the analysis of 4200 image-frames acquired with an exposure time of 500 milliseconds, each using the full-frame (1024x1024 pixels) acquisition mode.

Two important complementary analysis can be simultaneously performed: the ***Energy-filtered Imaging*** *(EfI)* and the ***Space-resolved Spectroscopy*** *(SrS)*.

- Since the spectrum contains the spatial information of the impinging photons, the selection of a energy range below the fluorescence peaks in the spectrum allows the imaging of the elemental distribution, and it is possible to distinguish the emission (and the correspondent image) coming from each material. The ***Energy-filtered***

Imaging consists in selecting only the pixels of the frames which are loaded by the photons having the given energy selected in the spectrum.

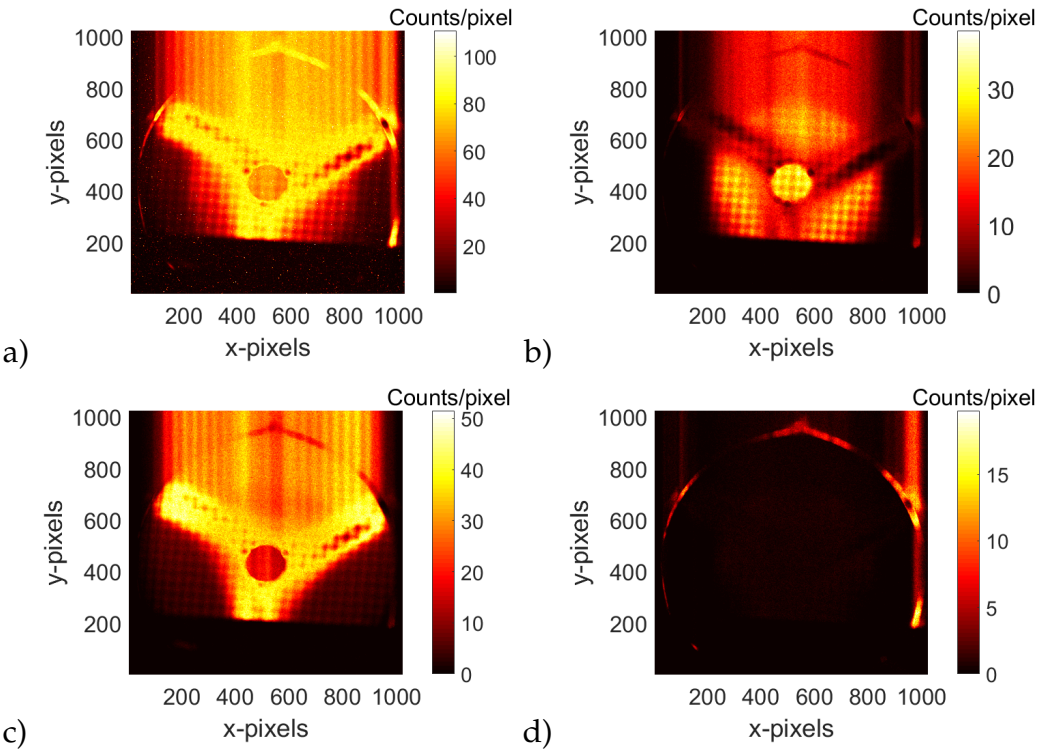

Figure 4.16: 2D energy filtered images showing fluorescence photons coming from the Argon plasma and signals coming from the metallic layers covering plasma chamber walls. a) Unfiltered image. b) Ar-energy filtered image. c) Ti-energy filtered image. d) Ta-energy filtered image.

It is possible, for example, to distinguish pixels of the frames which are loaded by the photons having energy corresponding to the lowest energy domain (i.e. E < 2 keV) or the higher one (i.e. E > 10 keV). It is also possible to select only the energy domain of a given fluorescence peak, e.g. the one of Argon in order to observe the spatial distribution of plasma only, or the fluorescence peak of Ti or Ta in order to study the walls radiation. Pixels corresponding

to these three intervals were selected and plotted, respectively, in figure 4.16.b), 4.16.c) and 4.16.d). Whilst the fig. 4.16.a) shows the event-counted image without any energy-filter.
As highlighted in figure 4.16, it is possible to distinguish the emission coming from Ar plasma only (selecting the fluorescence from Ar only), compared to the radial losses (Ta) or the axial losses (Ti), selecting the fluorescence from Titanium and Tantalum, respectively. The analysis allows to investigate in detail in addition to the plasma morphology change also about dynamics of losses, for example distinguishing the trend of the axial losses versus the radial ones (the details about results will be presented in chapter 5).

- A complementary analysis is the ***Space-resolved Spectroscopy***, which consists of selecting (in the whole image) a given ROI then plotting there the relative spectrum; this, consequently, enables to perform local estimation of the plasma parameters (electron density and temperature). Several ROIs (see fig.4.17) have been selected in the image to investigate the spectral composition in different regions inside the plasma chamber (the details will be discussed in the chapter 5).

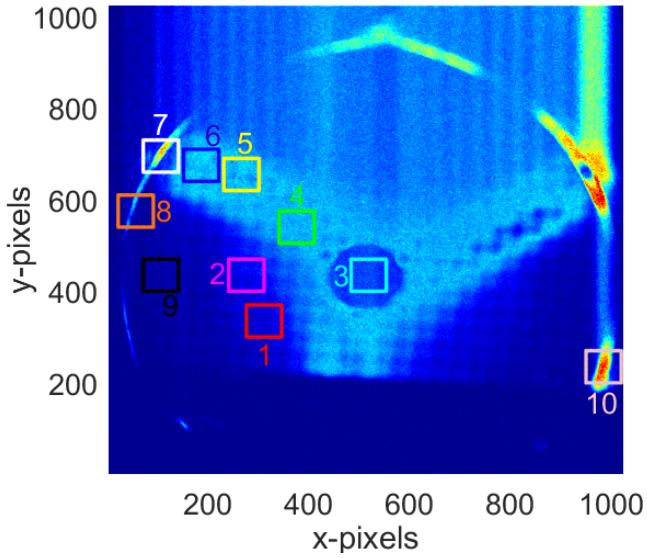

Figure 4.17: Image shown in fig. 4.15 with several highlighted ROIs.

Open issues and further analytical method steps

The analyzed images and spectra still present three issues:

I) Escape peak due to Ti fluorescence overlaps with the $Ar_{K\alpha}$ fluorescence. Several papers [85], [86], [87] demonstrated that the escape peak generation efficiency is typically of the order of 3% of the main $K\alpha$ peak. So, the algorithm considers an escape peak efficiency Z of the 3% of the main $Ti_{K\alpha}$ peak, and removes this contribution pixel-by-pixel both in the whole matrix and in the spectrum;

II) during the Gr-p some information are lost because 500 *msec* of exposure time is too high for the ROIs having very intense emission, i.e. the *magnetic branches* and the *magnetic pole* regions, which consequently do not result to be in photon counting (on the other hand, if we would reduce the exposure time, the statistic in the other ROIs with lower intensity collapsed). In order to overcome these issues, High Dynamical Range (HDR) analysis has been developed (see section 4.1.4 for the detailed description of the 4^{th} step of algorithm: **HDR-img** and **HDR-spect**);

III) since the readout time is of the order of 1 *msec*, in the images and spectra there is an *artefact* due to the readout noise. In fact, during the low exposure time (higher than the CCD readout time, but not too high) the photons continuously impacted the CCD also while the *charges were transferring in the readout register*. This produced kind of *strips* in the image, as it is possible to observe in the figg.4.16 and 4.17. A proper algorithm to filter out this spurious contribution has been developed (see section 4.1.5 for the detailed description of the 5^{th} (last) step of algorithm: the **RON-r**).

4.1.4 High Dynamical Range (HDR) Imaging and Spectroscopy

When intensities of an image vary of orders of magnitude from one ROI to another, it is very challenging to determine the correct exposure time (some ROIs often saturate, whilst others can be underexposed).Let us consider, as an example, the images shown in fig. 4.18: in this case four different exposure times have been used. Using the lowest exposure time, i.e. case a), the sky is completely underexposed; on the other side, when setting the higher exposure time, i.e. case d), some other ROIs, like the ones with the monument, saturate.

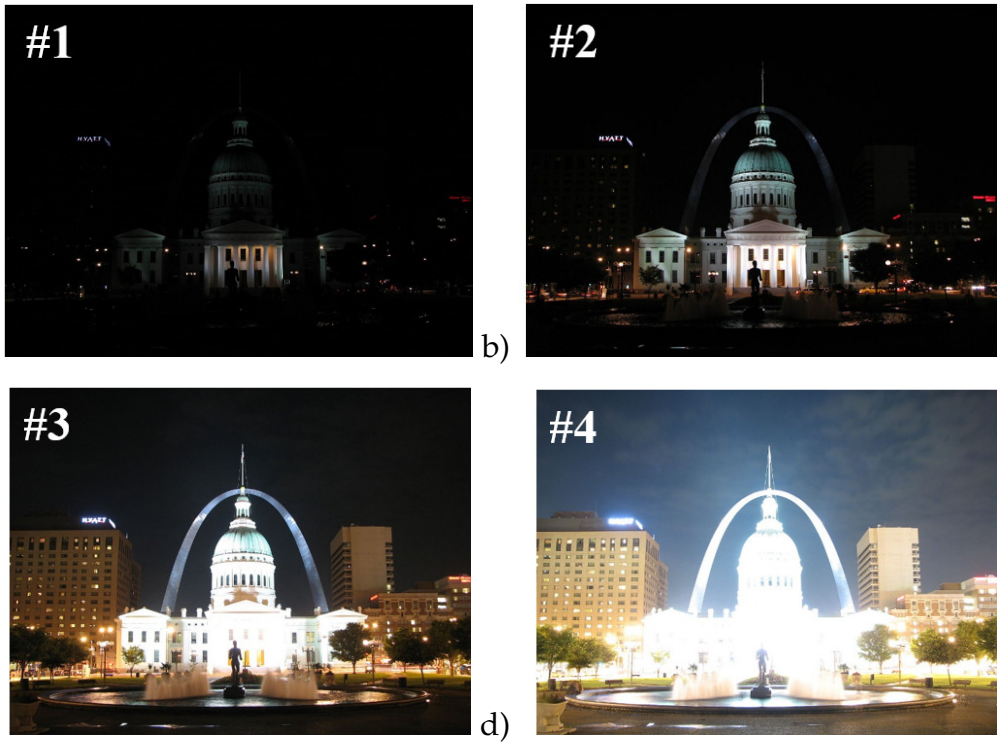

Figure 4.18: Example of an image acquired with four different exposure times.

The solution consists in the so called *High Dynamical Range (HDR)* analysis - commonly used in visible light imaging - which consists in acquiring the same image setting two or more different exposure times and

then producing, by means of advanced analytical methods, a weighted convoluted image, called HDR image (see fig.4.19). The HDR image shows high quality and resolution in each of its ROI without losing information.

Figure 4.19: HDR weighted convolution image analyzed starting from the four images shown in fig.4.18.

The images acquired by means of the X-ray pin-hole CCD system presents same characteristics. Considering, for example, the spectrally integrated image acquired with a very long exposure time of 50 seconds (see figure 4.20) it is possible to highlight that the radiation coming from plasma ROIs due to Argon fluorescence has intensities orders of magnitude lower than the one due to plasma magnetic branches (coming from the energetic electrons impacting in the extraction endplate) or the one of hot spots at the magnetic pole sites (electrons impacting in the lateral plasma chamber walls).
Of course, the same happens operating in SPhC mode.
In order to assure that the SPhC mode is verified in each ROI it is necessary to acquire image-frames setting different exposure times and number

of frames.
Consequently, for investigating the lower intensity ROIs an exposure time of 0,5 seconds has been used and a total of 4200 frames have been acquired, these images have been called I_{Plasma}.
Whilst, for the higher intensity ROIs, an exposure time of 0,05 seconds has been set and a total of 1000 frames have been acquired, these ones are called I_{Pole}. The number of image-frames and the exposure time are reported in the table 4.2.

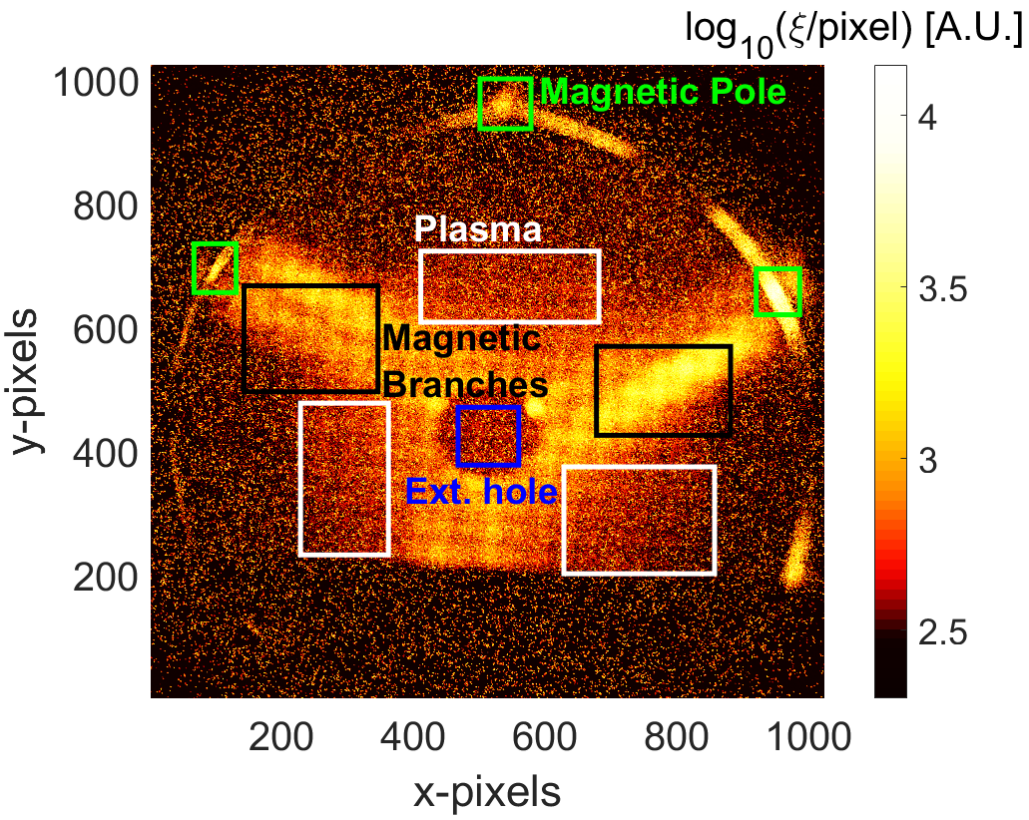

Figure 4.20: Pseudo-colour representation of X-ray flux, illustrating plasma branches (radiation coming from the extraction endplate), hot spots at the magnetic pole sites on the lateral chamber walls, the extraction hole and the plasma emission.

Table 4.2: Two acquisition modes, I_{Plasma} and I_{Pole}, with different exposure times and number of frames.

Acquisition	**Exposure Time [s]**	**N° frames**
I_{Plasma}	0,5	4200
I_{Pole}	0,05	1000

As an example, two event-counted single full-frames (before applying the Gr-p) are shown in fig.4.21.a) and b) for I_{Plasma} and I_{Pole}, respectively. It is possible to highlight the difference from I_{Plasma} and I_{Pole} considering two ROIs:

- the *plasma* ROI (red squared), shown in the images 4.21.c) and d) for I_{Plasma} and I_{Pole}, respectively. In this ROI the I_{Plasma} frame is not photon-counted and the clusters are overlapped, whilst the I_{Pole} frame is photon-counted and the loaded clusters are well isolated.
- the *magnetic pole* ROI (cyan squared), shown in the images 4.21.e) and f) for I_{Plasma} and I_{Pole}, respectively. In this ROI both the I_{Plasma} and the I_{Pole} frame are photo-counted, but only I_{Plasma} frame shows high enough statistic, whilst in the I_{Pole} frame it is too low.

After applying the Gr-p and summing over the whole event-counted frames, the images shown in figures 4.22.a) and b), for I_{Plasma} and I_{Pole} acquisition mode respectively, have been obtained (the frames have been also Ar-fluorescence energy-filtered). As expected, the I_{Plasma} image shows lack of information in the magnetic branches and in the magnetic pole ROIs.

The correspondent spectra (called *basic spectra* (BS)) and the basic spectra normalized by the exposure time and frames numbers are shown in fig.4.22.c) and in fig.4.22.d). The I_{Plasma} spectrum shows some missing (and under-represented) information too. It is in fact possible to note the total rate (CPS, counts per second) is about one order of magnitude lower than the total rate (CPS) of I_{Pole}. In this condition one necessitates to combine two images and spectra into a single image and spectrum, respectively, by means of the *High Dynamical Range* procedure.

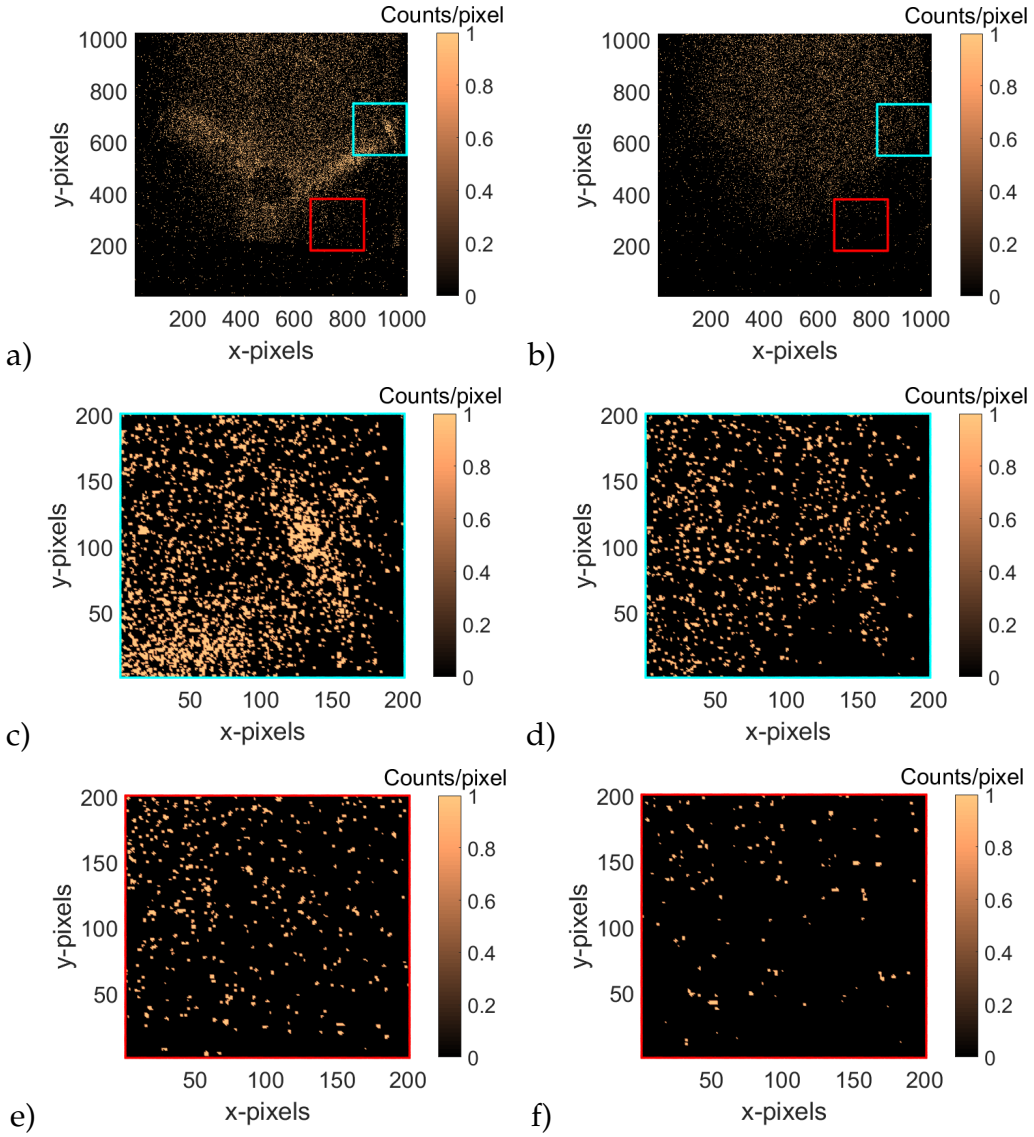

Figure 4.21: On the left, the I_{Plasma} frame. On the right, the I_{Pole} frame. a), b) - Event-counted single full-frame before applying the Gr-p. c), d) - image in the *plasma* ROI. e), f) - image in the *magnetic pole* ROI.

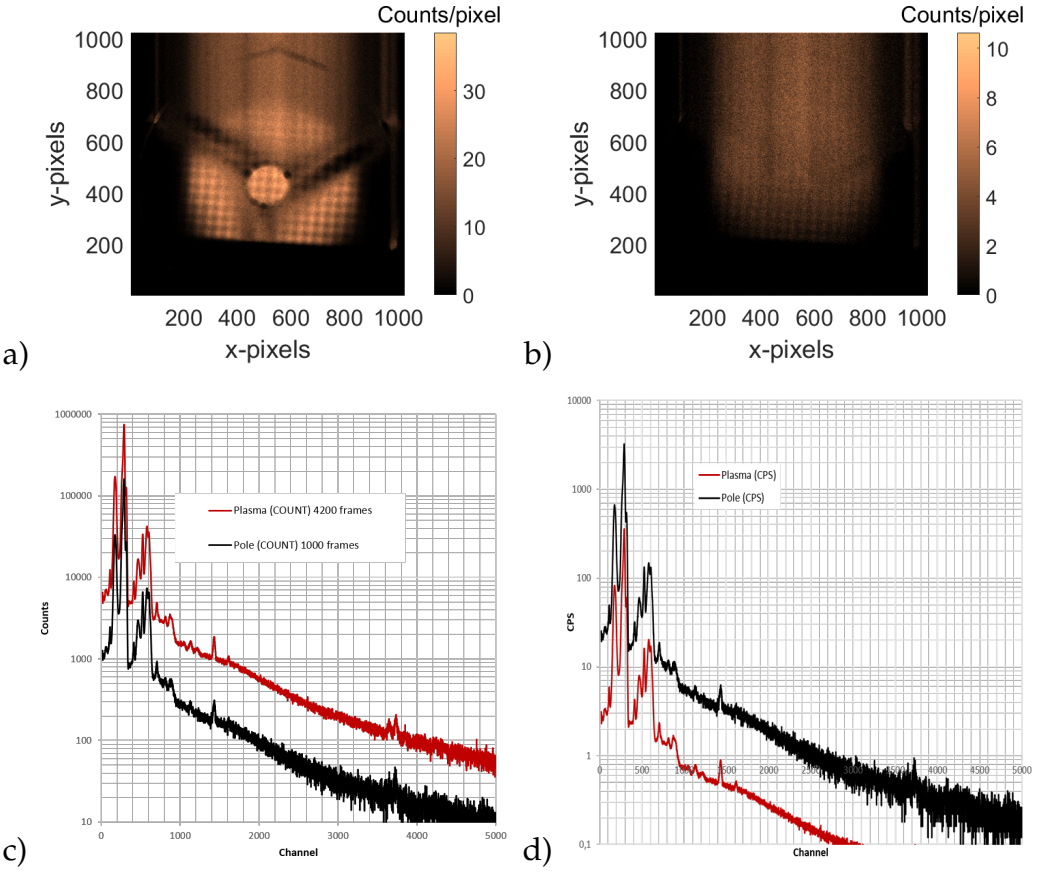

Figure 4.22: a) - Image acquired setting exposure time of 0,5 seconds and analyzing 4200 Ar-energy filtered image-frames. b) - Image acquired setting exposure time of 0,05 seconds and analyzing 1000 Ar-energy filtered image-frames. c) - Correspondent spectra to image a) and b) showing the total counts. d) - Correspondent spectra to image a) and b) expressed in counts per second (CPS).

Since the degree of the missing information is spatial-dependent, the implemented algorithm operate by exploring any pixel in each image-frame, as done for the Gr-p, but in this case the goal is to define two "*masks*" that are necessary to obtain the HDR image:

- ***HDR Mask***: this mask shows those pixels which were not photon-counted on I_{Plasma} images. It consists in a digital (0-1) array where position evaluated as 1 correspond to those pixels being part of a cluster larger than the *S parameter*, for each image-frame. The sum of those images, divided by the number of the frames gives the desired *HDR Mask*, where each number corresponds to the probability ρ_{pl}^{n-phc} normalized to 1 of a given pixel to be not photon-counted, as shown in the figure 4.23.a).

- ***Pole normalization Mask*** generation from I_{Pole} frames: even the I_{Pole} frames are not always photon-counted, therefore the counts are under-represented and the missing information is spatial dependent. Using the not-photon-counted matrix (NPhC) obtained from the I_{Pole} images (ρ_{pol}^{n-phc}), a normalization matrix has been obtained (shown in the figure 4.23.b)): Normalization matrix= 1/(1-NPhC/1000).

- ***HDR image*** = I_{Plasma} + I_{Pole} · HDR mask · Pole normalization mask. Of course, I_{Pole} has been normalized for exposure time and number of frames. The HDR image is shown in the figure 4.24.

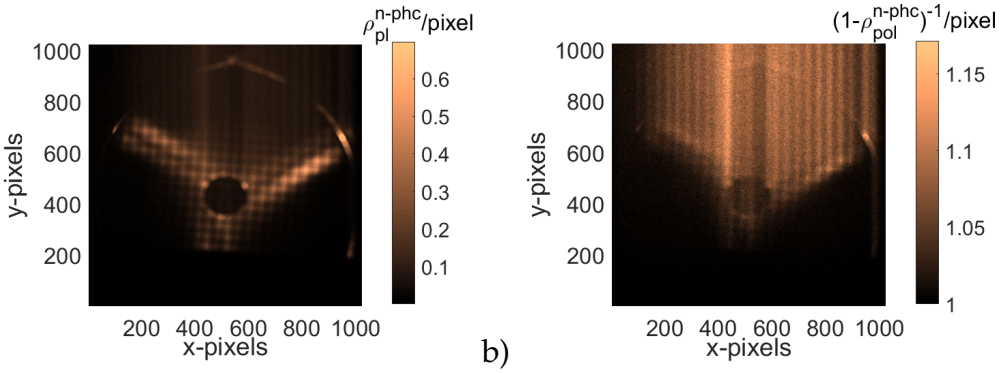

Figure 4.23: a) - Image of the HDR Mask, showing space-resolved probability to find pixels which were not photon-counted on I_{Plasma} images. b) - Image of the Pole normalization Mask, 1/(1-NPhC/1000), where NPhC is the not-photon-counted matrix obtained from the I_{Pole} images.

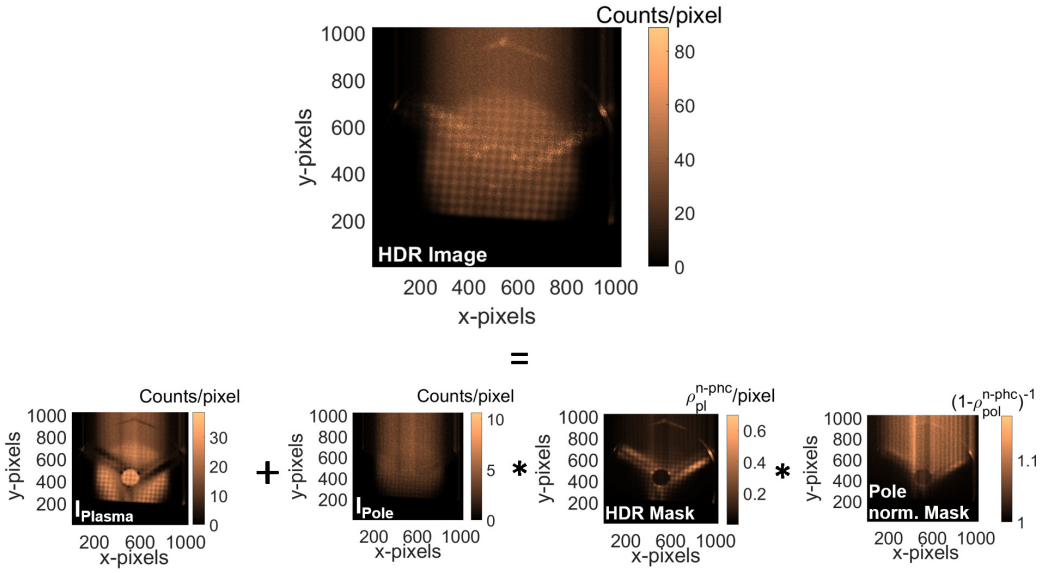

Figure 4.24: Top - HDR Image. Bottom - Procedure of multiplications and sums of matrices (I_{Plasma} + I_{Pole} * HDR mask * Pole normalization mask) to obtain the HDR Image.

Observing the fig.4.24, it is clear that the HDR image - compared to the I_{Plasma} and I_{Pole} - contains all the information, with a good statistic both in the plasma, branches and pole ROIs. Pixels clusters that in I_{Plasma} were filter out by the Gr-p, have been in fact replaced by the ones taken from the I_{Pole}, once weighted by the HDR and Pole normalization mask. Of course, the same analysis can be performed also in the other energy-filtered images, as shown in fig.4.25 for Titanium and Tantalum too.
The HDR procedure must be applied to the basic spectra too. In this case, the steps are the following:

- Make the product of the HDR and Pole normalization masks (called *WMk = Weighting Mask*). This product will give 1024·1024 weighting numbers ($WMk_{i,j}$, where i and j are the row and column of the *WMk*).

- Generate 1024 x 1024 spectra of I_{Pole} frames considering every pixels as a small (individual) ROI, in order to have spectra corresponding to every pixel position (called $SP_{i,j}$).

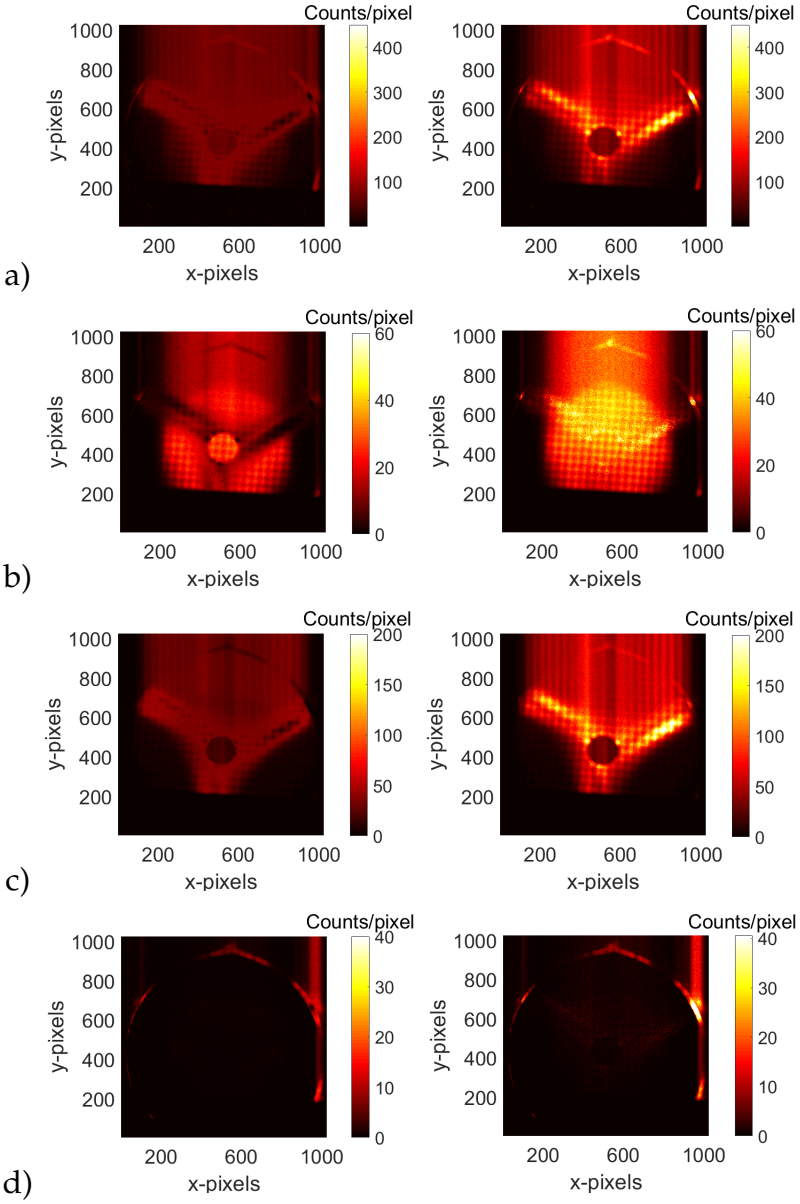

Figure 4.25: a) Event counted energy-unfiltered image. b) Ar-energy filtered image. c) Ti-energy filtered image. d) Ta-energy filtered image. On the left the I_{Plasma} image; on the right the HDR post-processed image.

- Multiply every spectra by the corresponding number from the weighting matrix: $WMk_{i,j} \cdot SP_{i,j}$ at every i, j. This will give a pixel dependently normalized "*Spectra Matrix*".
- Sum the *Spectra Matrices*, called *Pole Contribution* ***PC***. This will give only one spectrum representing the missing information from the basic spectra of I_{Plasma} (the blue spectrum shown in fig.4.26).
- Sum the BS of I_{Plasma} (in red in fig.4.26) and the PC. The obtained spectrum is the ***HDR Spectrum*** *(**HDRS**)* (in black in fig.4.26).

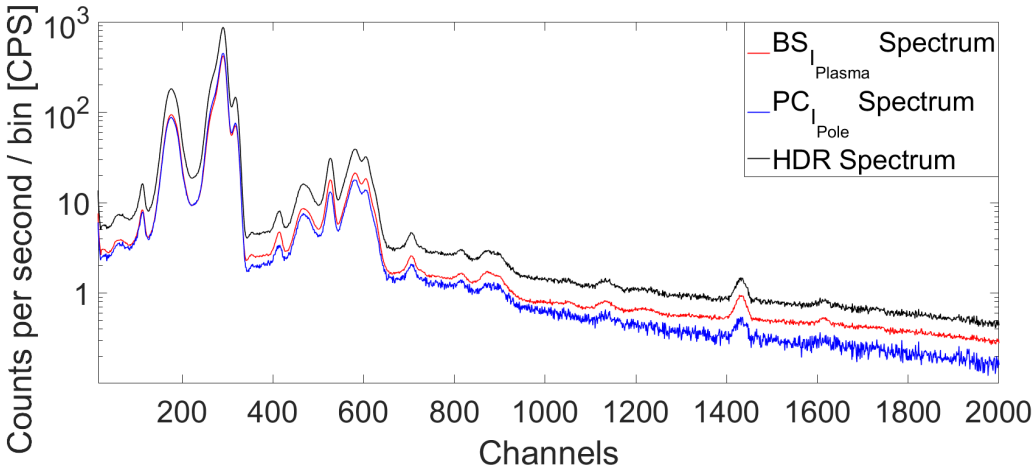

Figure 4.26: HDR Spectrum (black) obtained by summing the Basic spectrum of I_{Plasma} (red) and the Pole Contribution (blue).

The basic spectrum of I_{Plasma} and the pole contribution, normalized by the exposure time and number of frames, show a similar rate, expressed in counts per seconds. The HDR spectrum contains all information.

4.1.5 The readout noise (RON) removal algorithm

In order to complete the images analysis the last issue is to remove the *"strips"* due to the readout noise. This last step of the algorithm is described in this section. During the readout of the CCD camera the accumulated charges are transferred through the rows of the CCD from the top to the bottom, where the reading buffer is placed, see figure 4.27.

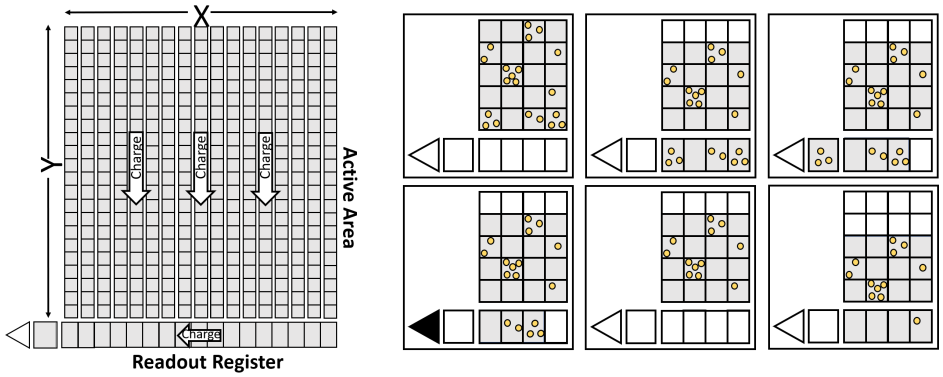

Figure 4.27: Sketch of the readout procedure: charge in the frame is shifted vertically by one row and this bottom row moves into the shift register; subsequently, charge in the row in the readout register it is moved horizontally by one pixel, passing to the analog-to-digital converter.

During this transition, the CCD is still active so it is sensitive to the impinging photons. Some photons are still detected but in a "*wrong place*", and as a consequence vertical "*strips*" in the images appear. If the read out time is comparable with the exposure time and if mechanical shutter is not used, the readout noise (RON) is remarkable and its contribution has to be removed from the images. An algorithm to eliminate this effect was written and applied.
In figure 4.28 the ADU matrix loaded by the CCD in the case of the RON is neglected is shown. Whilst, considering the RON contributions, the ADU matrix drastically changes, as it is possible to see in the fig.4.29. In the case shown in fig.4.29, it has been considered an impacting RON flux equal to half of the initial flux during the readout time of one row. This fraction (0.5, in this example) has been called β.

In more details, in the fig. 4.29, the matrix 1 shows the initial photons flux (yellow dots) impacting in the CCD. During the first row readout time an additional contribution, due to the RON flux, impacts in the CCD (red dots in the matrix 2), and it is half of the initial photons flux since we considered $\beta = 0.5$. In the matrix 3, another RON contribution (blue dots) impacts during the second row readout time. The same happens in the matrix 4 (green dots), and so on. The final ADU matrix (real case)

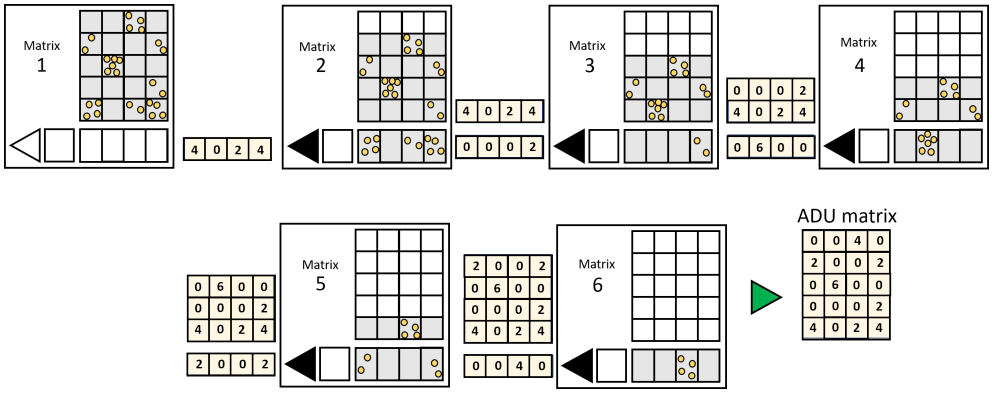

Figure 4.28: Sketch of the readout procedure, neglecting the RON contribution. The numbers in the matrix show the total loaded charge.

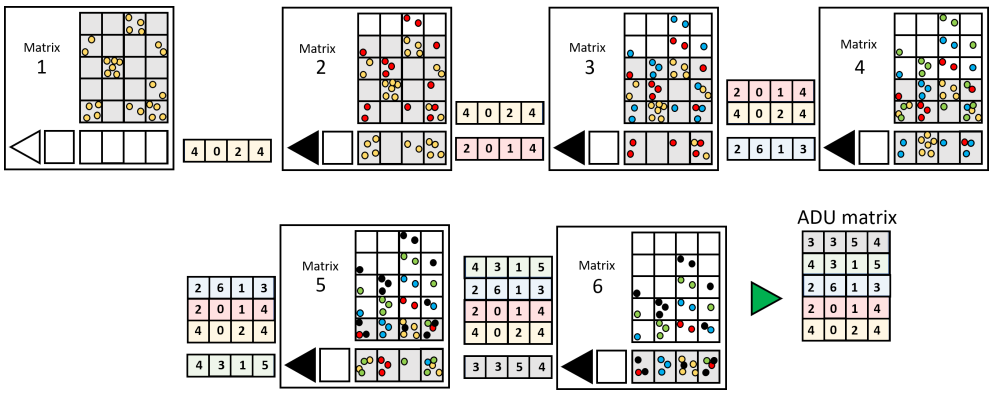

Figure 4.29: Sketch of the readout procedure, considering the RON contribution. The numbers in the matrix show the total loaded charge.

dramatically differs from the one where the readout noise was neglected (ideal case).
The developed algorithm, one given the amount of time needed for information transfer between the rows and the standard acquisition time of the CCD, starts with identifying the amount of photons collected in a wrong position, considering the spatial distribution of the photons collected in the exposure time (I step); once identified wrongly collected photons, the algorithm reallocates them in the right position (II step).

I step: The Forward Method

The first step of the algorithm (called *Forward Method*) consists in filtering out all the charges due to RON photons, which are pixel-position dependent. The algorithm works as shown in the example in fig. 4.30.

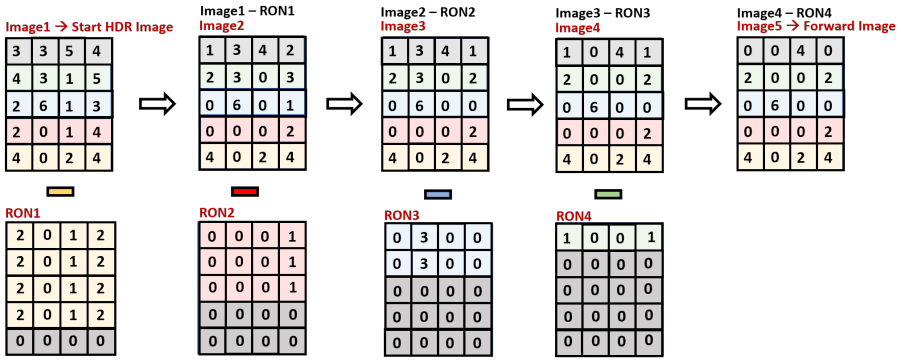

Figure 4.30: Overview of the I step of the step-by-step RON removal algorithm. Top, from left to right - $Image_1$: Start HDR Image. $Image_K$ (with K from 2 to 5): $Image_{K-1}$ where all rows j (with j≥K) have been subtracted by a contribution proportional (of a factor β) to the loaded charge in the $(K-1)^{th}$ row of $Image_{K-1}$. In the last post-processed image, the *Forward Image*, the whole RON has been filter out. Bottom - matrix subtracted from the corresponding image on the top, at each step.

Considering the Start HDR Image, only the first row (the one with yellow background) is unaffected by the RON, since it is read instantaneously. The second row (red background) contains both the charge due to photons impacting in it and the additional RON due to photons impacting during its readout time, proportional to the flux read in the previous rows (only the first row, in this case). The third row (blue background) contains both the charge of photons impacting in it and two additional RON contributions proportional to the fluxes read in the previous two rows, and so on. The algorithm, starting from the Start HDR image, subtracts step-by-step the RON contribution in each row loaded during the readout time.
Starting from the Start HDR Image (the 1^{st} image), 1023 images have been analyzed step-by-step: the K^{th} image (with K = 2 $\rightarrow$ 1024) corresponds

to the $(K-1)^{th}$ image in which all rows j (with j≥K) have been subtracted by a contribution proportional (of a factor β) to the loaded charge in the $(K-1)^{th}$ row of the $Image_{K-1}$. In the final post-processed image, called *Forward Image*, all RON contributions have been filter out. The *Forward Image* is characterized by the same ADUs of the image obtained neglecting the RON contribution (shown in fig.4.28). This demonstrates the effectiveness of the described procedure.
Moreover, considering the difference from the Start HDR Image and the Forward Image, it is possible to obtain the so called "*Displaced RON Image*" consisting of all RON photons collected during the RO time and placed in wrong positions (see fig.4.31).

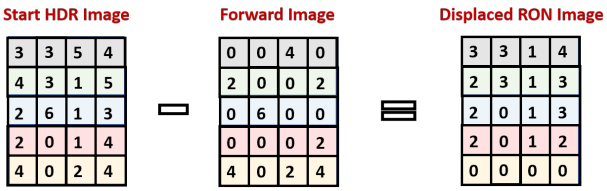

Figure 4.31: From left to right: Start HDR Image; Forward Image; Displaced Readout Noise Image.

These RON photons from one hand represent a spurious contribution because they are placed in wrong pixel position but, on the other hand, they are "*good*" events because are true photons coming from the plasma setup that impact in the CCD. It has been possible to relocate them in the correct pixel position, increasing the statistics.
In the previous example, a β parameter of 0.5 has been considered, but the real experimental β parameter (which depends of the readout time) has been estimated. The measurements have been performed setting a readout frequency of 1 MHz (10^6 pixels/sec), so the readout time of one single pixel t^p_{RO} is 10^{-6} sec; subsequently, the readout time of one row RO^r_t results $1024 \cdot 10^{-6} = 0.0010124\ sec$. Consequently, the β parameter is:

$$\beta = \frac{t^p_{RO}}{T_{exp}} \tag{4.1}$$

β, as mentioned before, represents the percentage of impacted flux in a single row during its readout time. Considering the I_{Plasma} images where

the exposure time T_{exp} is 0.5 *sec* the $\beta_{I_{Plasma}} = 0.002$, whilst for I_{Pole} images for which an exposure time of 0.05 *sec* was set $\beta_{I_{Pole}} = 0.02$.
The measured *Start HDR*, *Forward* and *Displaced RON* images are shown in fig.4.32.a), b) and c) respectively for Ar-, Ti- and Ta-energy filtering.

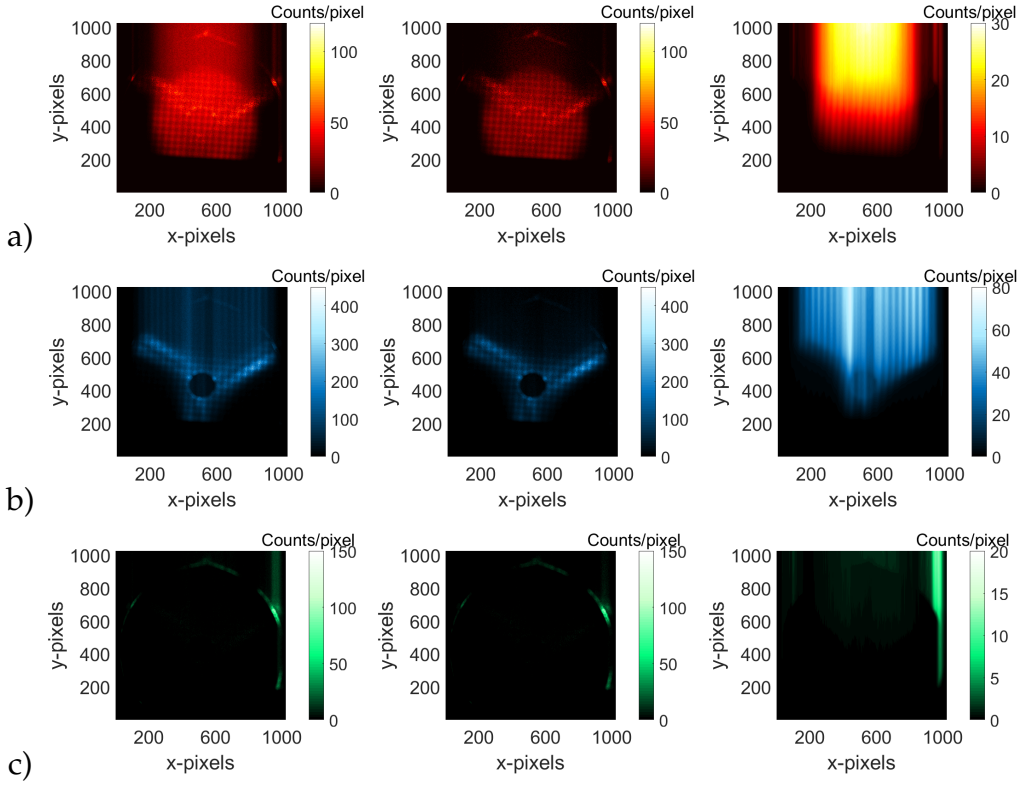

Figure 4.32: Left) Start HDR Image. Middle) Forward Image. Right) Displaced RON Image. a) Ar-energy filtered images. b) Ti-energy filtered images. c) Ta-energy filtered images.

II step: The Backward Method

The events shown in the *Displaced RON Images* in fig.4.32 must be "*relocated*" in the correct position by means of the second step of RON-r.
A new matrix called *Weight Matrix WM* obtained multiplying the Forward Image by β has been defined. A sub-matrix W_i has been associated

to each i^{th} row, normalized and expressed in percentage (with nonzero elements only in rows j≥i). The elements of the W_i matrices give the pixel-position dependent *weight* $w_{k,j}$ of the RON coming from each pixel during the readout time.
The second step of the algorithm consists of redistributing the charge loaded in each pixel (i,j) of the *Displaced RON Image*, in all the pixels (k,j), with k = (i+1) $\rightarrow$ 1024, of a new matrix called RON_i by means of the weights $w_{k,j}$. The W_i and RON_i are shown in fig.4.33, for i=2 *to* 4.

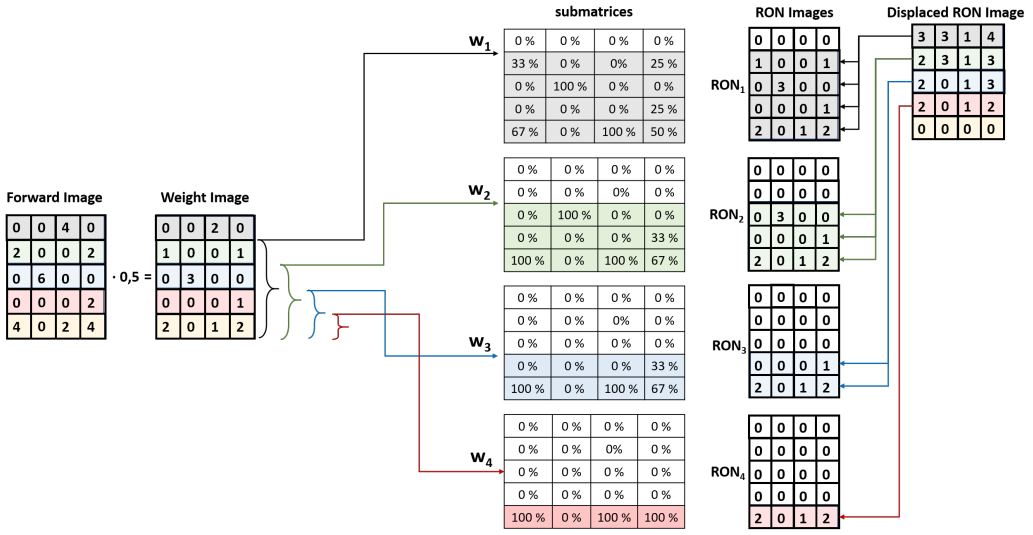

Figure 4.33: From left to right: Forward Image. *Weighting Matrix WM*. Sub-matrices W_i having j≥i associate at each WM i^{th} row. RON_i matrices obtained stating from the *Displaced RON Image* by means of weights $w_{k,j}$, elements of the W_i matrices for each row *i*. *Displaced RON Image*.

The sum of all the RON_i matrices gives the so called "*Placed Readout-Noise Image*", shown in fig. 4.34, that corresponds to the *Displaced RON Image* where all charge has been redistributed in the correct pixel-position. It is possible, in fact, to verify that the total charge is the same: total ADU=31 both in *Placed RON Image* and in *Displaced RON Image* (see also the table 4.3 for comparing ADU of the experimental acquired images).

Even if the Forward Matrix can be used to calculate the *Weight Matrix*, as shown in the previous example, it is possible to demonstrate that there

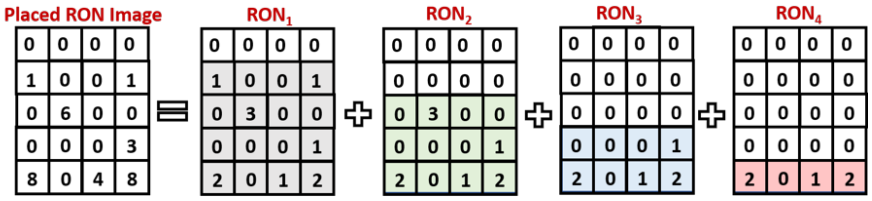

Figure 4.34: *Placed RON Image* obtained by the sum of all the RON_i.

is an improvement when replacing it with the one obtained applying in the Forward Matrix a pixel-position dependent threshold. The reason is due to the fact that there is the background (BGN) contribution too, that inevitably affects the experimental measurement; a preliminar removal of this contribution is very useful. On this scope, a pixel-position dependent threshold has been defined and applied in the *Forward Matrix*:

- first, 200 image-frames acquired setting the lowest exposure time possible in the driver (20 μs) have been used to estimate the BGN threshold. The sum of the 200 event-counted frames is shown in fig.4.35.a), it has been normalized for the frames number and the σ level, pixel-by-pixel, has been considered as BGN threshold (fig.4.35.b).

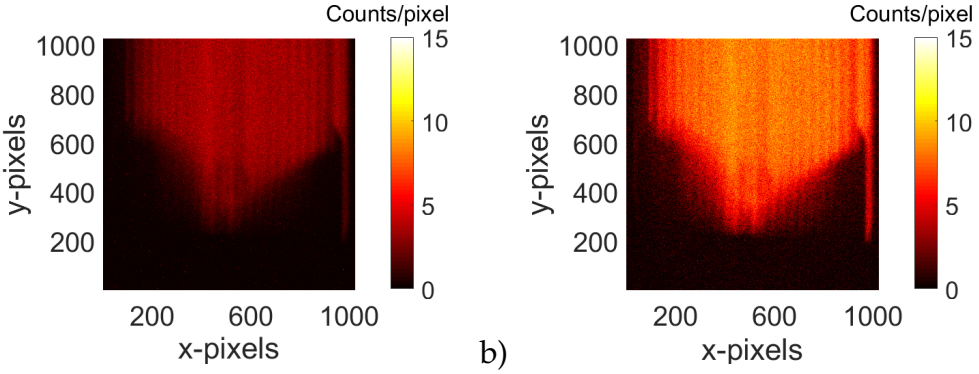

Figure 4.35: a) Background Image. b) Threshold Image.

- The *Start HDR*, *Forward* and *Displaced RON* images are shown in fig.4.36.a), b) and c) respectively.

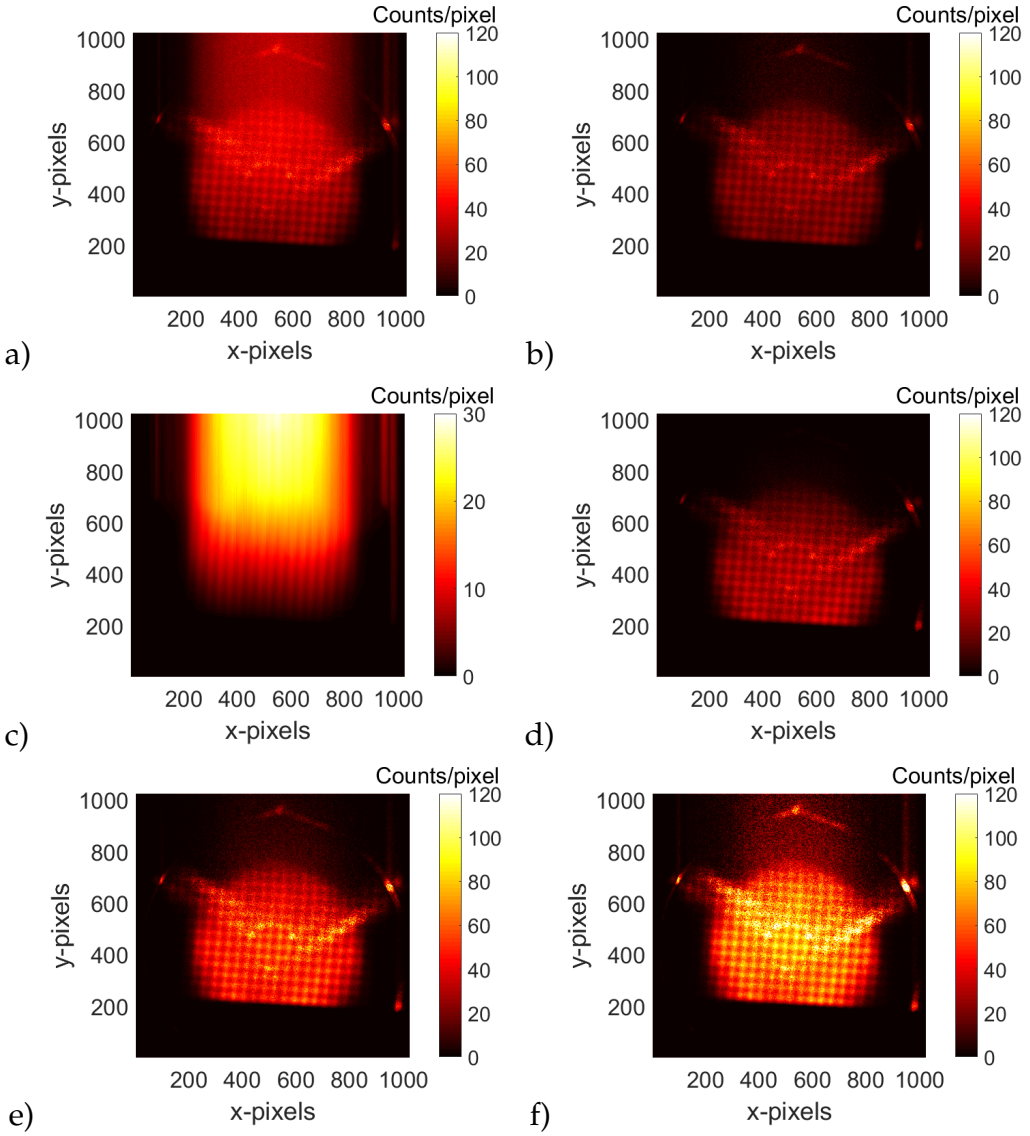

Figure 4.36: Sequence of the (Argon-energy filtered) images used during the RON-r algorithm. a) Start HDR Image. b) Forward Image. c) Displaced RON Image. d) Placed RON Image. e) Backward Image. f) Normalized Backward Image.

- Setting the background threshold in the *Forward Image*, the *Weight Image* has been obtained and used to estimate the *Placed RON Image*, shown in the figure 4.36.d). It contains the same RON charge collected in the *Displaced RON* image, but placed in the correct positions.

- The sum of the *Forward Matrix* and of the *Placed RON Image* gives the so called "*Backward Image*", shown in fig.4.36.e), which contains the whole charges (collected during the measurement time + RON time) in the correct pixel-positions.

- Since the exposure time, considering the RO time contributions, is pixel-position dependent, the *Backward Image* has been also time-normalized. The final post-processed image is called "*Normalized Backward Image*" and is shown in the fig. 4.36.f).

The images shown in fig.4.36 are Argon-energy filtered.
It is possible to highlight how the post-processed image quality dramatically improves if compared to the original one. The RON disappears almost totally, the signal intensity increases and the $\frac{signal}{noise}$ ratio improves very much. In fact, the "*Normalized Backward Image*" recovers information in its ROIs, and it contains the whole photons placed in the correct positions.
The spatial resolution increases as well: it is possible to better distinguish the mesh structure of the Al plate having a wire diameter of 400 μm.
In table 4.3) it is possible to observe that the total counts of the *Start HDR Image* (a) are the same of the ones of the *Backward Image* (e): the only difference is that all the RON photons have been relocated in the correct positions. The same observation can be done for the *Displaced RON Image* (c) and the *Placed RON Image* (d). Of course, the sum of the total counts of the *Forward Image* (b) and the *Displaced RON Image* (c) is equal to the one in the *Start HDR Image* (a). Finally, the slight difference between the counts of the *Weighing Image* (i) and the *Forward Image* (b) is due to the events filtering out due to background threshold.

Table 4.3: Total counts of each image (Argon-energy filtered) used in the RON-r algorithm.

	Name and description of the Image	**Total Counts**
a)	***Start HDR Image***: HDR Image with Readout Noise	$1.49 \cdot 10^7$
b)	***Forward Image***: Original Image without the Readout Noise removed by means of the forward method	$0.74 \cdot 10^7$
c)	***Displaced Readout-Noise Image***: Subtraction between the Original Image and the Forward Image	$0.75 \cdot 10^7$
d)	***Placed Readout-Noise Image***: Displaced Readout-Noise Image with photons placed in the correct position by means of the backward method	$0.75 \cdot 10^7$
e)	***Backward Image***: Sum pixel-by-pixel of the Forward Image and the Placed Readout-Noise Image	$1.49 \cdot 10^7$
f)	***Normalized Backward Image***: Time normalized Backward Image	$2.27 \cdot 10^7$
g)	***Background Image***: Mean image of 200 image-frames acquired setting an exposure time $\sim$ readout time	$0.16 \cdot 10^7$
h)	***Threshold Image***: Square root of the Background (and Normalized) Image pixel-by-pixel	$0.42 \cdot 10^7$
i)	***Weighing Image***: Forward Image filter out all events lower than the threshold pixel-by-pixel taken in the Threshold Image	$0.72 \cdot 10^7$

The corresponding Titanium-energy filtered images are shown in the figure 4.37.

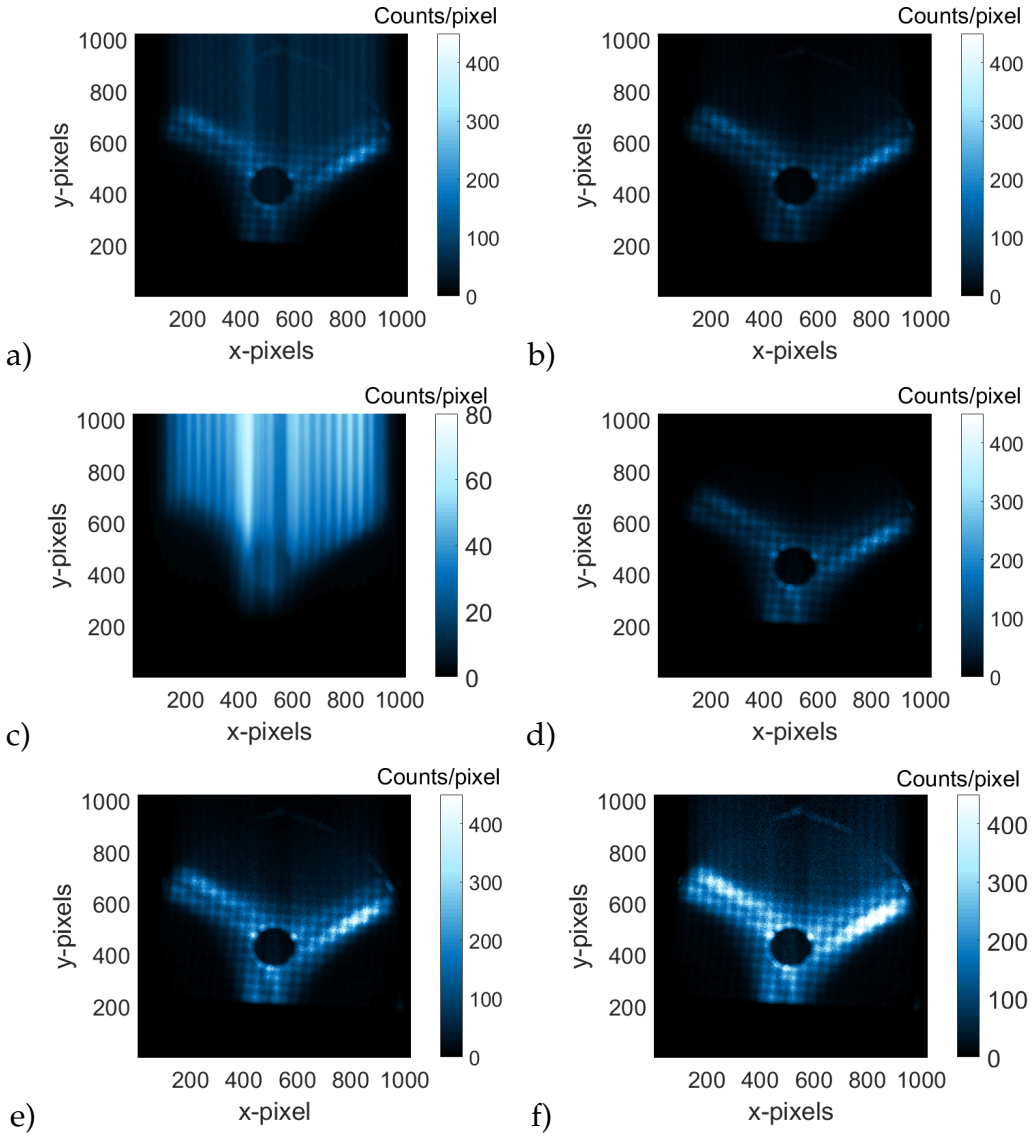

Figure 4.37: Sequence of the (Titanium-energy filtered) images used during the RON-rem algorithm. a) Start HDR Image. b) Forward Image. c) Displaced RON Image. d) Placed RON Image. e) Backward Image. f) Normalized Backward Image.

Whilst, the corresponding Tantalum-energy filtered images are shown in the figure 4.38.

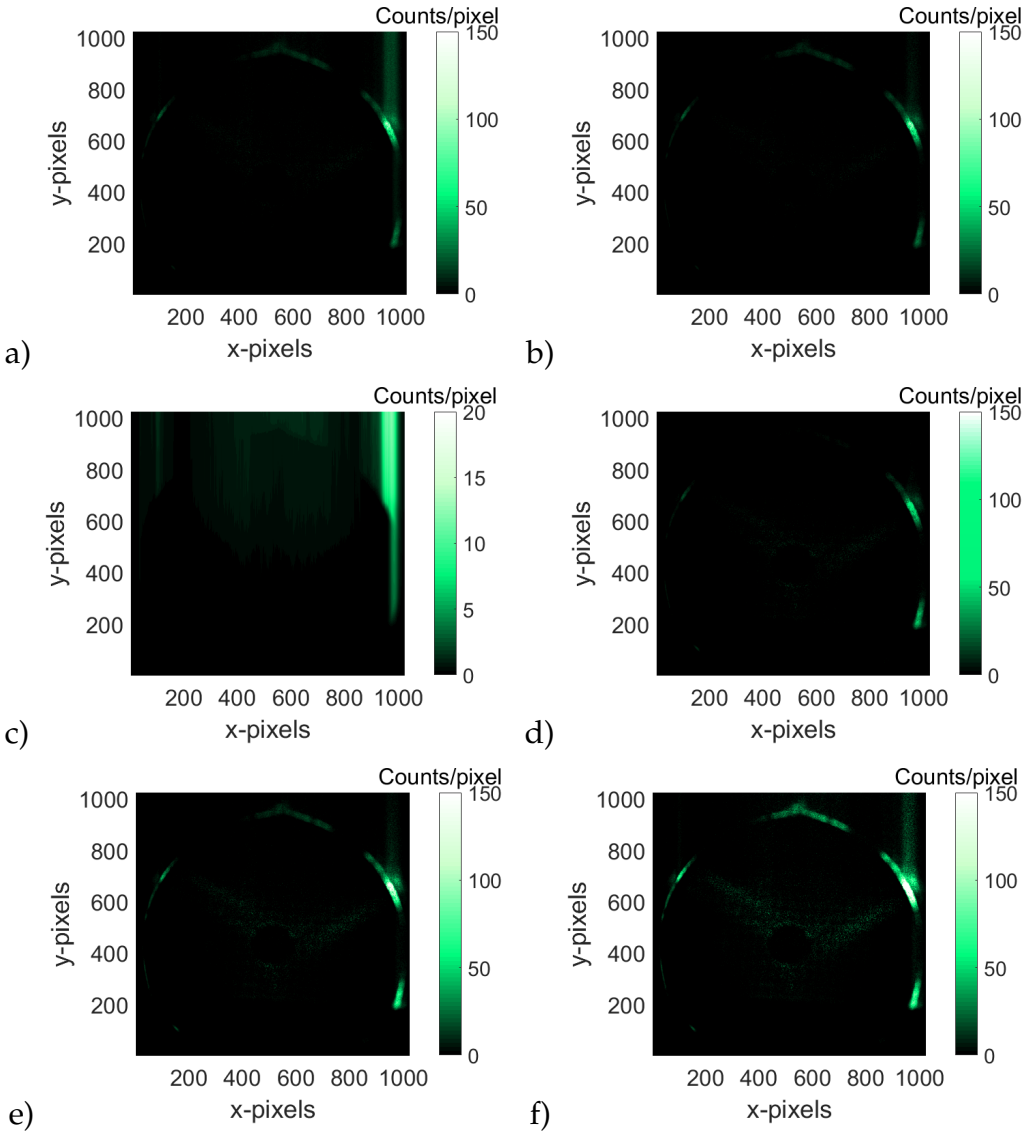

Figure 4.38: Sequence of the (Tantalum-energy filtered) images used during the RON-rem algorithm. a) Start HDR Image. b) Forward Image. c) Displaced RON Image. d) Placed RON Image. e) Backward Image. f) Normalized Backward Image.

In fig.4.39 the three different *RON-r* methods have been compared and it is possible to demonstrate that the complete RON-r sequence is very efficient in maximizing signal/noise ratio (yellow bar).
The signal-over-noise ratio increases of a factor 30 compared to the original image (blue bar). Whilst, if only a threshold is applied in the *Start HDR image* (red bar), the ratio increases of a factor 6 only. If the method stops at the *Forward Image* (green bar) the ratio increases of a factor 20.

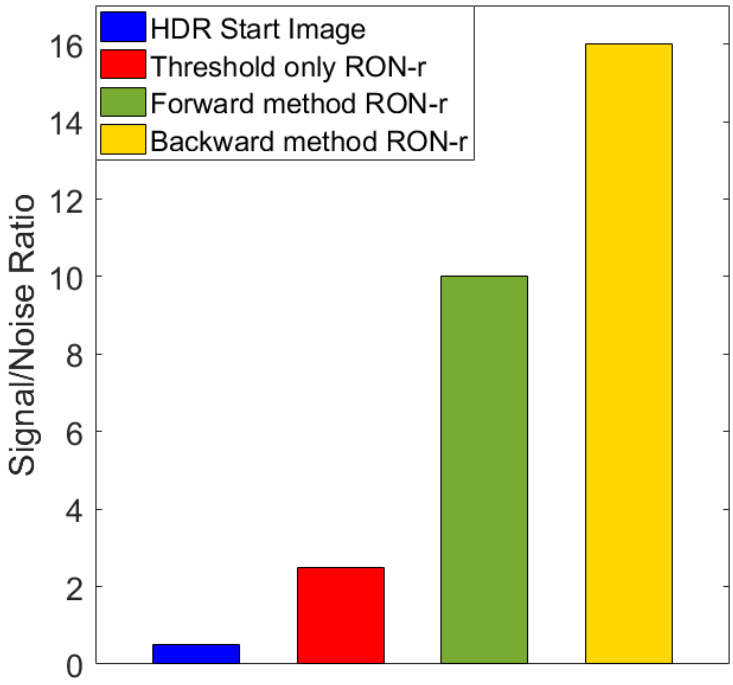

Figure 4.39: Comparison of the Signal/Noise Ratio between three different *RON-r* methods and the Original Image.

Finally, in the figure 4.40 the comparison between the I_{Plasma} images, the HDR post-processed images with RON and the Readout Noise Removed post-processed images is shown (note that the full scale is different in the I_{Plasma} images compared to the other ones). Event counted energy-unfiltered images (a), Ar-energy filtered images (b), Ti-energy filtered images (c) and Ta-energy filtered images (d) are shown.
It is possible to observe the improvement of the final post-processed im-

ages, where the *"strips"* due to RON completely disappeared. These ones have been analysed to perform plasma proprieties investigation, as described in the dedicate chapter 5.

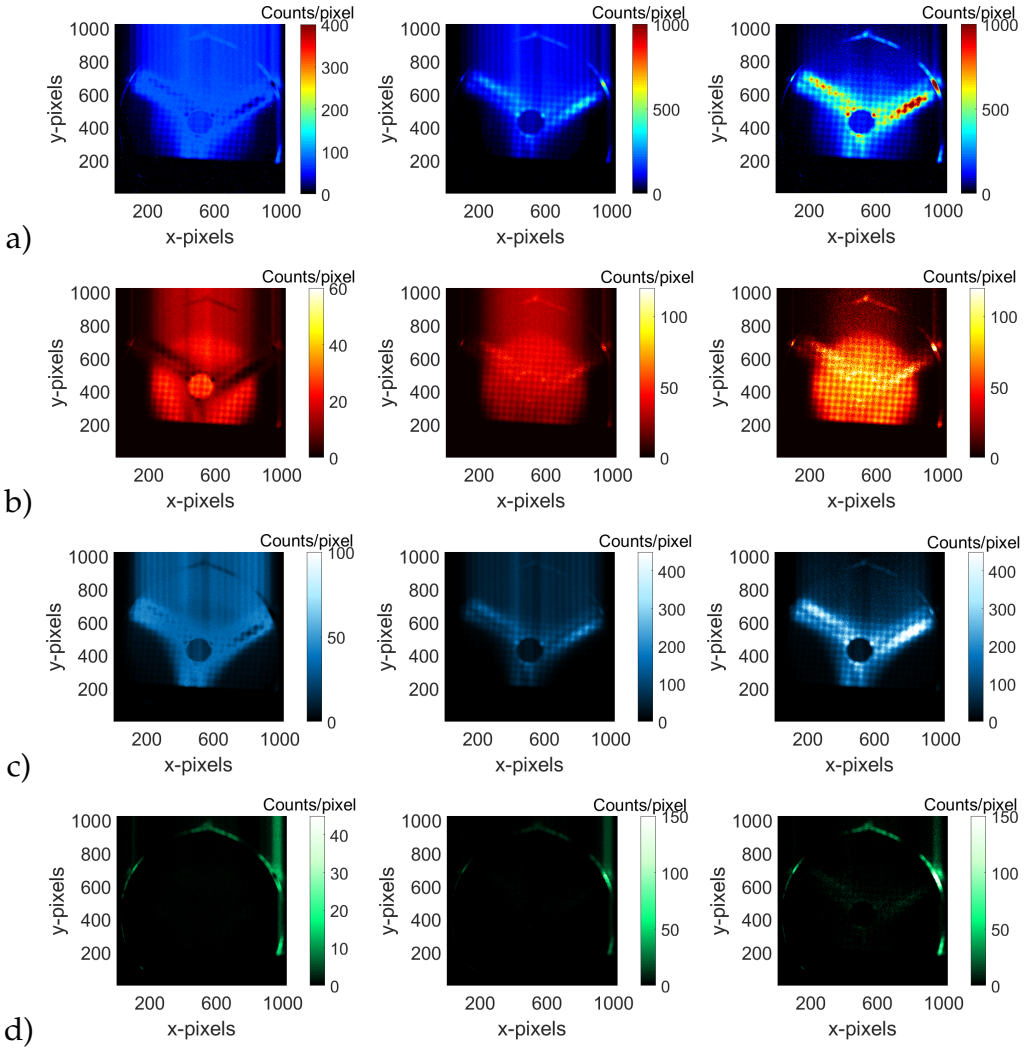

Figure 4.40: First column: the I_{Plasma} grouped image. Second column: the HDR post-processed image. Third column: the Readout Noise Removed post-processed image. a) Event counted energy-unfiltered image. b) Ar-energy filtered image. c) Ti-energy filtered image. d) Ta-energy filtered image. (Note the different the full scale in the first row.)

Error analysis of the number of counts in each pixel of the single photon counted-image has been estimated by the square-root of counts. The image 4.41 illustrates, for each pixel, the relative error σ_{rel} of the counts for the event counted Ar-filtered image (a) and for the event counted Ti-filtered image (b). The relative errors are $< 10 \div 15$ % in the plasmoid and lower than $< 4 \div 8$ % in the magnetic branches regions. In the magnetic poles the relative errors are around 10%. These are the typical uncertainties of the number of counts in each pixel, which affect the performed measurements.

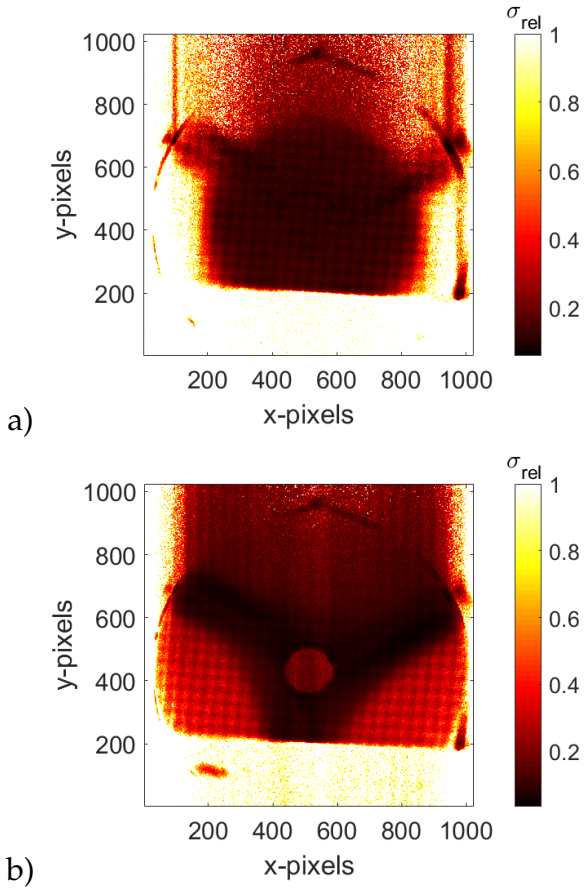

Figure 4.41: The images show the errors of the number of counts in each pixel: a) Ar-filtered image; b) Ti-filtered image.

4.2 RF spectral analysis

In this section we will discuss the RF spectral analysis. RF spectra were collected simultaneously to X-ray images and spectra in order to define a new method to characterize and study the ECR plasma kinetic turbulence regimes, for the first time in a quantitative way. The method allowed to semi-empirically define a new parameter, called I_S $(Instability\ Strength)$, able to give a quantitative estimation of the *strength* of the plasma instabilities for comparing stable and unstable regimes and to study an innovative plasma heating method able to master and eventually damp plasma turbulences (i.e. the TCFH effect), as it will be shown in chapter 5.

The kinetic instabilities shortly discussed in 1 cause the emission of microwaves bursts and the energy of fast electrons may be released as coherent (maser) electromagnetic radiation due to development of electron cyclotron instabilities. The emission frequency depends on the electron cyclotron frequency, i.e. on local magnetic field B. Thus, since plasma kinetic instabilities are characterized by fast RF and X-ray bursts, the plasma self radio-emission, in the GHz range, can be considered as a signature of the plasma instability regime, as described in [31, 29]. Consequently, plasma instabilities can be detected via RF spectra.

Four typical experimental spectra, acquired using a pumping RF power of 200 W and different single pumping frequency, have been reported in fig. 4.42.

The case a) is an example of a stable plasma regime spectrum. In fact, as it is possible to observe, the spectrum is characterized only by the pumping RF peak at 14.25 GHz, and there is not plasma self radio-emission. Whilst, the cases b), c) and d) show plasma unstable configurations and in addition to the main peak, plasma self emissions appear. In this cases, the plasma instabilities spectrum can be characterized by a low number of sub-harmonics with a high power in each one (as shown in fig. 4.42.b) or by a high number of sub-harmonics but at low power (as shown fig. 4.42.c); sometimes, the plasma unstable spectrum is characterized by the combination of both the previous conditions (as shown in fig. 4.42.d).

In order to correlate the instability strength of a given configuration with other parameters - such as RF power, RF pumping frequency, SFH or

TCFH operations - it is very important to find out a quantitative way to say how much the plasma is turbulent.

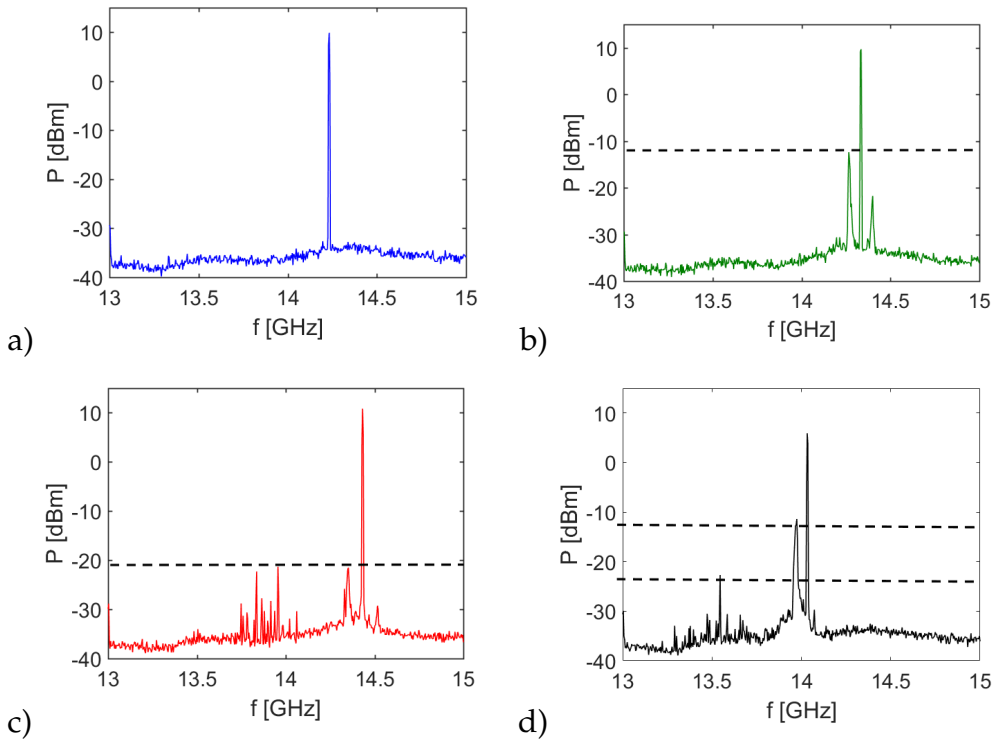

Figure 4.42: Sequence of SA collected spectra for: (a) stable; (b) unstable but with a small number of sub/up-harmonics at high power; (c) unstable but with a large number of sub-harmonics at low power. (d) unstable with both a sub/up-harmonic at high power and several number of sub-harmonics at low power.

4.2.1 Instability Strength: Parameter definition

Despite defining a rigorous way to describe the instabilities strength it is not easy, it has been demonstrated that the semi-empirical I_S definition follows in a reasonable way what happens in the plasma in more or less unstable conditions (depending on the power, magnetic field and

frequency), as will be in detail shown in the chapter 5.
The series of issues concerning the quantitative evaluation of the instability strength and, then, about the eventual correlation of confinement dynamics (plasma vs. losses X-radiation emission) and of other operative parameters, with the I_S parameter itself are the following:

a) Frequency spectra have been acquired by means of the setup shown in the section 3.2.1. They were collected by the SA with a temporal resolution around 0.7 ms, that means the signal at each frequency must be considered as an averaged value in the mentioned temporal window; on the other side, instabilities are by definition fast evolving phenomena whose temporal scale lies in the range of μsec or shorter; hence, any quantitative evaluation of I_S has to cope with frequency spectrum evaluation time of our spectrum analyzer;

b) Due to the still not-perfectly known physical mechanism governing the ECRIS instability dynamics, it is difficult to find rigorous quantitative criteria to evaluate I_S. A question arises: what is more important, the total integral of plasma self-generated sub-harmonics, or their number? Or their superposition?

To find a significant I_S definition able to quantitatively describe the instability strength of each configuration, it is necessary to be able to catch all RF spectra structures and details. For sake of example, we compared directly the spectra for two configurations: $f_{TWT} = 13.60$ GHz and $f_{TWT} = 14.05$ GHz, shown in fig. 4.43a) and b), respectively.
In these cases, the vertical axis scale is set in order to highlight the sub-harmonics contributions (thus pumping frequencies peaks saturate).
It is possible to highlight that, even if P_{sub} at $f_{TWT} = 14.05\ GHz$ is higher than at $f_{TWT} = 13.60\ GHz$, at $f_{TWT} = 13.60\ GHz$ the number of sub-harmonics N_{sub} is higher and many sub-harmonics are widely spread in frequency, with peaks far of more than 0.5 GHz.

This evidence is very important since the instability strength is not only related to the amplitude of the sub-harmonics, but also to the frequency spread of the self-generated sub-harmonics: not only the integral but also the broadening of frequency spectra reflects about the strength of instabilities. Consequently, this effect must be included in the numerical

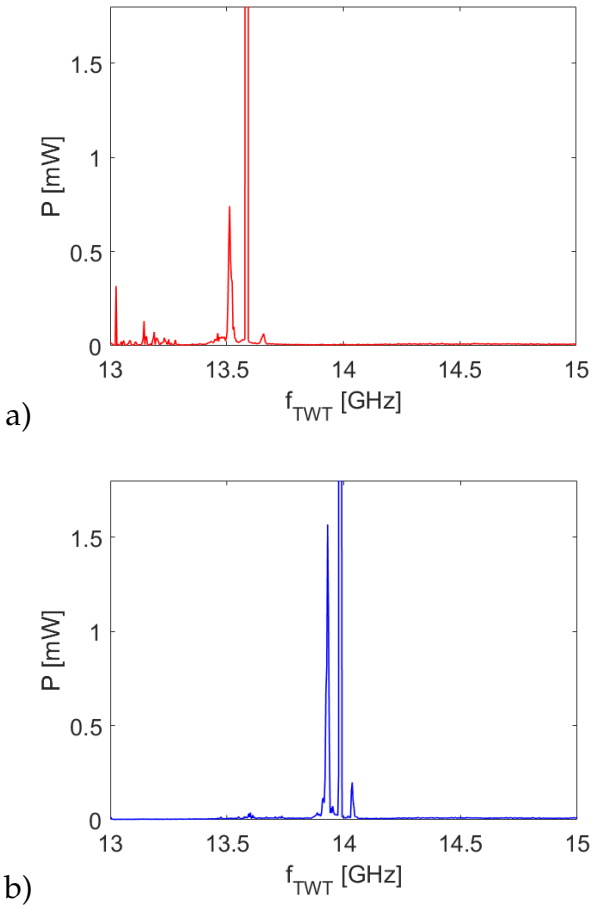

Figure 4.43: Experimental spectra: a) pumping frequency $f_{TWT} = 13.60$ GHz; b) pumping frequency $f_{TWT} = 14.05$ GHz.

definition of I_S.
The spectra are shown, expressing the power in dBm, in fig. 4.44.a) and b) too. Other cases are illustrated also in fig.4.44, where spectra having the same number of sub-harmonics N_{sub} can be compared: i.e., observing the spectrum at $f_{TWT} = 14.10\ GHz$ (c) and at $f_{TWT} = 14.30\ GHz$ (d), or the ones at $f_{TWT} = 14.40$ GHz (e) and at $f_{TWT} = 14.45$ GHz (f).

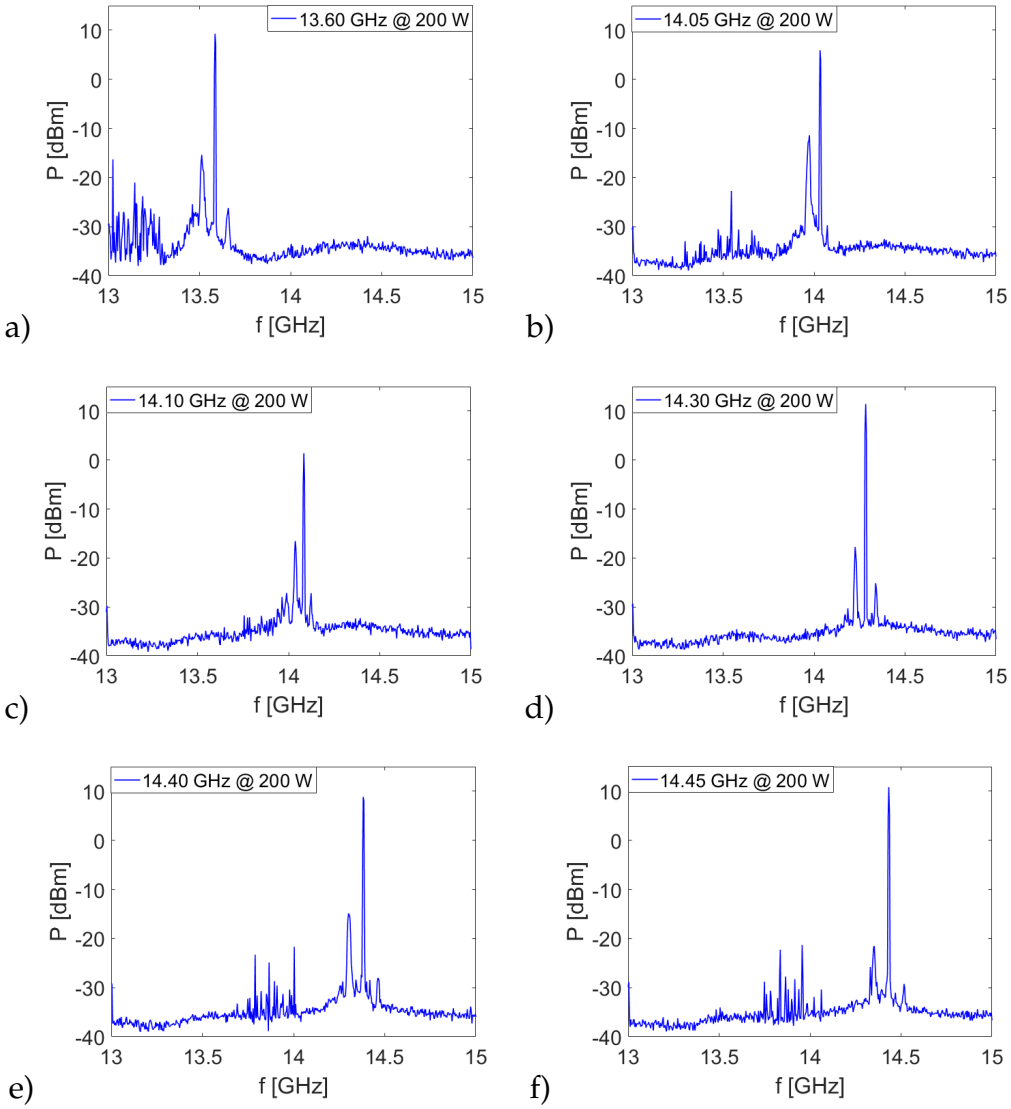

Figure 4.44: Experimental spectra at 200 W of pumping power and at a pumping frequency: a) $f_{TWT} = 13.60$ GHz; b) $f_{TWT} = 14.05$ GHz; c) $f_{TWT} = 14.10$ GHz; d) $f_{TWT} = 14.30$ GHz; e) $f_{TWT} = 14.40$ GHz; f) frequency $f_{TWT} = 14.45$ GHz.

Finally, after several attempts, trying to find a significant I_S definition able to quantitatively describe what we observed directly and to catch

all RF spectral structures, our choice was to define I_S considering both contributions, as it follows [11]:

$$I_S = \left(\int_{13GHz}^{15GHz} \frac{dP(f)}{df} df - P_{mp} \right) (1 + w\,(N_{sub} - 1)) \tag{4.2}$$

where P_{mp} is the integral of the power of the main peak of pumping frequency, N_{sub} the number of sub-harmonics and w a weight factor.
With this definition, the I_S parameter has been calculated considering the amplitude (integral of the power) of RF plasma-self emitted signal, once subtracted the main pumping wave contribution; this number has been then multiplied by a factor which takes into account the number of sub-harmonics N_{sub} with a proper weight factor w. The weight was introduced in order to give higher contribution to the total integral of plasma self-generated sub-harmonics than their number, so: $0 \leq w \leq 1$. It was calculated finding the best value of compromise between these two contributions.
Typically it is expected that plasma instabilities increase with the power [76, 48]. A helpful preview of experimental results about the trend of I_S versus the RF power is here reported, useful to correctly define the I_S parameter in a rigorous way. Whilst, all other results will be described in the chapter 5. Thus, the I_S parameter has been evaluated for ten configuration in SFH (at a fixed pumping frequency of 13.80 GHz) performing the power scan from 20 W to 200 W at step of 20 W. They have been estimated by means of the equation 4.2 setting a given weight (0.1, in this case). The plot of I_S versus RF power is shown in figure 4.45.

The plot displays a clear increase of I_S vs. power, as expected. So, in order to try to estimate in a quantitative way the best weight-parameter w to be used hereinafter, we calculated the Pearson coefficient R for evaluating the degree of correlation of I_S versus the RF power, for different values of w, at steps of 0.001.

The plot of figure 4.46 shows that during the power scaling (single frequency heating: TWT at 13.80 GHz) the data were very well linearly ted with almost all the choices of the w-parameter (very high correlation with $0.86 < R < 0.9$), even if - strictly speaking - the best agreement was found for $w = 0.1$. The plot, in our opinion, can be interpreted in two ways: on one hand, we have a quantitative estimation of the best w,

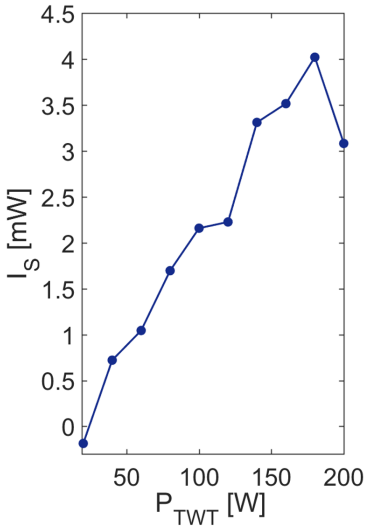

Figure 4.45: Trend of the I_S parameter versus the TWT power, during the single-frequency power scan at a frequency of 13.80 GHz.

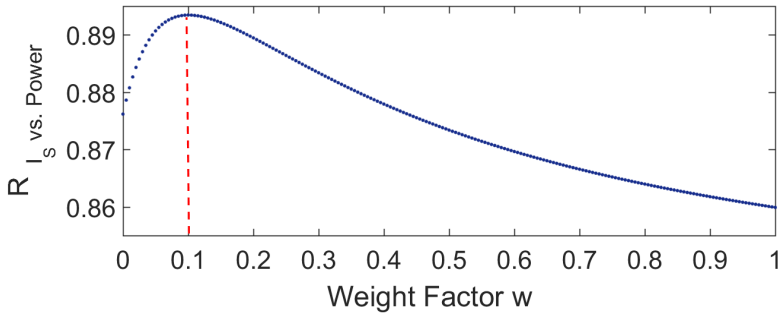

Figure 4.46: Trend of the Pearson coefficient R evaluating the I_S versus RF power correlation, for different values of weight factor w.

even if only a weakly predominant value was found. On the other hand, the fact that for all the w values the agreement is pretty good, we may conclude that this supports an arbitrary choice.
We decided to use the maximum value obtained $w = 0.1$, in the equation 4.2. In the algorithm, used to define the number of sub-harmonics, it has been also defined a threshold to filter out the spurious contribution due to background.

f_{TWT} [GHz]	N_{sub}	P_{sub} [mW]	I_S [mW]
13.60	**13**	**5.5442**	**12.7516**
13.65	3	1.4950	1.9435
13.70	2	0.7532	0.9039
13.75	2	0.9750	1.1700
13.80	9	4.9343	9.3752
13.85	12	3.5171	7.7376
13.90	15	3.3230	8.3074
13.95	6	1.5995	2.5592
14.00	5	6.6751	10.0127
14.05	**4**	**7.0335**	**9.8469**
14.10	**2**	**1.9479**	**2.3375**
14.15	2	0.6878	0.8253
14.20	2	1.9714	2.3657
14.25	4	1.8949	2.6528
14.30	**2**	**1.1571**	**1.3885**
14.35	3	3.9380	5.1194
14.40	**5**	**4.5128**	**6.7692**
14.45	**5**	**1.5166**	**2.2749**
14.50	7	2.2508	3.8263
14.55	4	2.3887	3.3442
14.60	2	0.6070	0.7284

Table 4.4: Contribution of the P_{sub} and N_{sub} to the I_S parameter at (single) frequency scan $f_{TWT} = 13.60 - 14.60\ GHz$, at step of $\Delta f = 50\ MHz$ and $Power = 200\ W$.

The different operative configurations series investigated during the experiment will be in detail described in the chapter 5, see the table 5.1. As example, the I_S parameters (for the SFH frequency scan characterization, $f_{TWT} = 13.60 - 14.60\ GHz$, at step of $\Delta f = 50\ MHz$ and $Power = 200\ W$) are shown in the table 4.4, listing also separately the two contributions: a) the total number of sub-harmonics N_{sub} and b) the total power integral of plasma self-generated sub-harmonics P_{sub}. This series will be investigated in the section 5.2.2.
The table reports also the cases shown in the examples above discussed

(fig. 4.43). It is possible to highlight from the table that, even if P_{sub} at $f_{TWT} = 14.05$ GHz is higher than at $f_{TWT} = 13.60$ GHz, considering also the number of sub-harmonics N_{sub} the I_S parameter results to be smaller. This is in accordance with the previous considerations.
For the other highlighted cases in the table 4.4 it is possible to observe how the I_S parameter changes due to the P_{sub} only, when the number of sub-harmonics N_{sub} is the same: comparing the spectra at $f_{TWT} = 14.10$ GHz and at $f_{TWT} = 14.30$ GHz, or the ones at $f_{TWT} = 14.40$ GHz and at $f_{TWT} = 14.45$ GHz.
Moreover, other experimental evidences demonstrated that I_S parameter, despite its definition was difficult to determine, follows in a reasonable way what happens in the plasma in more or less unstable conditions (depending on the power, magnetic field and frequency), as will be in detail shown in the chapter 5. Thus for each configuration it is possible to associate the I_S and correlate it with the operative parameters and with the plasma heating mechanisms.
In a nutshell, the code works in the following way:

- removing background noise by means of a power threshold;
- counting the number of sub-harmonics N_{sub} higher than the threshold (excluding the one (or twos) due to the pumping frequency (frequencies));
- integrating the total power $\left(\int_{13GHz}^{15GHz} \frac{dP(f)}{df} df\right)$;
- integrating the power of the one (or two) pumping frequency (frequencies) P_{mp};
- subtracting the total and the main peaks power in order to obtain the self emission only $\left(\int_{13GHz}^{15GHz} \frac{dP(f)}{df} df - P_{mp}\right)$;
- estimating the I_S by means of the equation 4.2;

Chapter 5

X-ray and RF Analysis of ECR plasmas: stable and unstable regimes

In this chapter a detailed analysis of experimental data collected using the X-ray pin-hole camera setup coupled to the spectrographic RF system (probe plus spectrum analyzer) is presented. Simultaneous collection of plasma radio-self-emission and high spatial resolution X-ray images, by simultaneously using and combining the two developed analytical methods, allowed deep investigations about stable vs. turbulent regimes of the plasma. The effect on the plasma instabilities of an Argon plasma in a Two Close Frequencies scheme has been explored using a frequency gap smaller than 1 GHz (i.e., operating in the TCFH mode).
The main experimental results presented in this chapter concern: the characterization of ECR plasma kinetic turbulence regimes, studied for the first time in a quantitative way; the most relevant result is the demonstration that the TCFH is a powerful plasma heating method able to master and damp the plasma turbulences. It is a very important result both for multidisciplinary and fundamental plasma physics (i.e., in the framework of the $PANDORA_{Gr3}$ project since ECR plasmas have to be maintained in stable regimes for weeks or even months to study nuclear-β-decays) and particle accelerator physics since the plasma turbulence

damping can improve the ion sources performances (i.e., in terms of high charge state beam intensity increasing and beam ripple minimization). These results will be discussed in the section 5.2.
In addition, studies about plasma confinement and loss dynamics have been performed by means of X-ray imaging analysis. The results have been correlated with the plasma instabilities *strength*. The results will be described in the section 5.3.
Moreover, spectrally integrated images allow to investigate plasma morphology and structure changes and to perform plasma radius measurement (see section 5.3.1). These analyses are relevant in order to estimate, likely on-line, the plasma volume (which is an important parameter, together with the density, to estimate the variation of the radionuclides lifetime (see chapter 6) in the $PANDORA_{Gr3}$ experiment).
Finally, the analysis of single photon counting images allows energy-resolved studies pixel-by-pixel for deep investigations about plasma proprieties. It allows imaging of the elemental distribution, distinguishing the emission coming from each material of interest, and the investigation of the spectrum in a given ROI, determining the elemental composition and, thus, distinguishing about X-ray emission by plasma electrons or deconfined electrons in the chamber walls. The results will be described in the section 5.4.

5.1 Physical background

Several experiments have demonstrated that plasma instabilities limit the flux of highly charged ions extracted from ECR ion sources, causing beam ripple [76, 88, 47]. Plasma kinetic instabilities are typically characterized by fast RF and X-ray bursts, and the instability threshold depends principally on the strength of the magnetic field in terms of B_{min}/B_{ECR} and from other parameters as RF pumping power and pressure [48]. Even if many studies have been done, the exact mechanism of turbulent regimes of plasmas is still unknown and a deeper investigation is necessary. Consequently, more studies aiming at characterizing in detail this still unknown process and at finding a way for damping the turbulence are required.

The investigation described in this chapter aims to investigate the role of the TCFH, when the two frequencies gap is consistent with the estimation given by [52], under which the two resonance zones are overlapped. Hereinafter this condition (i.e. the overlapping of the two resonance zones) will uniquely define the TCFH, thus distinguishing it from the classical TFH. The characterization has been carried out for the first time in TCFH mode, through the use of two frequencies with a difference of the order of some hundreds of MHz. Besides the above mentioned ECRIS improvement for the applied context, for $PANDORA_{Gr3}$ these studies are fundamental too. There is, in fact, the necessity to maintain ECR plasma in the same condition for weeks (as will be demonstrated in the chapter 6). Consequently, finding innovative plasma heating methods able to maintain the plasma stable, minimizing the turbulence, is crucial.
The results of an experiment carried out at ATOMKI, Debrecen (Hungary), where stable and unstable ECR plasmas in a B_{min} magnetic configuration have been characterized through the multi-diagnostic setup shown in the chapter 3, will be described. In particular, the data collected by the two-pin, plasma-chamber immersed antenna connected to the Spectrum Analyzer for the detection of plasma radio-self-emission when varying the pumping frequency in single versus double frequency heating mode will be presented. Data have been collected simultaneously to the X-ray images, acquired both in spectrally integrated and in SPhC mode, for different frequency gaps and relative power balances.
From a mathematical point of view, the $\delta\omega/\omega$ (ω is the heating frequency) condition fulfilling TCFH is given by the formula 1.22 described in chapter 1. For the estimation in the ATOMKI trap, the following parameters as described in ref. [52] have been used: $L = 0.055$, $\rho = 0.218$, $Y = 0.1$, whilst the amplitude of the heating electric field ϵ_i for both the frequencies was considered for propagating waves as equal to $95\frac{V}{cm}$. Fixing the first pumping wave frequency at $14.25GHz$ (the one amplified by the Klystron) calculation $\delta\omega/\omega$ provides $\pm$ 0.45 GHz. This estimation agrees with the empirical estimation of the resonance thickness, which is also reported in [43], which was used to roughly estimate the frequency gap for simulating the TCFH effect on the electron heating. The experimental measurements have been in fact performed using the second pumping

frequency amplified by the TWT in the range 13.60 GHz - 14.60 GHz.
The main theoretical aspects of the quasi-linear theory of two frequency heating used to give a robust explanation of TCFH consequences on the heating and confinement dynamics have been discussed in 1.3.2. Summarizing, in TCFH, the higher diffusion along $v_{\|}$ should reduce the growth rate, thus limiting the energy that the plasma can self-couple to the electromagnetic modes supporting the instability. This is our basic assumption that will be validated by experimental results in the following sections. Moreover, recent studies [31] predicted that turbulent regimes of plasma can generate precipitations of the energetic electrons in the loss cones (producing the X-ray burst emission when they impact in the plasma chamber walls) thus increasing the losses compared to the plasma emission. Our study can play a relevant role in order to verify the hypothesis of the *electrons precipitation*, thus trying to experimentally correlate the release of energy via RF and, especially, X-ray bursts with the onset of the instability. The measurements show, that the plasma-over-losses X-ray signal is correlated with the instability strength. The experimental results are interpreted by numerical simulations of how plasma electrons interact with the external electromagnetic field. Investigations about plasma morphology and volume changes have been performed and will be presented too.

5.2 Determination of stable vs. turbulent regimes

This section is focused on instability issues. All plasma instabilities were detected via RF spectra and characterized by I_S parameter. At the beginning the system has been characterized in single frequency heating mode in order to collect some reference configurations (see subsections 5.2.1, 5.2.2). Then, the system was characterized in TCFH mode in order to study the effect of the second frequency on plasma instabilities (see subsections 5.2.3, 5.2.4). The demonstration of plasma turbulences damping by means of the TCFH will be discussed in the subsection 5.2.5.

In order to validate the I_S consistency some plots concerning the I_S behaviour versus the RF power, in single and two close frequency heating mode, have been made. The definition of I_S resulted to be consistent with

Table 5.1: Different operative configuration series investigated during the experiment, labelled as a), b), c), d). The heating mode, the scan mode, the operative frequency/ies and the total net power are reported.

Heating Mode	**Scan Mode**	**Frequency$_1$ TWT**	**Frequency$_2$ Klystron**	**Total net Power**
a) SFH	Power Scan	$13.80 GHz$	//	$20 - 200 W$ step $\Delta P = 20 W$
b) SFH	Freq. Scan	$13.60 - 14.60\ GHz$ step $\Delta f = 50 MHz$	//	$200 W$
c) TCFH	Freq. Scan	$13.60 - 14.60\ GHz$ step $\Delta f = 50 MHz$	$14.25 GHz$	$200 W$
d) TCFH	Power Balance	$13.80 GHz$	$14.25 GHz$	$200 W$ step $\Delta P = 20 W$

the direct observation of the SA recorded spectrum, increasing steadily with the power, as expected [76, 48]. Moreover the frequency tuning, both in SFH and in TCFH mode, was systematically explored.
During the experiment four different operative configurations series have been characterized, they are reported in the table 5.1.
Precise error-analysis of the I_S evaluation has been skipped since this parameter has been only semi-empirically estimated (as described in 4.2.1) in order to follow general trends of the plasma behaviour. However, the validity of I_S was confirmed experimentally using procedures with quantitatively evaluating the Pearson correlation coefficients. Moreover, the frequency range ($13.0 \div 15.0\ GHz$) as the one covering most of the main features (spatial, temporal, and frequency modes) of the turbulence. Other contributions were negligible compared to the detected ones.

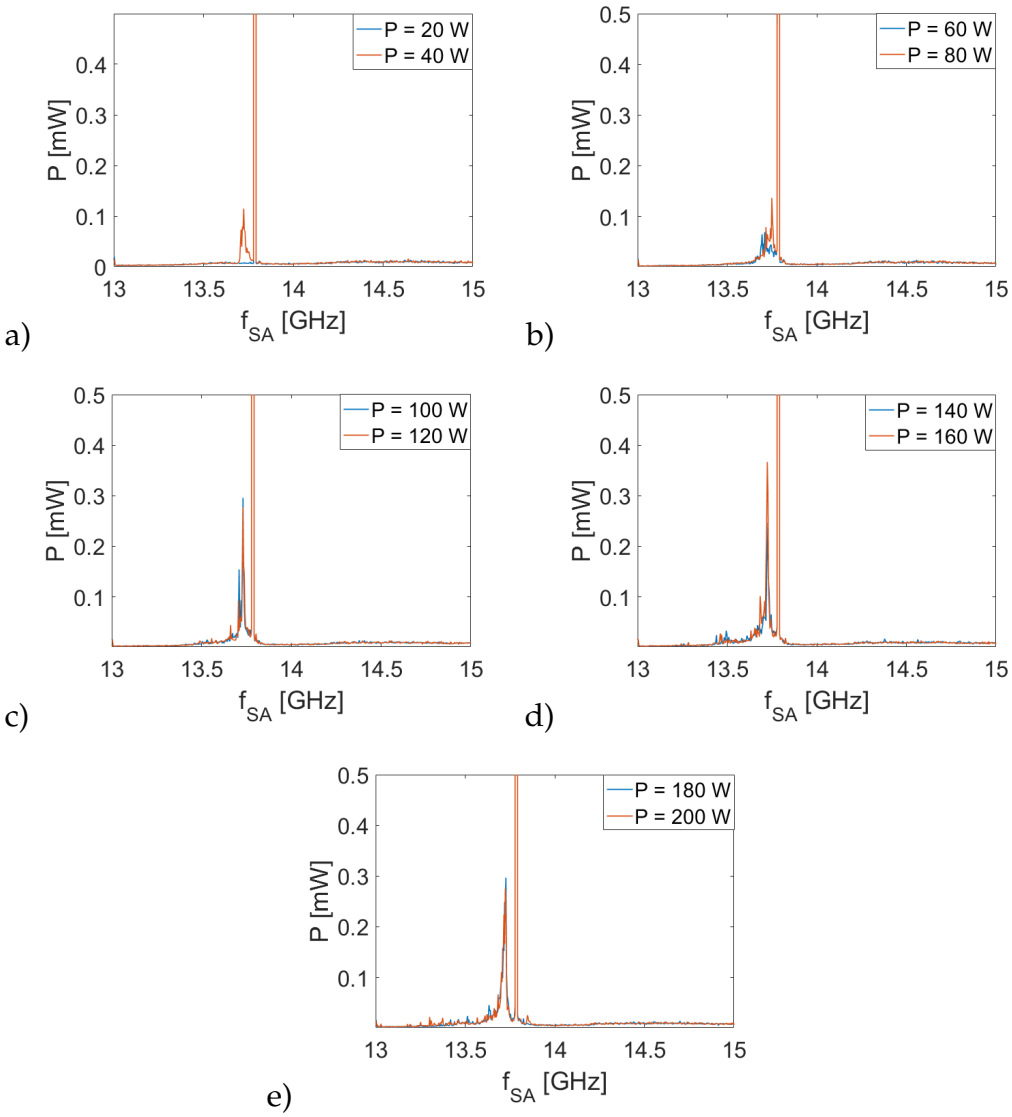

Figure 5.1: Experimental spectra in SFH at a fixed pumping frequency of 13.80 GHz and a RF power of: a) $P = 20W$ (blue), $P = 40W$ (red); b) $P = 60W$ (blue), $P = 80W$ (red); c) $P = 100W$ (blue), $P = 120W$ (red); d) $P = 140W$ (blue), $P = 160W$ (red); e) $P = 180W$ (blue), $P = 200W$ (red).

5.2.1 RF spectra in SFH - Power scan @ 13.80 GHz

Typically, it is expected that plasma instabilities increase with power [76, 48]. The acquired experimental RF spectra in SFH, at a fixed pumping frequency of 13.80 GHz, performing the power scan from 20 W to 200 W (step of 20 W) are shown in the figure 5.1. In these cases, the vertical axis scale is set in order to highlight the sub-harmonics contributions (thus pumping frequencies peaks saturate). Already from a visual inspection it is possible to observe the increasing of plasma-self emissions (both the intensities and the sub-harmonics number) versus the RF power. The power instability threshold is around $P = 40\ W$, in fact, as shown in fig.5.1.a), there is only the main pumping wave peak for $P = 20\ W$ (blue spectrum) and sub-harmonics start appearing for $P = 40\ W$ (red spectrum).

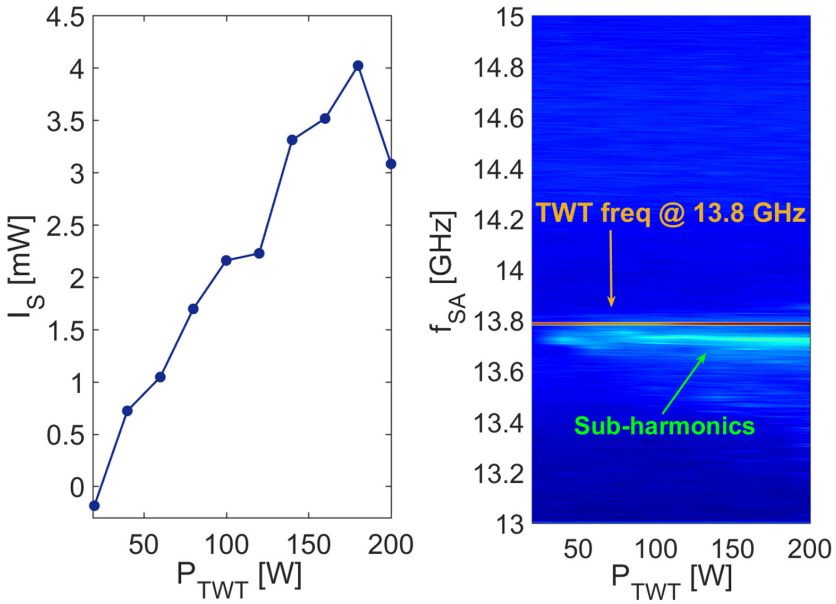

Figure 5.2: Left - Trend of the I_S parameter versus the TWT power, during the single-frequency power scan, case a). On the right, the spectral evolution of the RF probe detected signal versus the pumping wave power. Sub-harmonics generation is evident already at around 40 W; the image was plotted in logarithm colour scale.

For the quantitative estimation, the I_S parameters have been calculated

for each configuration. The plot of I_S versus RF power is shown in figure 5.2, displaying a clear increase of I_S, as expected, but anyway without any evident jump or non-linearity.
$I_S > 0$ condition occurs already at 40 W, and this is consistent with the direct observation of SA recorded spectrum, shown in fig.5.1.a).
Figure 5.2-right illustrates the RF probe detected signal via SA analysis, when increasing the pumping wave power: the red line represents the pumping frequency (TWT only @ 13.80 GHz) whilst the green shadows are the sub-harmonics, i.e. the plasma-self generated waves due to the instability onset. It is possible to observe how these additional components become more and more intense and their number increases for higher TWT powers. A "*down-shift*" of the emitted frequencies is also evident.
Also in fig.5.3, which is the 3D plot of the RF probe detected signal, analysed through the SA (it is equivalent to the pseudo-colours plot of figure 5.2-right), it is possible to observe the increase of characteristic sub-harmonic peaks for higher power.

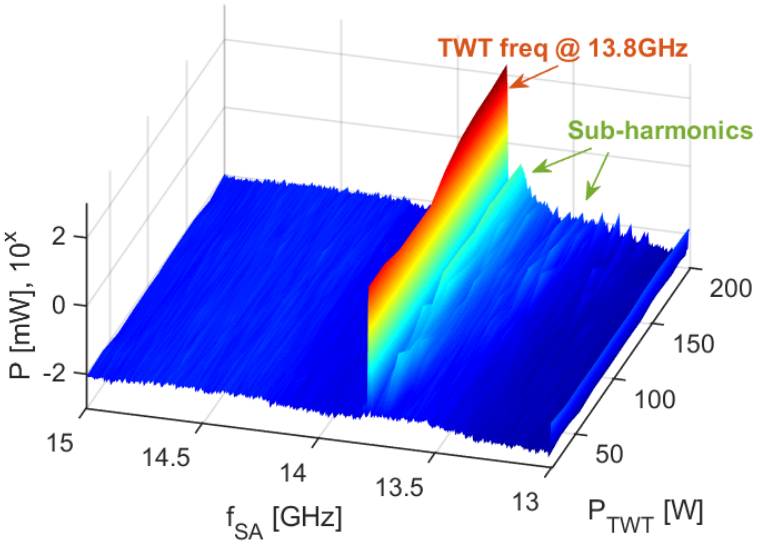

Figure 5.3: 3D plot of the RF probe detected signal, analysed through the SA. This plot is equivalent to the pseudo-colours plot of figure 5.2-right. The image was plotted in logarithm colour scale.

5.2.2 RF spectra in SFH - Frequency scan @ 200 W

The trend of I_S versus the RF frequency displays a frequency-dependent behavior (see figure 5.4).

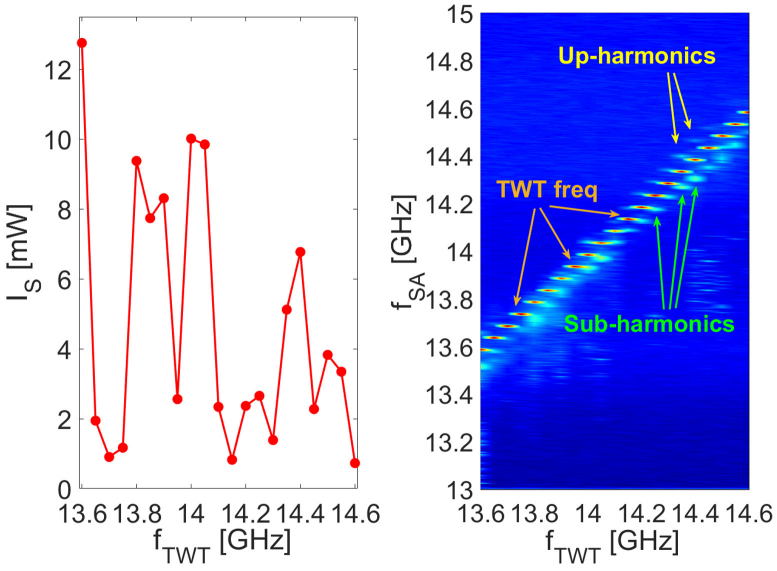

Figure 5.4: Left - Trend of I_S parameter during the one-frequency scan, case b); right - spectral structures as detected by the SA at different frequencies, during the single frequency scan; the image was plotted in logarithm colour scale.

This is the first time [11] the frequency tuning was systematically explored for the instability. I_S mirrors the strongest instability at the lowest frequency we used, i.e. 13.60 GHz. Even in this case, this is in agreement with the direct experience, both looking to the raw spectrum and to the general conditions of the source (at 13.60 GHz it has been obtained the largest high-energy X-ray flux, the largest total X-ray dose, etc.). This is also consistent with the fact that at 13.60 GHz the source is operated well above the $\frac{B_{min}}{B_{ECR}}$ threshold that is universally considered as the *trigger* for the instability onset [48, 76]. Anyway, the plot shows that the frequency also (and not only the RF power and $\frac{B_{min}}{B_{ECR}}$ value) affects the instability strength. The I_S parameters have been already shown, and discussed as

example, in the table 4.4 of chapter 4 listing separately the two contributions of the total number of subharmonics N_{sub} and of the total power integral of plasma self-generated sub-harmonics P_{sub}. Also several RF spectra of this configuration were already shown, in the fig. 4.44. Even if P_{sub} at other frequencies (i.e., $f_{TWT} = 14.05\ GHz$ or $f_{TWT} = 14.00\ GHz$) is higher than the one at $f_{TWT} = 13.60\ GHz$, considering also the number of sub-harmonics N_{sub}, the I_S parameter results to be smaller.
Also by looking at the plot 5.4 it is more evident why the integral only was not enough for evaluating I_S: in fact in the case of 13.60 GHz there is a higher number of sub-harmonics, with a lower emitted power, but many sub-harmonics are widely spread in frequency, with peaks at a distance of more than 0.5 GHz. The "*drop*" below the pumping-frequency (the pumping frequency lies all along the line y=x) gives just a qualitative indication about the instability strength which is not only related to the amplitude of the "*down-chirped*" spot, but also to the frequency spread of the self-generated sub-harmonics. This effect is included in the above mentioned numerical definition of I_S (as already discussed in 4.2.1).

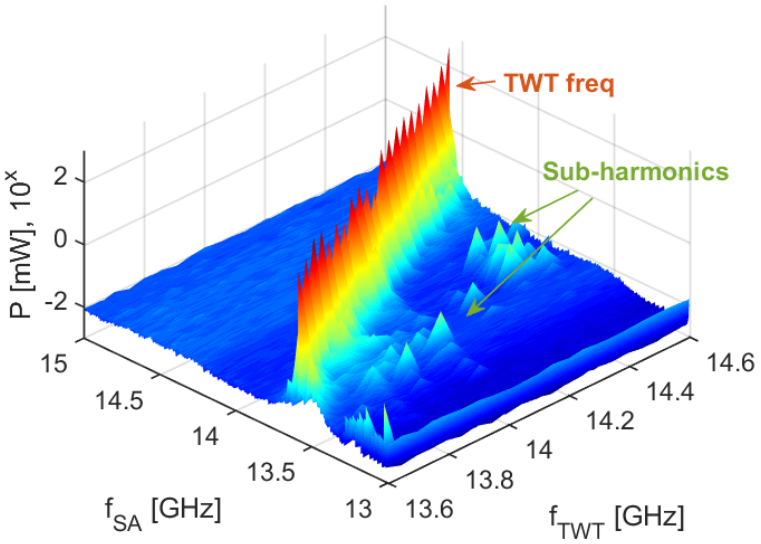

Figure 5.5: 3D plot of the RF probe detected signal, analysed through the SA. This plot is equivalent to the pseudo-colours plot of figure 5.4-right. The image was plotted in logarithm colour scale.

Also in figure 5.5 (3D plot of the RF probe detected signal analysed through the SA, equivalent to the pseudo-colours plot of figure 5.4-right) it is possible to observe characteristic sub-harmonic peaks. Another very interesting result is that instabilities generate sub-harmonics for all the selected frequencies by the TWT; the emitted radiation is predominantly at lower frequencies than the plasma heating frequency (as previously measured also in [29]), and some up-harmonics appear for higher frequencies only (in particular, above 14.20 GHz, see fig. 5.4). These plots demonstrate that, despite our definition of I_S was difficult, it seems to follow in a reasonable way what happens in the plasma in more or less unstable conditions (depending on the power, magnetic field and frequency).

5.2.3 RF spectra in TCFH - Frequency scan @ 200 W

The trend of RF spectra versus the frequency scan in the TCFH is shown in figure 5.6.

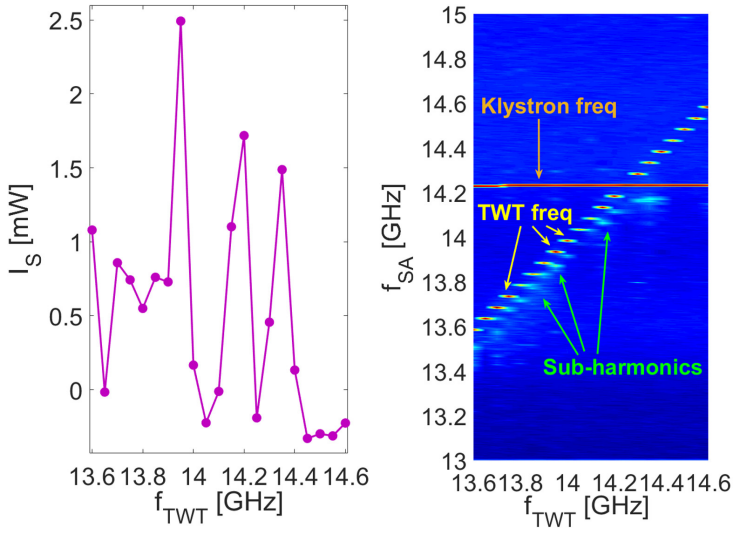

Figure 5.6: Left - trend of I_S parameter during the two-frequency scan, case c). Right - spectral structures as detected by the SA at different frequencies, during the double frequency scan (Klystron at fixed frequency, TWT varying from 13.60 *to* 14.60 GHz); the image was plotted in logarithm colour scale.

The plot shows that sub-harmonics in unstable regimes are always at frequencies below the lowest one of the two. In other words, in TCFH mode, up-harmonics disappeared everywhere, for any frequency.
If compared it with the SFH case, this result is really relevant. In such a configuration, most of the plasma self-irradiated energy in the RF domain came from the inner plasmoid regions, i.e. from regions of the plasma where $B < B_{ECR1}$. Evidence of an increase of the electron confinement inside the plasmoid region are argued, and interesting results confirming them, by means of the X-ray imaging, will be presented in the section 5.3.

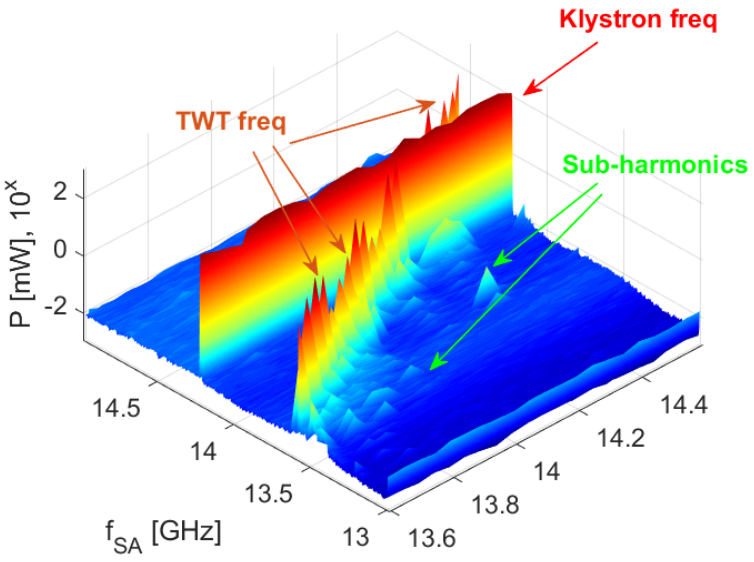

Figure 5.7: 3D plot of the RF probe detected signal, analysed through the SA. This plot is equivalent to the pseudo-colours plot of figure 5.6-right. The image was plotted in logarithm colour scale.

Also in figure 5.7, the 3D plot of the RF probe detected signal analysed through the SA, equivalent to the pseudo-colours plot of figure 5.4-right, it is possible to observe spectral structures as detected by the SA: it is possible to highlight the two different pumping frequencies and the characteristic sub-harmonic peaks.

5.2.4 RF spectra in TCFH - Power balance @ 13.8 GHz + 14.25 GHz @ 200 W

The RF spectra versus the power balance plot (figure 5.8) show that instabilities increase very much for higher power of TWT.

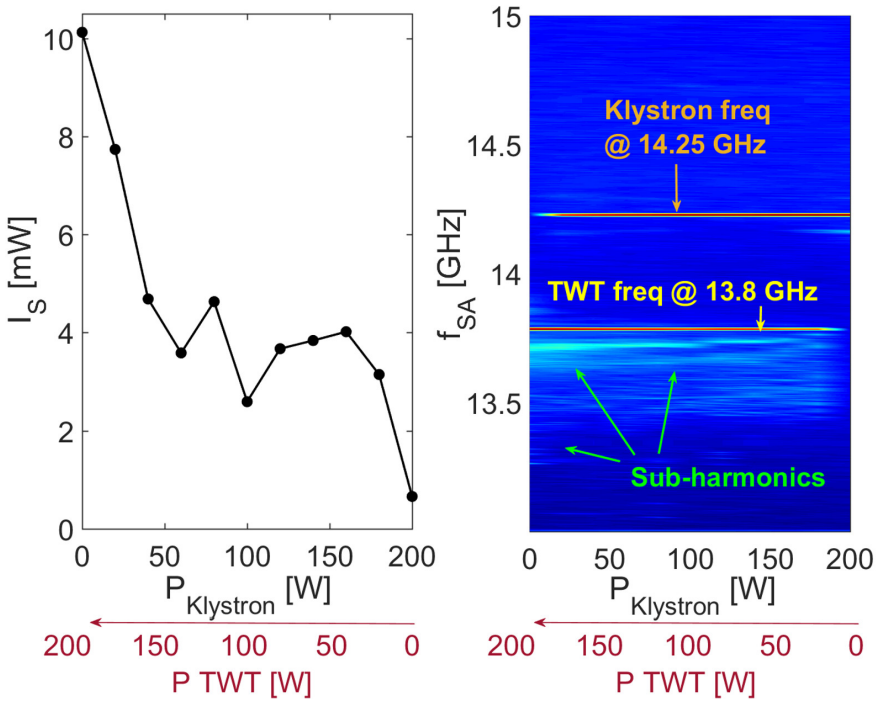

Figure 5.8: Power Balance scan in case of TCFH, case d); instability strength increases at increasing TWT power, as confirmed by the microwave spectrum depicted on the right; the image was plotted in logarithmic colour scale.

This result was somehow expected since the TWT frequency 13.80 GHz is much unstable due to the fact that $\frac{B_{min}}{B_{ECR}}$ value is closer to the instability threshold than the Klystron frequency at 14.25 GHz.
Figure 5.9 is equivalent to the pseudo-colour plot of figure 5.8 (right), and it is possible to better highlight characteristic sub-harmonic peaks.
Also these plots show that sub-harmonics in unstable regimes in TCFH are always at frequencies below the lowest one of the two.

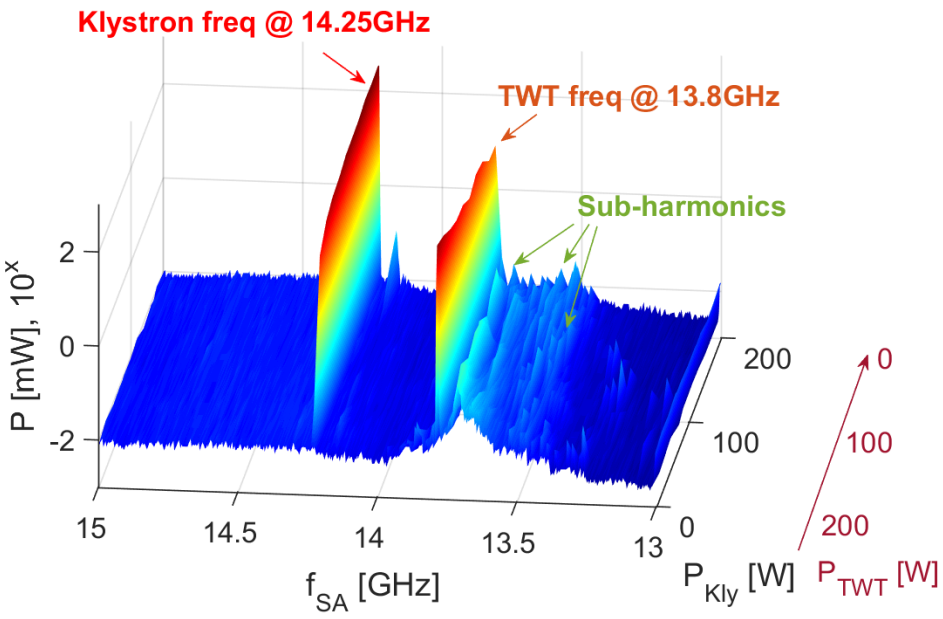

Figure 5.9: 3D plot of the RF probe detected signal, analysed through the SA. This plot is equivalent to the pseudo-colours plot of figure 5.8-right. The image was plotted in logarithm colour scale.

5.2.5 Instability damping by TCFH

In figure 5.10 we directly compare the I_S parameter in single frequency and in two close frequencies heating mode: it is possible to observe that the instability strength drops dramatically, confirming that the TCFH is able to damp the instabilities.
Figure 5.11 highlights the instability damping at 13.90 GHz and 200 W, which was a very unstable regime. It is clear that at this operative frequency plasma is highly unstable already at low power levels. Anyway, the addition of the second wave, coming by the Klystron, damps the instability even if the total amount of power reaches 200 W (120 W by the TWT plus 80 W by the Klystron).
This means that the instability can be damped by TCFH even if the second frequency brings additional RF power into the system.

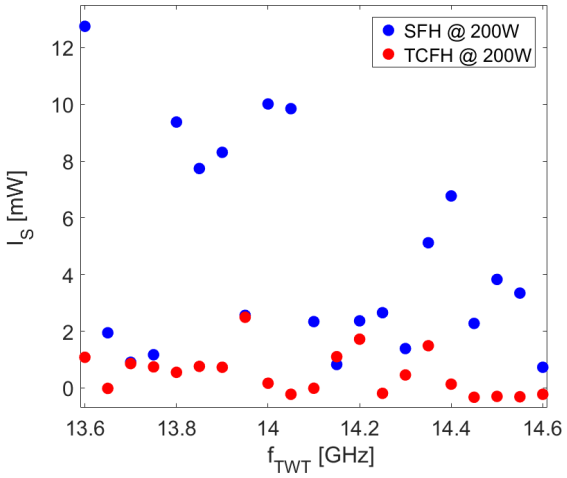

Figure 5.10: Comparison of the I_S parameter for SFH and TCFH, at fixed power. TCFH damps the instability almost over the entire frequency set.

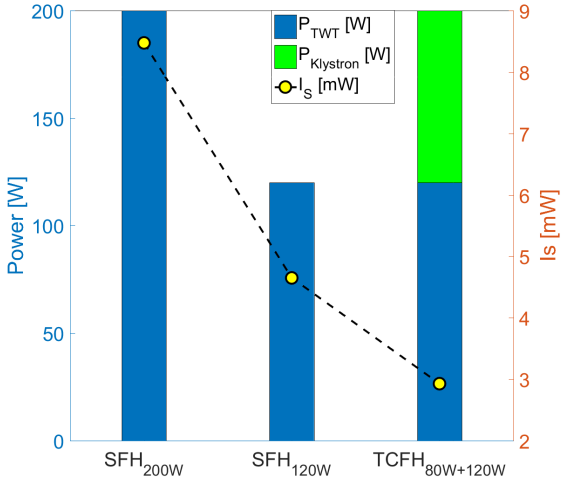

Figure 5.11: Histograms showing the RF power provided in SFH (only TWT @ 13.90 GHz) or in TCFH mode by the two generators (TWT @ 13.90 GHz + Klystron @ 14.25 GHz). Yellow dots are the relative I_S factor. The combination of two frequencies is in this case more stable than a single one, even if the power was increased of almost a factor 2.

It is possible to observe the same experimental evidence of instability damping also in the case when the TWT frequency was 14.50 GHz (figure 5.12). These results highlight that a key role for damping turbulences and increasing the electron confinement inside the "*plasmoid region*" is played by the TCFH.

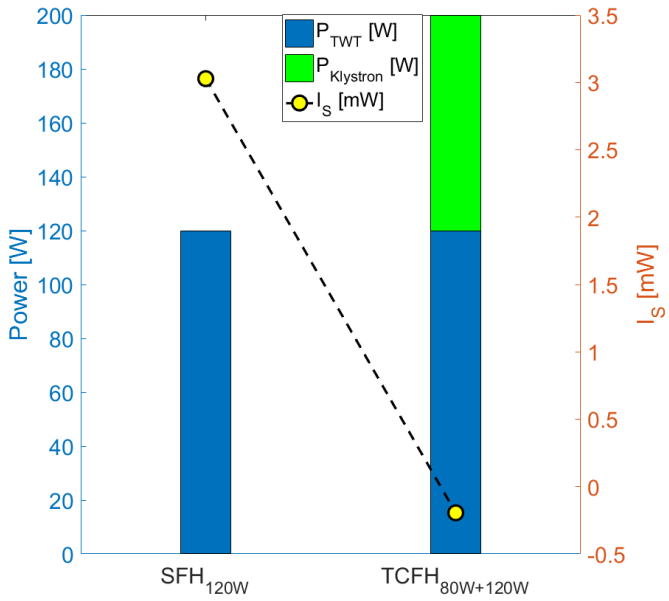

Figure 5.12: RF power provided in single-frequency (only TWT @ 14.50 GHz) or double-frequency mode by the two generators (TWT @ 14.50 GHz + Klystron @ 14.25 GHz). Yellow dots are the relative I_S factor. The combination of two frequencies is in this case more stable than a single one, even if the power is increased of almost a factor 2.

Data shown especially in figure 5.10 demonstrate that the instability suppression is effective almost over the entire investigated frequency spectrum. We investigated the trends of the ΔI_S (giving the effectiveness of damping ΔI_S=$I_S(SFH) - I_S(TCFH)$) versus the used $\delta\omega$, as illustrated in figure 5.13. From analysis of figure 5.10 it comes out that I_S data are quite scattered versus the TWT frequency. This is due to the frequency tuning effect that superimposes to the more or less intensity of the instabilities. Therefore we consider only very unstable regimes in SFH, for which the I_S parameter is high in absolute in order to see if under this

condition the instability effects dominate on the frequency tuning.
In this perspective, the selection is done by looking to those frequencies only featuring a significant variation in the equilibrium state of the plasma (from stable to unstable, and viceversa) when going from SFH to TCFH. A 3σ level on the fluctuation of I_S in TCFH mode can be inferred as the threshold above which we can consider ΔI_S versus $\delta\omega$ plot. Under this assumption (the threshold is around 2 mW), a weak but meaningful trend appears in figure 5.13. That is in agreement with what expected by the theory (as described in the section 1), namely by the estimation of $\delta\omega$ range over which the TCFH should be effective.

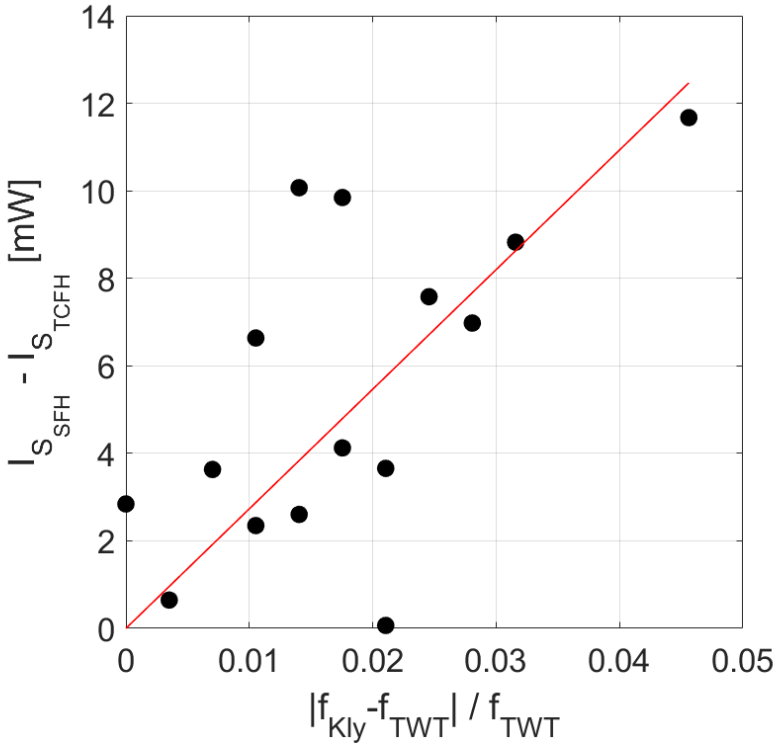

Figure 5.13: Trend of the instability suppression efficiency, in terms of ΔI_S, vs. the $\delta\omega/\omega$ considering the Klystron frequency as reference (14.25 GHz).

The basic assumptions on the quasi-linear diffusion (discussed in de-

tails in the section 1.3.2) are in qualitative agreement with the experimental observations. Summarizing, from theory comes out that the TCFH plays a relevant role in making less anisotropic the EEDF. From the relation 1.25 it follows that the parallel diffusion is enhanced, and strong enhancement is also expected for increasing the power on the lower frequency, due to the term $\frac{\mathcal{E}_2}{\mathcal{E}_1}$, but the predominant effect is anyway related to the different coupling of the global RF power, which directly affects the velocity jump δ_v: it now causes the δ_v scaling more than linearly with the RF power itself (i.e., as $\propto \mathcal{E}^{12/5}$).
The experimental results show that the most effective damping, in fact, as shown in figures 5.11 and 5.12, was obtained when applying even a higher power than single frequency operations, when normally the instability growth non-linearly with the power itself. Despite the total amount of power was increased of about a factor 2, the I_S parameter collapsed. In addition, figure 5.13 shows that the damping appears to be more effective, on average, at larger $\delta\omega/\omega$, again in agreement with the increase of parallel diffusion of equation 1.25.
In summary, the TCFH seems to be able to reduce the regions of velocity space where $\frac{\partial f(v_\perp)}{\partial v_\perp} > 0$ due to the much more efficient balancing of $\frac{T_\parallel}{T_\perp}$ ratio. This argument also helps to find a reasonable explanation to the spectral structure of the self-emitted radiation when the instability is active also in TCFH mode. Every time the emission has been observed to occur at frequencies lower than the lowest of the pumping frequencies. Considering the main claims of the quasi-linear theory, the diffusion in parallel velocity is expected to be maximal in the gap between the two pumping frequencies. There, the $\frac{T_\parallel}{T_\perp}$ ratio should be thus minimal, minimizing the amount of electrons able to support the instability and its related RF emission. As a consequence of the above arguments, anyway, also the particles losses into the loss-cone should be enhanced as well in TCFH mode. This probably explains the only moderate effect provided by the TCFH mode on the ion source's performances, as referred to in [12]. The TCFH should eventually results in broadening up the islands of

stability for an ECRIS, and other techniques could be applied for boosting further their performances.
Assuming the main action of TCFH is on the enhanced parallel diffusion, the study of plasma confinement and losses during SFH or TCFH mode has been carried out. In particular, it is interesting to measure fluxes of electrons escaping the magnetic trap during TCFH since the quasi-linear theory predicts average energy per particle lost scaling versus the discharge parameters, according to the following formula:

$$E_L = 2/3 \left(\frac{\delta\omega}{\omega} \right)^{1/3} M^{1/4} \Delta v^2 \tag{5.1}$$

The the pin-hole camera tool is suited for this purpose and is able to detect energies of electrons lost from the trap and impinging on the plasma chamber walls. The aim of separating electrons from enhanced parallel diffusion from the ones typically released as precipitation from the magnetic trap during the instability is accomplished with energy filtering, consequently via X-ray imaging in photon counting mode.

5.3 X-ray imaging results: stable vs. turbulent plasma

The measurements with the X-ray pin-hole camera for studies of the plasma structure and the intensities of the electron losses, will be commented in this section. Space resolved soft X-ray analysis have been performed in order to investigate dynamics of plasma versus plasma loss emissions, and to verify how the plasma turbulence and the TCFH induced parallel diffusion in the velocity space affect the plasma confinement and loss dynamics. These results will be discussed in the sections 5.3.2 and 5.3.3.
Moreover, the integrated X-ray imaging has been used to estimate the plasma radius and for characterizing the plasma structure versus the magnetic confinement and other operative configurations (see section 5.3.1). Details of correlations with other parameters (CSD, soft and hard volumetric X-ray measurements) are instead provided in [12].
To study the plasma shape and the loss dynamics the X-ray pin-hole camera has been used in spectrally integrated mode, collecting images with 50 *sec* of exposure time. As already mentioned, energy separation of the events is not possible in this case, however images are revealing the energy content of the plasma and plasma chamber complex important to study loss dynamics. In this section we deal with SpI images.

An example of acquired SpI image is shown in figure 5.14. The image was collected with an exposure time of 50 seconds, at 1 MHz of readout rate and using the full-frame (1024x1024 pixels) acquisition mode.
Several ROIs have been selected in order to distinguish among plasma emission and walls radiation, distinguishing among X-rays coming from the extraction Ti endplate from the ones coming from the lateral Ta walls. All the X-rays coming from branches and poles are deemed to come from bremsstrahlung and X-ray fluorescence radiation due to plasma lost electrons impinging on the metals of the plasma chamber.
In particular:

- white and blue rectangles enclose the regions where the X-photons are deemed to come from Ar-fluorescence;

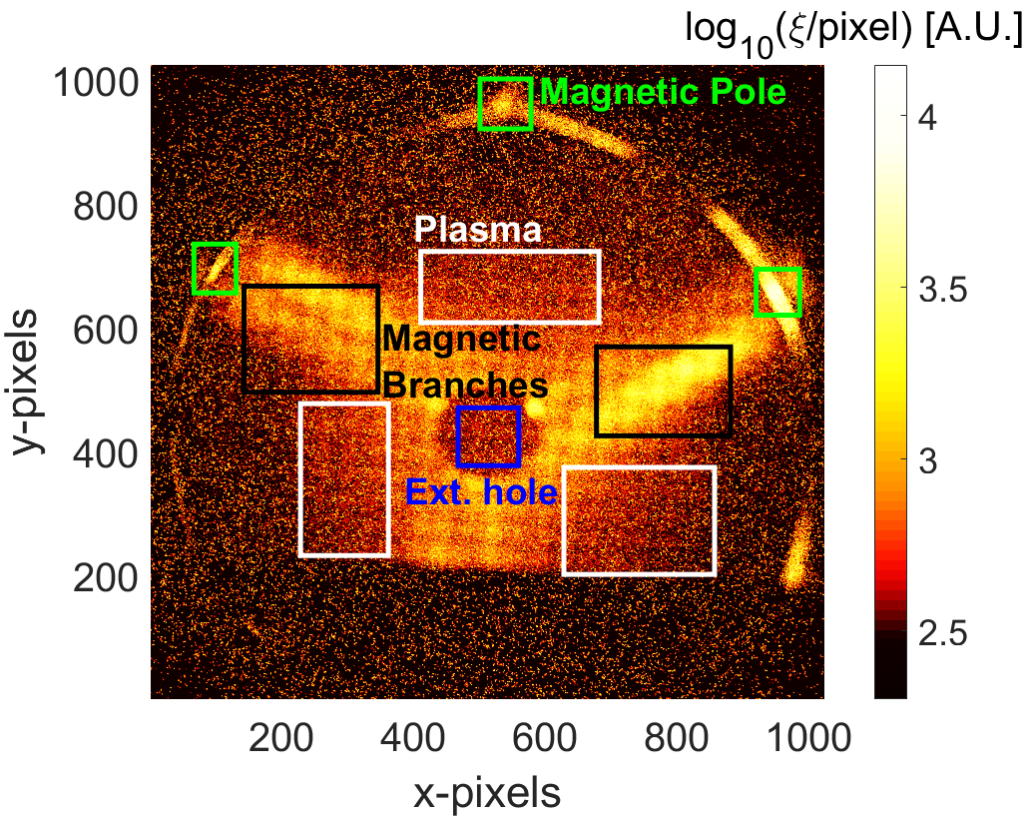

Figure 5.14: Pseudo-colour representation of X-ray flux (in logarithmic scale), coming from several plasma regions, including radiation coming from the extraction endplate, hot spots at the magnetic pole sites on the lateral chamber walls, the extraction hole and the plasma emission.

- black squares highlight the so-called *branches*, i.e. the regions where photons are coming from extraction endplate bremsstrahlung caused by plasma escaping electrons along the axial loss cones;

- green and smaller squares indicate the regions where the magnetic field lines intercept the lateral walls of the plasma chamber.

An example of a power scaling of the integrated images is shown in figure 5.15 (RF frequency = 13.80 GHz) where the pumping RF power is varied from 20 W to 200 W at step of 20 W (case (a) of the table 4.4).

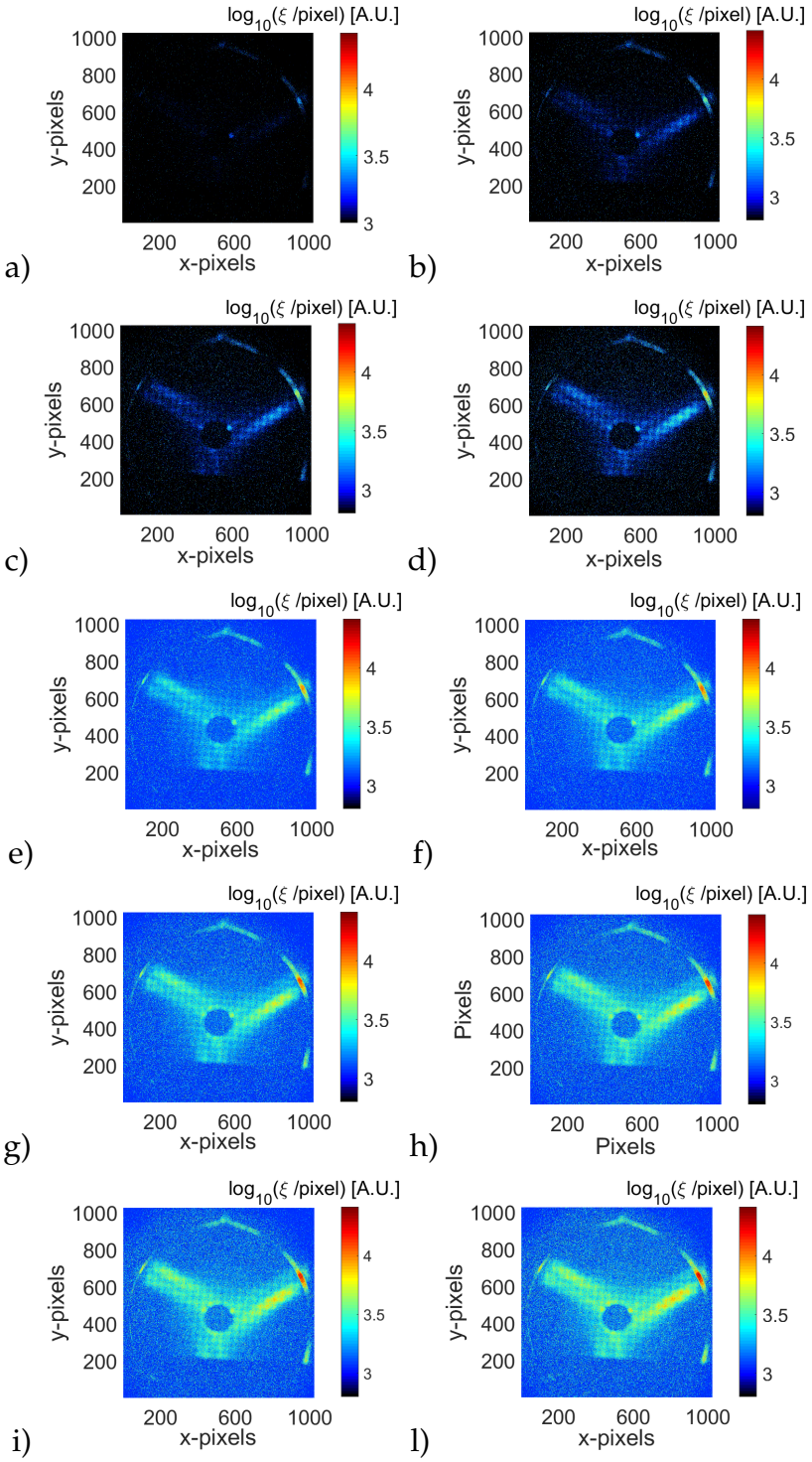

Figure 5.15: Pseudo-colour representation of X-ray images (in the same logarithmic scale) of the SFH power scan at frequency of 13.80 GHz and power from 20 W to 200 W at step of 20 W, from a) to l), respectively.

From a visual inspection it is possible to highlight how the energy content changes versus the pumping power. In particular, the flux coming from the axial and radial losses increases significantly at higher powers compared to the flux coming from Ar plasma core.
Another sequence of 2D SpI images of the power scaling at the frequency of 13.90 GHz in SFH varying the power from 40 W to 200 W at step of 40 W, is shown in the figure 5.16.

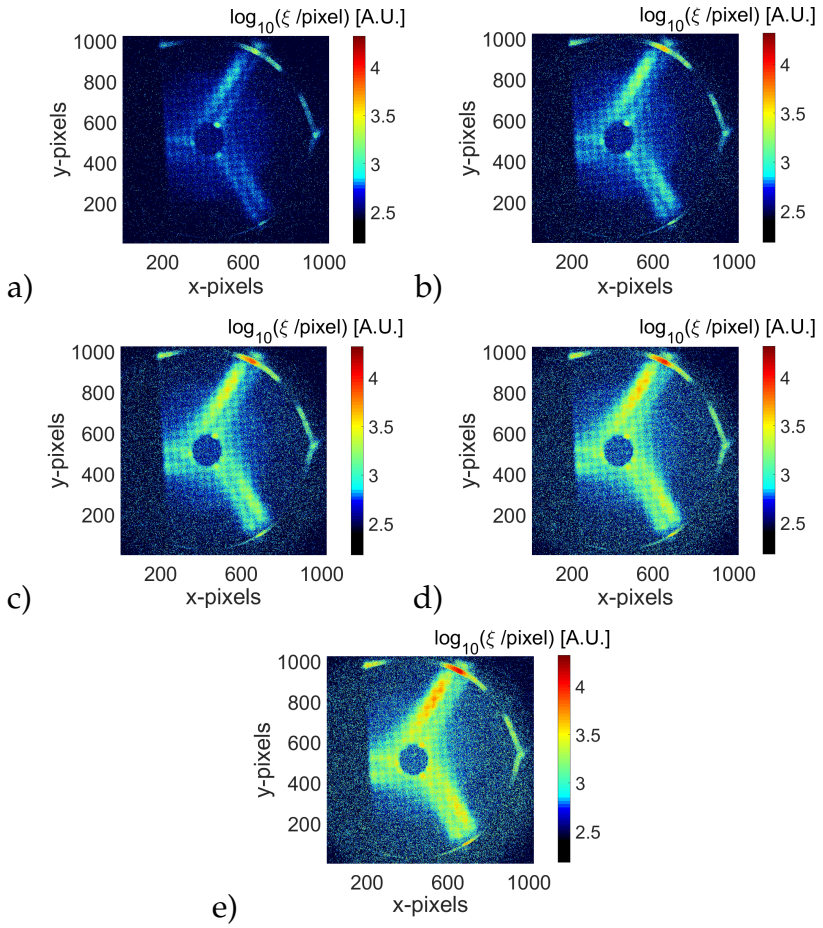

Figure 5.16: Pseudo-colour representation of the X-ray flux (in logarithmic scale) for a sequence of configurations: SFH using a TWT pumping frequency of 13.90 GHz and a net power from 40 W to 200 W at step of 40 W. a) 40 Watt. b) 80 Watt. c) 120 Watt. d) 160 Watt. e) 200 Watt.

5.3.1 Effect of the axial confinement and plasma radius evaluation

The analysis of the spectrally integrated images, besides investigating about dynamics of plasma losses, allows for mastering, likely *"on line"*, the changes of plasma structure and morphology and performing an evaluation of the plasma radius.
As an example, the analysis of plasma images taken at different axial field strengths are presented. In the figure 5.17 the images acquired in three different configurations are shown for changing coils current. In the figure 5.17.a), 5.17.b) and 5.17.c) both coil currents have been set to 60%, 80% and 100%, respectively (the 100% corresponds to 500 *Amperes*).

The images shown in fig. 5.17 are the only ones presented in this work that have been acquired without using the *multi-disks* collimator (see the section 3.2.3), in order to highlight the effect of the strong confinement and high microwave power on the image quality. In contrast, all other images shown in the previous sections and in the next ones have been acquired using the *multi-disks* collimator. From a preliminary examination, it is possible to observe how the plasma changes size and energy content: in the case a) the plasma (blue clouds between the loss-branches) covers all the plasma chamber volume and it is not too intense, since the axial magnetic field profile is the widest, providing weaker confinement. On the other hand, in the case c), the plasma is confined in a smaller volume, and it is possible to observe from the image that it has a very high energy content, resulting in a high-intensity X-ray emission.
A problem with this configuration is that the scattering effects are not negligible and they dominate in all the pixelated matrix as a noise contribution. The case b) depicts a middle-point between the case a) and the case c).
Further details can be obtained by observing the figure 5.18.
Zoomed-in images of the graphs in figure 5.17 has been performed and analysed, considering a down-sized matrix of [650 x 120] pixels in the central region of the images, shown in figure 5.18 on the right. On the left, the corresponding density distribution along the x axis (considering the mean value for the 120 pixels in y) are shown.

It is possible to distinguish the periodic grid-like modulation, caused

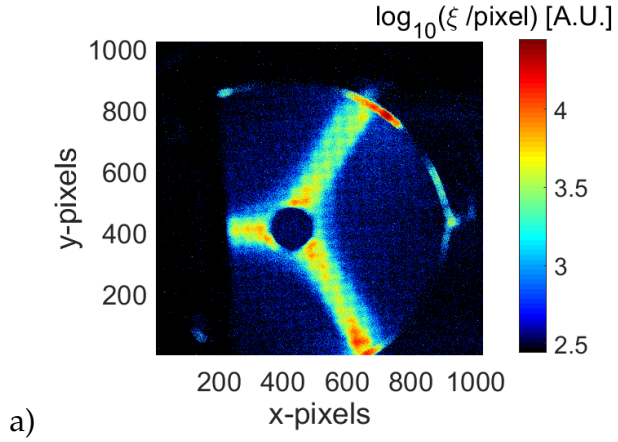

a)

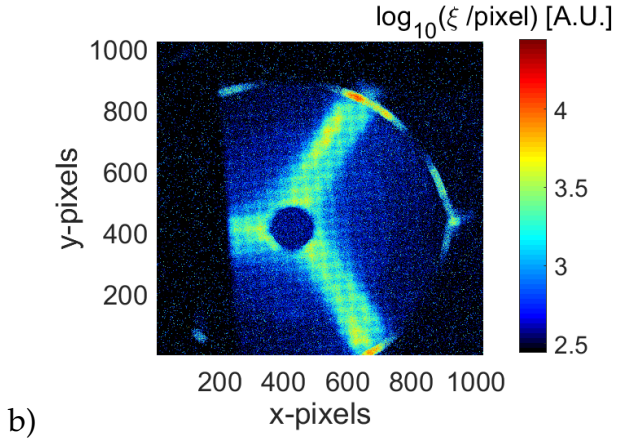

b)

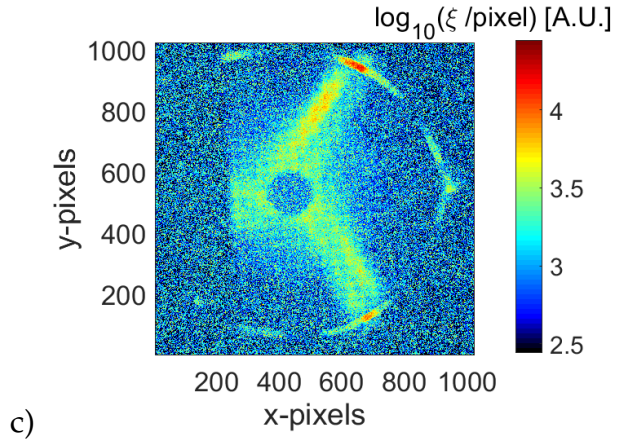

c)

Figure 5.17: Pseudo-colour representation of X-ray images (in logarithmic scale) for three different operation configurations of the magnetic field: a) 60% of the coil current, b) 80% of the coil current, c) 100% of the coil current.

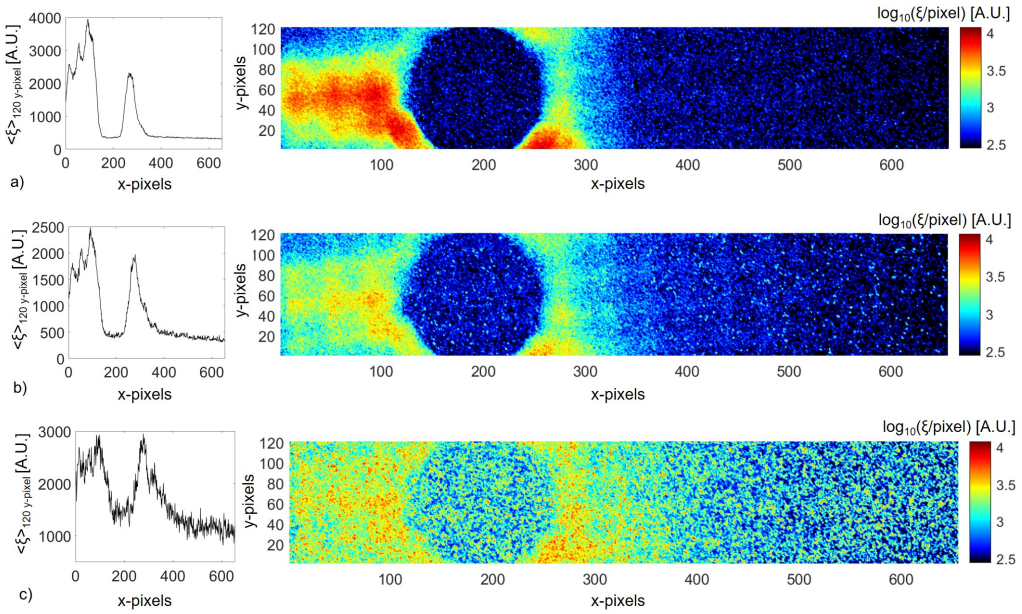

Figure 5.18: Right - Zoomed-in X-ray images for three different operative configuration of the magnetic field: a) 60%, b) 80%, c) 100% of the coil current. Left - Corresponding density distribution along the x axis

by the mesh structure of the Aluminum plate (shown in figure 3.16 of chapter 3, on the left) very well in the case a) only, for which the spatial resolution is very high. It is possible to argue the structure in the case b) also for which the resolution is still good, but, in the case c), the spatial resolution becomes very bad and it is impossible analyse the plasma spatial structure; moreover, in this last case, the scattering effects dominate and reduce a lot the ratio signal over noise. These are the main reasons for which X-ray spatial-resolved spectroscopy is very challenging and has never been done before with high RF pumping power: in 2014 space resolved X-ray spectroscopy was already performed, although with an order of magnitude lower RF power than the actual one (30 *Watt* versus 200 *Watt*) [78], [79]]. Only by installing the multi-disc collimation system it has been possible to remarkably increase the signal-to-noise ratio and the spatial resolution in these energetic plasma cases.

Plasma radius evaluation

Determination of the plasma radius was performed by studying the line distribution along some ROIs of a given image (as an example that has been considered is the configuration in SFH, at 13.90 GHz and 40 W). We chose a ROI of [1024x80] pixels (shown by the red rectangle in the fig. 5.19) and considered the mean of the 80 pixels along the y axis. We evaluated the line distribution along a column also, choosing a ROI of [80x1024] pixels (as shown by the green rectangle in the fig. 5.19) and determine the mean of the 80 pixels along the x axis. The two plots are shown in fig. 5.19.a) and 5.19.b) respectively.

In the two graphs the black and blue lines represent the mean value of X-ray flux coming from Argon plasma only and flux due to scattering noise, respectively.

They have been calculated considering:

- for the plasma emission, the mean value of a ROI placed in the centre hole (where there is not X-ray flux coming from the plasma chamber walls, since it corresponds to the extraction hole);
- for the scattering noise, the mean value of a ROI placed in the first two hundred pixels along the x axis where we can neglect any other contribution.

From the intersection of the plots and the black line it is possible to estimate the plasma radius in three different points of the image (shown as yellow dots: one in the graph 5.19.a) and two in the graph 5.19.b)). Plasma radius values estimated by the two intensity profiles reported in the table 5.2, with the mean value also.

The mean plasma radius is determined to be 16.04 $\pm$ 1.44 mm, which is compatible with the expected considering the magnetic field profile that confined and shaped the plasma. Using the realistic magnetic field of the Atomki-ECRIS the radius of the ECR-ellipsoid at 13.90 GHz is 15.5 mm. The slight difference may arise from the camera perspective.
The circumferences with the three different radii are shown in the image in fig. 5.20. It is observed that they are in good agreement and the maximum difference of radius amount to 0.48 mm. Considering additional

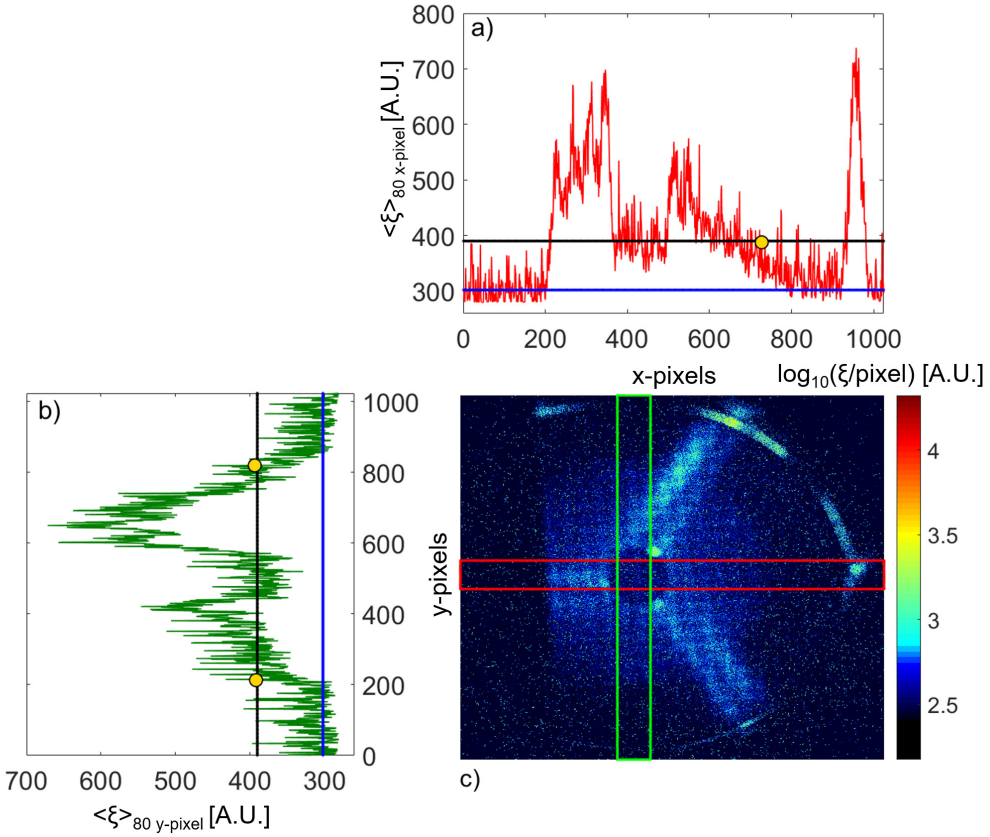

Figure 5.19: Pseudo-colour representation of the X-ray flux from the experiment with $P = 40\ W$, 13.90 GHz. The two ROIs indicate the regions where the intensity profiles have been evaluated. a) The intensity profile along the row. b) The intensity profile along the column.

intensity profiles in other ROIs it is possible to improve the plasma radius determination (by increasing the *statistics*).
By using two CCD pin-hole camera setups simultaneously (one along the axial line, another along the radial one) it will be possible to estimate the plasma volume and the plasma shape.
Typically it is not possible to radially investigate the plasma properties, since there is the hexapole which avoids any line of sight to install diagnostic tool. Whilst, the innovative $PANDORA_{Gr3}$ plasma trap (as will be

Table 5.2: Plasma radius estimated by means the two distributions are shown in figure 5.19, and the mean value.

	Plasma Radius [mm]
I point$_{Intensity\ profile\ fig.5.19\ a)}$	15.77 ± 2.24
II point$_{Intensity\ profile\ fig.5.19\ b)}$	16.25 ± 1.92
III point$_{Intensity\ profile\ fig.5.19\ b)}$	16.10 ± 1.92
Mean value	16.04 ± 1.44

shown in the chapter 6) will contain 18 radially lines of sight, allowing for a detailed determination of the plasma volume and shape.

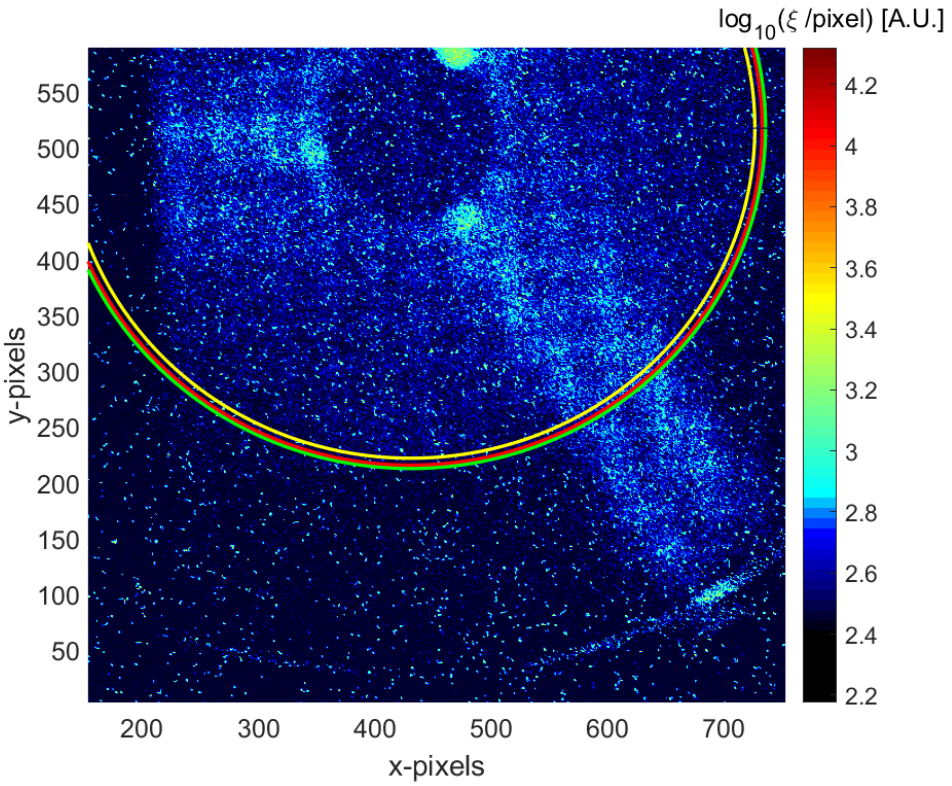

Figure 5.20: Zoomed-in image of the X-ray emission shown in the fig. 5.19 image, including the circumferences with the three different radius delimiting the plasma shape.

5.3.2 Study of Plasma losses vs. instabilities

In the figure 5.14 the ROIs illustrating the plasma losses on the chamber lateral walls and on the plasma electrode (green and black rectangles, respectively). Argon plasma related regions are marked by white rectangles. Data coming from each ROI have been taken for several investigated configurations and then plotted against the I_S parameter.
We have decided to plot the $\frac{L}{P}$ *ratio*, defined as the sum of counts in the branch plus pole regions (the losses L) divided by the sum of counts in the plasma ROIs (the plasma contribution P). The number of counts detected by the X-ray pin-hole camera is normalized for each ROI area. This ratio has been mathematically labelled as R_{LP}.
SFH power scan measurements are displayed in figure 5.21.a) on the left. It is clear that R_{LP} increases with the RF power, and the I_S parameter increases as well. That means, a direct correlation between plasma losses and instability can be argued. A similar trend is observed also in the case of TCFH power balance (figure 5.21.a) on the right).
In order to quantitatively evaluate the degree of correlation, R_{LP} versus I_S plots have been included in the figure 5.21.b). Data are displayed without any error-bar since the errors were negligible, they have estimated and are of about 0.1%. We fitted the data with a linear law and the correlation is confirmed by the R parameter, being $R = 0.93$ and $R = 0.75$, respectively, for the two configurations in SFH and TCFH.
Considering the number of points ($N = 10$) in the best-fit procedure, tables for statistical consistency say this value provides a very high probability of dataset correlation to the linear law for the SFH case with a very high significant correlation, and an high probability for the TCFH case with a significant correlation.

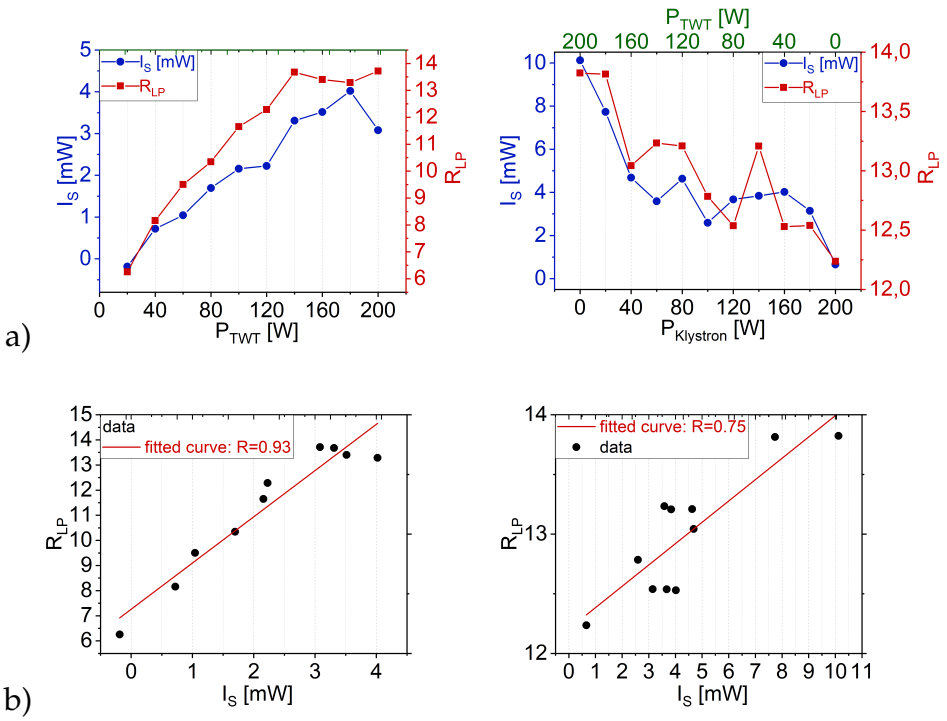

Figure 5.21: a) - Trend of the R_{LP} of total counts detected by the X-ray pinhole camera vs. (left) SFH power; (right) TCFH power balance. In any figure, I_S parameter is also plotted. b) - Correlation plots of the R_{LP} vs. I_S parameter; the line corresponds to the linear fitted curve. (Left) SFH power scan (very high significative correlation: $R = 0.93$); (right) TCFH power balance (significative correlation: $R = 0.75$). R_{LP} are displayed without any error-bar since the errors are negligible, of about 0.1%.

Plot of I_S and R_{LP} trends for the frequency scan in SFH and TCFH are displayed in figure 5.22.a). Even if the correlation plots, displayed in figure 5.22.b), show a no correlation at all both in SFH and in TCFH, in these cases it is possible to distinguish two domains of frequencies.
We performed two different correlation plot of the data distinguishing frequencies lower than 13.90 GHz 5.22.c) and frequencies higher than 13.90 GHz 5.22.d). We find a weakly correlation in SFH only for lower frequencies (R parameter is 0.65) but not for higher frequencies ($R = 0.09$). No correlation at all was found in TCFH scan ($R = 0.21$ for lower frequencies, $R = 0.24$ for higher frequencies).

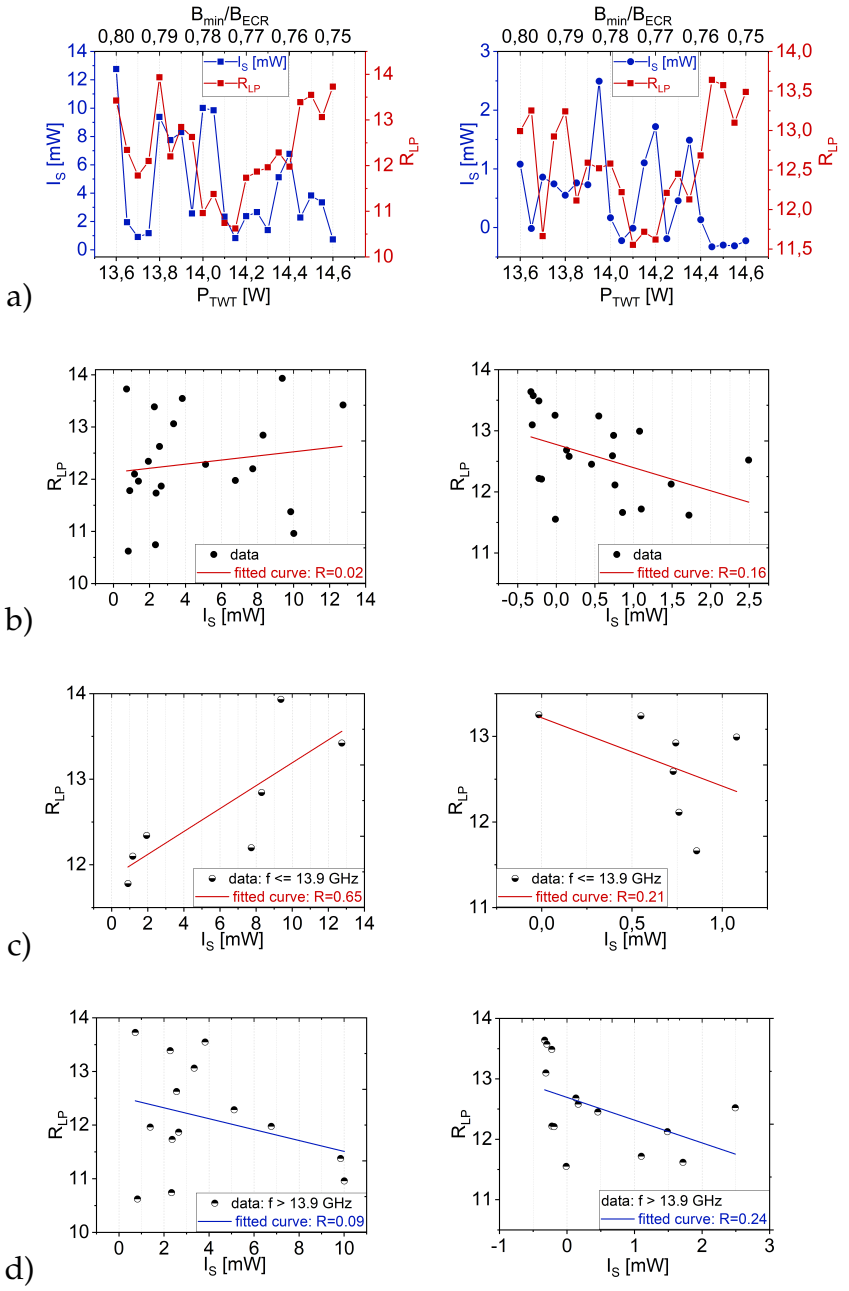

Figure 5.22: a) - Trend of the R_{LP} of total counts detected by the X-ray pin-hole camera vs. (left) SFH, frequency scan; (right) TCFH scan. I_S parameter is also plotted. b) - Correlation of R_{LP} vs. I_S linear fit. (Left) SFH, frequency scan (no correlation, R=0.02); (right) TCFH scan (no correlation, R=0.16). c) Correlation plots only for frequencies lower than 13.9GHz; (Left) SFH, frequency scan (significant correlation, R=0.65); (right) TCFH scan (no correlation, R=0.21). d) Correlation plots only for frequencies higher than 13.9GHz; (Left) SFH, frequency scan (no correlation, R=0.09); (right) TCFH scan (no correlation, R=0.24). R_{LP} are displayed without any error-bar since the errors are negligible, of about 0.1%.

In the section 5.2, we have shown that the spectral structure of the self-emitted radiation behaves consequently when the instability is also active in the TCFH mode (subharmonics are detected along with the main frequencies); every time, the emission has been observed to occur at frequencies lower than the lowest of the pumping frequencies. As an example, we present the SA spectra recorded at single 14.25 GHz and at 14.25 $GHz + 13.9$ GHz double frequency heating mode in figure 5.23.

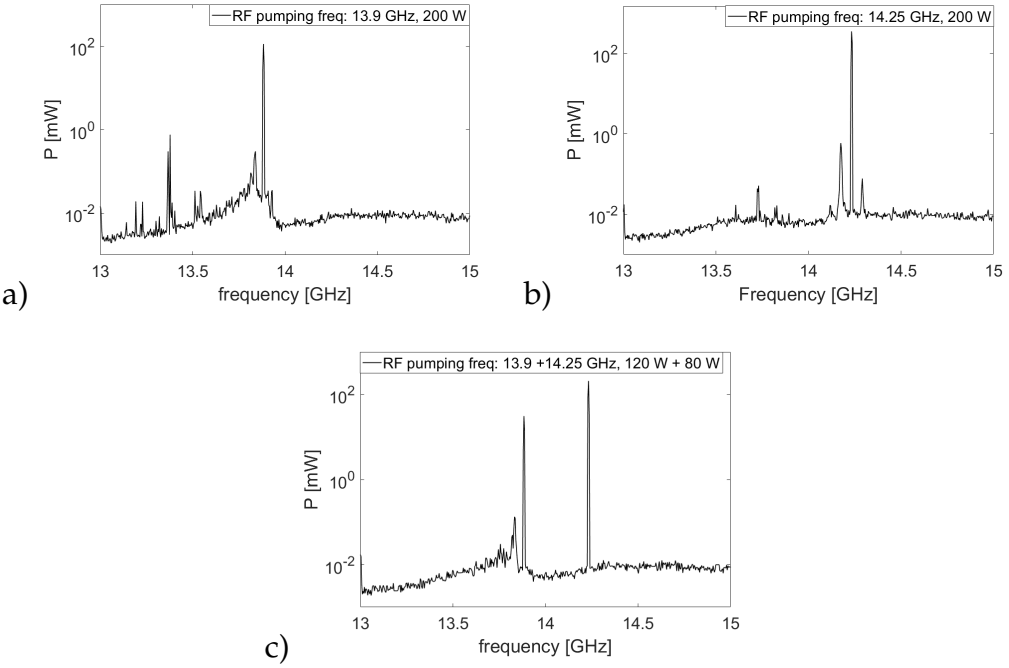

Figure 5.23: RF spectra measured by the spectrum analyser generated by: a) single (13.90 GHz, 200 W), b) single (14.25 GHz, 200 W) and c) double frequency (13.9 $GHz + 14.25$ GHz, 120 $W + 80$ W) operation mode.

These results indicate that the plasma density distribution is rearranged at TCFH mode, becoming denser in the central region of the plasma chamber (where the B-field is lower). To verify this dynamic process caused by the second frequency the counts measured in the plasma ROIs at different radial positions have been analysed. A parameter corresponding to the image to describe the degree of the centralization of the plasma has been introduced and defined. This parameter is calcu-

lated as the ratio of the (area normalized) ROI counts of central (blue ROI in the figure 5.14) and side (white ROIs in the figure 5.14) regions of the plasmoid. The higher this parameter, the plasma is more centralized. This parameter has been estimated both for single and double frequency scans. As a consequence of the second frequency it becomes about 10% more centralized. As an example the centralisation parameters and the I_S parameters are plotted corresponding to single and double frequency modes at 13.90 GHz, 14.25 GHz and 13.90 $GHz + 14.25$ GHz (200 W net power) in figure 5.24.

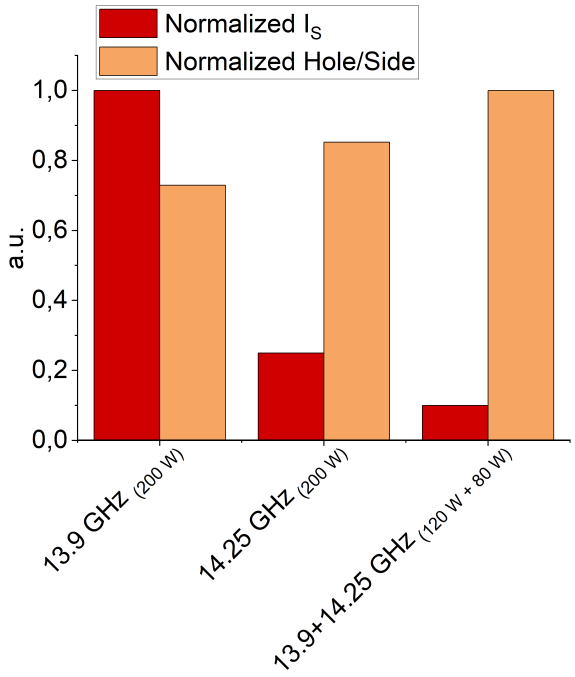

Figure 5.24: Centralisation parameter and the I_S parameters corresponding to single and double frequency modes at 13.9 GHz, 14.25 GHz and 13.9 GHz + 14.25 GHz (200 W net power).

Moreover this parameter has been calculated both for SFH and TCFH scans and we have compared them at those frequencies where the instability strength was pronounced (i.e. I_S parameter is higher than 7 mW) at single frequency operation mode. These frequencies are 13.60 GHz,

13.80 GHz, 13.85 GHz, 13.90 GHz, 14 GHz, 14.05 GHz. The corresponding centralization parameters are plotted in figure 5.25.

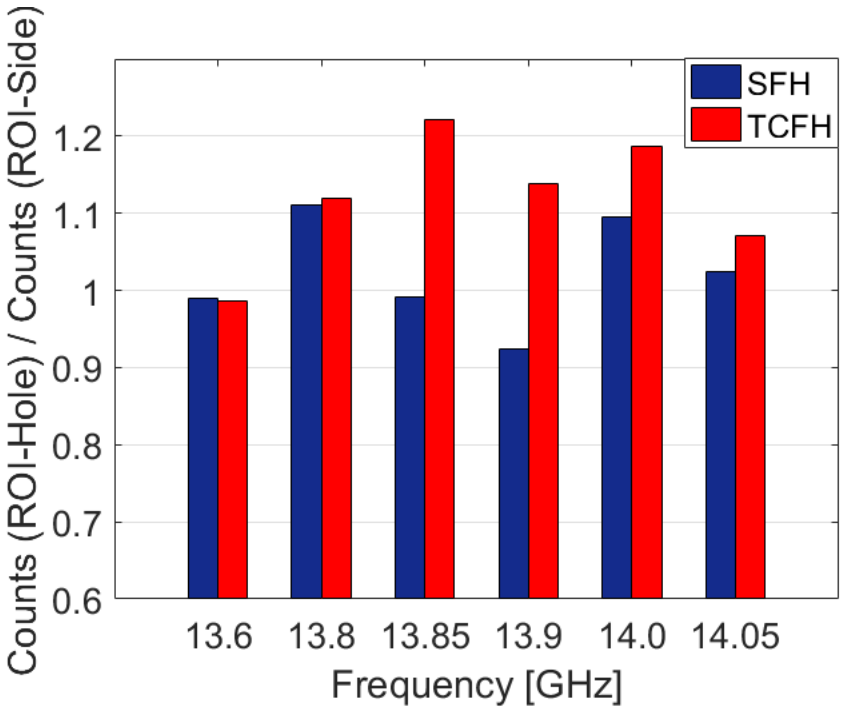

Figure 5.25: Centralization parameters at single and two frequency operation mode.

This figure together with the figure 5.10 clearly demonstrate that in two close frequency heating mode the instability is effectively damped by the second frequency, meanwhile the plasma is rearranged to be denser in a central region of the plasma. This observation is in good agreement with the tendency obtained from the RF spectra, presented in figure 5.23.

5.3.3 Impact of TCFH: comparison with simulations

As described before, the kinetic plasma instabilities are caused by the strongly anisotropic distribution of the plasma electrons in the velocity phase space, in particular the strength of the instability depends on the velocity space for which $\frac{\delta f(v_\perp)}{\delta v_\perp} > 0$. It has been discussed that, according to the quasi-linear theory of TCFH [52], is enhanced along $v_\parallel$ and it is described by the term expressed in the equation 1.25.
This diffusion rate is about two times larger at the double than in the single frequency mode. As a possible explanation TCFH can reduce and damp the instabilities by controlling the velocity space distribution, possibly making it more isotropic.
To interpret the experimental data, simulation of the plasma electrons in the magnetic trap of Atomki ECRIS under ECR conditions in single and at two close frequency heating mode have been performed [16]. The simulation was done by TrapCAD [89], [46], which is a numerical code using a single electron and plane wave approximation. This code, despite based on a single-particle, seems however perfectly suitable to capture at least the main underlying physical mechanisms regulating the electron heating in single versus double frequency mode, including linear and nonlinear wave-particle interaction.
First, the SFH mode was modelled by running the code for 15 configurations. The RF frequency was scanned from 11 GHz – 18 GHz with 500 MHz steps. The corresponding ratio $\frac{B_{min}}{B_{ECR}}$ is increasing from 0.60 to 0.99 by changing the frequency from 18 GHz – 11 GHz. 100,000 electrons were started from the resonant zone with $5,5\ eV$ initial average kinetic energy both for parallel and perpendicular velocity components. Simulation is ended after 200 ns (i.e. after many RF cycles and thus giving the opportunity to the whole simulated electron bunch to interact with the wave), while the RF power was set to 200 W which corresponds to 134 $\frac{V}{cm}$ electrical field in the given cylindrical ECRIS plasma chamber. Figure 5.26.a) shows the total energy transferred from the microwave toward the plasma electrons (during the simulation time) as function of $\frac{B_{min}}{B_{ECR}}$. It is clear that,

the energy content of the plasma is increasing nonlinearly above $\sim$ 0.8. The non linear increase has been quantitatively evaluated by checking the correlation parameter R with an increasing number of points in the dataset. It is clearly shown that the increase of the average energy turns to exponential around $0.75 - 0.80$ when R approaches 1, there. This value is in perfect agreement to the known value found by other authors [29] and sets the threshold for the onset of instabilities such as cyclotron maser.
Figure 5.26.b) shows the average kinetic energy of the electrons corresponding to the parallel and the perpendicular component. This plot underlines the escalation of the anisotropy toward higher $\frac{B_{min}}{B_{ECR}}$ ratios. An "*anisotropy parameter*" *Anis* has been then calculated as the ratio of the average kinetic energy corresponding to the parallel and perpendicular velocity component of the electron:

$$Anis = \frac{E_{\perp}}{E_{\parallel}} \tag{5.2}$$

Roughly speaking, it is possible to say that the higher *Anis*, the stronger the anisotropy in the phase space. *Anis* versus $\frac{B_{min}}{B_{ECR}}$ trend is reported on the same plot in figure 5.26.b), on the right axis, showing a non-linear increase of anisotropy, as expected.
Even though the onset of the kinetic plasma instabilities are out of the possibilities of our numerical simulations, however, the trend of the energy content and the anisotropy is consistently showing nonlinear trends at high $\frac{B_{min}}{B_{ECR}}$ ratios, providing appropriate conditions for turbulent regimes.
Then the effect of the second frequency to the anisotropy was investigated by the simulation code and compared with the experimentally obtained I_S parameters.

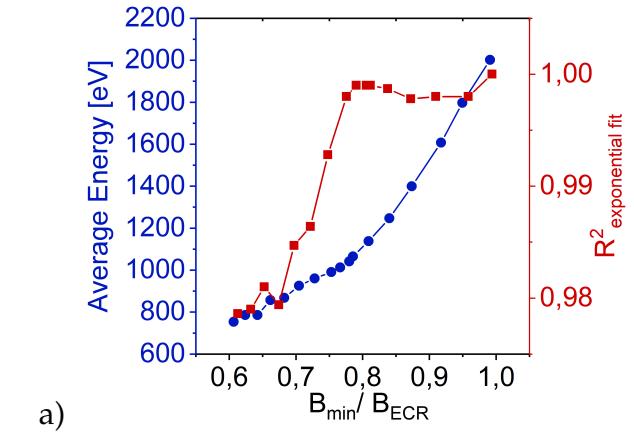

a)

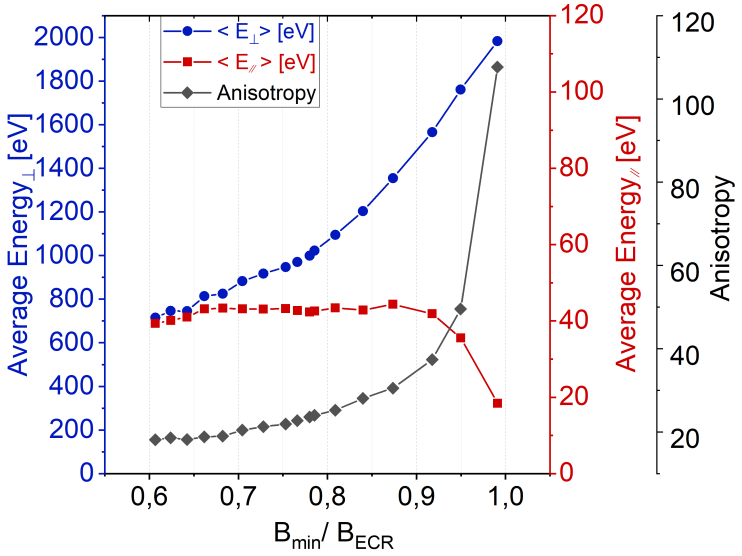

b)

Figure 5.26: Results of the TrapCAD simulation at single frequency scan. Energy content (a) and the average energies corresponding to the parallel and the perpendicular components (b) are plotted as function of the $\frac{B_{min}}{B_{ECR}}$.

Figure 5.27 shows both the anisotropy and the instability strength for the single and in double frequency operation modes, as well. For the comparison of the anisotropy and the instability strength we adopted the

normalized anisotropy parameter (normalized by 13.90 *GHz Anis* parameter). Results are shown in figure 5.27.

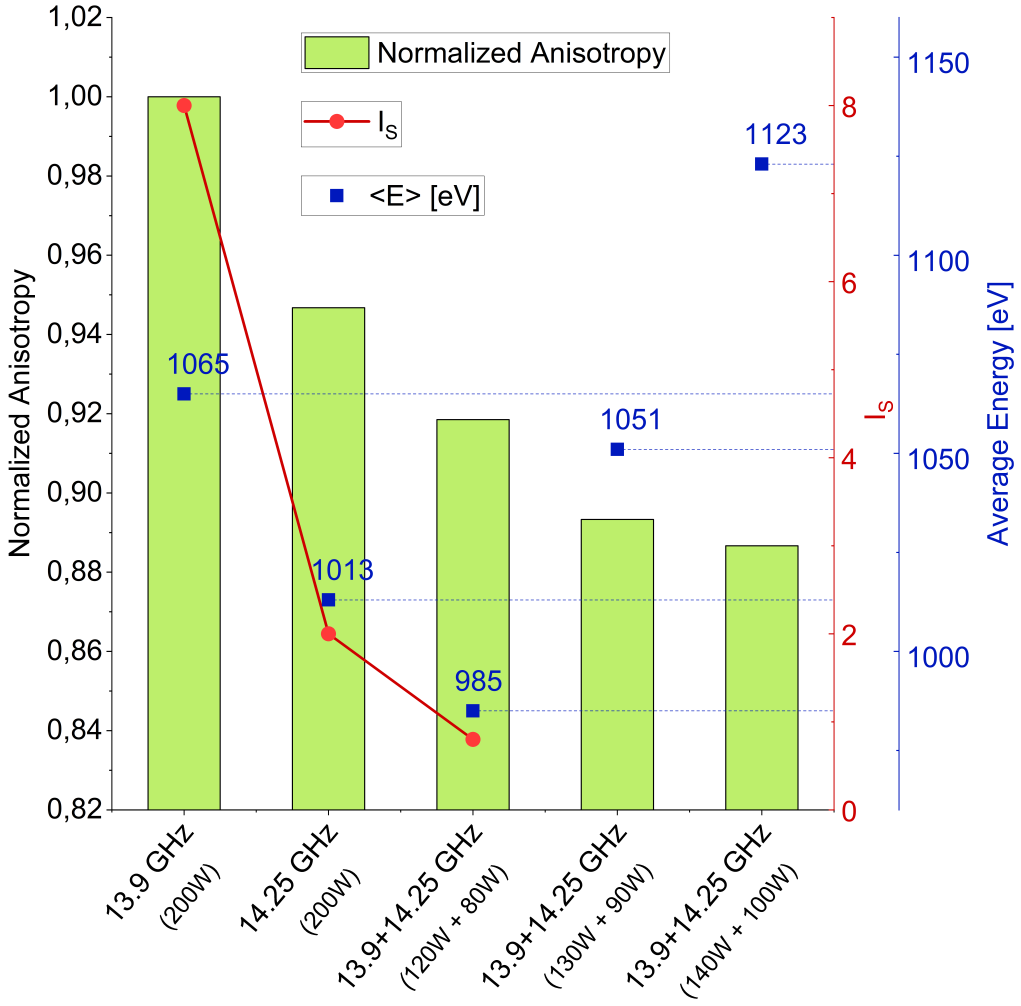

Figure 5.27: Anisotropy and the instability strength at single and at two close frequency mode.

Each bar of the histogram represents the normalized *Anis*. The red curve is the experimentally measured I_S parameter, while labels over columns report the average energy of the electrons in each simulated configuration. It can be seen that, in addition to the three experimen-

tal scenarios, also other two conditions in which the RF power of the two waves used for TCFH has been increased with respect to the experimental case have been simulated. In summary, this plot shows that:

- At the same net power cases the anisotropy is decreasing when we apply two close frequencies, however not only the anisotropy but also the average energy is decreasing.
- However, TrapCAD runs in TCFH at higher total net powers, by increasing the power for both frequencies in parallel, show that it is in principle possible to increase the average energy of the electrons (even above the energy corresponding to 13.90 GHz) and maintain the anisotropy at low level.

This is a really remarkable result, since it seems the TCFH is making the parameter space broader, allowing operations (using high amounts of RF power) at $\frac{B_{min}}{B_{ECR}}$ values that are normally impeded by the onset of strong instabilities in the plasma.
In addition, the plot shows that there is a very good agreement between the simulated anisotropy in the velocity space and the instability strength. At single frequencies the anisotropy is more pronounced and the corresponding I_S parameters are high especially in case of 13.90 GHz, meanwhile at TCFH mode the instability is damped effectively and the anisotropy shows lower level, even respect to the single 14.25 GHz operation mode.
In summary, it is now possible to reassume loss dynamics is due, in addition to interparticle collisions, to the parallel diffusion in the velocity space. It is possible thus to define thereby three parallel diffusion parameters $D_{\|T}(E, \frac{df}{dv_\perp})$, $D_{\|2f}(\frac{E_1}{E_2})$ and $D_{\|}(E)$, the first two defining diffusion as due to, respectively, Turbulence and TCFH, and the third being the usual single frequency diffusion parameter in a quiescent plasma. From the correlation studies of the plasma instability versus dynamics of plasma losses, it is possible to argue that when instability is strong, $D_{\|T} >> D_{\|}(E)$ and other plasma losses, whilst, when instability is weak (since $\frac{B_{min}}{B_{ECR}} < 0.75$, or it is damped by TCFH) losses are dominated by

the frequency tuning [90], i.e. terms $D_{\|2f}$ or $D_{\|}$ regulate the losses basically depending by the local value of the wave's electric field E_1 (or, in case of TCFH, also E_2) at the ECR. Both for the power scan in SFH at a given fixed frequency and for the power balance in TCFH with two fixed frequencies - where the tuning effect does not affect the data - the correlation results to be high and significative.
Instead, in the frequency scan characterization, there are different behaviours. Already in [11] it has been demonstrated that even if the instability suppression - due to the TCFH effect - is effective almost over the entire investigated frequency spectrum, the I_S data are quite scattered versus the TWT frequency (when they should theoretically linearly increase). This is due to the frequency tuning effect that is superimposed on the greater or lesser intensity of the instabilities. It has been demonstrated that, considering only very unstable regimes in SFH (for which the I_S parameter is high in absolute value in order to see if, under this condition, the instability effects dominate the frequency tuning) a weak but meaningful trend - in accord to the theory - appeared.
The same thing can appear when we study the dynamics of losses and to correlate the I_S with the R_{LP}: in the frequency scan cases it is possible that the tuning effect dominate to the instability. We find a weak correlation in SFH only for lower frequencies - where the $\frac{B_{min}}{B_{ECR}}$ results to be very near, or even higher, to the threshold of instability - but not for higher frequencies that typically are less unstable than the lower ones, and the tuning effect can be dominant.
In the case of the TCFH frequency scan, where no correlation at all was found, the situation results to be even more challenging. In this case, we already demonstrated that the I_S is one order of magnitude lower than the SFH case, and so again the tuning effect over the term $D_{\|2f}(\frac{E_1}{E_2})$ can dominate in all the frequencies domain.
So, we could potentially try to select only very unstable regimes for which the precipitation effect should be higher; but there is, in this case, also a competitive effect that can increase the losses: in the TCFH - as a consequence of higher diffusion in the parallel direction of the particles' energy - the particles scattering into the loss cone are hugely enhanced and become more competitive with collisions, so the diffusion due to TCFH is

more than a factor of two larger than collisions. So, also the less unstable regimes can present high losses.
Thus it seems that three different processes can be present simultaneously in the TCFH: 1) *the tuning effect*; 2) *the instabilities damping effect*; 3) *the increasing of particles into the loss cones*.
So, it is possible that even if the configuration is stable - because the TCFH damp the kinetic instabilities by means the the effect 2) - the losses are high due to the effect 3).
The TCFH hence appears to be a powerful tool for controlling both EEDF and loss dynamics. The results summarized by figure 5.27 open the perspective to increase the plasma energy content by simultaneously damping the instability. As a relevant impact on the ECR Ion Sources performances, it is possible here discuss about the "stability island" mentioned in [48] and regarding the portion in the tuning parameters space (made of RF power, frequency, magnetic field profile, gas pressure, etc.) that ensures reliable and effective operations of an ECR ion source. Using the same frame of that article's authors, it can be concluded the TCFH has the potentiality to make broader the parameters space allowing more reliable and powerful tunings of ECRIS.

5.4 SPhC Imaging and Spectroscopy: results

As mentioned in the chapter 4, two important complementary analyses of the SPhC images can be simultaneously performed: a) the ***HDR Energy-filtered Imaging*** and b) the ***HDR Space-filtered Spectroscopy***.
In the next two sections the results from, respectively, the two analyses will be presented. A typical SPhC mode (in our set condition) required a total acquisition time of around 4-5 hours: about 2-3 hours for acquiring the 4200 I_{Plasma} image-frames, 1 hour for the 1000 I_{Pole} image-frames and 0,25 hours for the 200 BKG image-frames. The experimental configuration in SFH at a pumping frequency of 13.90 GHz and a total net power of 200 W (the case (a) reported in the table 4.4) has been investigated and the results are shown in the next sections.
Furthermore, in perspective, other configurations both in TCFH and in SFH will be investigated and compared to this one.

5.4.1 High Dynamical Range Imaging

By means of the HDR energy-filtered imaging it is possible to select only the pixels of the frames which are loaded by the photons having energy corresponding to a well-defined energy range, to show the intensity distribution of the pixels which are fulfilling the filtering requirements. It allows the imaging of the elemental distribution, distinguishing the emission, and the correspondent image, coming from each material.

Table 5.3: Selected energy intervals in the HDR spectrum.

		Selected energy
a)	$Ar_{K_\alpha}, Ar_{K_\beta}$	2.96 keV and 3.19 keV
b)	$Ti_{K_\alpha}, Ti_{K_\beta}$	4.51 keV and 4.93 keV
c)	Ta_{L_α}	8.15 keV
d)	$Not\ Filtered$	
e)	Ta_{L_γ}	10.90 keV
e)	$E_{>\ 3.80\ keV}$	$>$ 3.80 keV

In the table 5.3 the selected energy intervals which have been investi-

gated are summarized. Pixels highlighting photons due to fluorescence peaks (i.e. Ar, Ti or Ta) have been investigated.
For each configuration ten ROIs have been selected and highlighted in order to investigate the plasma emission proprieties.
In particular they are:

- the ROI_1, i.e., near axis zone, denominated "*hole*" region, corresponding to the extraction hole;
- the ROI_2 and ROI_3, inside the ECR surface, are the so-called "*plasma*" regions;
- the ROI_4, ROI_5 and ROI_6 are placed along the "*magnetic branch*" region; moreover, the ROI_4 is placed both in the *plasma region* and in the *magnetic branch region* too;
- the ROI_7, ROI_8 and ROI_9 are placed in the so called "*magnetic pole*" region;
- the ROI_{10}, called "*empty*" region, is placed both outside the ECR region and the magnetic branches and pole regions;

ROI_1 counts not all but just those photons produced by the plasma electrons since there is no overlapping area "*behind*" the plasma from where wall bremsstrahlung appears. And it corresponds to the *plasmoid core* region. ROI_2 and ROI_3 correspond to the *plasmoid side* regions and they can contain an additional bremsstrahlung contribution too, due to the extraction plate placed *behind* the plasma in the frontal perspective of view. While ROI_4, ROI_5 and ROI_6 count not all but just those photons that are produced by the escaping electrons to the axial endplate of the plasma chamber, since the coordinates of those spots are corresponding to the magnetic branches structures. Finally the ROI_7, ROI_8 and ROI_9 count not all but just those photons that are produced by the escaping electrons to the lateral wall of the plasma chamber, since the coordinates of those spots are corresponding to the superficies of the plasma chamber. The ROI_{10} counts the bremsstrahlung contribution only coming from the extraction endplate.

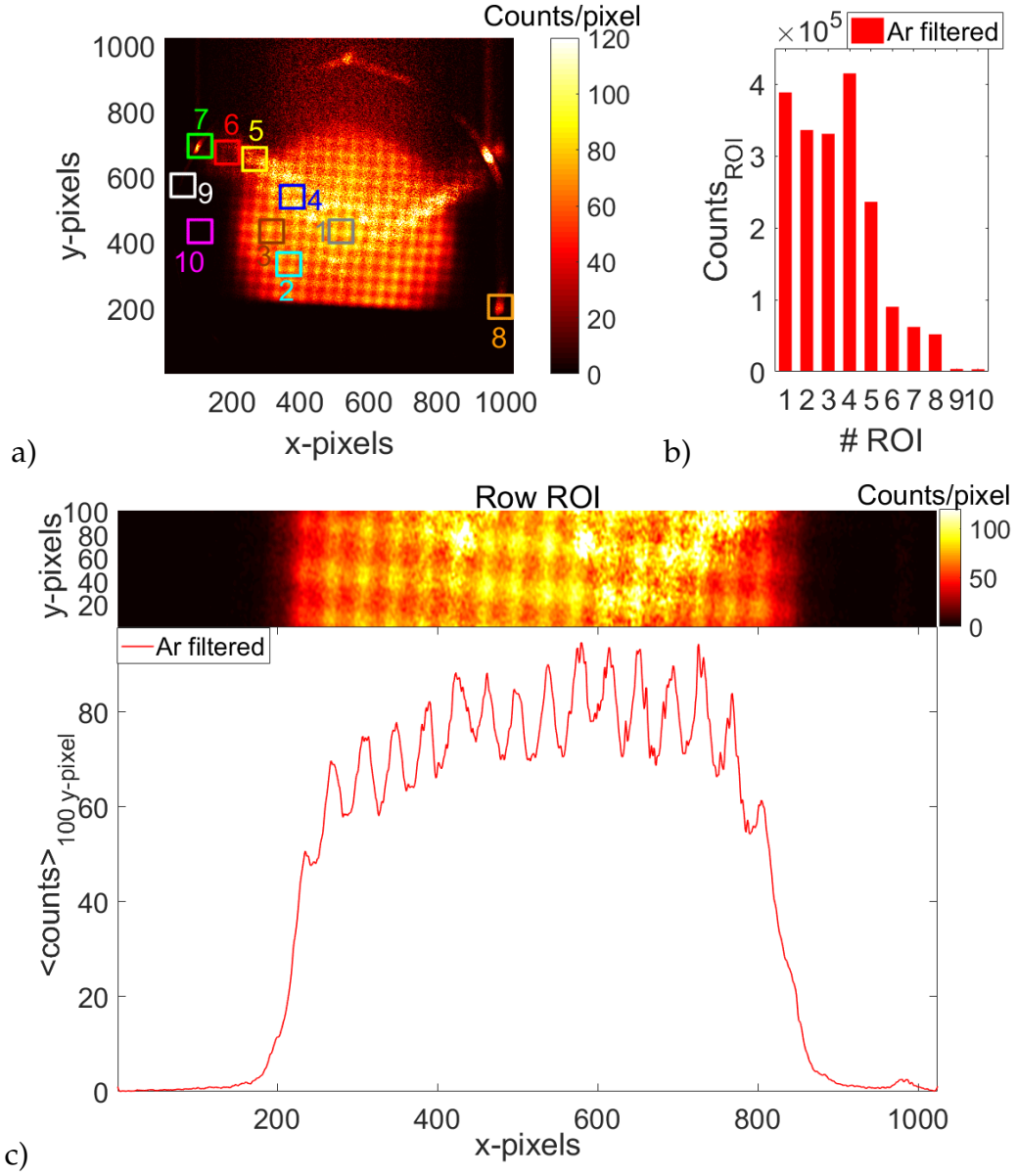

Figure 5.28: a) Pseudo-colour representation of the HDR Ar-energy filtered image, including the ten selected ROIs. b) Histograms of the total counts of each ROI. c) The intensity profile evaluated along a "row ROI" of [100x1024] pixels (shown on the top) containing the ROI_1.

The sequence of figures 5.28.a), 5.29.a), 5.30.a), 5.32.a) illustrates the

obtained X-ray images for the Ar-, Ti-, Ta- and not-energy -filtered mentioned above in the table 5.3, where all the ROIs have been highlighted. For each investigated image the total counts in each ROI have been estimated (the ROIs areas are the same) and reported in the table 5.4. The histogram showing the ROIs total counts is shown in the sequence of figures 5.28.b)-5.32.b).

Table 5.4: Total counts in each selected ROI of the not-filtered, Ar-filtered, Ti-filtered and Ta-filtered images.

	Total Counts Not-filtered	**Total Counts Ar-filtered**	**Total Counts Ti-filtered**	**Total Counts Ta-filtered**
	[Counts $\cdot 10^5$**]**	**[Counts** $\cdot 10^5$**]**	**[Counts** $\cdot 10^5$**]**	**[Counts** $\cdot 10^5$**]**
ROI 1	6.505 ± 0.008	3.887 ± 0.006	1.860 ± 0.004	0.419 ± 0.001
ROI 2	6.004 ± 0.008	3.364 ± 0.006	1.975 ± 0.004	0.711 ± 0.001
ROI 3	6.870 ± 0.008	3.311 ± 0.006	2.767 ± 0.005	0.783 ± 0.001
ROI 4	21.407 ± 0.015	4.153 ± 0.006	10.392 ± 0.010	1.822 ± 0.001
ROI 5	25.932 ± 0.016	2.364 ± 0.005	14.445 ± 0.012	1.729 ± 0.001
ROI 6	18.203 ± 0.014	0.903 ± 0.003	11.457 ± 0.011	0.725 ± 0.001
ROI 7	6.240 ± 0.008	0.623 ± 0.003	2.374 ± 0.005	5.017 ± 0.002
ROI 8	4.446 ± 0.007	0.520 ± 0.002	0.331 ± 0.002	9.660 ± 0.003
ROI 9	0.804 ± 0.003	0.038 ± 0.001	0.186 ± 0.001	0.819 ± 0.001
ROI 10	0.805 ± 0.003	0.034 ± 0.001	0.484 ± 0.002	0.032 ± 0.001

Starting analysing the Ar-energy filtered image (i.e., the one shown in the fig.5.28) it is possible to observe that the plasma emission in the ROI_1, i.e. in the plasma core, is higher than the one in the ROI_2 and ROI_3, i.e. in the plasma side. The ratio between ROI_1 and the mean of ROI_2 and ROI_3 emissivities is 1.13. It demonstrates the plasma is more concentrated in the *core*. The ROI_4 shows the higher plasma emissivity, it is a clear sign of enhanced electrons deconfinement, demostrating that the plasma is deconfined by the magnetic branches too. It is also possible to distinguish the plasma emission from the deconfined plasma one. This last one can be estimated by the counts in the magnetic branches ROIs, i.e. the ROI_5 and ROI_6. The counts ratio between the ROI_5 and ROI_1 is 0.63, whilst between the ROI_6 and ROI_1 is 0.24. Moreover it is possible to note that the sum of the counts of the plasma ROI_3 and the

deconfined one estimated by the counts in the ROI_6 is equal to the one of the ROI_4 corresponding both to the plasma side and magnetic branch regions. Consequently, around the 27% (counts ratio between the ROI_6 and ROI_3) of plasma is deconfined by magnetic branches. Finally, the plasma emission due to radially deconfined electrons is about the 16% of the plasma side emission.
Moreover also the intensity profile along a "*row ROI*" of [100x1024] pixels, containing the ROI_1 inside it, has been evaluated and it is shown in the figure 5.28.c) (the *row ROI* is illustrated on the top of the same figure). From this intensity profile, it is possible to note the very high spatial resolution where it it possible to well distinguish the mesh structure of the Al injection plate, even more that as is possible to get by the Spectrally Integrated Imaging. With the same method described in the section 5.3.1 the plasma radius has been estimated also in this configuration. The plasma radius results to be $15.53 \pm 0.87\ mm$, that is perfectly compatible with the radius awaited ($15.50\ mm$) considering the magnetic field profile that confined and shaped the plasma using the realistic magnetic field of the Atomki-ECRIS.
2D and following 1D-profile analysis is important for putting in evidence characteristic scale-length of plasma density variation. We have here the profile of K_α emission intensity that can be considered as:

$$I_{K_\alpha} \propto n_{Ar} n_e < \sigma_{K_\alpha} v > \tag{5.3}$$

where σ_{K_α} is the K_α fluorescence cross section, the term $n_{Ar} n_e < \sigma_{K_\alpha} v >$ is the total reaction rate. Since $\sigma \equiv \sigma(n, T_e)$, being known T_e from the bremsstrahlung part of the X-ray spectrum the relation between I_{K_α} and $n^2 = n_{Ar} n_e$ can be deconvolved at any position and this will be the subject of a paper now in progress [91].
Here it worth to be mentioned the fact that despite a variation of density is evident just looking the I_{K_α} profile, such variations have small gradients in that region and anyway they can be followed by this diagnostics method.
Moreover, beyond the microwave Interfero-polarimeter setup able to measure only the line-integrated plasma density, we are developing a dedicated microwave inverse profilometry (MIP) technique, based on inverse scattering, in order to retrieve the 1D-plasma density profile along the

horn-to-horn antenna path; simulations are already available [81].

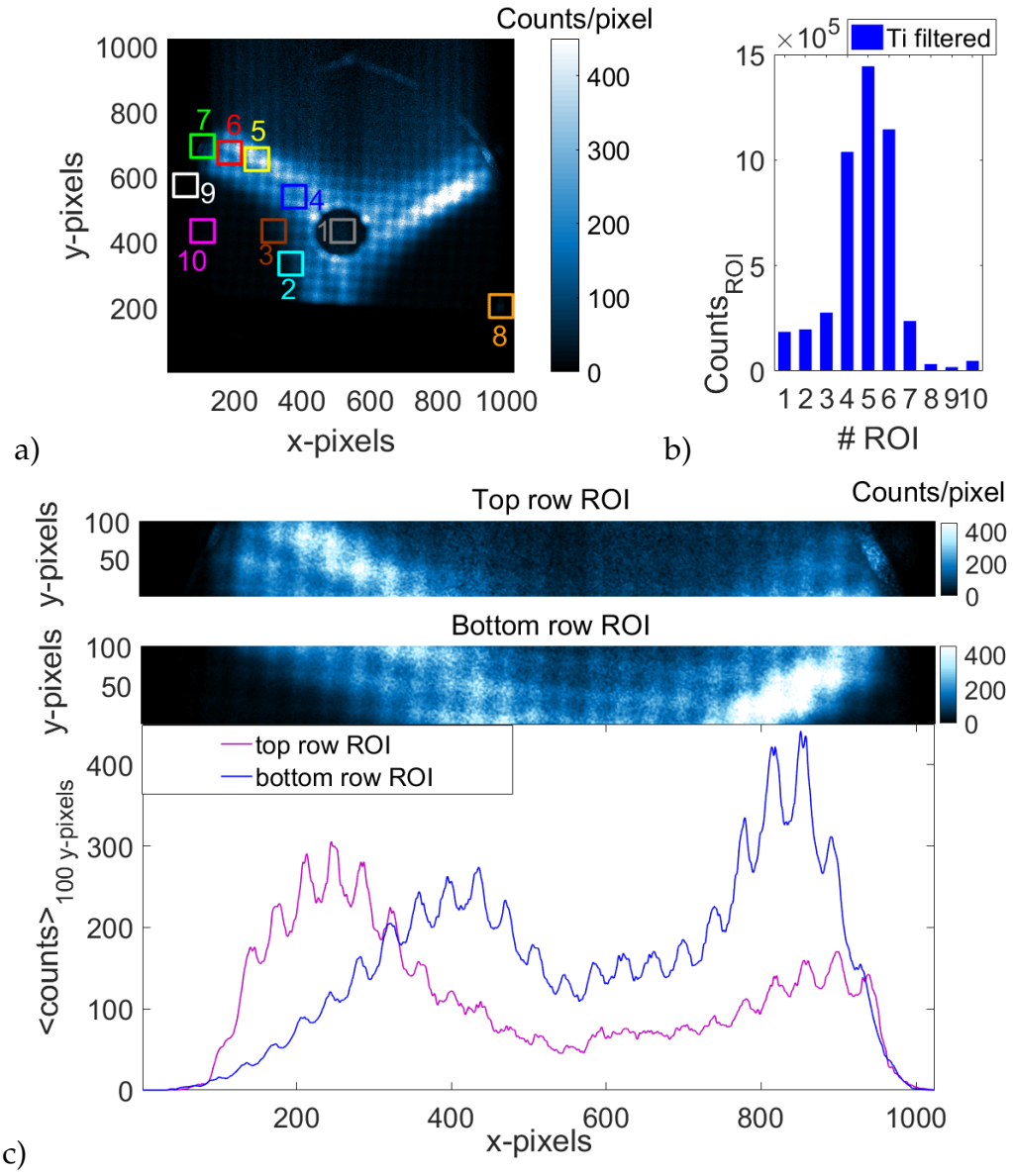

Figure 5.29: a) Pseudo-colour representation of the HDR Ti-energy filtered image, including the ten selected ROIs. b) Histograms of the total counts of each ROI. c) The intensity profiles evaluated along two "*row ROI*" of [100x1024] pixels (both shown on the top).

Considering the Ti-energy filtered image, shown in the fig.5.29, of course the higher numbers of counts are in the *magnetic branches ROIs*, i.e. the ROI_4, ROI_5 and ROI_6. Moreover, already from a visual inspection it is possible to observe a "*fine structure*" in the magnetic branches. It seems that each magnetic branch is characterized by an asymmetrical emissivity: an higher emissivity on the top (bottom) of the left (right) magnetic branch, compared to the emissivity on the bottom (top). This evidence is highlighted evaluating the intensity profile along two *row ROI* of [100x1024] pixels, just on the top of the extraction hole region. The profiles are shown in the fig.5.29.c, and the two *row ROIs* are illustrated on the top of the same figure. Further investigation are needed to study the origin this effect, which could be generated from the RF frequencies.
In the figure 5.30 is shown the Ta-energy filtered image, where four of the total six spot due to the magnetic poles are well visible. The other two are not visible due to the injection plate. The higher numbers of counts are in the *magnetic pole ROIs*, i.e. the ROI_7 and ROI_8. The intensity profile along a *row ROI* of [100x1024] pixels (shown in the fig.5.30.c) on the top, containing the ROI_7 inside it) has been evaluated and it is shown in the fig.5.30.c), on the bottom. It is also important to remember that only the peak of Ta_{L_α} at 8.15 keV is here investigated. There are other fluorescence peaks, visible in the HDR spectrum, that can be also studied. In fact, at the moment, we are performing structural investigation about the emission displacement considering the ROI as a sample of the whole population, but, of course, the quantitative investigation has been performed analysing the HDR spectra, as will be described in the next section 5.4.2.
As an example, the image corresponding to another Ta-filtered fluorescence peak, i.e. the Ta_{L_γ} is shown in the fig.5.31, corresponding to an energy of 10.90 keV. Moreover, the unfiltered image is shown in the figure 5.32. It shows all the previous investigated emissions more the other ones due to other fluorescence peaks and to the Bremsstrahlung emission. As an example, the intensity profile along the *row ROI* containing the extraction hole ROI is shown in the fig. 5.32.c).

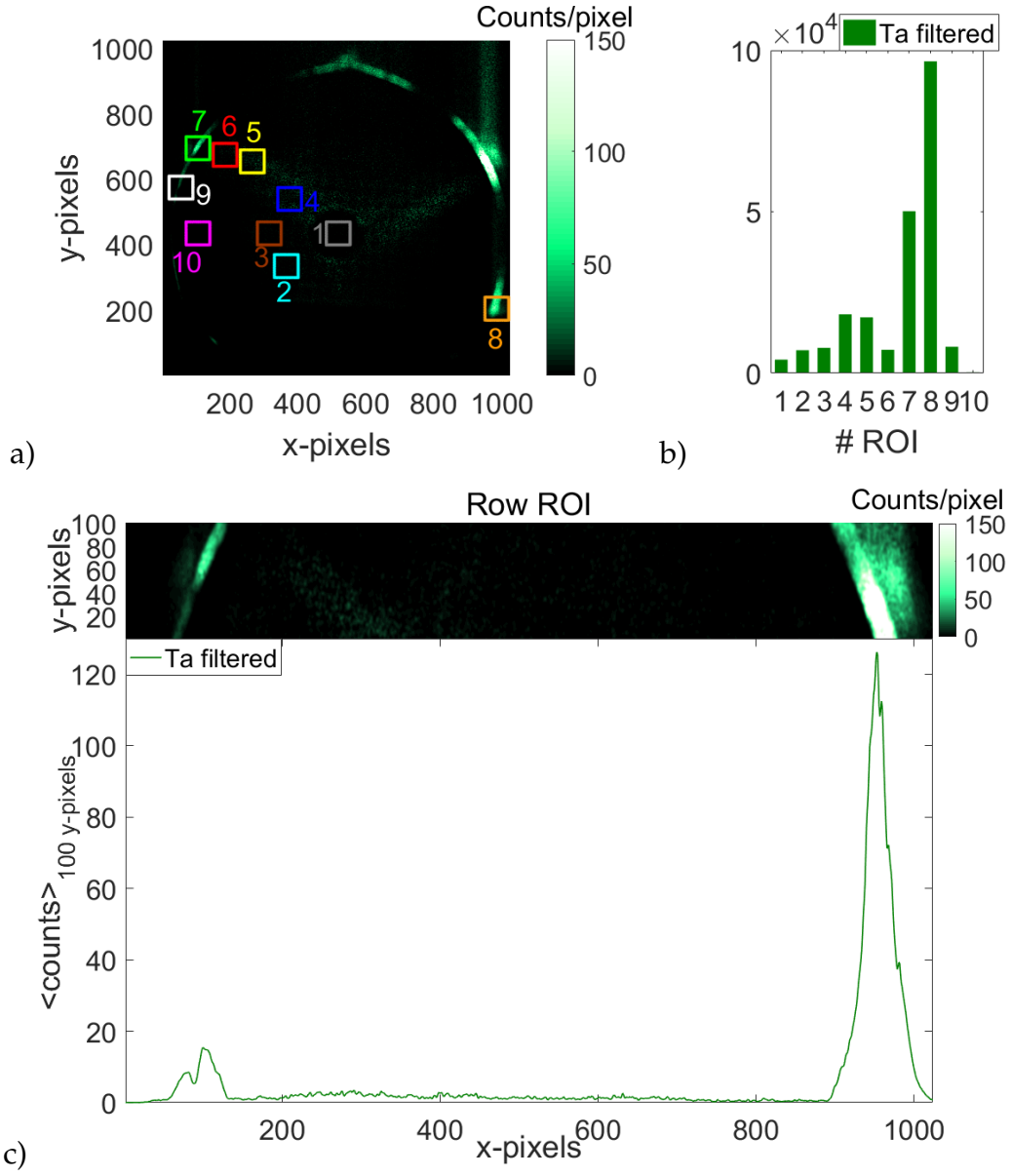

Figure 5.30: a) Pseudo-colour representation of the HDR Ta-energy filtered image, including the ten selected ROIs. b) Histograms of the total counts of each ROI. c) The intensity profile evaluated along a *row ROI* of [100x1024] pixels (shown on the top).

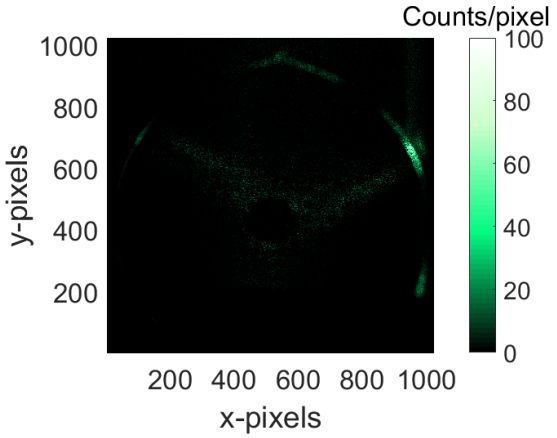

Figure 5.31: a) Pseudo-colour representation of the HDR Ta-energy filtered image (fluorescence peak Ta_{L_γ} at 10.90 keV).

Finally, the $\frac{L}{P}$ *ratio* estimation has been evaluated by means of the SPhC image analysis, in which the counts are decoupled from the energy. On this purpose, another energy-filtered image with $E > 3.80\ keV$, has been evaluated (see the figure 5.33). The image counts only the Titanium and Tantalum fluorescence lines and Bremsstrahlung contributions, i.e. the total losses, whilst The Argon fluorescence lines are filtered out. The same ROIs selected in the integrated images analysis (see section 5.3.2) have been chosen. From a visual inspection it is possible to observe that the plasma ROIs have very low counts compared to the ones in the unfiltered image 5.32.a). The plasma emission contribution has been evaluated summing the plasma ROIs counts of the Ar-energy-filtered image, whilst the total losses emission has been estimated summing the counts of the magnetic branches ROIs and of the magnetic pole ROIs of the image energy-filtered with $E > 3.80\ keV$.

The measured $\frac{L}{P}$ ratio is 15.7. It is slightly higher than the one estimated by the spectrally integrated image (for the same configuration) but still compatible. So the previous measurements are significant except for minor corrections can be made by the more accurate SPhC analysis.

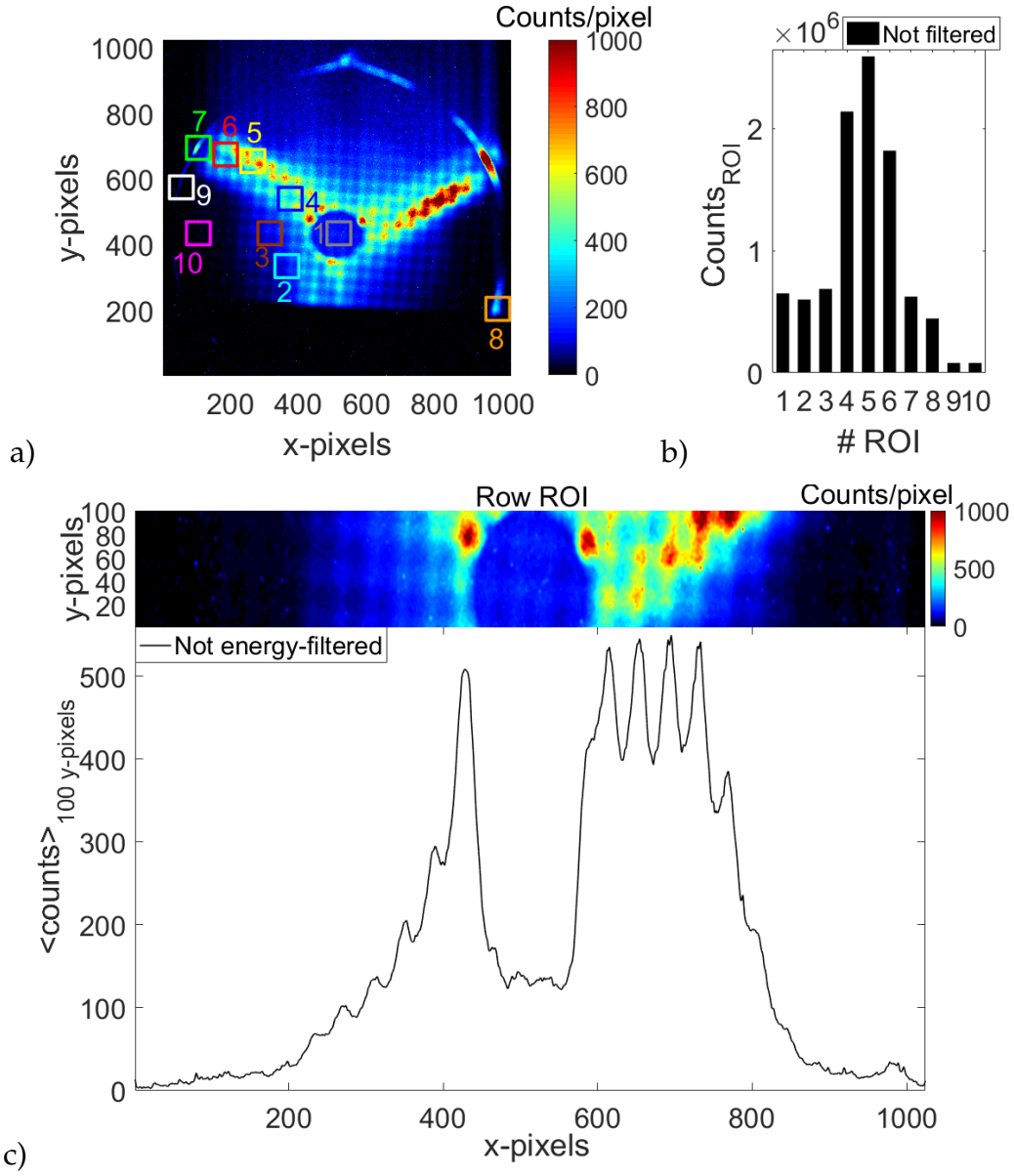

Figure 5.32: a) Pseudo-colour representation of the HDR unfiltered image, including the ten selected ROIs. b) Histograms of the total counts of each ROI. c) The intensity profile evaluated along a *row ROI* of [100x1024] pixels (shown on the top), containing the extraction hole ROI.

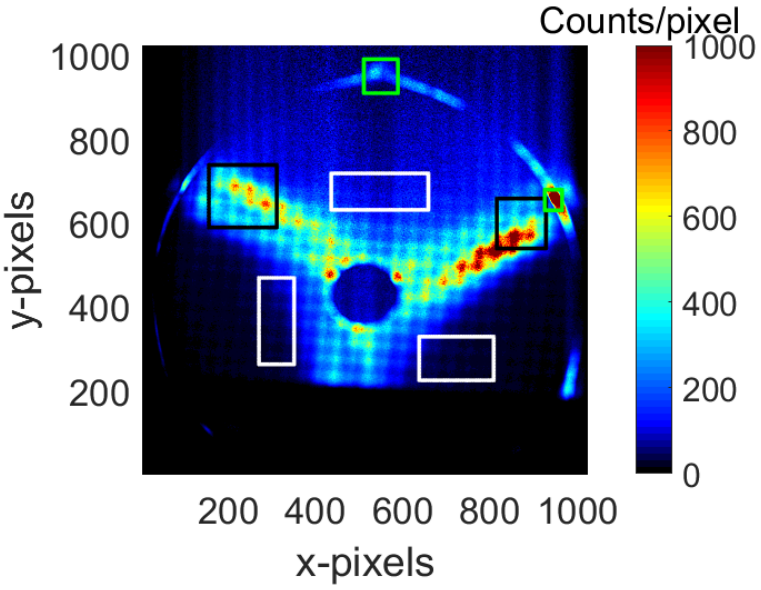

Figure 5.33: Pseudo-colour representation of the HDR image, energy-filtered with $E > 3.80\ keV$, where the plasma ROIs and the losses ROIs are visible (the same already used to analyse the spectrally integrated images).

5.4.2 High Dynamical Range Spectroscopy

A complementary analysis to the previous one can be also performed. It is possible to select a dedicated part of the not-energy filtered HDR image and to investigate the spectral composition of that part only. In this case the image is not processed by energy-filtering but by space-filtering. The ***Space-filtered Spectroscopy*** consists in fact in selecting a "*collection*" of pixels of the ROI and evaluating the correspondent spectrum in order to investigate about X-ray emission proprieties by plasma electrons or deconfined electrons in the chamber walls. It is also possible to locally perform plasma parameters (electron density and temperature) estimation. The previous selected and highlighted ROIs (see fig.5.32) have been chosen.
The HDR spectrum is reported in the figure 5.34.a). The spectrum affected of a small contribution from readout noise that can not reconstruct as done for the HDR images.

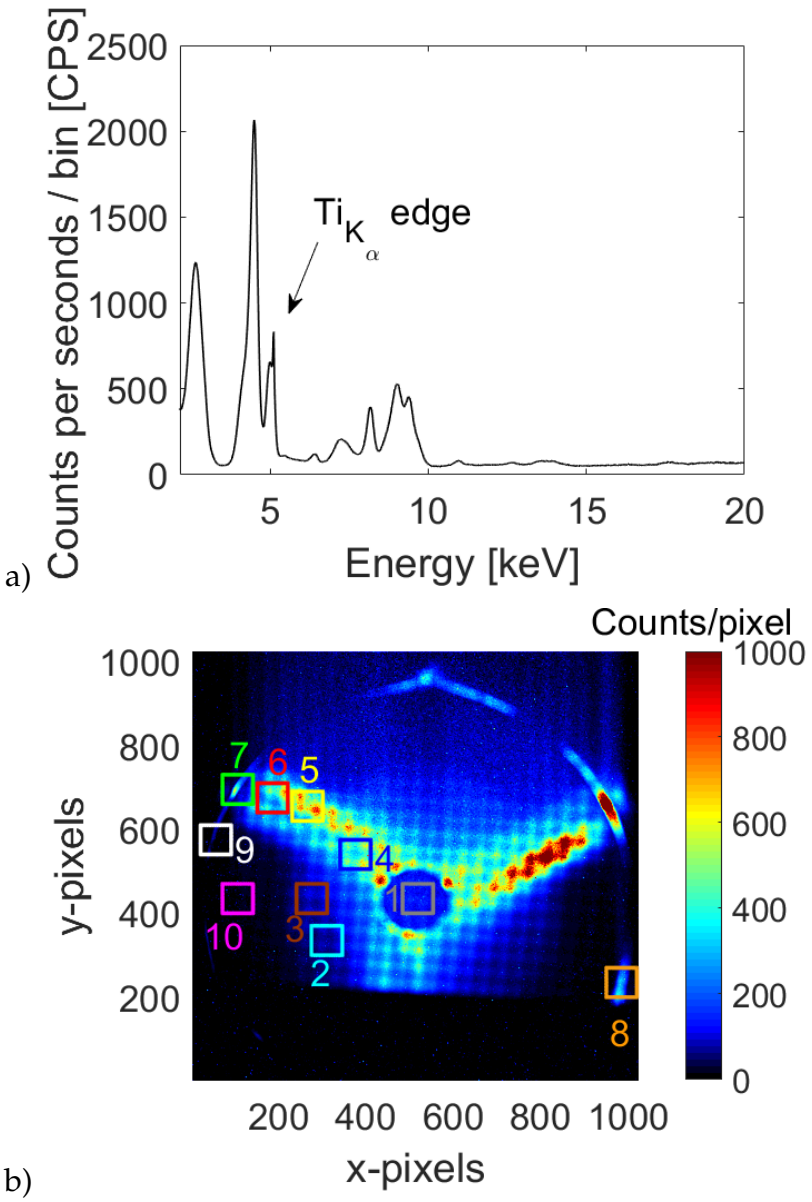

Figure 5.34: a) HDR spectrum of the investigated configuration at a pumping frequency of 13.90 GHz and at a power of 200 W in SFH. b) Corresponding event-counted HDR image, with several highlighted ROIs.

A zoomed-in HDR images of different selected ROIs is shown in the sequence of figures 5.35 I - X, respectively, for the ROI_1 - ROI_{10}. The corresponding spectra are shown both in the figure 5.36 and in the sequence of figures 5.38, 5.39, 5.40.

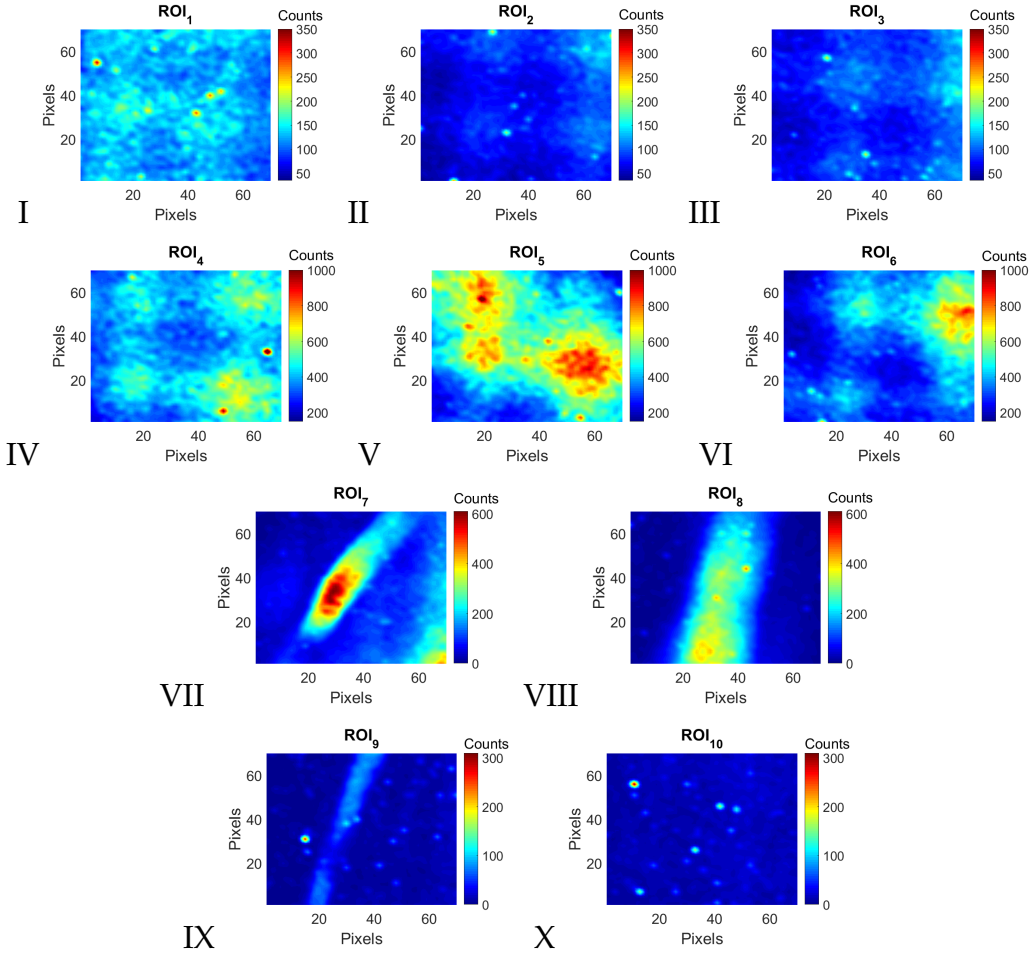

Figure 5.35: Zoomed-in HDR images of the different selected ROIs. Note that the colour scale is different in the images; it is the same in I, II, III in order to directly compare the plasma regions, in IV, V, VI to compare the magnetic branch regions, in VII, VIII the magnetic pole regions comparison and for the set IX, X where the emissivity is very low.

In the figure 5.36, the comparison between four spectra, one for each

region (plasma, plasma & magnetic branch, magnetic branch and magnetic pole) is shown: i.e., the ROI_2 plasma region, the ROI_4 as both plasma region and magnetic branch regions, the ROI_6 magnetic branch region and the ROI_8 magnetic pole region.

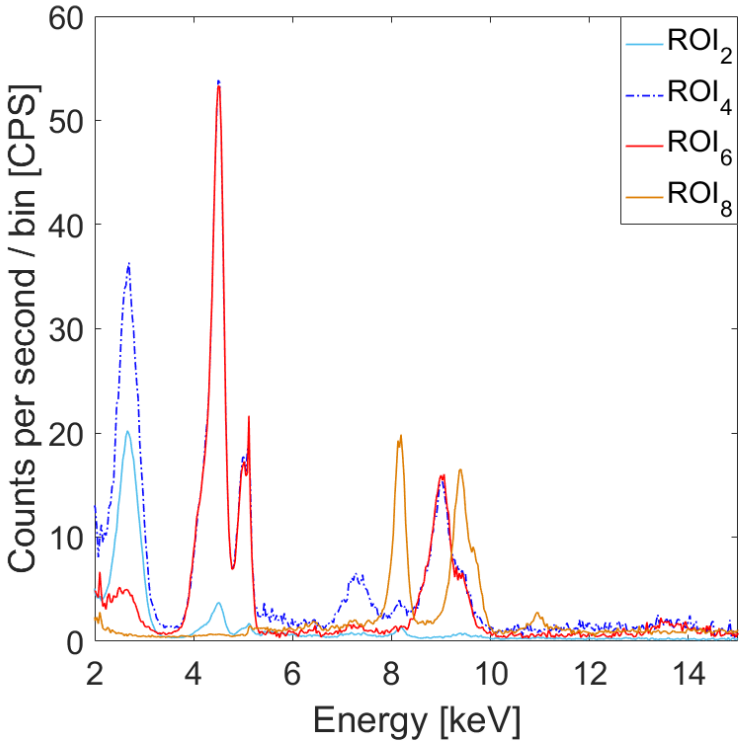

Figure 5.36: Spectra evaluated in the four selected *ROIs*: ROI_2 (cyan) placed in the plasma region, ROI_4 (blue) placed both in the plasma region and in the magnetic branch region, ROI_6 (red) placed in the magnetic branch region only, ROI_8 (orange) placed in the magnetic pole region.

Already from a visual inspection, it is possible to observe the Argon plasma emission comes only from ROI_2 and ROI_4: i) the spectrum evaluated in the ROI_2 shows the Ar_{K_α,K_β} fluorescence peak (since ROI_2 is placed inside the ECR surface) and low intensities of the Ti_{K_α,K_β} fluorescence peaks; ii) the ROI_4 shows very intense Ti_{K_α,K_β} fluorescence emissions, almost one order of magnitude higher than the ones in ROI_1, whilst

the $Ar_{K_\alpha,\ K_\beta}$ is slightly higher: the ROI_4 is placed both inside the ECR surface and in the magnetic branch (the deconfined energetic electrons lost on the Titanium electrode produce very intense characteristic Ti_{K_α,K_β} lines); iii) the position of the ROI_6 is in the magnetic branch and outside the ECR surface, the Ti_{K_α,K_β} is almost the same of the one in the ROI_4 but the Ar_{K_α,K_β} line almost totally disappears. Moreover it is possible to highlight that both in the ROI_4 and ROI_6 there are still dimer Ti_{K_α,K_β} peak around 9 keV. Finally, in the ROI_8, i.e. the magnetic pole region, both Ar_{K_α,K_β} and Ti_{K_α,K_β} disappear and the three Ta_{L_α}, Ta_{L_β} and Ta_{L_γ} fluorescence lines are well visible. Additional interesting details can be obtained by investigating the other ROIs spectra and comparing them. A quantitative estimation of the total counts per second emitted in each energy interval of interest has been performed by means of fitting the main peaks of Argon, Titanium and Tantalum. The results are reported in the table 5.5 and are shown in the figures 5.37.

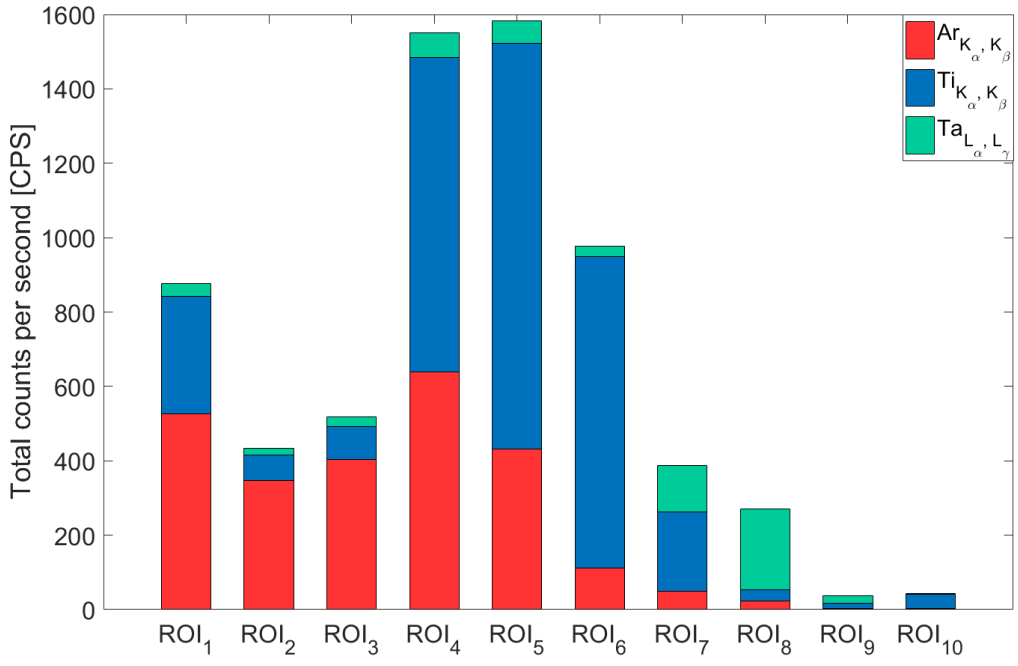

Figure 5.37: The histogram shows the total counts per second of each fluorescence lines (Ar_{K_α,K_β}, Ti_{K_α,K_β}, Ar_{L_α,L_γ}) loaded in each ROI.

The histogram in figure 5.37 shows the total counts per second of each fluorescence lines (Ar_{K_α,K_β}, Ti_{K_α,K_β}, Ar_{L_α,L_γ}) for each ROI, i.e. elemental composition. The sum of the counts of Ti_{K_α} and Ti_{K_β} is labelled as Ti_{K_α,K_β}, whilst the one of Ta_{L_α} and Ta_{L_γ} as Ta_{L_α,L_γ}. The plasma emission characterizes both the internal ECR surface, as expected by the magnetic confinement, both the external one (ROIs 5 and 6). This is the evidence of the deconfined plasma by the magnetic branches and it appears also in the more external region ROI_6. The plasma regions emissivity is also illustrated and compared in the spectra shown in the figure 5.38.

Table 5.5: Total counts of the fluorescence Ar_{K_α,K_β}, Ti_{K_α,K_β}, Ar_{L_α,L_γ} lines, for each ROI.

	Total Counts Ar_{K_α,K_β}	**Total Counts** Ti_{K_α,K_β}	**Total Counts** Ta_{L_α,L_γ}
ROI 1	527.2 ± 3.1	316.6 ± 2.5	33.3 ± 0.4
ROI 2	347.7 ± 1.2	68.6 ± 0.3	18.3 ± 0.3
ROI 3	403.6 ± 2.7	89.6 ± 1.4	26.5 ± 0.4
ROI 4	638.3 ± 3.5	847.7 ± 4.1	65.9 ± 0.6
ROI 5	432.4 ± 2.9	1091.8 ± 4.6	59.2 ± 0.6
ROI 6	111.5 ± 1.5	838.1 ± 4.1	29.5 ± 0.4
ROI 7	49.4 ± 1.1	214.6 ± 2.2	124.4 ± 0.9
ROI 8	24.8 ± 0.8	29.7 ± 0.8	217.9 ± 1.2
ROI 9	3.0 ± 0.3	15.4 ± 0.6	19.2 ± 0.3
ROI 10	4.3 ± 0.9	37.4 ± 0.9	1.3 ± 0.1

In the spectra shown in the figure 5.39.a) the magnetic branch regions emissivity has been compared, whilst the magnetic pole regions emissivities comparison are highlighted in the spectra of figure 5.39.b). It is possible to note the difference between the pole region ROI_7 and ROI_8: in the ROI_8 there is not any Titanium contribution because in this case the magnetic branch are headed for the injection side where there is the Al injection flange branches. In the spectra it is possible to note, in fact, that the dimer Ti peaks typically overlapped with the Ta_{L_β} lines are missing and only the Ta_{L_β} lines are well visible.

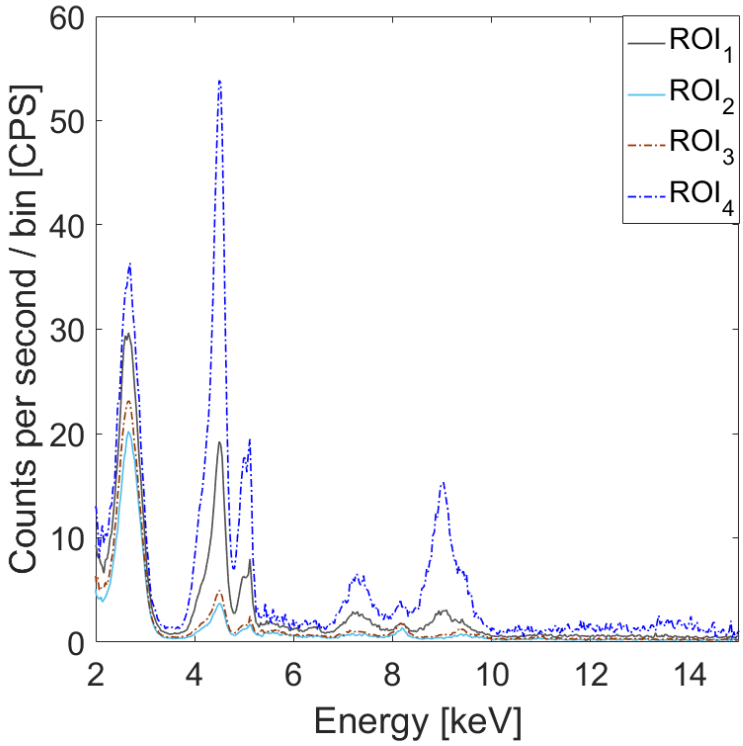

Figure 5.38: X-ray spectra from the different plasma ROIs: ROI_1 (grey) placed in the extraction hole region, ROI_2 (cyan) and ROI_3 (brown) placed in the plasma region, ROI_4 (blue) placed both in the plasma region and in the magnetic branch region.

Finally, in the figure 5.40 it has been compared the spectrum in two region where the plasma emissivity is very low, since they are displaced outside regions both ECR surface, the magnetic branches and the magnetic pole regions.

It is possible to observe that in the ROI_9 there are both the Ti and Ta fluorescence peaks, even if with a lower intensities of the previous analysed ROIs. Whilst, in the ROI_{10} there is only Ti. In particular, since it is placed outside the magnetic branch region, it is due to fluorescence only and can be used to estimate this contribution and to subtract it by the other ROIs.

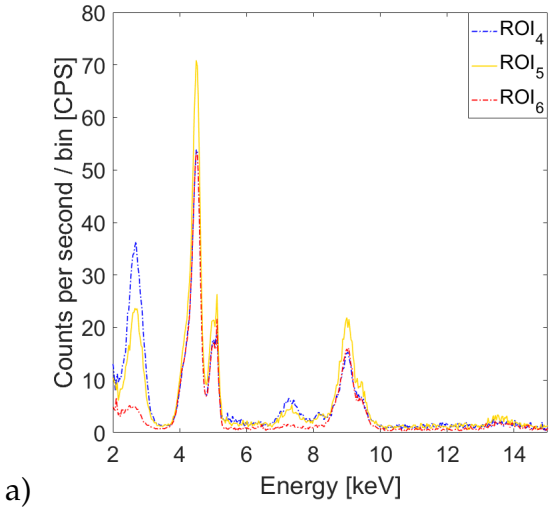

Figure 5.39: X-ray spectra evaluated and compared magnetic branch and pole ROIs: ROI_4 (blue) placed both in the plasma region and in the magnetic branch region. ROI_5 (yellow) and ROI_6 (red) placed in the magnetic branch region only. ROI_7 (green) and ROI_8 (orange) placed in the magnetic pole region. ROI_9 (black) placed in a region of the chamber lateral wall. a) Comparison between ROI_4, ROI_5, ROI_6. b) Comparison between $ROI6$, ROI_7, ROI_8, ROI_9.

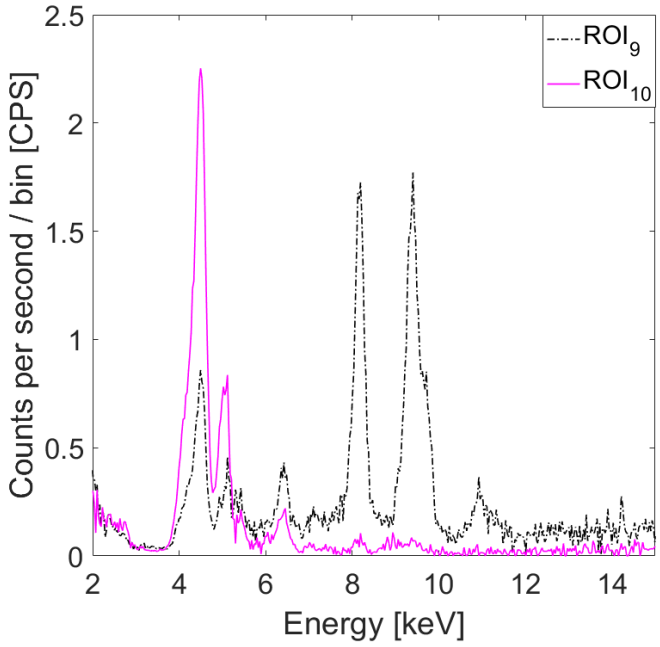

Figure 5.40: The image shows the comparison between the spectra evaluated in the regions outside both plasma, magnetic branches and magnetic pole regions: ROI_9 placed in a region of the chamber lateral wall and ROI_{10} placed in a "*empty*" region.

The histogram illustrated in the figure 5.41 summarises the above mentioned results and shows, for each fluorescence line reported in the horizontal axis, the contribution (expressed in total counts per second) in the vertical axis, coming from each ROI (colour of the histogram).
Finally, it is important to mention that both the whole spectrum and the ROIs spectra can be analysed in order to locally estimate the plasma parameters, in term of electron temperature and electron and ion densities. The plasma emitted spectrum can be reelaborated in order to measure the so-called *spectral emissivity curve* providing the total equivalent number of photons emitted in the given energy interval over the entire sold angle measured by the detector. Typically, for a precise detector's solid angle estimation dedicated Monte Carlo simulations are implemented.

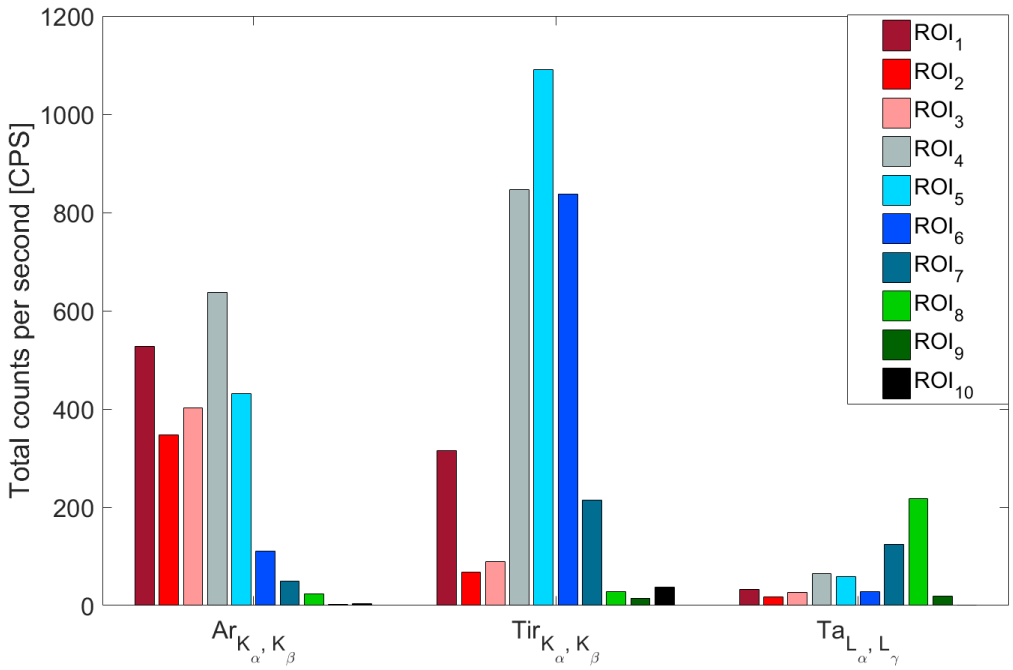

Figure 5.41: The histogram of the emission contribution (expressed in total counts per second) from each ROI (ROI_{1-10}), for each fluorescence line (Ar_{K_α,K_β}, Ti_{K_α,K_β}, Ar_{L_α,L_γ}).

After evaluating the emissivity for each measured spectrum, it is fitted by a theoretical curve, following models for X-ray spectra fitting like the approach described by Gumberidze et al. [83] (which assumes fully isotropic emission). Finally, the electron/ion densities can be extracted, along with the plasma temperature, from the linear fit parameters. The electron temperature is inversely proportional to the slope curve (expressed in semi-logarithmic scale) whilst the electron and ion densities can be estimated from the other fitting parameter. The experimental errors typically result within $10\% - 15\%$.
This approach is typically used for the volumetric X-ray spectroscopy analysis, i.e. using detector like the SDDs for the soft X-ray characterization or the HPGe detectors for the hard X-ray component (see [82, 79]). To perform this analysis, however, it is strongly preferable to reduce as much as possible the fluorescence peaks (like the ones coming from the plasma chamber, typically like Fe, Cr) in order to highlight the Bremsstrahlung tail. Typically, this condition is assured by means of using a very good collimation system.
As an example the direct comparison of the spectrum evaluated in the magnetic pole region and the one evaluated in the plasma region is shown in the figure 5.42. A visual inspection shows that the spectrum slope in the magnetic pole ROI_7 is lower (i.e., corresponding to a higher electron temperature) than the one in the plasma ROI_2.

Consequently, it is possible to argue the losses of the high energy electrons are dominant along the radial direction. However, in order to quantitatively evaluate the temperature by means of the above mentioned approach, the fit of the experimental emissivity has to be performed in a range around of $2\ keV\ to\ 30\ keV$; the lower limit of the energy range has to be chosen to avoid any influence of the Compton effect and escape of high energy photons from the Si crystal, which leads to only a partial deposition of the photon energy in the detector. The upper limit is given by the photon energy for which, both, the detector efficiency becomes too small and the statistical uncertainty too large. The weights in the emissivity fit, in fact, are evaluated by taking, at each point of the spectrum, the square root of the measured intensity.

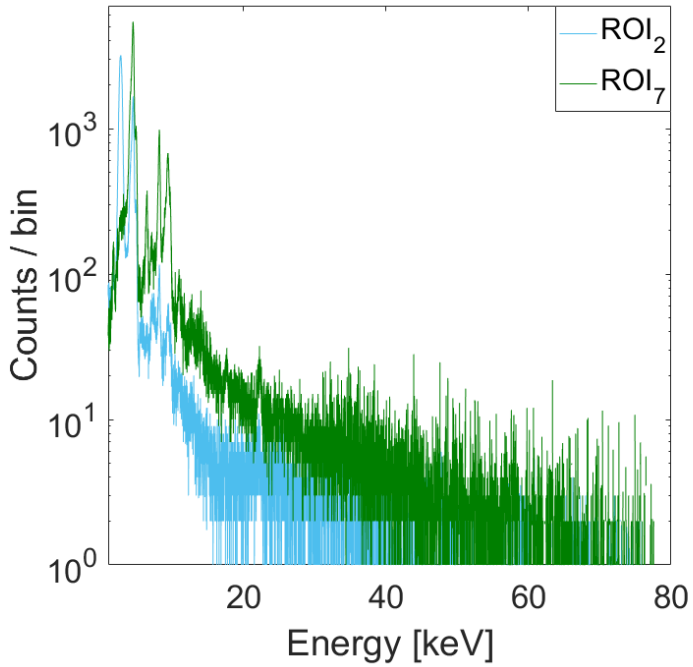

Figure 5.42: Spectra evaluated in plasma region (cyan) and magnetic pole region (green). It is possible to qualitative note the shape spectrum (inversely proportional to the electron temperature) is higher in the ROI_7 compared to the one in the ROI_2, i.e., the losses of the high energy electrons are dominant along the radial direction.

Another analysis can be done, instead, focusing the attention to the Ar fluorescence. Following the relation 5.3, and introducing a proper estimation of the K_α ionization and radiation yield cross section, it is possible to retrieve the local argon density. For both Bremsstrahlung and fluorescence part of the spectrum, the results here presented are crucial since it is now possible to have reliable data for both the contributions, with high enough statistics, minimization of noise and spurious signals (such as dimers and escape peaks), etc.; the analysis for getting the plasma density and temperatures is ongoing and will be the subject of the paper in the near future.

Chapter 6

Towards $PANDORA_{Gr3}$: simulations for the γ-rays detectors array design

In the framework of $PANDORA_{Gr3}$ [6, 7], as mentioned in the chapter 2 and 3, it is necessary to measure the radionuclide lifetime variations, correlating them with the plasma proprieties. Thus, methods and tools described in the previous chapters form "*the first part*" of the needed advanced experimental setup. They will be mainly devoted to perform the accurate on-line monitoring of all plasma parameters aiming to characterize in detail the plasma *environment*, also in a time- and space-resolved way. In order to perform fundamental physics studies of $\beta-$decay it is necessary to implement the *second part* of the setup, consisting of an array of $\gamma - ray$ HPGe detectors for the decay products tagging (several physics cases involve emission of γ-rays, and in these cases the total amount of decays become detectable via γ-rays). Simulations with GEANT4 have been carried out in order to estimate the total detection efficiency and to dimension the array [17]. Results will be presented in this chapter.
As mentioned in the chapter 1, the total amount of decays can be determined according to the following formula:

$$N(T_{meas}) = \lambda n_i V T_{meas} \tag{6.1}$$

where t_{meas} is the overall measurement time over which the $\gamma - rays$ produced by the excited states of the decays products. It worth to be noticed that as said in the section 5.4 $n \equiv n(x, y, z)$ whose spatial dependence can be determined by SPhC X-ray Imaging.
Hence, the number of measured decays scales linearly with the measurement time, provided that a dynamic equilibrium has been established. Under this assumption, the decay constant λ is simply the proportionality constant of eq. 6.1. Equation 6.1 implies also that the plasma density and volume must be known and on-line monitored all along the measurement in order to deconvolve λ.

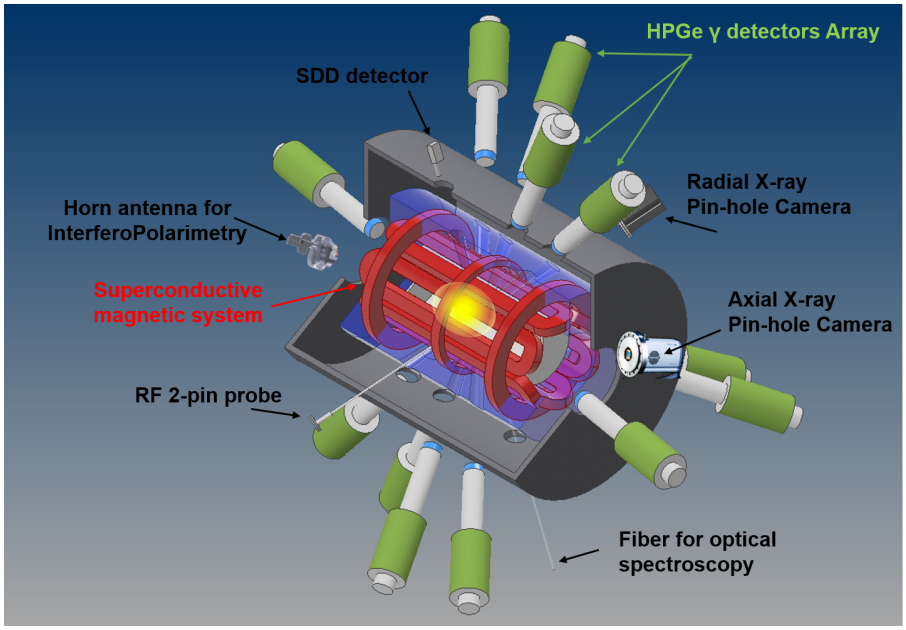

Figure 6.1: Rendering of the $PANDORA_{Gr3}$ trap with the experimental setup to be used for the measurement of the in plasma activity (14 HPGe detectors array) and on-line monitoring of plasma density and temperature (i.e., two X-ray CCD cameras, optical spectrometer, horn antennas for microwave Interfero-Polarimetry, two-pin RF probe and SDD).

The sketch of the whole diagnostic system will equip the $PANDORA_{Gr3}$ plasma trap is illustrated in the figure 6.1).
The plasma volume can be correctly diagnosed with very high resolution

by means of the X-ray imaging through the pin-hole camera setup, using, in particular, two CCD cameras simultaneously, one along the axial line, another in the radial one, as shown in the figure. Whilst, the microwave InterferoPolarimeter tool is able to measure the total density. It is possible observing also the other tools which surround the trap: a RF probe, an optical spectrometer and a SDD.
The possible physics cases (see the section 2.3.1) include, among the others, the ^{176}Lu which plays a crucial role as cosmo-clock, the ^{134}Cs and ^{94}Nb, involved in *s-processes* of nuclear astrophysical interest.
Considering the ^{176}Lu physical case, starting from the lifetime of the neutral isotope to the values of lifetimes predicted by the theory and that are feasible in our plasma trap, the expected collapse of the lifetime as theoretically evaluated is about 6 order of magnitude (at around 10 keV of plasma temperature), as already shown in the plot 2.3. Considering these lifetimes, and known the plasma volume and isotope density (around 1500 cm^3 in volume with a concentration of 1% of Lu with respect to the buffer density of 10^{13} ions/cm^3) the effective activity in the plasma can be estimated. By means of the GEANT4 simulation the detection efficiency of the $\gamma-$ray detectors array has been evaluated for investigating the measurement feasibility and the required measurement time in order to reach a 3σ level of confidence. These simulations indicate that a measurement lasting from tens of days to a couple of months is needed.

6.1 Design of the $PANDORA_{Gr3}$ Setup in GEANT4

GEANT4 simulations were used to implement the geometrical design, using the magnetic design described in the section 3, with the same materials and dimensions of each component. The implemented final design of the $PANDORA_{Gr3}$'s trap consists of:

- A **stainless steel chamber** of an external radius of 150 mm, length of 700 mm and thickness of 10 mm. The chamber has been drilled with 12 holes of diameter 40 mm, connected to cryostat collimators for detection of $\gamma - rays$. We simulated a total of 12 azimuthal holes placed along four rings, symmetrically placed at 6 cm and 12 cm away from the midplane of the chamber (see fig. 6.2). Three holes spaced at 120°

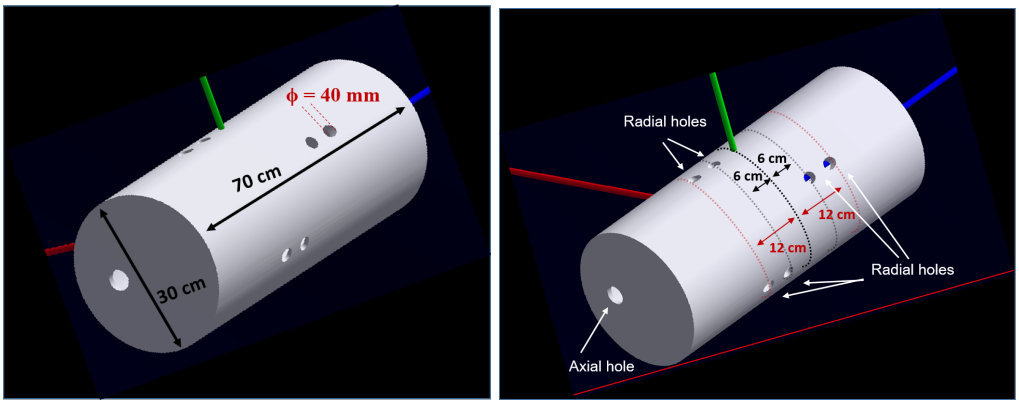

Figure 6.2: Stainless steel plasma chamber drilled with 12 radial holes of diameter 40 mm, and two axial holes of diameter 40 mm.

were drilled for each rings building a geometrical configuration symmetrical respect to the center of the chamber.
The **stainless steel chamber has been** also **drilled** with two axial (injection and extraction) tilted conical holes of diameter 40 mm, in order to connect axial collimators for γ-rays detection (also shown in fig. 6.2). **In each hole we placed an Aluminium window** of thickness of 3 mm and diameter 40 mm.

- **The overall magnetic system** (fig. 6.3.a)) **consists in three NbTi superconducting coils** (coloured in yellow) **and in a NbTi six-conductor hexapole** (coloured in red);

- **A single cryostat, that contains the three coils plus the hexapole magnets**, has been simulated as an Aluminium cylindrical structure (fig. 6.3.b), coloured in pink) surrounding the overall magnetic system and distant 30 mm both from the hexapole ends (along the axis), both from the INJ, EXTR axial coils outer radius.

- **The cryostat structure** has been drilled - along the conductor hexapole interspaces - in order to use it as multi-collimator and suppress, as much as possible, the photon flux coming from the walls and not directly from the plasma core, improving the ratio signal-over-noise. We drilled the cryostat with:

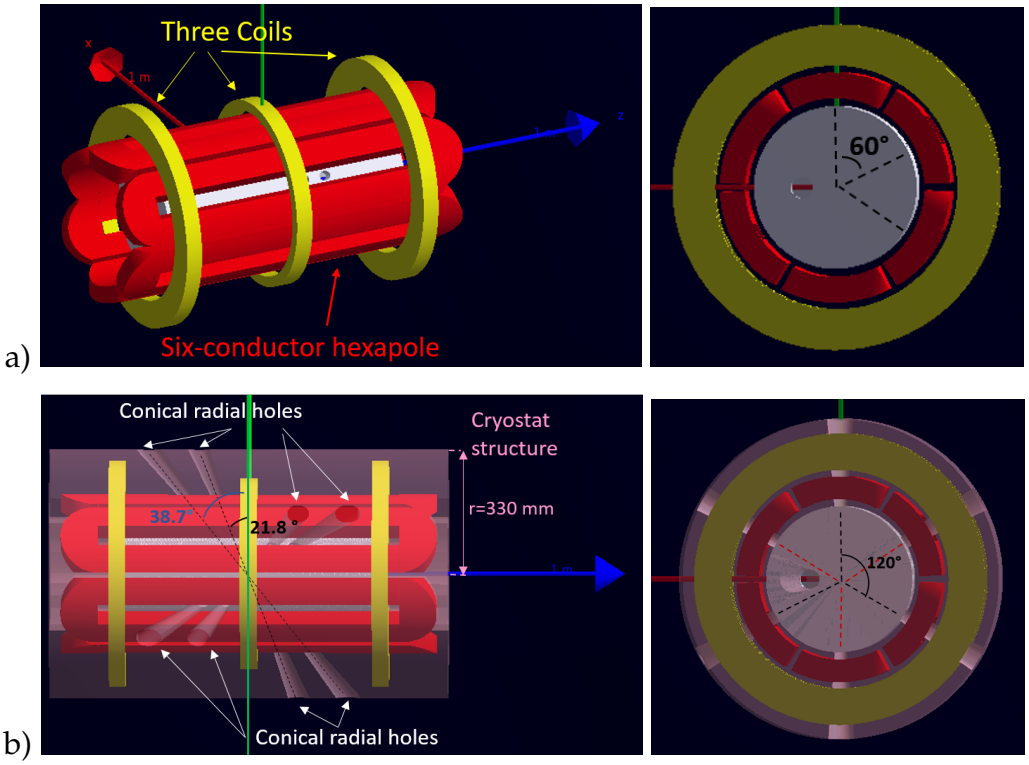

Figure 6.3: a) Plasma chamber surrounded by superconducting coils (yellow) and hexapole (red); b) The magnetic system has been surrounded by the cryostat structure (pink), drilled with axial and azimuthal tilted conical holes in order to use them as collimators.

  - 2 **tilted conical holes of lower diameter** 40 *mm* **along the axis**, connecting them with the two axial holes performed in the plasma chamber. The conical holes are collinear and point to the center of the plasma chamber;
  - 12 **tilted conical radial holes of lower diameter** 40 *mm*, connecting them with the twelve radial holes performed in the plasma chamber (6.2). The conical holes are collinear and point to the center of the plasma chamber.

- **The magnetic trap is surrounded by an ARMCO iron yoke**, distant 150 *mm* from the hexapole ends (along the axis), 200 *mm* from the INJ,

EXTR axial coils outer radius and having thickness of 25 *mm*. The iron yoke is visible (coloured in blue) in figure 6.4. Also the iron has been drilled with 14 hole (of diameter 88 *mm*) along the cone of view of the 14 collimators.
At the end of each collimator we placed a quartz window of thickness of 3 *mm* and diameter 88 *mm* (coloured in yellow);

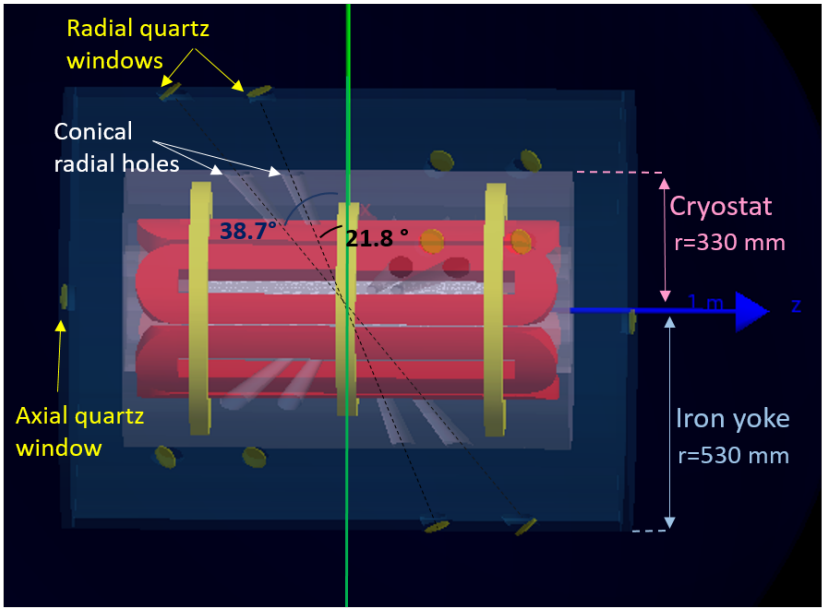

Figure 6.4: ARMCO iron yoke surrounding the magnetic plasma trap.

- **An array of** 14 γ**-ray detectors** (two axially placed and 12 radially) **has been placed collinearly at each collimator** (6.5). HPGe detectors have a length of 82 *mm* and a radius of 38 *mm*, and are surrounded by a layer of Al of thickness of 1 *mm*. The Al cylinder is shown in transparent pink, whilst the active part of the detector is coloured in cyan inside of it.

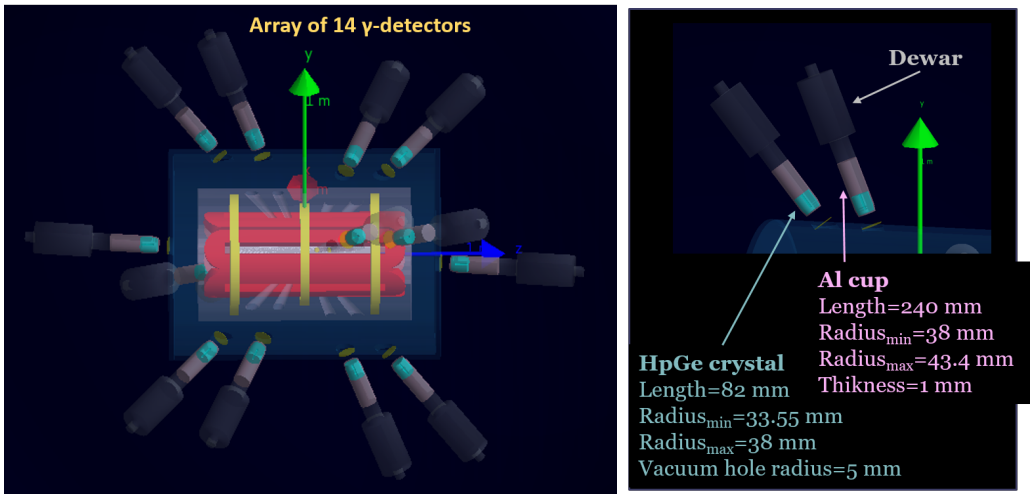

Figure 6.5: Top) The implemented final design of the $PANDORA_{Gr3}$'s trap with the magnetic system (coils in yellow, hexapole in red, cryostats in pink, the iron joke in blue), and the array of detectors placed collinearly at each collimator. Bottom) details of the HPGe array showing the size of the detectors used in the simulations.

The position and orientation of the collimators and γ-ray detectors has been chosen in order to avoid intercepting so called magnetic branches within the field of view (region of the magnetic trap where the B field lines are more intense), for which background noise due to intense bremsstrahlung X-rays emission (due to axial and radial losses impinging on the plasma chamber walls) is expected to be more intense (see fig. 6.6).
Figure 6.6 shows 3D views of the detectors array surrounding the trap: each pair of HPGe has been placed out of the regions where the magnetic field lines intercept the plasma chamber walls.

An example of ray-tracing simulations for γ-rays in the 100 keV – 1 MeV range and trajectories of the γ-rays impinging in the detectors is sketched in fig. 6.7 (on the left and on the right, respectively).

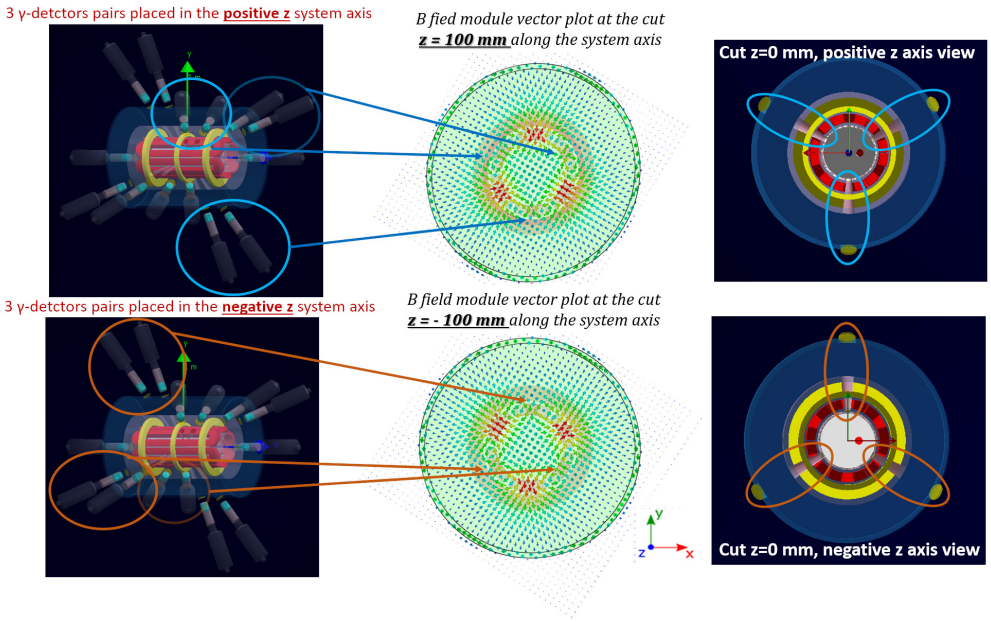

Figure 6.6: Sketch of the detector positions compared to B field lines distribution.

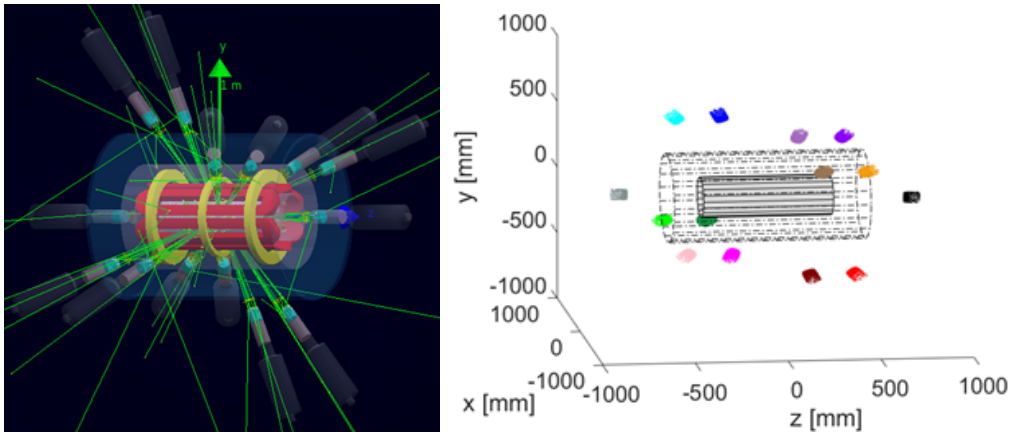

Figure 6.7: On the left, ray-tracing simulations for γ-rays in the 100 keV – 1 MeV range. On the right, example of impact positions of the γ-rays impinging in the 14 detectors, performed by simulation.

6.2 Evaluation of the array's efficiency

The aim of the simulations has been to estimate the total detection efficiency in order to evaluate the feasibility of the experiment using γ-rays, and to choose the best type of detector in terms of efficiency and resolution. We performed the simulation implementing and comparing two different types of detector: the Hyper-Pure Germanium (HPGe) and the Lanthanum bromide scintillation detector ($LaBr_3$).
As a first step we performed simulations considering the emission from an isotropic point-like source placed in the center of the plasma chamber. The efficiency of detecting γ-rays of different energies was simulated by changing the energy of the source in the range from 100 keV to 2 MeV (typical energies of the decay-products of the radionuclides of the $PANDORA_{Gr3}$ physical cases). The results are shown in fig. 6.8 for the array of 14 HPGe detectors (on the left), and for the array of 14 $LaBr_3$ (on the right), using the same detector size. These plots show the total efficiency of the array, which includes both geometrical and photopeak efficiency. The efficiency for the two types of detector is very similar (of the order of 10^{-3}).

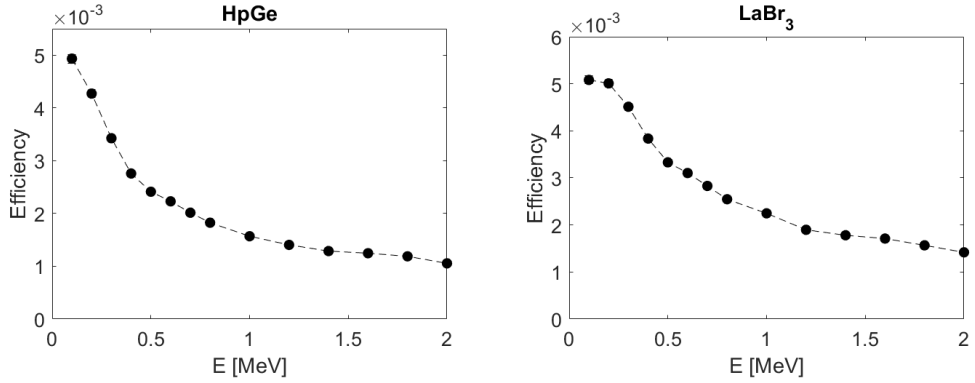

Figure 6.8: Efficiency vs. energy for HPGe detectors (left) and $LaBr_3$ (right) detectors.

However, the main difference between the two types of detectors is the energy resolution. The typical resolution as a function of the incident energy is shown in fig. 6.9 for HPGe (on the left) and $LaBr_3$ (on the right)

detectors, respectively. They differ more than one order of magnitude, and this strongly affects the signal to noise ratio (in this case the noise is represented by the in plasma self-emission).

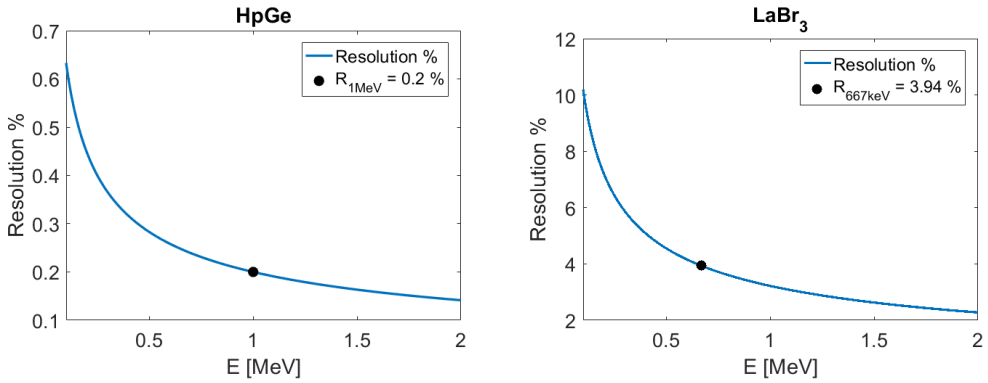

Figure 6.9: Energy resolution vs. the energy for HPGe (left) and LaBr3 (right).

A typical noise spectral shape, due to plasma self-emission at $n = 10^{13}\ cm^{-3}$ having a Volume of 1500 cm^3 is shown in fig. 6.10.

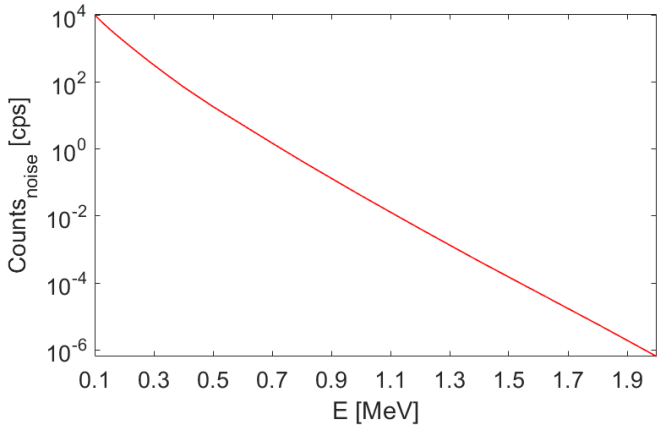

Figure 6.10: Typical noise spectrum, due to plasma self-emission (the width of the bin in the x axis corresponds to 10 eV).

It has been evaluated starting from measurements on existing traps and rescaling them to higher densities and volumes according to an emis-

sivity model. The spectrum shown has been normalized by the total efficiency of the system and represents the counts per second that would be measured by the $PANDORA_{Gr3}$ setup.
The noise spectrum was used to evaluate the time needed to have a 3σ level of confidence, and to compare the response of the HPGe detectors array with the $LaBr_3$ detectors array. Considering, for the sake of example, a signal of 0.25 *cps* (counts per second) in the multi detector array at a given energy, the procedure adopted was to integrate the noise spectrum – estimated by the spectrum in fig. 6.10 - in the same energy window used to integrate the gamma peak, for each type of detector.
In fig. 6.11 (left for HPGe, and right for $LaBr_3$) the trend of the signal counts (in red) and of the 3 times the noise (in black) are shown, in order to see where and when the cross-over point between the two curves occurs.

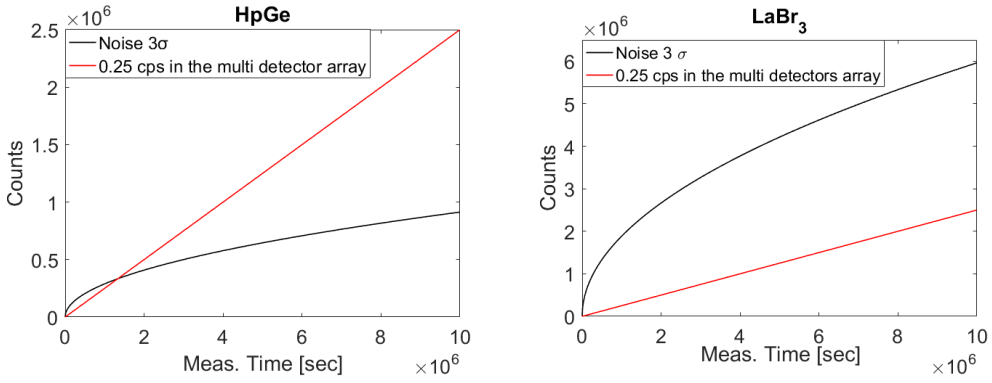

Figure 6.11: Trend of the "*real*" signal counts (in red), considering a rate of 0.25 *cps* (counts per second) in the multi detector array, and of the 3σ the noise level (in black).

The intersection from the two lines shows the point where the signal overcomes the 3σ noise level, and the correspondent abscissa is the measurement time needed to have a 3σ level of confidence. The comparison shows that after about several days it is possible to obtain a 3σ level confidence using the array of HPGe detectors, whilst in the case of the array of $LaBr_3$ a much longer time is needed, the measurement is very challenging or, eventually, not-feasible, depending on the physics case investigated

(as shown in figure 6.11).
Due to the observed strong difference in the array performances additional simulations were focused only on the HPGe detectors array.
In order to estimate the time needed for reaching 3σ confidence level taking into account different lifetimes, i.e. different rates in the detectors' array we built plots showing the correlation between time measurement vs the decay-rate (or the lifetime) of the radionuclide. Examples of these plots are shown for Lutetium and ^{134}Cs in figures 6.12 and 6.20.

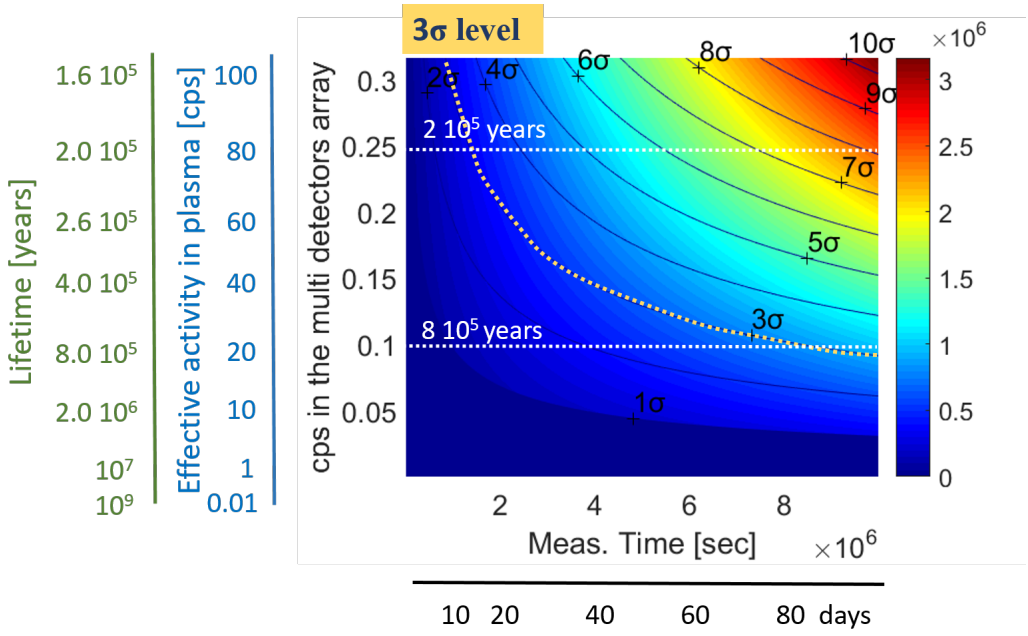

Figure 6.12: Confidence levels that it is possible to obtain after a given measurement time, reported on the x axis, vs the decay-rate (or the lifetime) of the Lutetium radionuclide.

The green vertical axis reports on the lifetime expressed in years, starting from the lifetime of the neutral isotope to the values of lifetimes predicted by the theory and that are feasible in our plasma trap (the expected collapse of the lifetime as theoretically evaluated is about 6 order of magnitude for the case of Lu). Considering these lifetimes, the effective activity in the plasma (expressed in cps) – assuming a plasma of 1500 cm^3

in volume with a concentration of 1% of Lu with respect to the buffer density (10^{13} ions/cm^3) – are shown in the blue vertical axis and finally, taking into account the efficiency estimated by GEANT4 simulation, we obtained the cps detected in the multi detectors array (black vertical axis). Along the x-axis the measurement time is reported. As done for figure 6.11, the error over the background is estimated as the square-root of counts in the energy resolution window, whilst the counts due to the real decays occurring in the plasma are summed-up linearly with time. Black lines (and, in particular, the dotted-yellow) represent contours giving sigma-confidence-level at each given combination of expected activity vs. measurement time. Pseudo-colours give the total number of counts at the peak of interest.
This plot summarizes the feasibility of the measurement and shows that for the variations of the lifetime expected from the theory in our laboratory plasmas, we expect that a measure lasting from tens of days to a couple of months is needed in order to obtain a 3σ level of confidence. Similar plots, for the other physics cases, have been performed.
Moreover, in the present calculations only one-peak of γ-rays for each radionuclide has been considered, while in the reality we can take profit of the multi-peak structure of the emitted gamma spectra, which will improve the confidence even at shorter acquisition times.

6.2.1 Evaluation of the array's efficiency: ellipsoidal source

As next step, simulations have been performed considering an isotropic ellipsoidal source placed in the center of the plasma chamber, having semi-axes lengths 79 mm, 79 mm and 56 mm, respectively for the x, y and z axis (corresponding to the plasma volume and shape provided by the magnetic field profiles in the $PANDORA_{Gr3}$ plasma trap). In a similar fashion to what was previously done, the $\gamma - ray$ energy range explored for the efficiency evaluation of the array was in the range from 100 keV to 2 MeV. For the noise evaluation due to plasma self-emission we considered a density of $n = 10^{13}\ cm^{-3}$, and a volume of 1500 cm^3. The trend of the array efficiency is shown in fig. 6.13 assuming, as before, 14 HPGe detectors.

The comparison between the results shown in the plots 6.13 and 6.8

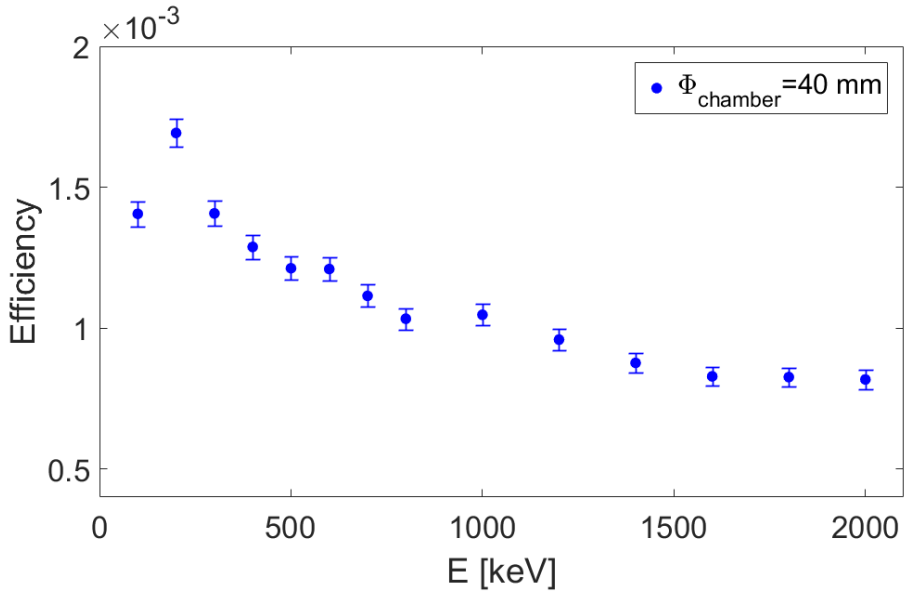

Figure 6.13: Detection efficiency as a function of the γ-ray energy for HPGe detectors for an ellipsoidal source.

(left) indicates that the efficiency in the case of the ellipsoidal source is a factor 2.5 lower compared to the one for a point-like source for the lower energies while the difference is about a factor 1.5 for higher energies.
The multi-parametric plot of measurability of the Lutetium Lu assuming an ellipsoidal source and a detection array with 14 HPGe is shown in fig. 6.14.

6.2.2 Characterizations of collimator-holes position and shape

Further simulations have been performed in order to investigate other configurations in terms of positions and diameters of the collimator holes. The values shown in the section 6.1 are in fact the best values from this study. The scope of the characterization has also been to define a tolerance interval for each parameter, considering the technical limitations that can arise in the design study of the magnetic trap (e.g., mechanical constraints imposing a certain angle for the conically-shaped holes).
We investigated the effects due to a reduction of the conical holes and to

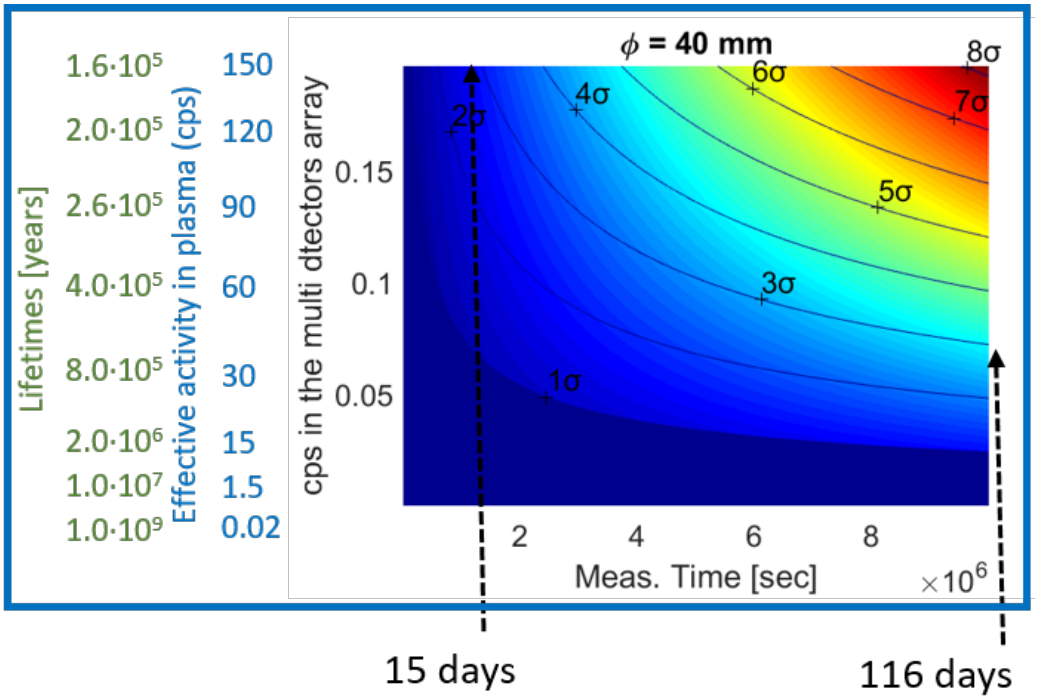

Figure 6.14: Confidence levels that it is possible to obtain after a given measurement time, reported on the x axis, versus the decay-rate (or the lifetime) of the Lutetium radionuclide.

different choices of the inclination angle and the position. The simulated efficiency plots associated to four different smaller diameter ϕ chamber are shown in fig. 6.15, the corresponding multi-parametric plots of measurability of the physic case of Lutetium Lu are shown in fig. 6.16.

At 300 keV (energy of the emitted γ-ray for the physic case of Lutetium Lu) the efficiency changes a factor of 2 from the higher diameter case to the lower one; consequently, the measurement time in order to obtain a 3σ level of confidence ranges from 15 days (considering the maximum variation in the lifetimes from the ionized Lu to the Lu neutral state) to 28 days (see fig. 6.16).

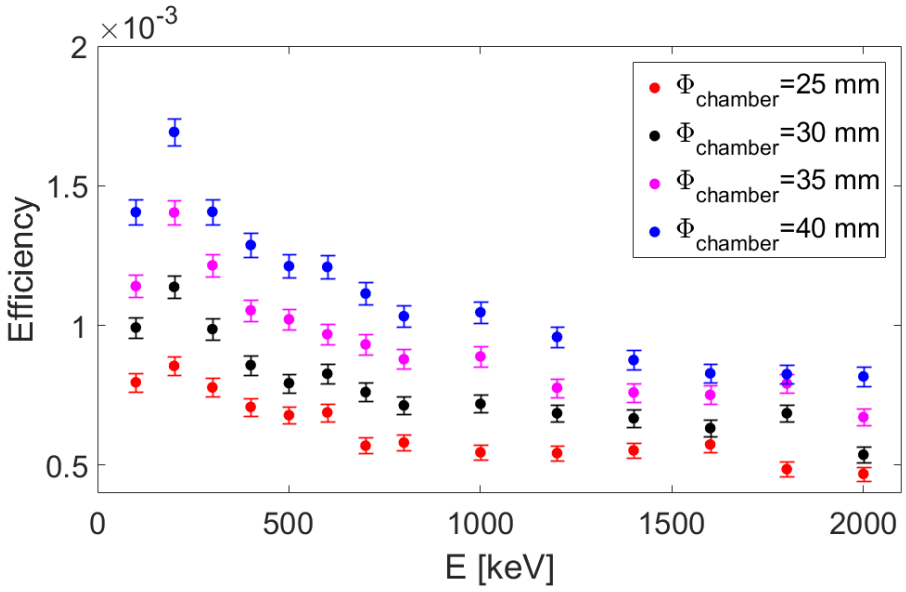

Figure 6.15: Efficiency plots versus the energy for HPGe detectors for a ellipsoidal source, versus different lower diameter of ϕ chamber of the conical holes.

Finally, we also investigated the effect related to three different choices of the inclination angle of the collimators. The efficiency plots are shown in figure 6.17.
Figure 6.17 shows that the overall average variation of the efficiency at the three representative angles we opted for is less than 20%. This is a promising outcome, meaning that the angle of the holes in the cryostat is less critical than shape and geometrical size. In terms of cryostat machinery, it will relax any requirement from this point of view.

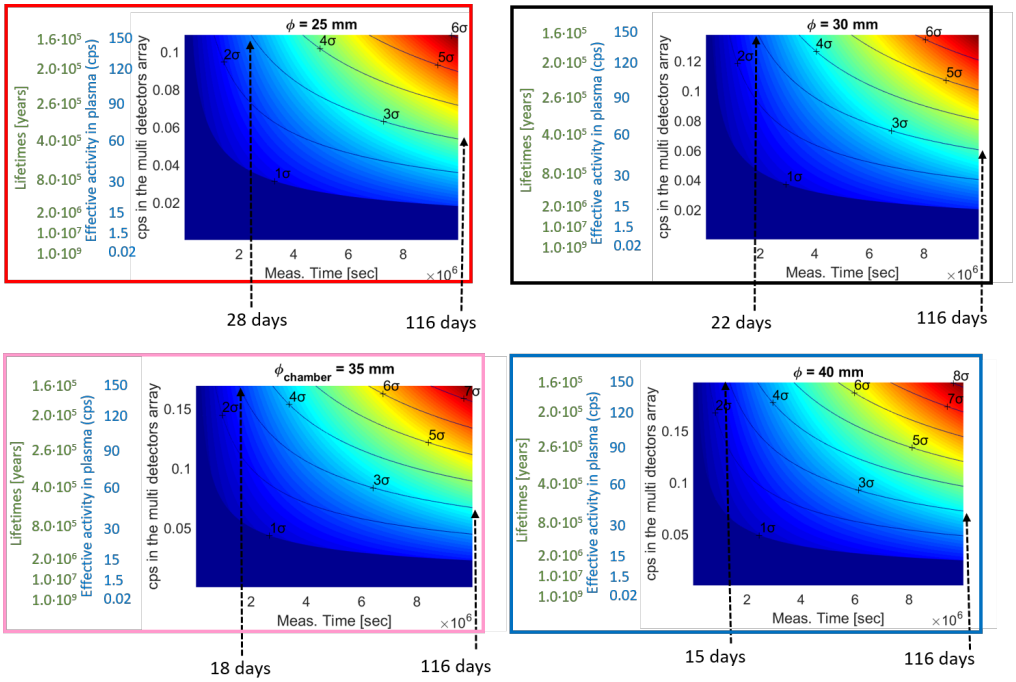

Figure 6.16: Confidence levels that it is possible to obtain after a given measurement time, reported in the x axis, versus the decay-rate (or the lifetime) of the Lutetium radionuclide for four different values of the hole diameter of the detector collimator.

The results of simulation coming from the complete characterization confirm the feasibility of the measurement with the simulated HPGe array and the implemented geometry. Using the maximum hole diameter of 40 *mm*, the correspondent plot shown in fig. 6.16 (bottom-right) shows that, for the Lu physical case, for the variations of the lifetime expected from the theory in our laboratory plasmas, we expect that a measure lasting from about 15 days to three/four months is needed in order to obtain a 3σ level of confidence. These results highlight: i) the necessity to maintain ECR plasma in the same condition for weeks and, consequently, the crucial role played by innovative plasma heating methods able to maintain the plasma as much as possible stable, minimizing the turbulences trigger. ii) the necessity to perform an accurate on-line monitoring of all plasma parameters, also in a time- and space-resolved.

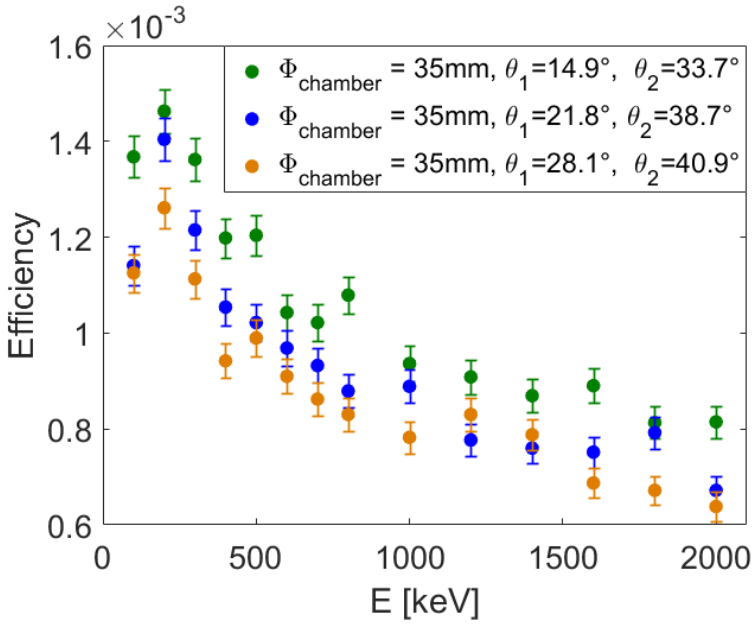

Figure 6.17: Efficiency vs. energy for HPGe detectors for a ellipsoidal source, versus different inclination angle of the conical holes.

6.3 Feasibility of the measurement for ^{134}Cs and ^{94}Nb

Confidence plots for the ^{134}Cs case has been also performed and is shown in figure 6.18.

The green vertical axis reports on the lifetime expressed in years, starting from the mean lifetime of the neutral isotope (2.97 years) to the values of lifetimes predicted by the theory (the expected collapse of the lifetime as theoretically evaluated in [69] is about 2 order of magnitude, around 20 keV). Considering these lifetimes, the effective activity in the plasma (expressed in cps) – assuming an ellipsoidal plasma of 1500 cm^3 in volume with a concentration of 0.00001% of Cs with respect to the buffer density (10^{13} ions/cm^3) – are shown in the blue vertical axis and, taking into account the efficiency estimated by GEANT4 simulation, we obtained the cps detected in the multi detectors array (black vertical axis). Along the x-axis the measurement time is reported.

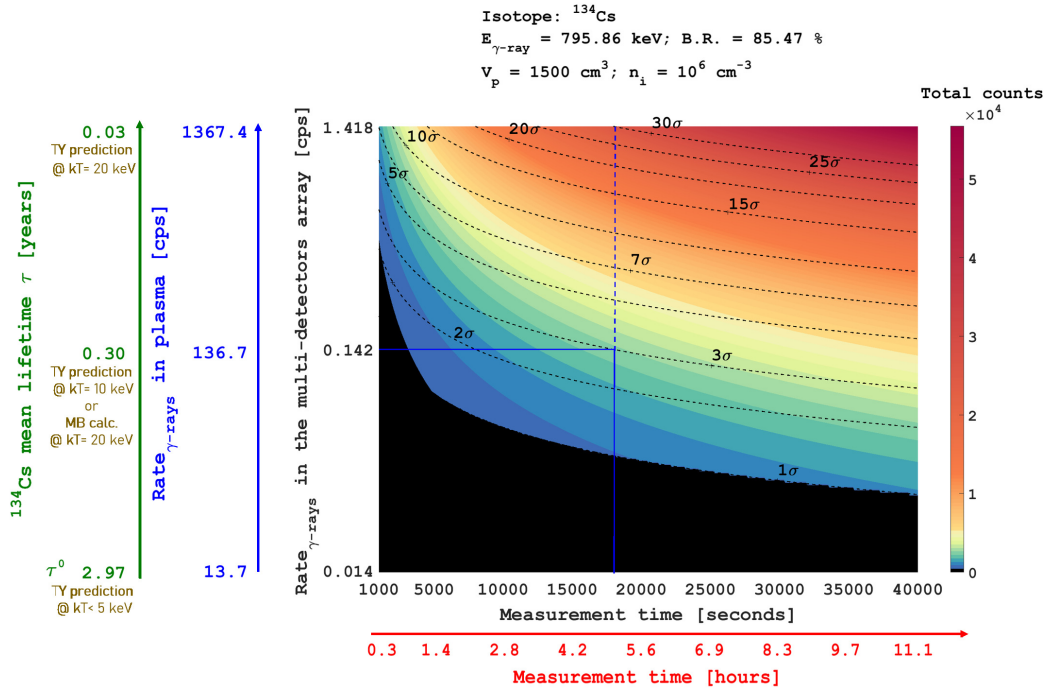

Figure 6.18: Confidence levels that it is possible to obtain after a given measurement time, reported on the x axis, vs the decay-rate (or the mean lifetime) of the ^{134}Cs radionuclide.

Several confidence-levels in the range 2σ-30σ are labelled in the plot and the black region is the one for which the confidence-level is below 1σ. Pseudo-colours give the total number of counts at the peak of interest. Assuming, for example, a variation of the mean lifetime of an order of magnitude (rate 0.142), about 5 hours are necessary to obtain 3σ confidence-level, whilst about 2 hours are enough to reach 2σ confidence-level, etc. In the plot 6.19 the "*iso-significance*" at 3σ and 5σ were reported (in log-log scale). These plots summarize the feasibility of the measurement and show their specific sensitivity for discriminating, eventually, among different theoretical predictions.
Similar plot for the ^{94}Nb has been performed, it is shown in fig. 6.20. In this case, the expected collapse of the lifetime as theoretically evaluated in [69] is about 5 order of magnitude (at around 10 *keV*). We assumed an

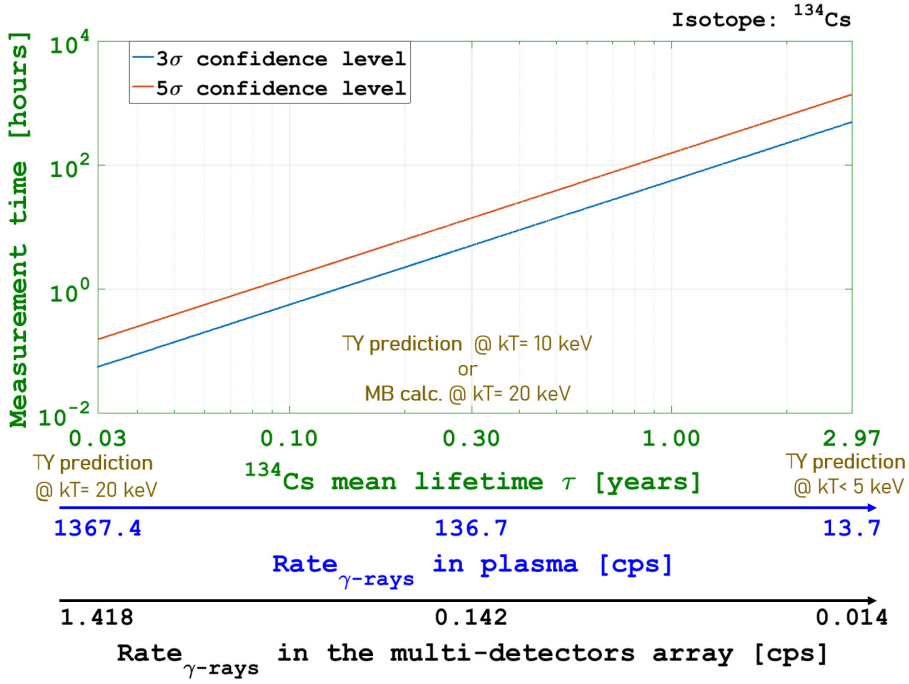

Figure 6.19: "*Iso-significance*" level at 3σ and 5σ reached after a given measurement time, reported on the y axis, vs. the decay-rate (or the lifetime) of the ^{134}Cs radionuclide.

ellipsoidal plasma of 1500 cm^3 in volume with a concentration of 0.0001%. In the plot 6.21 the "*iso-significance*" at 3σ and 5σ are shown, for ^{94}Nb (left). Also in these cases it is possible to evaluate the feasibility of the measurements and their specific sensitivity for confirming or, even, contradict the theoretical predictions. I.e., it will be possible to obtain 3σ confidence-level in a reasonable measurement time for PANDORA_Gr3 (within three months) only if the variations will be at least of 3 orders of magnitude compared to the mean lifetime of the neutral isotope.

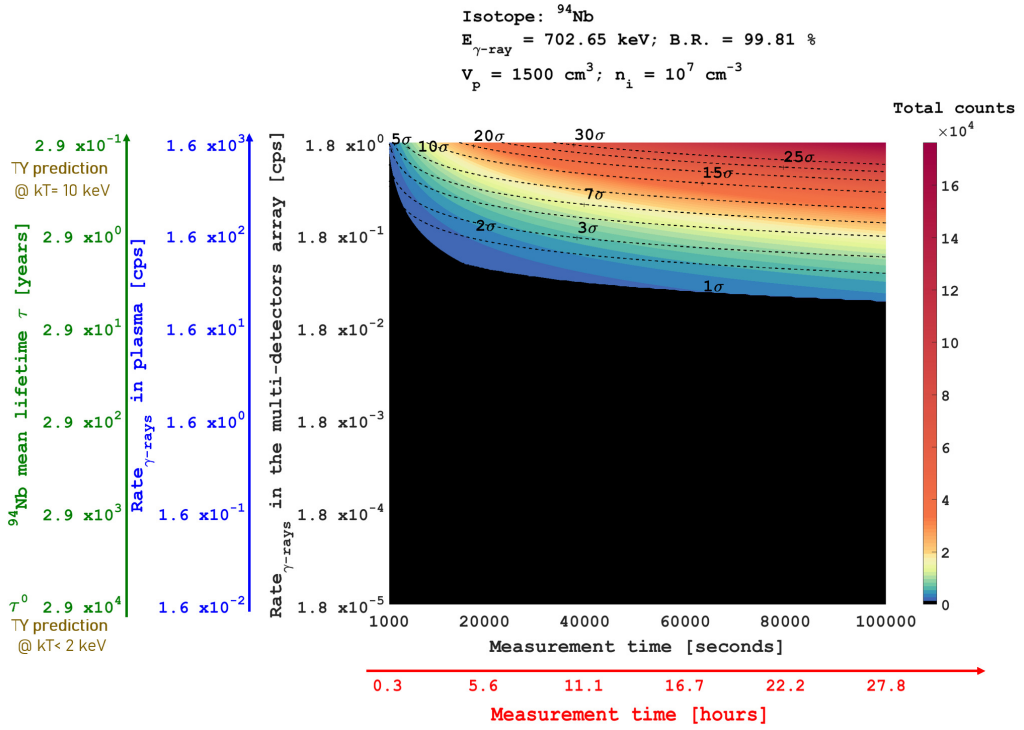

Figure 6.20: Confidence levels that it is possible to obtain after a given measurement time vs the decay-rate (or the lifetime) of the ^{94}Nb.

6.3.1 Plan for further work: the noise suppression investigation

More investigations about the noise suppression have been also performed in order to increase the signal-over-noise ratio and to reduce the very high rate coming from the intense plasma emission, necessary to obtain the optimum performance of the HPGe detectors.
For this purpose: 1) we started to perform simulations considering the noise contribution coming from the plasma directly in GEANT4, in order to estimate the other effects (such as the Compton contributions) and to estimate the absolute efficiency; 2) since the radiation emitted from the plasma is very high (mainly for energies lower than 200 keV, as show in the figure 6.10), we will study a specific shield for the detectors.
Preliminary simulations, assuming the emission from an isotropic point-

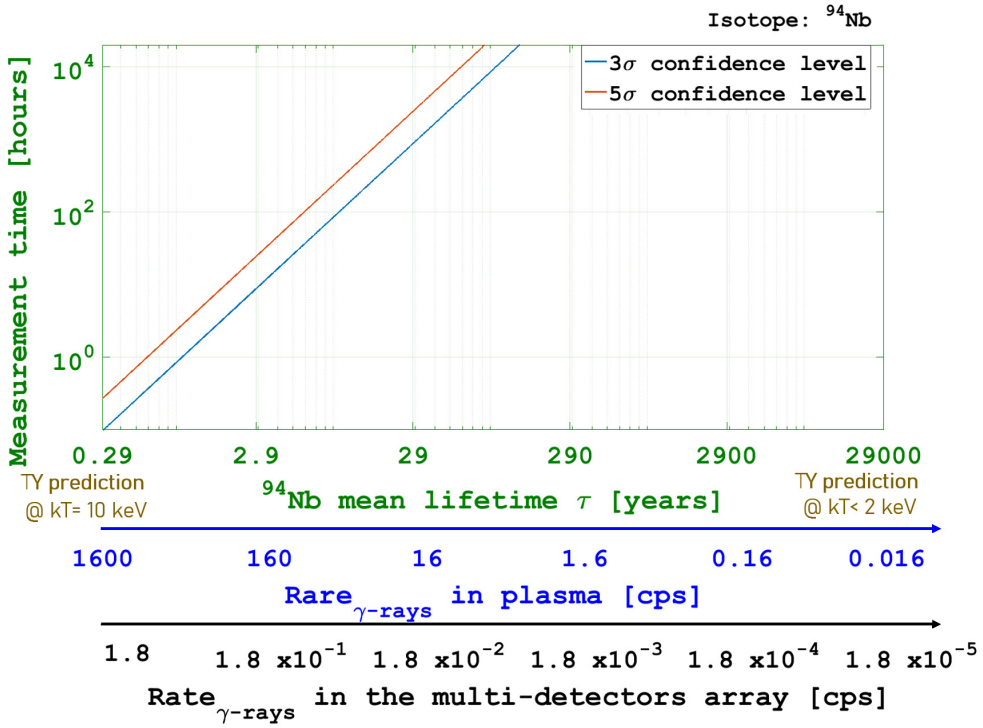

Figure 6.21: "*Iso-significance*" level at 3σ and 5σ reached after a given measurement time vs. the decay-rate (or the lifetime) of the ^{94}Nb.

like source placed in the center of the plasma chamber, having an energy distribution as the typical noise spectrum due to plasma self-emission at $n = 10^{13}\ cm^{-3}$ and with volume of 1500 cm^3 have been performed.
Fig. 6.22 shows the comparison of the spectra including only events depositing full energy in the detector (indicated as photopeak counts) and the spectrum of total detected events. The difference in the yield is of the order of 10% and this result supports the previous estimate of the background contribution to the detected γ-ray spectrum.

Simultaneously, in order to reduce the intense rate in the detectors due to plasma emission, a specific shield will be used: it is necessary to reduce as much as possible the radiation up to 250 keV, but at the same time reach a good transmission at 306 keV. Some preliminary considerations have been done, comparing the transmission trends (*NIST* database) of different thickness of lead with an additional shield of Cd or Cu, in or-

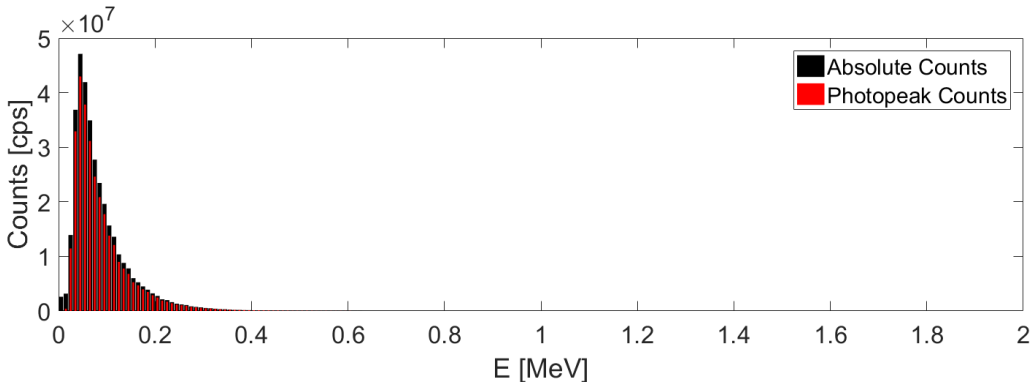

Figure 6.22: Counts versus energy for HPGe detectors array, comparing the absolute counts with the photopeak ones.

der to fully suppress the contribution up to 100 keV (also the radiation due to the lead K-edge). In figure 6.23.a) some transmission trends of different materials are shown as a function of the $\gamma - ray$ energy. In our specific case, due to the noise spectral shape, a shield made of 1 mm of Pb or 1 mm of Pb + 1 mm of Cd could be effective in significantly reduce the background noise. A preliminary evaluation of the two different shields effects on the noise spectrum is shown in figure 6.23.b). The noise below 200 keV decreases significantly. We will perform simulations finalized to characterize the system in order to have the best compromise between the increase in signal-to-noise ratio (measurability plot, in terms of measurement time and confidence level) and the reduction of the noise rate.

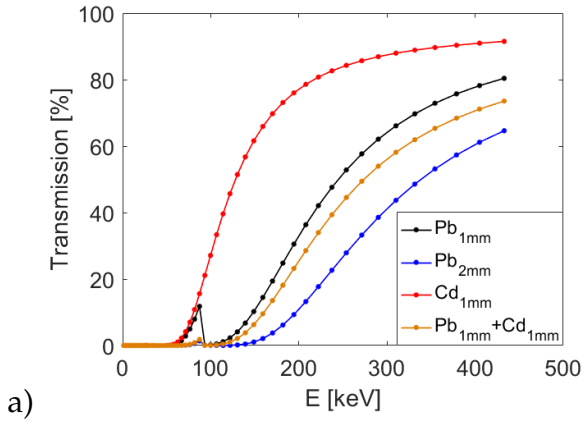

a)

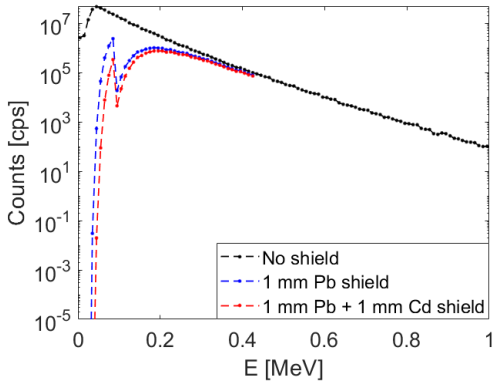

b)

Figure 6.23: a) Transmission trend versus the energy for different shield thickness and/or material. b) Shields effects on the noise spectrum (Log scale).

6.4 The Flexible Plasma Trap (FPT) Setup: Benchmark measurements

In order to validate Monte Carlo simulations performed using GEANT4 shown in the previous paragraph, benchmark measurements in the simple-mirror Flexible Plasma Trap (FPT) installed at INFN-LNS (see section 3.1.2), have been carried out.
We put a ^{152}Eu γ-ray source (13.6 kBq) inside the FPT-plasma chamber (as shown in fig. 6.24.a)) and used a HPGe detector (having quantum

efficiency Q.E. $\sim 30 \div 2000\ keV$) with a radius of 3 cm, to perform the measurement. In order to minimize the background, the HPGe detector has been shielded with lead, using only one slit in front of the detector with an aperture of about 3 cm (see fig. 6.24.b)).

a) 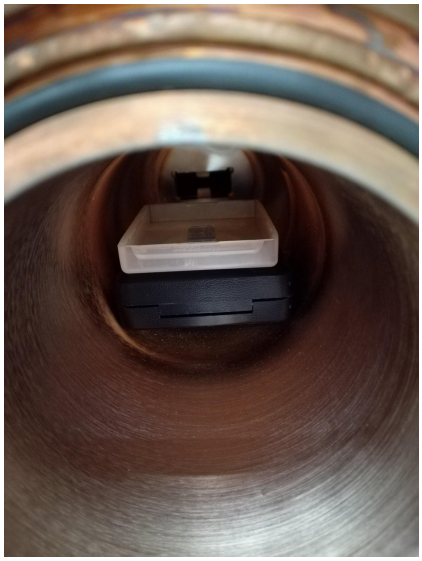 b) 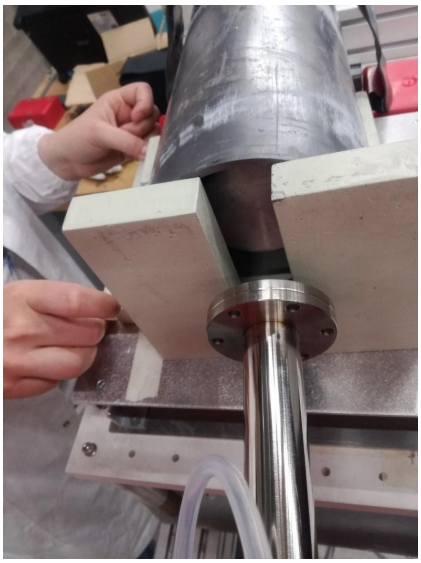

Figure 6.24: a) A ^{152}Eu source at 13.6 kBq inside the FPT plasma chamber. b) The HPGe detector shielded by lead.

A typical experimental spectrum with a measurement time of 3600 seconds is shown in fig. 6.25, where it is possible to distinguish all the characteristic peaks of ^{152}Eu (the background has been already subtracted). The experimental background rate is shown in fig. 6.26.

The measured background rate is negligible compared to the typical noise spectrum due to plasma self-emission (it is sufficient to compare data in figure 6.10 and 6.26).
Using GEANT4, we performed the simulations aimed at validating the design and the physics included in GEANT4 model, in the energy domain of interest for $PANDORA_{Gr3}$ implementing the geometry of the system (as illustrated in fig. 6.27).

Despite the size and shapes of the FPT are pretty different from the ones of the $PANDORA_{Gr3}$ full-scale setup, materials and overall characteristic are practically the same, and this can be very helpful for a direct

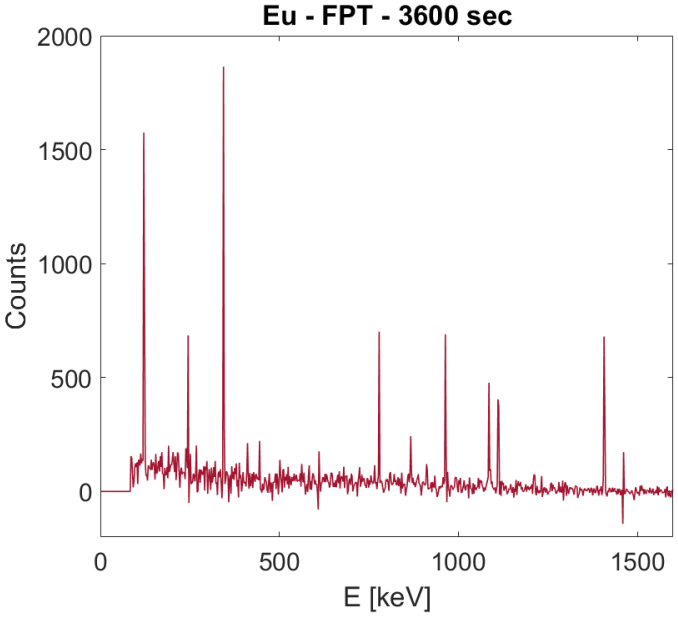

Figure 6.25: Experimental spectrum measured by a HPGe detector.

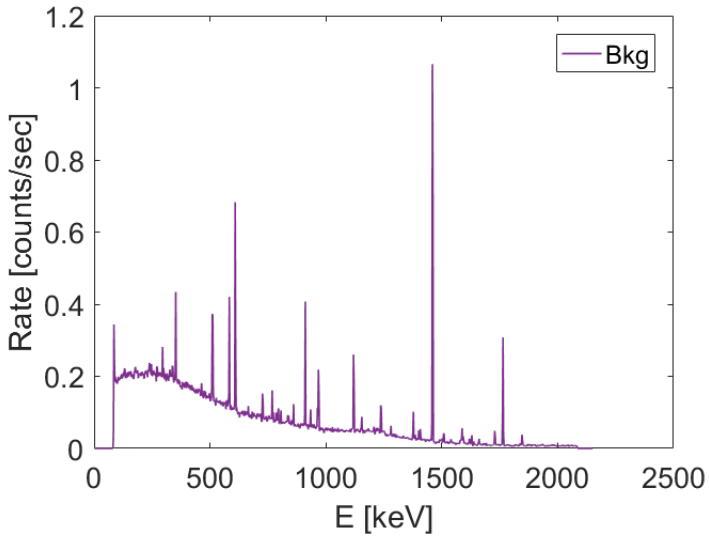

Figure 6.26: Experimental background rate versus the energy.

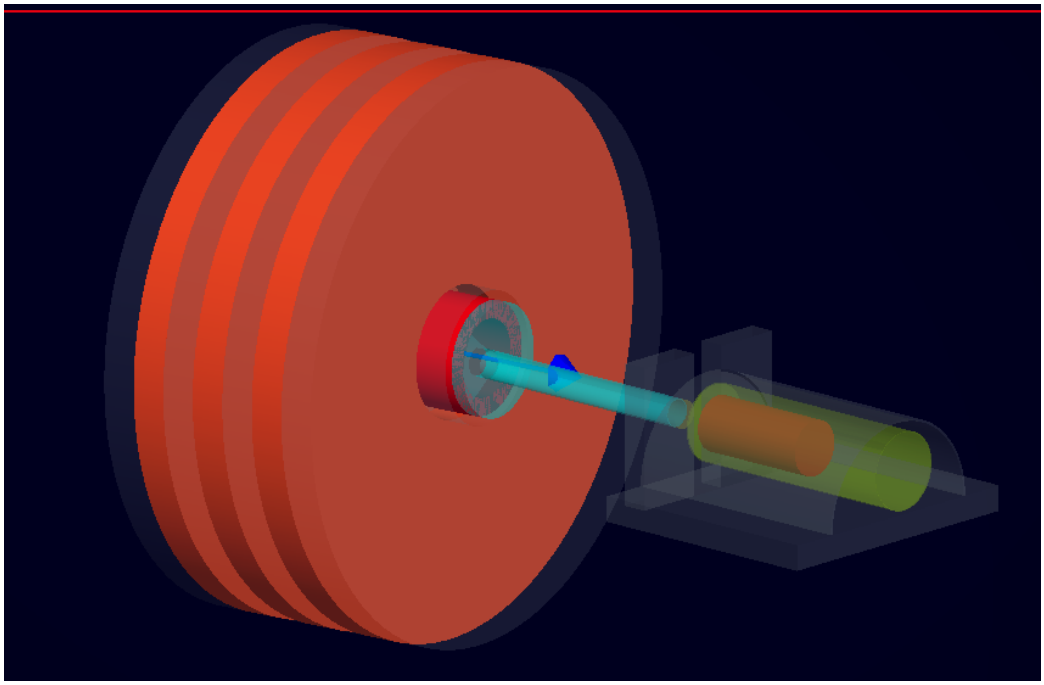

Figure 6.27: Complete geometry of the test-bench as designed in GEANT4, including the HPGe detector (represented in red, inside the green Aluminium cylinder layer) shielded by lead (in grey); the flange (in cyan) connected with the FPT-plasma chamber (in red). Also the other materials, such as the coils surrounding the plasma chamber, have been simulated (in orange).

rescaling of the results, other than for the validation of simulations outcomes.
Results of the Monte Carlo simulations of the detection efficiency were compared to the measured experimental efficiency. A very good agreement between data and simulation was found as shown in figure 6.28.

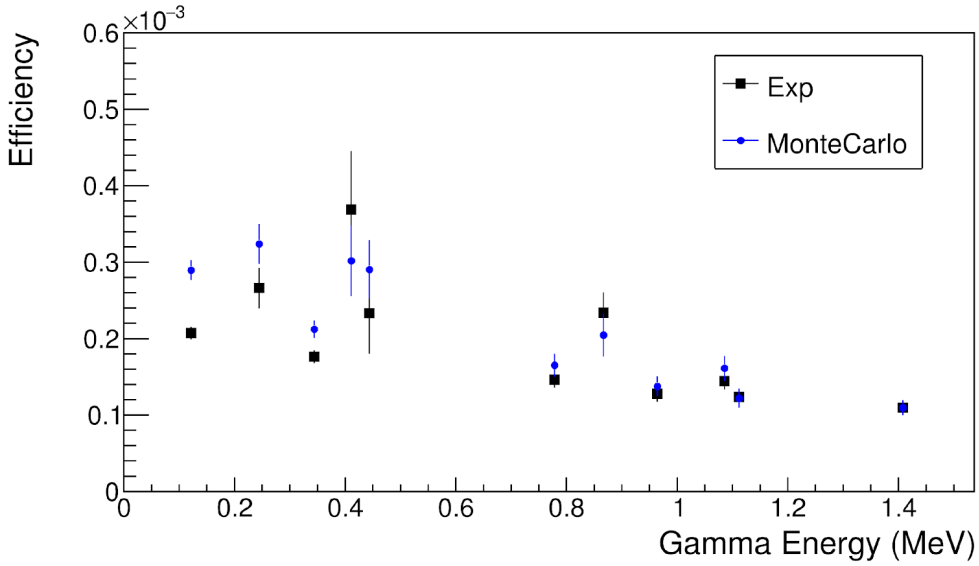

Figure 6.28: Simulated efficiency as a function of the $\gamma - ray$ energy (in blue) are compared to the measured experimental efficiency (in black).

Conclusions and Perspectives

The experimental study presented in this work has aimed at investigating ECR magnetoplasmas proprieties, in stationary versus turbulent regimes, by means of a multi-diagnostics system. The experimental results demonstrated the plasma diagnostic plays a crucial role in the new scientific scenario where laboratory ECR plasmas can become new environments for fundamental nuclear physics investigations. Any measurement, in fact, has been done in the frame of the preparatory phase of PANDORA_Gr3 project, that for the first time will use the plasmas investigated by the techniques here presented for studying nuclear β-decay in an astrophysical-like scenario.
In this framework, plasma diagnostics has to work synergically with detection system (i.e. the array of HPGe detectors) principally in a twofold way:

I) to assure an accurate on-line monitoring of the all plasma parameters aiming to characterize the plasma environment;

II) to estimate the mean lifetime of the in-plasma isotopes; the total amount of decays is detectable by γ-rays tagging.

The direct correlation of the plasma environment and the decay itself is possible only by simultaneously identifying and discriminating radiation emitted by the plasma (from microwave to hard X-ray) and γ-rays emitted after the isotope β-decay. The simultaneous use of all tools and analytical techniques, now available at INFN-LNS and here reported in details (see chapter 3), allows now an unprecedented capability of mastering these

magnetoplasmas properties, in the whole energetic domain, also by high resolution space- an time-resolved analysis (about this latter statement, the work here presented has been focused on the X-ray part of the energy spectrum).
In summary, the main outcomes of this thesis are that the plasma temperature and density can be measured - eventually in space and resolved way - with an uncertainty that is around 7% for the temperature, and around 25% for the total density. Partial densities of warm and hot electrons are measured via X-ray spectroscopy with about 10% uncertainty, while the use of OES (optical emission spectroscopy) in the next future will allow to reduce density measurement uncertainties of at least a factor 2.
A short-list of the original thesis' outcomes is here given:

(1) developments of an X-ray pin-hole camera system and CCD images analysis and post-processing procedures (see section 4.1) capable to evaluate the spatial distribution of the warm electron energy distribution (see section 5.4);

(2) the proposal of using, for the first time, a semi-empirical parameter, named I_S, as an indication of the plasma instability strength (see section 4.2);

(3) the experimental demonstration of the plasma turbulence suppression, when using the TCFH which caused a clear reduction of I_S (see section 5.2) also improving the plasma confinement (see section 5.3);

(4) the demonstration of the measurability of in-plasma isotopes lifetimes, checked in a "*virtual experiment*" of PANDORA_Gr3, obtained by GEANT4 simulations (see chapter 6).

These results have been crucial for supporting the feasibility study of the PANDORA experiment, but at the same time - as confirmed by the several invited talks and published papers - have been highly recognized in plasma physics and ion source physics research fields [8, 9, 10, 11, 12, 13, 14, 15, 16, 17, 6]. In particular, they allowed to gain a wider

knowledge of plasma turbulent regimes in linear, non-axisymmetric magnetic systems, and also to investigate more efficient plasma heating methods.

Progresses have been done both in the context of instruments and methods: concerning the *item (1)* above, although the system uses already existing methodologies, the PhD thesis has contributed to a relevant optimization of the overall setup, including the implementation of the multi-disk collimator and the system integration, allowing measurements at unprecedented RF power regimes . The multi-disks collimator has allowed a remarkably increase of the signal-noise ratio up to 200 W of pumping RF power and, consequently, to study the plasma turbulence regimes occurring at these power levels and not below (see section 3.2.3). The integrated X-ray imaging allowed to unveil and investigate simultaneously the local energy content of the plasma and the energy released as bremsstrahlung radiation caused by fluxes of deconfined electrons impinging on the plasma chamber walls. Since these acquisitions are typically fast (tens of seconds), they **allow to monitor, in an on-line mode, any change of plasma structure and of plasma losses** (see section 5.3.1).

New and advanced analytical methods have been developed for post-processig PhC images, as detailed described in the section 4.1. It allowed **powerful investigations in terms of space-resolved spectroscopy** (section 5.4), putting in evidence the local displacement of electrons at different energies, as well as of plasma ions, highlighted by fluorescence lines emission. By this system and analytical methods - reaching high spatial and energy resolution of, respectively, 500μm and 0.326keV at 8.1keV - the study of the confinement and dynamics of losses was possible. It allowed **to perform the imaging of the elemental distribution, distinguishing the emission coming from plasma only, versus the ones coming for the plasma chamber walls materials**, as reported in the section 5.4.1. A complementary analysis was carried out not by energy-filtering of the images but rather making a local energy resolved analysis of the emitted X radiation (see 5.4.2). A proper combination of these techniques make possibile **the local plasma parameters monitoring** (i.e., local evaluation of plasma density and temperature).
Finally, the plasma radius was measured with an uncertainty of about

5%. In perspective, by using two CCD pin-hole camera setups simultaneously (along the axial line and the radial one) it will be possible **to estimate the plasma volume**. Its determination will be very useful for PANDORA_Gr3, since the activity of the in-plasma isotopes directly depends on plasma volume.

For *item (2)*, **the validity of I_S was confirmed experimentally** using analysis procedures based on the evaluation of Pearson correlation coefficients. The definition of this parameter was introduced, as described in the section 4.2, **to study, for the first time in a quantitative way, the level of kinetic turbulences**.

As it for *item (3)*, the study of turbulence vs stable regimes allowed to demonstrate the damping of the instability under the TCFH plasma heating mode (section 5.2.5). This result has a twice relevant outcome: a) from one side a new "knob" for mastering the plasma instabilities and to improve the plasma confinement is now available, being very useful for PANDORA in order to maintain the plasma in a stationary dynamical equilibrium for weeks; b) from the other side, the mechanism of plasma instability is scientifically relevant by itself, since there is the attractive opportunity to reproduce and study these interesting phenomena of astrophysics interest (such as the Cyclotron Maser Instability) in the laboratory plasmas, measuring several properties even in the transient regimes.

Concerning the *item (4)*, the numerical simulations performed in GEANT4 were focused on the design of the array of γ-ray detectors, investigating the total efficiency of the array in terms of detectors type and of their optimal displacement around the trap (including collimation systems). The results of the **numerical simulations** demonstrated, in a "*virtual experiment*", **the feasibility of the measurement in terms of signal/noise ratio and σ-confidence level that it is possible to reach** (section 6.2). The run duration needed to get statistically meaningful results was estimated. Expected measurement time, needed for at least 3-σ level of confidence, range from few hours (for ^{134}Cs physical case) to 70-80 days (for ^{176}Lu physical case, which is the most challenging case in PANDORA_Gr3) assuming the theoretically expected variation in the lifetime of the radionu-

clides in our laboratory plasmas (at around 10 keV of electron temperature).

In conclusion and in perspective, the simultaneous use of all tools and methods here presented will guarantee to good operate following the experimental procedure of PANDORA_Gr3. In a nutshell, by mastering and maintaining the plasma stable, in dynamical equilibrium, even for weeks; by detecting through the HPGe detectors array the γ-rays emitted after the β-decay of the isotopes, statistically meaningful (at least with 3-σ level of confidence); finally, by correlating the in-plasma radioactivity directly to the plasma density and temperature, monitored by the multi-diagnostics also in time- and space-resolved way.

Perspectives: towards simultaneous spatial- and temporal-resolved X-ray spectroscopy

Experiments aiming to investigate turbulent plasma regimes performing space- and time-resolved spectroscopy, simultaneously, are expected as the *next step*, in the near future. The idea is to trigger the pin-hole CCD camera at the onset of the plasma turbulences: this will allow to reach unprecedented capability of analysis of plasma dynamics, since it will possible to study how the plasma shape and morphologies change during the time in a turbulence regime, also locally determining plasma parameters. Towards this perspective, a preliminary characterization, in quiescent and turbulent Electron Cyclotron Resonance-heated plasmas, has been already performed, studying, in particular, the temporal and spectral evolution of the X-ray volumetric emission. In particular, in order to improve the resolution (both in time and in frequency), the RF probe has been connected with a diode and a scope in order to obtain the high-resolution time-resolved but totally integrated power emitted from the plasma, using this value as trigger signal for two HPGe detector, in order to perform volumetric X-ray spectroscopy. The time-resolved setup, sketched in figure 3.14, consists in fact in two multi-pins probe (one for the axial line inspection and the other for the radial one) connected with a diode and an 80 Gs/s scope, for studying very fast phenomena (with time scales below ns).

The preliminary detection and characterization (for the first time) of a Cyclotron Instability in both Radio and X-ray domains has been performed at INFN-LNS on the axis-symmetric Flexible Plasma Trap based on a Simple Mirror configuration, in which a plasma is sustained via Electron Cyclotron Resonance heating at 4 *and* 7 GHz.
The Radio and X-ray bursts produced by the unstable plasma have been characterized in a time resolved way: a) radio-signals detected along and across the magnetic axis have been measured in a timescale < 100 *nsec* via 80 Gs/sec, 20 GHz band scope; a dedicated wavelet analysis shows the inner-plasma self-generation of waves far from the pumping frequency; b) fast Germanium detectors provide the evolution of the X-rays emitted axially and radially, allowing time-resolved spectroscopy; typical observed X-ray bursts lie in the timescales of *ms* or tens of *ms*, depending on the mirror ratio, especially, and are emitted by the plasma few ms after the RF ones.
Both RF and X-ray signals can be ranked on a temporal sequence which provides the whole characterization of the instability. Typical images of the X-ray and RF bursts and of the spectrogram, acquired by scope during the experimental measurement, are shown, as an example, in fig. 6.29.a) and .b), respectively. The same trends are also visible in the data plot analysis illustrated in fig.6.30.
It has been also observed that instability onset depends on the axial magnetic field profile only, in particular in term of: a) time duration of X-ray bursts; b) intensity of the X-ray burst; and time repetition of X-ray and RF bursts.

What it has been done and here shortly commented is still under data analysis and will be the subject of a paper in preparation. Beside, the further optimization of the experimental technique is ongoing, and it includes the use of the X-ray pin-hole camera tool in order to perform simultaneously space- and time-resolved X-ray analysis. This study will allow to open new scenarios since it will be possible to study if and how do the plasma shape and internal structures change with time when occurring the kinetic turbulences. On this purpose, an X-ray shutter has been recently procured and it will be installed, tested and used during the experiment in order to further reduce the noise, and improve

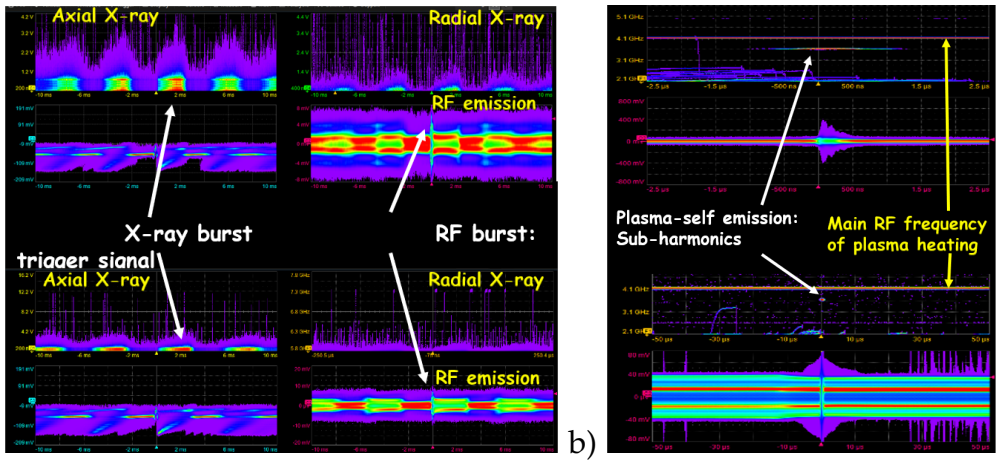

Figure 6.29: Typical images of the X-ray and RF bursts (a) and spectra (b) acquired by a scope. Both the RF burst used as trigger signal and the sequence of X-rays emitted bursts axially and radially are visible.

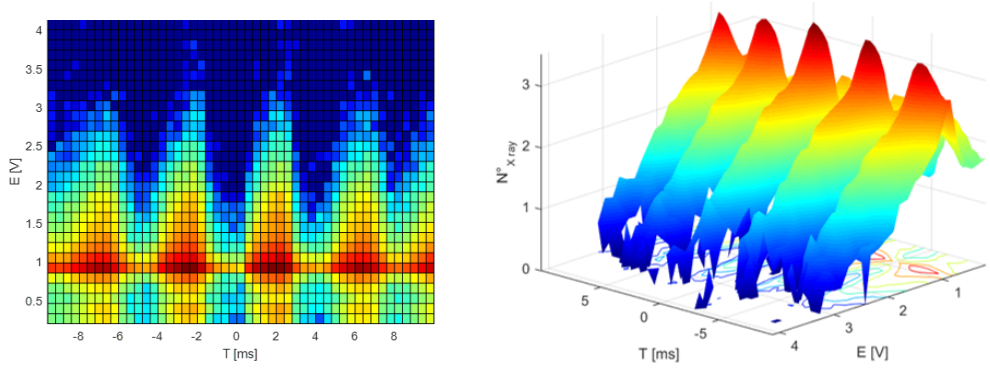

Figure 6.30: Data plot of the sequence of X-ray bursts performed in a time scale of 20 *milliseconds* corresponding to the acquired configuration shown in fig. 6.29.

the overall reliability and performances of the setup, also increasing the space-resolution.
This experimental campaign will be also focused on Cyclotron Maser Instability investigation in laboratory plasmas. In the astrophysical framework, several studies, very relevant in this field, have been published by

astrophysicists [70, 71, 72] thus motivating further experiments in magnetic traps.

Bibliography

[1] Y. Litvinov and F. Bosch, Rep. Progr. Phys. **74**, (2011).

[2] Takahashi et al., Phys Rev C **36**, (1987).

[3] F. Bosch et al., Phys. Rev. Lett. **77**, (1996).

[4] M. Jung et al., Phys. Rev. Lett. **69**, (1992).

[5] Y. Litvinov et al., Phys. Rev. Lett. **99**, (2007).

[6] D. Mascali, EPJ Web Conf. **227**, (2020).

[7] D. Mascali, European Physical Journal A **53**, (2017).

[8] E. Naselli et al., Journal of Instrumentation **14**, (2019).

[9] E. Naselli et al., JINST **13**, (2018).

[10] S. Biri et al., Journal of Instrumentation **13**, (2018).

[11] E. Naselli et al., Plasma Sources Science and Technology **28**, (2019).

[12] R. Racz et al., Journal of Instrumentation **13**, (2018).

[13] E. Naselli et al., submitted to Il Nuovo Cimento C (2021).

[14] E. Naselli et al., Proceedings of the 24th International Workshop on ECR Ion Sources, Italy, Catania, JACow (2020).

[15] S. Biri et al., accepted for publication on JINST (2021).

[16] R. Racz et al., Proceedings of the 24th International Workshop on ECR Ion Sources, JACow (2020).

[17] E. Naselli et al., EPJ Web Conf. **227**, (2020).

[18] Unsold A. et B. Baschek, *The New Cosmos: An Introduction to Astronomy and Astrophysics* (Springer, New York, 2002).

[19] Chen F. F., *Introduction to the Plasma Physics and Controlled Fusion: Plasma Physics* (U.K.:London Press, London, 1986).

[20] G. Shirkov et al., Riken Accelerator Research Facility (2000).

[21] Geller R, *Electron Cyclotron Resonance Ion Sources and ECR Plasmas* (J. W. Arrowsmith Ltd, Bristol, UK, 1996).

[22] G. Gibson et al., Phys. Rev. Letters (1960).

[23] Krall N. A., *Principles of Plasma Physics* (CA: San Francisco Press, San Francisco Press, San Francisco, 1986).

[24] M. S. Ioffe et al., Plasma Physics (1965).

[25] M. A. Lieberman and A. J. Lichtenberg, Plasma Phys. (1973).

[26] A. Girard et al., Phys. Rev. E (2000).

[27] D. Leitner et al., Rev. Sci. Instrum. (2008).

[28] S.V. Golubev and A.G. Shalashov, PhysRevLett. **99**, (2007).

[29] I. Izotov et al., Plasma Sources Sci. Technol. **24**, (2015).

[30] O. Tarvainen et al., Proc. 20th International Workshop on ECRIS, Sydney, Australia (2012).

[31] A.G. Shalashov et al., Phys. Plasmas **24**, (2017).

[32] A. G. Drentje et al., Rev. Sci. Instrum. (2003).

[33] G. Melin et al., Proc. 10th International Workshop on ECRIS, Knoxville, Tennesse, USA (1990).

[34] L. Celona et al., Rev. Sci. Instrum. (2010).

[35] C. Z. Q. Xie et al., Rev. Sci. Instrum. **66**, 4218 (1995).

[36] L. Celona et al., Rev. Sci. Instrum. (1999).

[37] R.C. Vondrasek et al., Rev. Sci. Instrum **77**, (2006).

[38] L. Celona et al., Report CERN **7**, 443 (2013).

[39] H. Koivisto et al., Rev. Sci. Instrum **77**, (2006).

[40] H. Koivisto et al., Rev. Sci. Instrum **87**, (2016).

[41] V. Skalyga et al., Phys. Plasmas **22**, (2015).

[42] T. Kalvas et al., IEEE Trans. Plasma Sci. **36**, (2018).

[43] S. Gammino et al., IEEE Trans. Plasma Sci. **36**, (2008).

[44] S. Biri et al., Rev. Sci. Instrum. (2013).

[45] A. Kitagawa et al., Proc. 22nd International Workshop on ECRIS, Busan, Korea (2016).

[46] S. Biri et al., High Energy Physics and Nuclear Physics **165**, (2007).

[47] A. Kitagawa et al., Rev. Sci. Instrum. (2012).

[48] O. Tarvainen et al., Plasma Sources Science and Technology **23**, (2014).

[49] D. Hitz et al., Advances in Imaging and Electron Physics **144**, (2006).

[50] M. Sakildien et al., AIP Conf. Proc. (2011).

[51] V. Skalyga et al., AIP Conf. Proc. 2011 (2018).

[52] A J. Lichtenberg et al., Phys. Fluids **29**, (1986).

[53] Puccella G., *Fisica dei Plasmi* (Zanichelli, Bologna, 2011).

[54] D. Giulietti et al., La Rivista del Nuovo Cimento (1998).

[55] H.R. Griem et al., New York: McGraw-Hill (1964).

[56] G.T. Emery et al., Annual Review of Nuclear Science **22**, (1972).

[57] H. Mazaki et al., Physical Review C **5**, (1972).

[58] H.-K. Chung et al., High energy Density Physics **1**, 3 (2005).

[59] S. Palmerini et al., to be published ApJ (2021).

[60] L. Sun et al., Proceedings of the 23th International Workshop on ECR Ion Sources, Italy, Catania, JACow (2018).

[61] M. Busso et al., Ann Rev. Astron. Astropys. **37**, (1999).

[62] S. Cristallo et al., Astrophys. J. Suppl. **197**, (2011).

[63] R. Gallino et al., Proceedings of the International School of Physics "Enrico Fermi" (1986).

[64] M. Raiteri et al., ApJ **371**, (1991).

[65] R. Gallino et al., Apj (1998).

[66] B. Butcher et al., J. Phys.: Conf. Ser. (2013).

[67] X.D.. Butcher et al., Phys. Rev. Lett. (2015).

[68] M. Pignatari et al., Ap. J. (2013).

[69] K. Takahashi and K. Yokoi, ADNDT (1983).

[70] G.Q. Zhao et al., The Astrophysical Journal **822**, (2016).

[71] R. Bingham et al., Astronomy and Astrophysics **370**, 1000 (2001).

[72] M.J. Aschwanden et al., Solar Physics **97**, 159 (1985).

[73] T. Nakagawa et al., Proceedings of the 23th International Workshop on ECR Ion Sources, Italy, Catania, JACow (2018).

[74] S. Gammino et al., Rev. Sci. Instr. **72**, .

[75] S. Biri et al., Rev. Sci. Instrum **83**, (2012).

[76] S. Gammino et al., Plasma Sources Science and Technology **18**, (2009).

[77] G. Torrisi et al., IEEE Trans. Antennas Propag. **67**, 2142 (2019).

[78] R. Racz et al., Plasma Sources Science and Technology **26**, (2017).

[79] D. Mascali et al., Review of Scientific Instruments **87**, (2016).

[80] D. Mascali et al., Rev. Sci. Instrum. **87**, (2016).

[81] G. Torrisi et al., JINST **14**, (2019).

[82] D. Mascali et al., Review of Scientific Instruments **85**, (2014).

[83] A. Gumberidze et al., Review of Scientific Instruments **81**, (2010).

[84] NIST National Institute of Standards and Technology, X-Ray Form Factor, Attenuation and Scattering Tables.

[85] T. Ryohei et al., Wiley Online Library (2016).

[86] S.X. Kang et al., Nuclear Instruments and Methods in Physics Research B **192**, 365 (2002).

[87] A.G. Karydas and T. Paradellis, AIP Conference Proceedings **475**, 858 (1999).

[88] O. Tarvainen et al., Rev. Sci. Instrum. **86**, (2015).

[89] J. Vamosi et al., Computer Physics Communications **98**, (1996).

[90] F. Consoli et al., Review of Scientific Instruments **79**, (2008).

[91] B. Mishra et al., to be published EpJ-D (2021).

Acknowledgements

The results here described have been obtained in the frame of the PANDORA_Gr3 collaboration, and in particular based on the strict synergy and collaboration between the INFN and ATOMKI-Debrecen plasma and ion sources teams. I wish to thank the support of both the institutions and, in particular, the actual director – Dr. Santo Gammino – and the former – Dr. Giacomo Cuttone – of the LNS that was my host institution during the three years of PhD, and all the laboratory staff.
I would like to express my gratitude to Prof. Francesco Leone, who followed my PhD activities as the academic tutor. I deserve my sincere gratitude to the scientific tutor Dr. David Mascali for giving me an opportunity to carry out the research activities in the attractive field of research of the PANDORA_Gr3 project, and for his invaluable guidance and support in the course of this work.
Several activities of the work described in this thesis have been carried out at the ATOMKI Laboratories: in particular, I wish to thank the Dr. Sandor Biri and the Dr. Richard Racz for the opportunity to stay there during several experimental activities, in a friendly and intellectually fertile environment and for their precious help and collaboration for the measurements carried out.
The supports of the PhD course coordinators, the actual – Prof. Sebastiano Albergo – and the former - Prof. Vincenzo Bellini – are especially acknowledged.
I wish to thank Dr. Domenico Santonocito, Dr. Luigi Cosentino, Dr. Alessio Galatà and Dr. Luigi Celona for professional help and fruitful.

I extend my thanks to all people, and friends, working with the research group, especially Dr. Giuseppe Torrisi, Dr. Giorgio Mauro, Dr. Maria Mazzaglia, Dr. Simone Amaducci and Dr. Vincenza Bonanno for the support during all the PhD experimental activities at INFN-LNS and for enjoyable and friendly moments shared with me.
Finally, thanks to my parents, to my brother Adriano and to Salvo for always sustaining me: my work would not possible without your support.